UNIVERSITÉ LOUIS PASTEUR STRASBOURG

Thèse présentée pour obtenir le grade de
Docteur de l'Université Louis Pasteur
Strasbourg I

Discipline : Science du Vivant

par Patrick Pirrotte

Applications biologiques du NanoSIMS

Soutenue publiquement le 27 novembre 2007

Membres du jury

Directeur de Thèse : M. François Lasbennes, Professeur, Université Louis Pasteur
Directeur de Thèse : M. Claude P. Muller, Professeur, Université de Trèves
Rapporteur Interne : M. Jean-Pierre Bucher, Professeur, Université Louis Pasteur
Rapporteur Externe : M. Ron M. Heeren, Professeur, Université d'Utrecht
Rapporteur Externe : M. Alain Croisy, Docteur, Institut Curie

This doctoral thesis has been performed at the Département d'Immunologie

Laboratoire National de Santé, Luxembourg

under the guidance of

Professor Claude P. Muller, Département d'Immunologie, Laboratoire National de Santé, Luxembourg

and

Professor François Lasbennes, Institut des Neurosciences Cellulaires et Intégratives, Strasbourg

---

Part of this work was performed at

Centre de Recherche Public – Gabriel Lippmann – Science and Analysis of Materials, *Luxembourg*

Centre de Recherche Public – Santé, Luxembourg

Plateau technologique de l'IFR 37 des Neurosciences, Strasbourg

Plateforme RIO d'Imagerie Cellulaire Strasbourg Esplanade

Acknowledgments

I am deeply indebted to my promoter Professor Claude P. Muller who allowed me to join his team at the *Department of Immunology* of the *Laboratoire National de Santé, Luxembourg*. He managed to provide excellent scientific guidance and support whilst allowing me to develop my own ideas.

I thank my second promoter Professor François Lasbennes from the *Institut des Neurosciences Cellulaires et Intégratives, Strasbourg* for his interest in the project and the unyielding support he gave me in the last 6 years to further my career in Biological Imaging.

I would like to express my gratitude towards the staff of the *Centre de Recherche Public - Gabriel Lippmann Science and Analysis of Materials*, *Luxembourg,* Dr Jean-Nicolas Audinot, operator of the NanoSIMS, Dr Henri-Noël Migeon, Jérôme Demange and Esther Lentzen for sharing their expertise and for allowing me to use the facilities available in their laboratory.

Most of the electron microscopy work presented in this thesis was performed at the *plateau technologique de l'IFR 37 des Neurosciences, Strasbourg.* I am grateful to Valérie Demaïs and Dr Yannick Bailly for their assistance in developing this technique.

I would also like to thank Dr Matthieu Erhardt from the *plateforme RIO d'Imagerie Cellulaire Strasbourg Esplanade* for his help in analysing lichen samples by electron microscopy.

I would like to thank Dr Emmanuel Prodhomme and Dominique Revets for their scientific support and encouragement, their critical reading of the manuscript and their continuous help in fighting daily frustrations.

I would also like to thank Sandrina Azevedo for introducing me to the interesting world of lichens and Ana Fernández-Salegui for providing samples from her lichen study for me to analyze on NanoSIMS.

Special thanks go to Dr Jérôme Mutterer without whom I probably would not have discovered the joys of digital image processing and whose knowledge on confocal microscopy enlightened me.

I am indebted to Professor André Steinmetz and Dr Céline Hoffmann for granting me access to the confocal platform of the *Centre de Recherche Public – Santé, Luxembourg* and for their useful advices.

A special mention goes to Dr Jean-Luc Guerquin-Kern from the *Centre de Recherche Imagerie intégrative : de la molécule à l'organisme* at the *Institut Curie, Paris* for his insightful ideas in SIMS.

I acknowledge the *Centre de Recherche Public – Santé*, the *Fond National de la Recherche*, *Ministère de la Culture, de la Recherche et de l'Enseignement Supérieur* and the *Fondation Reinert-Schwachtgen* that trusted me with a research scholarship. Without their financial assistance, this research would not have been possible.

Many thanks go to Claude Schwachtgen for the proofreading of the manuscript and to Daniel Toth for his help in printing this manuscript.

I would also like to acknowledge my colleagues from the *Department of Immunology* who shared their knowledge and expertise with me, amongst them most specially Wim Amerlaam, Dr Jacques Kremer, Dr Stefan de Buck, Sophie Farinelle, Stéphanie Willième, Julia Kessler, Dr Fabienne Bouche, Dr Jonathan Turner. Special thanks go to Dr Fred Fack, whose encyclopedic knowledge was a fountain of challenging ideas. I am grateful to Ulla Muller and Carole Weis for their continuous assistance.

I would like to thank Joana for all her constant support, encouragement and so much more.

I am deeply indebted to my parents, who supported me patiently for all these years.

Abstract

Secondary Ion Mass Spectrometry (SIMS) is based upon the sputtering of a few atomic layers from the surface of a sample, induced by a 'primary ion' bombardment. An energetic primary ion impact triggers a cascade of atomic collisions resulting in an erosion of atoms and molecules. Some of the ejected particles can be spontaneously ionized and are representative of the target area composition. In a SIMS instrument, these "secondary ions" are accelerated and separated in function of their mass/charge ratio (m/z) before detection. The NanoSIMS is a dynamic SIMS ion microprobe capable of imaging the distribution of elemental ions at high lateral resolution (50 nm) with a high mass resolution.

The aim of this thesis was to define the requirements of such instruments, to evaluate their utility in life sciences and to develop potential applications in biology. In order to do so, preparative and analytical methods had to be devised to improve ion imaging by SIMS. The limited knowledge about the behaviour of biological samples under a primary ion beam impeded the identification of tissue and cellular features and required supplementary confirmation by complementary techniques. The ability of SIMS to discriminate isotopes of a same element has encouraged us to develop isotopically labelled biomolecules of varying specificity. Abiding to the experience gained in the course of the thesis, several applications are proposed in the areas of trace metal detection, antigen uptake and protein localization. Finally, NanoSIMS is compared to other techniques of microanalytical imaging and the role of the ion microprobe in life sciences is discussed as well as its prospects.

Keywords: SIMS, NanoSIMS, imaging, stable isotope, 15-Nitrogen, immunolabelling, pulse chase, metabolic labelling, trace metal detection, implantation, ratiometric analysis

List of abbreviations

AA	Amino acid
ABC	Ammonium bicarbonate buffer
APC	Antigen presenting cells
ATCC	American Type Culture Collection
Beta	Beta-actine
BrdU	5'-bromo-2-deoxyuridine
BSA	Bovine serum albumine
CHAPS	3-[(3-Cholamidopropyl)dimethylammonio]-1-propanesulfonate
CLSM	Confocal Laser Scanning Microsope
DHB	2,5-dihydroxybenzoic acid
DMSO	Dimethyl Sulfoxide
dSIMS	Dynamic secondary ion mass spectrometry
EDTA	Ethylenediaminetetraacetic acid
FBS	Fetal bovine serum
Fitc	Fluorescein isothiocyanate
GAPDH	Glyceraldehyde-3-phosphate dehydrogenase
HA	Hemagglutinin
HCCA	α-Cyanohydroxycinnamic acid
LNS	Laboratoire National de Santé
MALDI	Matrix assisted Laser Desorption Ionization
MOI	Multiplicity of infection
MV	Measles Virus
MW	Molecular weight
NP	Nucleoprotein
NS50	Cameca NanoSIMS 50
OM	Optical microscope
PBS	Phosphate buffered Saline
PI	Propidium iodide
PMA	Phorbol myristate acetate
PMF	Protein mass fingerprint
PSD	Post-source decay
SAM	Service Analyse des Matériaux
SEM	Scanning Electron Microscope
SIMS	Secondary ion mass spectrometry
sSIMS	Static secondary ion mass spectrometry
TEM	Transmission Electron Microscope
TFA	Trifluoroacetic acid
TOF	Time of flight

Table of Contents

Figure Index

Table Index

Le résumé de thèse de doctorat est rédigé en français.
Le corps de la thèse est rédigé en anglais.

Résumé de thèse de doctorat

I Introduction (Chapitre I)

La spectrométrie de masse à ions secondaires (« Secondary Ion Mass Spectrometry », SIMS), évoquée pour la première fois dans les travaux de thèse de Georges Slodzian en 1963, est une technique d'analyse de surface répandue dans les laboratoires d'analyses des matériaux (Castaing and Slodzian 1962). Son principe, qui n'est pas sans rappeler celui d'un microscope électronique à balayage, réside dans l'utilisation le plus souvent d'une source de césium, de gallium ou d'oxygène, émettant un faisceau à ions primaires érodant un échantillon sous ultra-haut vide (10^{-10} Torr). L'impact des ions primaires provoque une cascade de collisions atomiques causant un déplacement des éléments constitutifs de l'échantillon. Une fraction de ces ions, réelle empreinte caractéristique de la composition chimique du spécimen, est émise sous forme d'ions mono- ou polyatomiques, extraite sous forme de faisceau d'ions secondaires et séparée selon les critères d'énergie et de masse par un spectromètre. Deux modes d'émission d'ions secondaires peuvent être distingués, dépendant tous deux de la concentration d'ions implantés dans l'échantillon lors de l'analyse.

En mode statique, le faisceau d'ions primaires est d'intensité faible et l'émission d'ions secondaires est provoquée par une concentration définie en ions primaires implantés (10^{13} atomes/cm^2 pour des ions primaires de Cs^+). Dans ce mode le phénomène d'érosion par le faisceau primaire est faible et permet l'analyse de couches monoatomiques à la surface de l'échantillon. En moyenne, moins d'1% de la matière de l'échantillon est pulvérisée dans ce mode et la fragmentation des molécules de l'échantillon est limitée. Les ions émis en SIMS statique sont principalement moléculaires et permettent l'identification par la technique dite « d'empreinte moléculaire ».

En SIMS dynamique, l'intensité du courant primaire du faisceau est supérieure à celle du mode statique. Dans ce mode, l'émission des ions secondaires dépend de l'entrée en régime dynamique déclenché par une concentration en ions primaires implantés supérieure au mode statique (10^{17} atomes/cm^2 pour des ions primaires Cs^+). L'échantillon est entièrement pulvérisé, la fragmentation totale et les ions émis sont de nature élémentaire. Ce mode permet de réaliser des profils en profondeur des échantillons afin de connaître la distribution élémentaire par rapport aux couches successives analysées.

Le profilage en profondeur ultrasensible (ppm au ppb) est très répandu dans les domaines des semi-conducteurs, de la métallurgie, de l'industrie du verre, de la céramique et des polymères où il est un outil de choix aussi bien pour le contrôle-qualité que pour la caractérisation formelle d'un échantillon. Les microsondes SIMS, véritables microscopes ioniques, ont une

particularité supplémentaire : ils sont capables d'opérer en mode imagerie et de cartographier la distribution latérale des ions.

En dehors de quelques applications relevant pour la plupart de cas d'école, les conditions d'analyses astreignantes pour des échantillons biologiques et la méconnaissance de la méthode en sciences de la vie, ont été un frein à l'essor de la microscopie ionique en dehors du domaine de l'analyse des matériaux. Les travaux présentés dans ma thèse de doctorat, intitulée «Applications biologiques du NanoSIMS » tentent de mieux définir l'utilité et la place de la microscopie ionique élémentaire en sciences de la vie. Ils se basent sur le NanoSIMS 50, un SIMS dynamique récemment développé par Georges Slodzian pour CAMECA. Cet instrument fait partie d'une nouvelle génération de spectromètres de masse à ions secondaires, construit pour l'imagerie ionique à haute résolution latérale (inférieure à 50 nm) et dont la bonne résolution en masse permet la discrimination isotopique (Slodzian, Daigne et al. 1991; Hillion, Daigne et al. 1993). Les travaux présentés dans cette thèse sont axés d'une part sur le développement de techniques de préparations d'échantillons biologiques pour le NanoSIMS, et d'autre part sur la recherche d'applications biologiques où le NanoSIMS apporte une forte valeur ajoutée. Pour ce faire, plusieurs outils informatiques ont été développés afin de permettre le traitement d'images provenant de cet instrument. Certaines suggestions sont proposées afin d'améliorer les conditions d'analyses et d'acquérir des images de meilleure qualité.

La thèse est présentée sous forme de chapitres distincts, reprenant tout d'abord les développements orientés sur la technique (Chapitre II et Chapitre III) avant de passer aux chapitres exposant les possibilités et les applications potentielles du NanoSIMS (Chapitres IV à VI). Chaque chapitre est clos par une discussion dont les points principaux sont repris dans la *Discussion Générale* située en fin de thèse. Les points majeurs des résultats et de la discussion sont repris dans ce résumé, de manière non exhaustive.

II Résultats

II.1 Développement d'outils informatiques (Chapitre II)

L'usage de la microscopie confocale constitue la base de l'imagerie biologique et en servant de référence elle permet dans le cadre de cet ouvrage de mieux mettre en perspective l'usage du NanoSIMS. Ayant développé un logiciel de traitement d'images confocales lors de mon DESS en Imagerie Biologique, nous avons utilisés les sources de ce programme afin de développer un logiciel similaire pour le NanoSIMS. Depuis 2004, l'utilisation de ce

programme s'est fortement répandue dans de nombreux laboratoires de microscopie confocale.

Devant utiliser pour les travaux de cette thèse des logiciels peu adaptés au traitement post-acquisition de cartographies ioniques SIMS, il était nécessaire de développer un nouveau logiciel incluant des méthodes de traitement d'images de type ratio isotopiques telle que la méthode dite « standard » ou la transformation « Hue, Saturation, Intensity »). Cette méthode permet de multiplier le ratio entre les pixels de deux images par des facteurs de poids variables et d'attribuer une palette couleur hautement contrastée à l'image du ratio afin de rehausser des signaux faibles du bruit de fond. Courante en calcul de ratios calciques (Tsien and Harootunian 1990), elle a été introduite pour la première fois en SIMS par Doug Benson et Claude Lechene (Benson and Lechene 2005). En plus de ce traitement analytique, le logiciel propose des fonctions de conversions et de traitements automatisés des fichiers images. Il extrait tous les paramètres d'acquisition présents dans les fichiers et il est à notre connaissance le seul logiciel le permettant. Finalement, l'utilisation d'un algorithme d'équilibrage des histogrammes (« histogram matching ») basé sur une distribution gaussienne bimodale (Gonzalez, Woods et al. 2004) a permis l'amélioration de la qualité des cartographies ioniques.

Ces deux outils ont été développés dans le langage Java de Sun Microsystems et sont compatibles avec de multiples systèmes d'exploitation. Un avantage supplémentaire réside dans le fait qu'ils fonctionnent sur de nombreuses plateformes (Apple Macintosh, PC Windows, Sun). Ils ont tout deux été publiés sous la licence « Gnu Public License » du logiciel libre, et sont téléchargeable gratuitement.

II.2 L'implantation en SIMS (Chapitre III)

Une étude de modélisation du phénomène d'implantation sur des résines époxys homogènes et des effets de la modulation de paramètres (intensité du faisceau d'ions primaires et surface) a été réalisée afin de mieux comprendre le processus physique de l'implantation d'ions primaires de Cs^+, responsable de l'émission d'ions secondaires élémentaires négatifs. Deux modèles différents, respectant les caractéristiques analytiques du NanoSIMS, ont été utilisés lors de cette étude.

Le modèle TRIM, développé par J. P. Biersack et L. G. Haggmark, suit le cheminement des ions implantés sans prendre en compte la pulvérisation de l'échantillon à l'impact (Ziegler 1977-1985; Biersack and Haggmark 1980; Biersack and Eckstein 1984).

TRIDYN, une évolution de TRIM, paramètre l'ablation continue de la matière par le faisceau d'ions primaires lors d'une analyse SIMS. Les résultats obtenus par modélisation ont été corroborés par des observations sur l'implantation de cellules et de tissus inclus dans une résine époxy. Aucune différence dans l'émission d'ions secondaires n'a été décelée entre les différents types d'échantillons.

Ces travaux ont standardisé l'analyse d'échantillons biologiques par microscopie ionique et ont permis de trouver un compromis entre la durée d'implantation et la qualité de la cartographie des zones implantées tout en identifiant l'entrée en régime dynamique à une dose d'implantation de 10^{17} atomes/cm^2. En outre, une implantation de Cs^+ à une intensité de 2 nA au lieu de 160 pA, a fortement diminué le temps nécessaire à l'entrée en régime dynamique tout en conservant la qualité des images acquises par la suite. Des intensités de courant supérieures à 2 nA ont provoqué une dégradation de l'échantillon due à une pulvérisation hétérogène. L'augmentation du profil de surface est probablement à l'origine d'une extraction différentielle des ions secondaires selon la profondeur de la surface de l'échantillon dans le champ électrique des lentilles d'extraction.

Une implantation préalable dans un SIMS tel que l'IMS-6f, implantant une surface jusqu'à 40 fois supérieure, suivi d'un transfert au NanoSIMS a permis de se placer dans le régime dynamique dès le début de l'analyse à haute résolution Deux méthodes de transfert ont été examinées, l'une sous vide à l'aide d'une cassette de transfert à 10^{-7} Torr et l'autre à pression atmosphérique après équilibrage en atmosphère azotée. Ces deux méthodes ont donné des images de bonne qualité tout en réduisant la réaction dommageable à l'échantillon du Cs^+ très réactif implanté en surface avec l'oxygène de l'air. En rendant l'implantation sur le NanoSIMS facultative, la pré-implantation sur l'IMS-6f a considérablement augmenté le nombre d'analyses journalières (en moyenne 50% en plus).

En outre, la caractérisation de l'implantation de Cs^+ dans les échantillons biologiques a permis de réduire le nombre d'images présentant une implantation insuffisante, traduite par une orientation particulière de l'intensité de l'image ou par des émissions basses d'ions secondaires.

II.3 Imagerie SIMS (Chapitre IV)

L'outil SIMS ayant un caractère expérimental, et dont les processus physiques ne sont pas encore bien maitrisés, il a fallu optimiser de nombreux paramètres afin d'obtenir des résultats reproductibles. La préparation d'échantillons, apparentée à celle de microscopie électronique à transmission (MET) doit tenir compte de plusieurs facteurs tel que (i) la sensibilité de la

technique où les pollutions élémentaires sont à éviter dans le cas d'une analyse de ces mêmes éléments, (ii) le type de support utilisé (plot acier, feuillet de cuivre, plaques de silice), (iii) le type de fixation à préférer selon le type d'analyse afin d'éviter la diffusion des ions mobiles de petite masse (cryogénique par opposition à chimique).

Il s'est avéré que l'interprétation des images provenant du NanoSIMS est complexe et que la confirmation des résultats biologiques par d'autres techniques d'analyses est nécessaire. Lors de mes travaux, j'ai été amené à utiliser différentes techniques d'imagerie telle que la microscopie à épifluorescence, la microscopie confocale et la microscopie électronique à transmission afin de confirmer des aspects morphologiques (identification de tissus et cellules) ou moléculaires (immunomarquages). La similitude des préparations d'échantillons en SIMS et MET font de la microscopie électronique une technique de comparaison de choix. En première approche, et afin d'optimiser les protocoles de préparation d'échantillons aux conditions analytiques de la microscopie ionique, des tissus et cellules de provenances variées ont été préparés et analysés. L'identification de la morphologie de tissus de souris tel que le cœur, le rein, le cerveau, ou les plaques de Peyer, un tissu lymphoïde secondaire, a favorisé la familiarisation avec la cartographie ionique à haute résolution.

II.4 Etude de la distribution de métaux dans des organismes bioindicateurs (Chapitre V)

L'expérience obtenue lors de l'analyse des tissus précédents (Chapitre IV) a été mise en exergue dans une étude de la pollution environnementale. Les lichens sont des organismes symbiotiques composés d'algues ou de cyanobactéries (« photobiont ») et de champignons (« mycobiont »). Ces organismes sont considérés comme d'excellents bioindicateurs grâce à leur capacité d'accumulation de métaux provenant de l'environnement. Une association entre des algues du genre *Trebouxia* et un ascomycète de la famille des *Parmeliacée*, le lichen *Evernia prunastri (L.) Ach*., provenant de plusieurs sites pollués en Espagnel nous a été fournis dans le cadre d'une collaboration avec les universités d'Aveiro au Portugal et de Léon en Espagne. Une étude GCMS a déterminé des concentrations jusqu'à 30 fois supérieures à la normale pour certains métaux tel que le cuivre, l'aluminium ou le zinc. Les lichens ont été préparés par cryofixation et cryosubstitution afin de réduire le déplacement d'ions de faible masse. Une étude préliminaire sur la physiologie des tissus préparés a été réalisée par MET afin de déterminer la qualité de la préparation et la physiologie de l'échantillon. Grâce à un portoir d'échantillons permettant d'analyser des grilles MET en SIMS, ces mêmes préparations ont été observées sur le NanoSIMS. Une accumulation des éléments traces

susnommés a été identifiée par microscopie ionique au niveau des parois cellulosiques des algues. Une étude par sonde nucléaire μ-PIXE a montré une distribution orientée à basse résolution (>2 μm) au niveau des tissus, avec une accumulation de ces éléments au niveau du cortex supérieur et de la couche d'algues sous-jacente (Ayrault, Clochiatti et al. 2007). Ceci corrobore nos résultats sur la distribution d'éléments traces en provenance de la pollution atmosphérique, tout en détaillant leur localisation à haute résolution au niveau de cellules individuelles.

III.5 Suivi de la phagocytose d'un antigène marqué par NanoSIMS (Chapitre VI)

Le NanoSIMS peut séparer, sous certaines conditions, des isotopes d'un même élément. La difficulté principale qui se pose est l'existence d'interférences en masse qui peuvent se présenter sous la forme d'isobares polyatomiques, tel que $^{12}C^{15}N$, $^{13}C^{14}N$ $^{13}C_2H$, $^{12}C^{13}CH_2$ et $^{12}C_2H_3$ tous à la masse atomique de 27. L'excellente résolution en masse du NanoSIMS permet d'atteindre un M/ΔM de 4272 nécessaire pour résoudre $^{12}C^{15}N$ de $^{13}C^{14}N$. Plus la masse des ions augmente, plus le nombre d'interférences augmente, ce qui explique pourquoi des isotopes d'éléments de basse masse tel que le ^{13}C ou le ^{15}N sont utilisés majoritairement en SIMS. Leur importance dans les échantillons biologiques en fait des éléments de choix pour le marquage par SIMS.

Une approche de marquage étudiée lors de cette étude est le marquage métabolique par addition de nutriments composés d'isotopes stables. Les bactéries *Escherichia coli* ont été cultivées dans un milieu minimum enrichi en chlorure d'ammonium ($^{15}NH_4Cl$) comme seule source d'azote. La présence de ^{15}N a été démontrée par MALDI-TOF, où l'incorporation de l'isotope a pu être suivie au niveau d'une protéine bactérienne ubiquitaire. L'analyse par MALDI-TOF d'une digestion tryptique de la protéine a indiqué l'intégration de ^{15}N au niveau des peptides et des acides aminés.

Le processus d'ingestion d'un antigène marqué, ici les bactéries marquées à l'^{15}N, par des monocytes différenciés en macrophages a été suivi par NanoSIMS. Le microscope ionique a notamment permis de visualiser dans le temps, la distribution en gradient des métabolites issus de la digestion des bactéries dans les phagosomes, et leur utilisation progressive comme constituant cellulaire des macrophages. Certaines régions n'ont pas ou peu incorporé de ^{15}N, et correspondaient probablement à des organelles ayant un turnover protéique faible ou dont le rôle dans la dégradation de l'antigène marqué n'était pas clairement défini.

III.6 Immunomarquage par NanoSIMS (Chapitre VII)

A ce jour, les quelques marquages utilisés en SIMS sont des molécules de faible masse, à spécificité variable, contenant des éléments halogènes tels que le fluor, l'iode ou le brome. Les plus communs sont le 5'-bromo-2'-deoxyuridine (Galle 1991), un analogue de la thymidine, et l'iodobenzamide ciblant la mélanine (Chehade, Michelot et al. 1996). Afin de profiter au mieux de la haute résolution en masse du NanoSIMS, nous avons développé une sonde hautement spécifique marquée au ^{13}C et au ^{15}N. Pour ce faire, le milieu de culture d'hybridomes sécrétant des anticorps monoclonaux contre la nucléoprotéine (NP) du virus de la rougeole a été supplémenté de deux acides aminés doublement marqués, la $^{13}C_6$ $^{15}N_2$ L-Lysine et la $^{13}C_6$ $^{15}N_4$ L-Arginine. La reconnaissance des sites antigéniques de la nucléoprotéine par l'anticorps a été confirmée par microscopie confocale.

L'anticorps marqué a été utilisé dans le cadre d'une étude sur l'accumulation de nucléoprotéine virale dans des cellules infectées et sur la formation potentielle d'agrégats entre la NP et la MxA, une protéine humaine ayant des propriétés antivirales. Afin de déterminer la chronologie d'une infection par la rougeole de monocytes humain (lignée THP-1), la microanalyse par NanoSIMS a été précédée d'une étude de l'expression de l'ARN messager de (i) l'hémagglutinine virale, favorisant la fusion du virus enveloppé aux membranes cellulaires, (ii) la nucléoprotéine virale, protéine structurale de la capside du virus, et (iii) la MxA. Une expression fortement augmentée de ces protéines a été relevée 24 h après infection, à un taux de mortalité des cellules en dessous de 5%. La préparation d'échantillons pouvant identifier les sites d'accumulation de NP par l'anticorps marqué sur le NanoSIMS s'est apparentée à l'immunomarquage pour MET et a permis de démontrer la présence de sites riches en NP dans le cytoplasme des cellules. C'est à ce jour la première description d'un immunomarquage isotopique pour SIMS.

Une seconde application de SIMS, résultant d'un marquage non spécifique des protéines néosynthétisées, a également été élaborée et figure dans ce chapitre. Elle se base sur une expérience « pulse-chase » qui se divise en trois parties : (i) la partie déplétion où la cellule est placée dans un environnement appauvri en un métabolite défini, (ii) la partie « pulse », où le milieu est supplémenté du métabolite marqué (couramment par un radio-isotope), et (iii) la partie « chase », où le milieu est remplacé par un milieu contenant le métabolite non marqué. Cette expérience permet de suivre l'incorporation différentielle du métabolite et sa progression pendant le « turnover » protéique.

Cette technique, adaptée au SIMS en utilisant comme « pulse » métabolique un isotope stable, a permis de visualiser une modification du turnover protéique entre des cellules infectées et

des cellules non infectées. De plus, des régions du cytoplasme de cellules infectées plus fortement marquées pourraient correspondre à des zones d'accumulation de la NP, protéine virale formée majoritairement par la machinerie cellulaire lors d'une infection avancée.

IV. Discussion (Chapitre VIII)

Afin de répondre à la question de l'utilité et de la praticabilité du NanoSIMS en Sciences de la Vie, une approche prospective a été choisie, alliant développements techniques et applicatifs. Les volets principaux de cette thèse sont la préparation d'échantillons, les conditions d'analyses, le traitement des données d'images de microscopie ionique et confocale. En outre, ce document soulève des hypothèses, des possibilités de modifications particulièrement à ces niveaux, permettant d'améliorer la technique SIMS et la rendre plus attractive aux biosciences.

Une importante partie des résultats porte également sur la recherche d'applications potentielles pour le NanoSIMS dans différents domaines, de l'imagerie purement morphologique, à la localisation d'éléments traces et à l'utilisation de marqueurs halogènes et isotopiques.

Trois grands axes se sont dessinés lors de l'évolution des travaux présentés dans cette thèse. La sensitivité de l'instrument ainsi que sa résolution latérale, le rendent particulièrement intéressant pour des études de pollution atmosphérique et la localisation de métaux. Cette affirmation est soutenue par une étude sur la distribution de plusieurs métaux dans des lichens, des bioindicateurs de pollution environnementale.

Grâce à sa résolution en masse, il permet de suivre directement des molécules marquées par des isotopes au lieu de suivre des greffons fluorescents sur ces molécules, s'affranchissant ainsi de certains désavantages de fluorophores volumineux dont la taille peut influencer la migration, la spécificité ou la fonction de la molécule observée.

Finalement, il a été démontré que le marquage métabolique avec des isotopes stables suivis par NanoSIMS dans le cadre d'une expérience « pulse-chase » constitue une alternative viable au marquage différentié par radioisotopes.

Pour conclure, il important de souligner qu'à ce jour peu de NanoSIMS ont été construits, cet état de fait se traduit par une faible dissémination de l'imagerie ionique à haute résolution. Les instruments, s'apparentant à des prototypes, entraînent une méconnaissance de la technique et un nombre d'applications peu développés qui à leurs tours limitent l'utilisation et la productivité. Malgré ces problèmes, entre autre liés à la complexité de l'analyse et à la stabilité d'un tel appareil, le NanoSIMS mérite sa place dans les techniques de cartographie

microanalytique, à condition de lui adjoindre des techniques alternatives, tel que la MET, la microscopie optique classique ou confocale, ou encore le MALDI-Tof pour la caractérisation de sondes isotopiques.

IV. Références

Ayrault, S., R. Clochiatti, et al. (2007). "Factors to consider for trace element deposition biomonitoring surveys with lichen transplants." Science of The Total Environment **372**(2-3): 717.

Benson, D. and C. Lechene (2005). "Quantitating MIMS Ratios Using Hue, Saturation, and Intensity Displays."

Biersack, J. P. and W. Eckstein (1984). "Sputtering studies with the Monte Carlo Program TRIM.SP." Applied Physics A: Materials Science & Processing **34**(2): 73.

Biersack, J. P. and L. G. Haggmark (1980). "A Monte Carlo computer program for the transport of energetic ions in amorphous targets." Nucl. Instr. and Meth. **174**: 257.

Castaing, R. and G. Slodzian (1962). "Microanalyse par émission ionique secondaire." J Microscopy(1): 395-410.

Chehade, F., J. Michelot, et al. (1996). "Localization of N-(2-diethylaminoethyl)4-iodobenzamide in the pigmented mouse eye: a microanalytical study." Cell Mol Biol (Noisy-le-grand) **42**(3): 343-50.

Galle, P. (1991). "Cartographies moléculaires ultrastructurales par microscopie ionique." **7**(9): 944-952.

Gonzalez, R. C., R. E. Woods, et al. (2004). Digital Image Processing using Matlab, Prentice Hall.

Hillion, F., B. Daigne, et al. (1993). A new high performance instrument: the Cameca Nanosims 50. Proceedings IXth Conference on SIMS, Yokohama, Elsevier.

Slodzian, G., B. Daigne, et al. (1991). A high resolution scanning ion microscope with parallel detection of secondary ions. Proceedings VIIIth Conference on SIMS, Amsterdam, Elsevier.

Tsien, R. Y. and A. T. Harootunian (1990). "Practical design criteria for a dynamic ratio imaging system." Cell Calcium **11**(2-3): 93-109.

Ziegler, J. (1977-1985). The Stopping and Range of Ions in Matter, Pergamon Press. **2-6**.

Chapter I Introduction

For countless ages, seeing the invisible has been man's dream. What started as simple curiosity, to watch either small objects from daily life or the distant stars, has ultimately led to the development of a modern scientific approach of analytical and descriptive imaging. While written reports of optical lenses appeared as early as 500 BC in Ancient Greece, their use was limited to the rich and educated and their magnifying properties mainly regarded as an artistic curiosity. The major turmoil provoked by the fall of the Roman Empire and the ensuing fragmentation of the Greater Europe and the Mediterranean Basin resulted in a major loss of knowledge and art. As a result, lenses resurged only at the end of the early Middle Ages but applications had diversified, the most notable being the appearance of spectacles as a help to the ailment of failing vision. In the last centuries, discoveries and inventions, backed up by mathematical descriptions of optical phenomena such as *Abbe's sine condition* and *Snell's law,* have led to modern optics and the building of microscopes and telescopes.

In retrospective, the history of lenses is a quest that has spanned over two millennia to image both big and small, or differently put, far and close. The accumulated facts gained during that quest were instrumental in the definition of most of the scientific knowledge as we know it, from the descriptive study of flora and fauna to the investigation of medical conditions. Thus was born the scientific field of "Imaging".

Over time and with a better understanding of nature, curiosity of man took over again with the need to observe not only the photons that form light, but also other particles that form our environment such as atoms and electrons. Over the last hundred years, Imaging has expanded accordingly, accommodating new techniques and instruments. Roger Y. Tsien, a pioneer in the field of biological molecular imaging, stated in his famous article, "Imagining Imaging's future", that

"I believe this quest will depend heavily on molecular imaging, which shows when and where genetically or biochemically defined molecules, signals or processes appear, interact and disappear, in time and space. Therefore, molecular imaging synergistically draws on physics, chemistry, anatomy, physiology, biochemistry and genetics." (Tsien 2003).

Moreover, Figure 1 depicts Tsien's classification of common imaging techniques using the criteria of lateral resolution, depth of analysis and time resolution of biological processes.

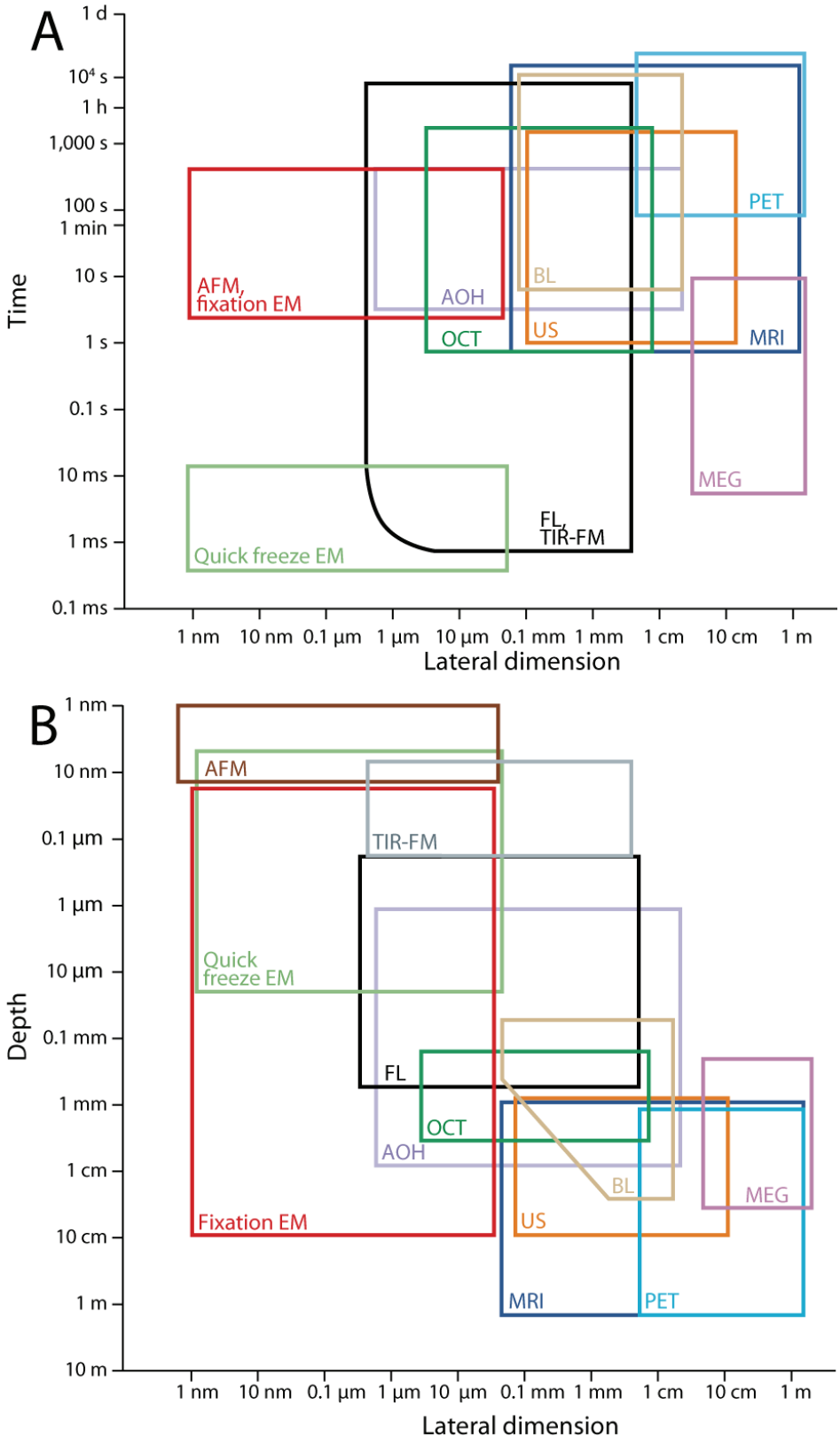

Figure 1: Imaging methods compared by their timescales, penetration depths and ranges of lateral dimensions. *All scales are logarithmic, and all box boundaries are estimates of typical present practices and are much fuzzier than the crisp lines shown. (A) Each time span, except for electron microscopy (EM) techniques, indicates the range from the shortest time difference that can be comfortably resolved by a particular technique to the maximum duration of continuous observation. For EM techniques, the timescale indicates the estimated*

time required for freezing or fixing the tissue. Lateral dimensions range from the finest spacing over which separate objects can be discriminated up to the maximum size of a single field of view. (B) Depth dimensions range from the minimum thickness for an adequate signal, to the maximum depth of imaging without a severe loss of sensitivity or lateral resolution. Note that far-red or near-infrared fluorescence can be comparable to bioluminescence in terms of depth resolution. Again, lateral dimensions range from the finest spacing over which separate objects can be discriminated up to the maximum size of a single field of view. AFM, atomic-force microscopy; AOH, all-optical histology; BL, bioluminescence; FL, fluorescence microscopy at visible wavelengths; MEG, magnetoencephalography; MRI, functional magnetic resonance imaging; OCT, optical coherence tomography; PET, positron emission tomography; TIR-FM, total internal reflection fluorescence microscopy; US, ultrasound. Reproduced with permission from Nature Reviews Molecular Cell Biology (Tsien 2003) copyright (2003) Macmillan Magazines Ltd.

Clearly, photons are not the hallmark of imaging anymore. Furthermore, in highly industrialized countries imaging instruments are not the exclusivity of life sciences or the product of purely academic cooperation. Quite the contrary, today's technology transfers between industry and academia go both ways to the benefit of all parties involved. One of these instruments, widely used in industry, is based on Secondary Ion Mass Spectrometry (SIMS) to characterize charged elemental or atomic particles, termed ions. However, the value of SIMS in life sciences has not yet been fully explored. The imaging technique under focus in this thesis is called NanoSIMS, a subfamily of SIMS instruments, recently introduced on the market by mass spectrometer manufacturer Cameca. Devised for high resolution imaging of ions, it claims to revolutionize the way we look at biological samples. This thesis will try to shed some light on potential biological applications by presenting several routes that one may wish to explore with this novel instrument. It will also present several technical improvements in the sample preparation for SIMS, crucial to each imaging technique, in the development of specific molecular probes and in the processing of the resulting imaging data.

I.A. Secondary Ion Mass Spectrometry

I.A.1. General SIMS Principle

Secondary Ion Mass Spectrometry (SIMS) is dedicated to the chemical microanalysis of surfaces based on the phenomenon of secondary ions emitted by the specimen upon impact of a primary ion beam. Introduced in 1962 (Castaing and Slodzian 1962), it relies on the bombardment of primary ions onto the surface of a sample, triggering a cascade of atomic collisions. Some of the ejected particles can be spontaneously ionized as atoms or clusters and are representative of the chemical composition of the target area. In a SIMS instrument, these

"secondary ions" are accelerated and separated in function of their mass/charge ratio (m/z) before detection.

I.A.2. Sputtering, Ionization, Implantation

While the exact ionization processes involved in SIMS are not fully understood, the collision cascade model (Figure 2) is generally accepted as the most intuitive explanation to SIMS ion-matter interaction. At impact, the kinetic energy of primary ions in SIMS analysis is in the range of several keV, resulting only in energy and momentum transfer to a limited area surrounding the point of impact. In the collision cascade model, this energy is transferred in a series of binary collisions from primary ions to target particles, called recoil atoms. A fraction of the recoil atoms from the collision cascade penetrate deeper into the condensed phase, alongside the primary ions during a process termed *implantation.* The backscattered recoil atoms are ejected from the specimen as electrons, photons, atoms and cluster atoms with a kinetic energy of several hundreds eV. During this phenomenon of erosion (*sputtering*), atomic and molecular surface species are removed from the uppermost atomic layers of the bombarded surface. The sputtering phenomenon is characterized by the primary ion beam energy, the primary ion fluence (implantation dose in atoms/cm^2) and the primary ion type.

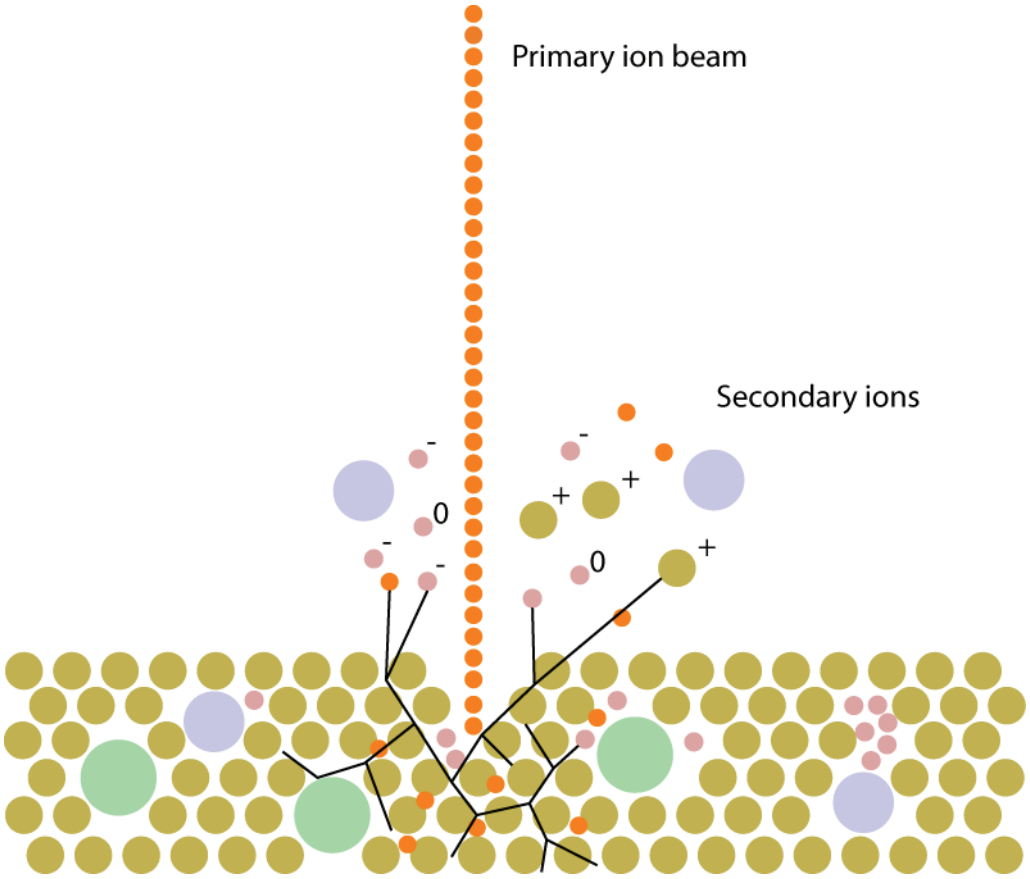

Figure 2: Primary ion beam particles (atoms or clusters) impacting on the sample surface, *causing perturbation on several atomic layers (up to 80 nm). A fraction of ions from the first few atomic layers (several nm) is eroded and forms the secondary ion beam. Surface atoms can penetrate up to 10 nm into the sample.*

Although SIMS is generally considered a destructive technique, the sample erosion is controlled by the modulation of the primary ion dose and two secondary emission regimes can be highlighted.

In the static regime, with a primary ion fluence under 10^{13} atoms/cm^2, roughly one atomic layer is sputtered during the analysis. The operation of a SIMS instrument in the static regime provides elemental and molecular information from the uppermost layers of the specimen. At the low sputtering rates of the static regime, contaminants (e.g. water films or dust) may be, if not the target of the analysis, responsible for the obfuscation of lower layers. Imaging with static SIMS is briefly mentioned in the section "I.D Imaging techniques directly related to SIMS". In the dynamic regime, the fluence is several orders of magnitude higher than in the static regime and the increased rate of bombardment of the sample enhances the effect of surface erosion. The analyzed surface continuously moves down into the sample, driven by the ion beam ablation. The stress induced at the impact favours the breaking of chemical bonds (*total fragmentation*) and the emitted secondary ions are primarily of elemental origin. The enhanced sputtering rate translates into an increase of detection events, resulting in

improved sensitivity (ppm to ppb). This aspect of SIMS is employed to profile variations of elemental composition in relation to depth (*depth profiling*), useful to study layered structures of integrated circuits in the semiconductor industry. The characteristics of the primary ion beam also relate to the achievable depth resolution (discrimination between atoms in adjacent layers) which mainly depends on: (i) the nature of the exerted ion beam, (ii) the uniformity of etching by the incident ion beam and (iii) the depth below the original surface to which etching has already been carried out.

I.A.3. Secondary ion intensity and ionization efficiency

For a given ion species M_i, the *secondary ion intensity* (in counts/s) is described as follows:

$$I(M_i) = T \times Y_i \times d_b \times S \times S_y \times [M]$$

T: instrumental transmission

Y_i: ion yield of Mi

d_b: primary beam density ($A/cm^2/sr$)

S: sputtered area (μm^2)

S_y: sputter yield

[M]: atomic fraction of the species M in the sample

The *sputter yield* S relates to the number of sputtered ions per primary ion, typical values are between 1 and 10. The ion yield Yi is given by the following ratio:

$$Y_i = \frac{M_i}{M}$$

The *useful yield* is dependant on both instrumental and physical conditions:

$$\tau = T \times Y_i$$

τ^{-1} corresponds to the mean number of atoms M that need to be sputtered from the sample to detect a M_i ion.

The ionization efficiency describes the ionization probability of a given element or molecule. It is dependent on the state of the specimen, contributed by the composition of the surrounding matrix (Yu 1986), the implantation of primary ions, the diffusion induced by the particle bombardment and the surface reaction with the vacuum gas phase. For a given primary ion beam species, bombarding a matrix of known composition and homogeneity, the elemental composition of dopant element can be determined quantitatively. This led to the elaboration of a series of tables where the relative sensitivity factors (RSF) are shown for each element of the periodic table as a measure of their respective ionisation efficiency. As these

classifications are related to a simple, homogeneous chemical environment for a given primary ion beam species, an absolute quantification cannot be conducted in heterogenous materials of high complexity such as biological specimens. Nevertheless, these tables are a good starting point to identify ions that emit well for a defined biological specimen.

Table 1 summarizes the candidates for secondary emission as anions under a caesium beam (in blue) or as cations under an oxygen beam (in orange). Table 2 shows the RSF, measured for a Cs+ beam generating negative secondary ions in a homogenous Si matrix doped with the element to be observed (Wilson 1995). A similar table, for a negative oxygen primary beam generating positive secondary ions was also measured (table not shown). Low RSF factors imply high secondary yield and thus high sensitivity. Interestingly, both

Table 1 and Table 2 hint to a relation between electronegativity and ionisation efficiency.

Table 1: Ionization efficiencies, in relation to the primary ion beam. *In orange, elements that should be observed under a negative ion beam, yielding cations. In blue, elements that should be observed under a positive ion beam, yielding anions.*

H																He
Li	Be											B	C	N	O	F	Ne
Na	Mg											Al	Si	P	S	Cl	Ar
K	Ca	Sc	Ti	V	Cr	Mn	Fe	Co	Ni	Cu	Zn	Ga	Ge	As	Se	Br	Kr
Rb	Sr	Y	Zr	Nb	Mo	Tc	Ru	Rh	Pd	Ag	Cd	In	Sn	Sb	Te	I	Xe
Cs	Ba	La	Hf	Ta	W	Re	Os	Ir	Pt	Au	Hg	Tl	Pb	Bi	Po	At	Rn
Fr	Ra	Ac															

Table 2: Relative sensitivity factors measured using a positive ceasium primary beam, and a Si matrix doped with each element of the periodic table. *Color legend below.*

H																He
Li	Be											B	C	N	O	F	Ne
Na	Mg											Al	Si	P	S	Cl	Ar
K	Ca	Sc	Ti	V	Cr	Mn	Fe	Co	Ni	Cu	Zn	Ga	Ge	As	Se	Br	Kr
Rb	Sr	Y	Zr	Nb	Mo	Tc	Ru	Rh	Pd	Ag	Cd	In	Sn	Sb	Te	I	Xe
Cs	Ba	La	Hf	Ta	W	Re	Os	Ir	Pt	Au	Hg	Tl	Pb	Bi	Po	At	Rn
Fr	Ra	Ac															

In atoms/cc:	$<10^{22}$	10^{22}-10^{23}	10^{23}-10^{24}	10^{24}-10^{25}	10^{26}-10^{27}	$>10^{27}$	N/A

As isotopes of a same element share identical physicochemical properties, relative quantification as isotopic ratios is possible, even in biological materials. Therefore, the choice of elements for relative quantification is modulated by (i) the ionization efficiencies of the

element (Table 1 and Table 2) and (ii) the existence of isotopes for this element. Good candidate elements are C, O, N, P, I. As detection of isotopes is based on their mass, and not based on their radioactive emission, stable isotopes (e.g. ^{13}C and ^{15}N) are often preferred to radioisotopes for their simplicity of use.

The great discrepancy between ionization efficiencies of different elements has induced the modulation of parameters, such as primary ion beam species and chemical environment, to obtain an increase in their capacity to ionize. This is exemplified by using reactive primary ions to modify the surface chemistry of the sample resulting in an increase of the secondary ion yield of etched species, with a low ionization potential and a high electron affinity. This discovery led to the development of oxygen and caesium primary ion sources to promote the ionization efficiencies of a broad range of elements. In opposition, it has been shown that secondary emission induced by rare gas or gallium sources was characterised by low ionization efficiencies (Storm, Stein et al. 1976; Schuhmacher, Migeon et al. 1992).

I.A.4. Primary ion sources

Primary ion sources are key components of SIMS instruments. In dSIMS, they usually generate either oxygen, gallium or caesium ions, which are extracted into a tightly focused beam. The brightness of the beam is relative to its energy spread and defines the density of the ion probe. These essential ion beam characteristics include other factors such as the spot size, the current density at the target and the long term and stable operation of the sources, which determine the outcome of a SIMS microanalysis.

Oxygen beams are generally produced by a duoplasmatron source, providing positive (O_2^+) or negative (O^-) oxygen ions. Advantages of duoplasmatron sources are their high brightness, their long lifetime and their ability to form stable ion beams of either polarity.

Positively charged caesium beams can be produced either by surface (thermal) ionization sources or by field emission liquid metal ion guns (Shichi, Umemura et al. 1992). In caesium liquid metal ion guns, a needle type emitter is partially immersed in a reservoir containing liquid Cs melted by a heating unit. An extracting electrode produces a bright ion beam (in the range of 10^5 A/cm^2/sr) at high energy dispersion. Due to the high reactivity of liquid caesium, such sources are unstable and short-lived. In surface ionization sources, atoms with a low ionization potential, such as Cs, are ionized at contact with a heated filament. These sources have a lower brightness than liquid metal ion sources (around 150 A/cm^2/sr at 10 keV energy) but are preferred in SIMS due to their low energy dispersion (< 1 eV).

Positively charged gallium beams are produced by liquid metal ion guns. They are characterised by good stability and lifetime at a high brightness (10^5 A/cm^2/sr). However, the high energy dispersion of ions emitted by field emission liquid metal ion guns lead to chromatic aberrations which impair the ion probe density in the primary column. Operating these sources at high accelerating voltage (> 25 kV) reduces chromatic aberrations to the detriment of the depth resolution.

As mentioned previously, the ionization efficiency is highly dependant on primary ion species, specimen matrix and analysed secondary ions.

I.A.5. The acceleration of secondary ions and their separation according to the ratio mass/charge

The secondary ions extracted from the specimen surface are accelerated in the secondary ion column before being injected into the mass spectrometer. In the design of conventional SIMS instruments, the secondary ion extraction system is close to the sample surface. Therefore, the objective lens of the primary column operates at a long working distance (several centimetres) (Figure 3).

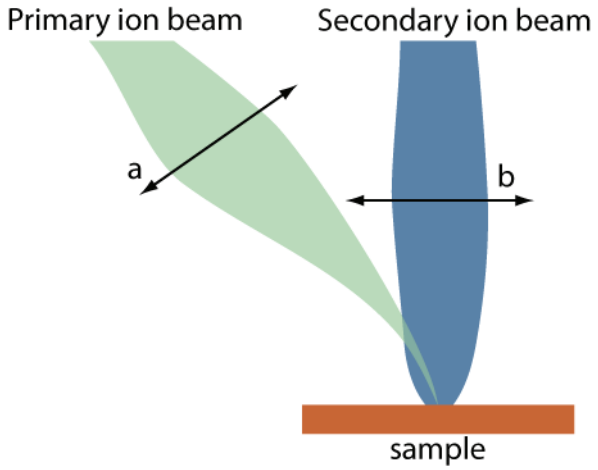

Figure 3: Schematic representation of the conventional probe forming configuration. *(a) primary ion beam focusing lens. (b) secondary ion extraction lens.*

After acceleration, the secondary ions are selected according to their m/z ratio by a mass analyzer of which essentially three types are found in SIMS instruments: (i) quadrupoles, (ii) single focusing mass spectrometers and (iii) double focusing mass spectrometers.

A *quadrupole* can only accept ions within a small energy band-pass (15 eV), resulting in reduced sensitivity compared to a double focusing mass spectrometer. Quadrupoles provide low mass resolution (m/z = 0.5) at a transmission relative to the element mass.

Single focusing magnetic sectors have excellent mass dispersive properties, with a large energy band pass (>150 eV). However, the first-order chromatic aberrations deteriorate the mass resolution when an ion beam, with an intrinsic energy spread, is analyzed by a single focusing magnetic sector field.

The combination of a magnetic and an electrostatic sector produces a *double focusing mass analyzer*. This double focusing spectrometer provides high and constant transmission along the entire mass range. In this configuration, mass spectrometers are capable of achieving high mass resolution, usually at the expense of transmission (Figure 4).

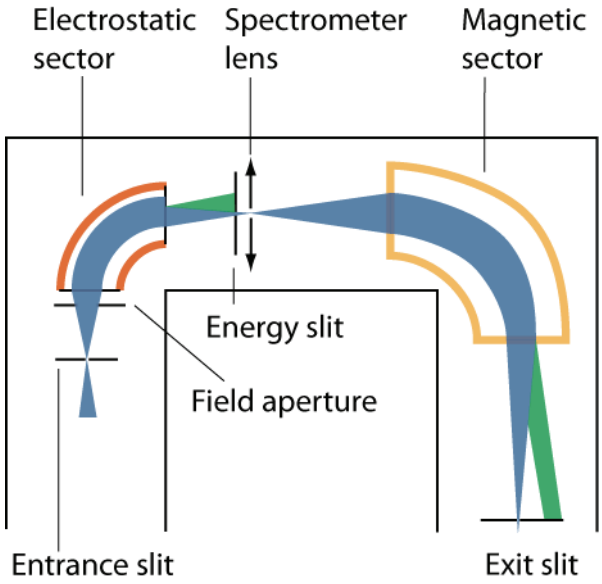

Figure 4: The double focusing mass analyzer, a combination of an electrostatic sector and a magnetic sector.

I.A.6. The detection of secondary ions

In dynamic SIMS, several modes of detection are possible, depending on the type of analysis. In the direct imaging secondary ion mass spectrometer (*ion microscope*) the sample is illuminated by a large diameter primary ion beam. The resulting image is projected from the sample surface through the mass analyzer to the channel plate, a phosphorescent screen placed at the focal plane of the ion image. The magnified image obtained from the sample surface depicts an ion cartography, or ion micrograph, of the sample for each specific ion.

In the scanning secondary ion mass spectrometer (*Scanning Ion Microscope; Ion Microprobe*) a highly focused primary ion beam is scanned across the sample surface and the secondary ion image is produced by registering synchronously several mass resolved

secondary ions with electron multipliers. Currently, most SIMS work as scanning ion microprobes and support both depth profiling and imaging.

While the size of the focused primary beam (lateral resolution) needs to be adapted to the mode of detection, the intensity of the primary ion beam decreases with the size of the primary ion beam. Consequently, the secondary ions current is also reduced.

I.B. The NanoSIMS 50

In order to design a new generation ion microprobe, whose analytical parameters would be of interest for life sciences, a collaborative effort between the researchers of the Materials and Structures department of the *Office National d'Etudes et Recherches Aérospatiales* (the French Space Agency), Professor George Slodzian's research unit at the university of Paris-Sud, and Cameca, a French company world-leader in SIMS instruments, resulted in the CAMECA NanoSIMS 50 (Cameca S.A., Courbevoie, France, http://www.cameca.fr) (Slodzian, Daigne et al. 1991; Hillion, Daigne et al. 1993). A picture of the NanoSIMS at the Centre de Recherche Public Gabriel Lippmann is shown in Figure 5.

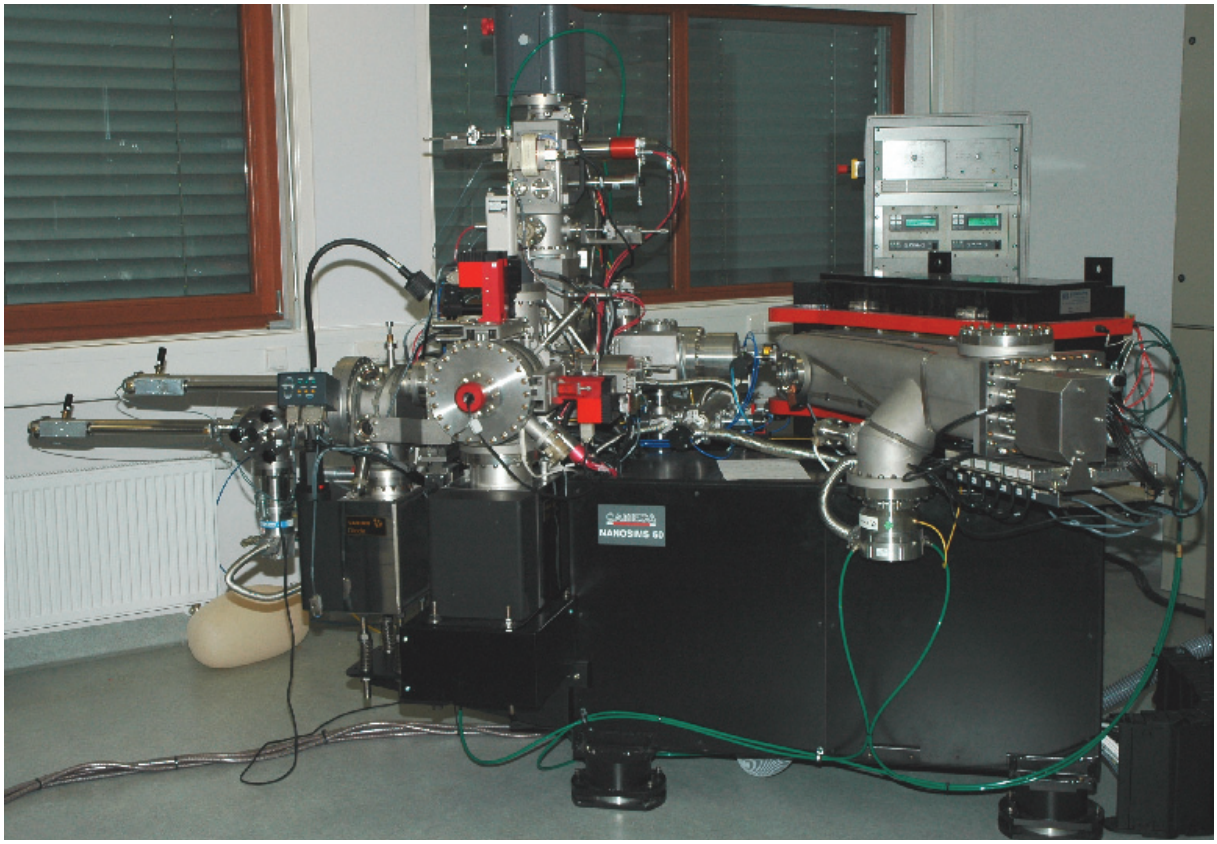

Figure 5: The NanoSIMS 50 at the Centre de Recherche Public Gabriel Lippmann in Luxembourg. *Operating desks are not shown.*

In the NanoSIMS 50 (NS50), an 8 keV primary ion focused on a sample brought to a potential of -8 keV, results in 16 keV impact energy. Emitted secondary ions, of the same charge sign

than the sample, are extracted by an extraction lens (electrostatic immersion lens). The secondary beam is focused and guided through several transfer lenses to the entrance of the mass spectrometer, consisting in a double-focusing filter analyzer. The first filter is an electrostatic sector which acts as an energy dispersive prism which separates secondary ions according to their kinetic energy, independently of their masses. An energy slit at the exit of the analyzer allows the band pass selection of ions in a specific energy range. The second filter is a magnetic sector where a variable magnetic field, perpendicular to secondary ion motion, deflects ions according to their momentum. According to the mass-to-charge (m/z) ratio, ions are discriminated by their differential deviation in the magnetic field. The topological information of the origin of the emission is kept throughout the secondary column. Ions of identical m/z ratio are selected and directed on the exit slit of the mass spectrometer in a beam, which is guided and widened by a set of projection lenses either to a Faraday cylinder, for total ion current measurement, or to a visualization screen for imaging purposes. The whole system is maintained under ultra-high vacuum with a decreasing gradient from the analysis chamber at 10^{-10} Torr, through the primary and secondary columns at 10^{-9} Torr, to the detector compartment where the vacuum is at 10^{-8} Torr. As for TEM, vacuum analysis is performed to reduce the particle collision probability, which drastically affects the transmission on the ion path.

For this instrument, a new design of the optical system has been developed by Slodzian et al (1992). It uses the same optical system to co-axially focus and collect both the primary ion probe and secondary ions. Compared to the conventional configuration (Figure 3) this optical arrangement (Figure 6) considerably shortens the distance between the sample and the lens forming the probe (a few hundred μm), minimizing the focal length and reducing aberrations of the objective lens. This ultimately leads to a smaller probe diameter for a given ion current. Furthermore, in this instrumental configuration, the sputtering of the specimen surface by the primary beam is at a normal angle of incidence, reducing the shadowing effects that occur when eroding a non-flat surface at an oblique angle of incidence.

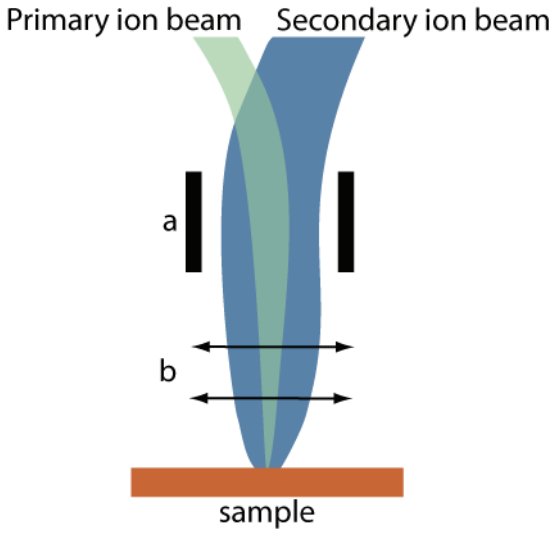

Figure 6: Schematic representation of a co-axial probe forming configuration. *(a) deflection plates, (b) lens for probe formation and extraction.*

The NanoSIMS is fitted with a Caesium source and a duoplasmatron oxygen source.

The Cameca Microbeam caesium source is a thermal ionization source designed by Cameca for their ion mass spectrometers. Caesium carbonate (Cs_2CO_3) or caesium chromate (Cs_2CrO_4) is heated to 400 °C in a container. The resulting caesium vapours are ionized to Cs^+ at contact with a tungsten plate at 1100 °C. A potential of 6 kV to 10 kV is applied to the tungsten plate. The extraction electrode, consisting in two annular filaments, is at ground potential. The Cs^+ ions are extracted by the electric field and focused into a beam by a set of electrostatic lenses (Slodzian, Daigne et al. 1991).

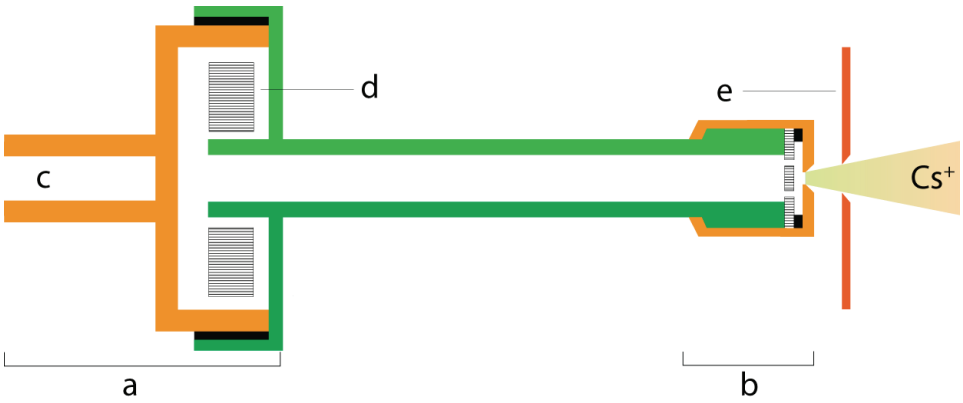

Figure 7: The Cameca Microbeam caesium source. *(a) caesium reservoir (b) ionizer (c) high voltage input (d) caesium chromate pellets (e) extraction electrode.*

The duoplasmatron emits a series of oxygen ions. Gaseous oxygen is ionized by an electric arc of several 100 V. The resulting plasma is concentrated into the axis by a magnetic field and a fraction is transferred into a second chamber and extracted through a 400 µm diameter hole in the anode. In positive mode, the duoplasmatron emits an ion beam of O_2^+ and O^+ in a ratio of 10:1. In negative mode, the ion beam is constituted of O_2^- and O^- in a ratio of 1:4.

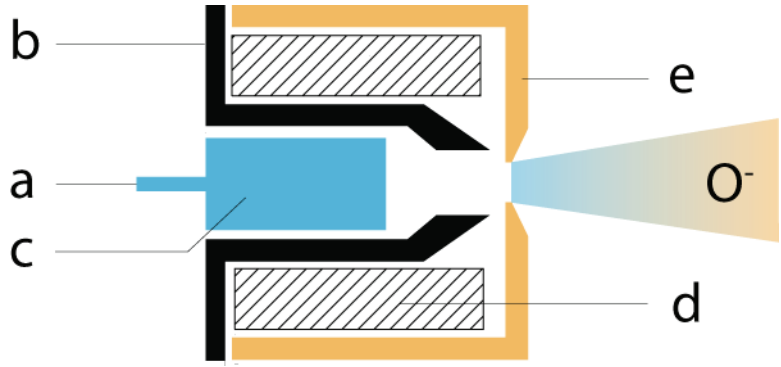

Figure 8: The duoplasmatron source. *(a) gas (b) intermediate electrode (c) cathode (d) coil (e) anode*

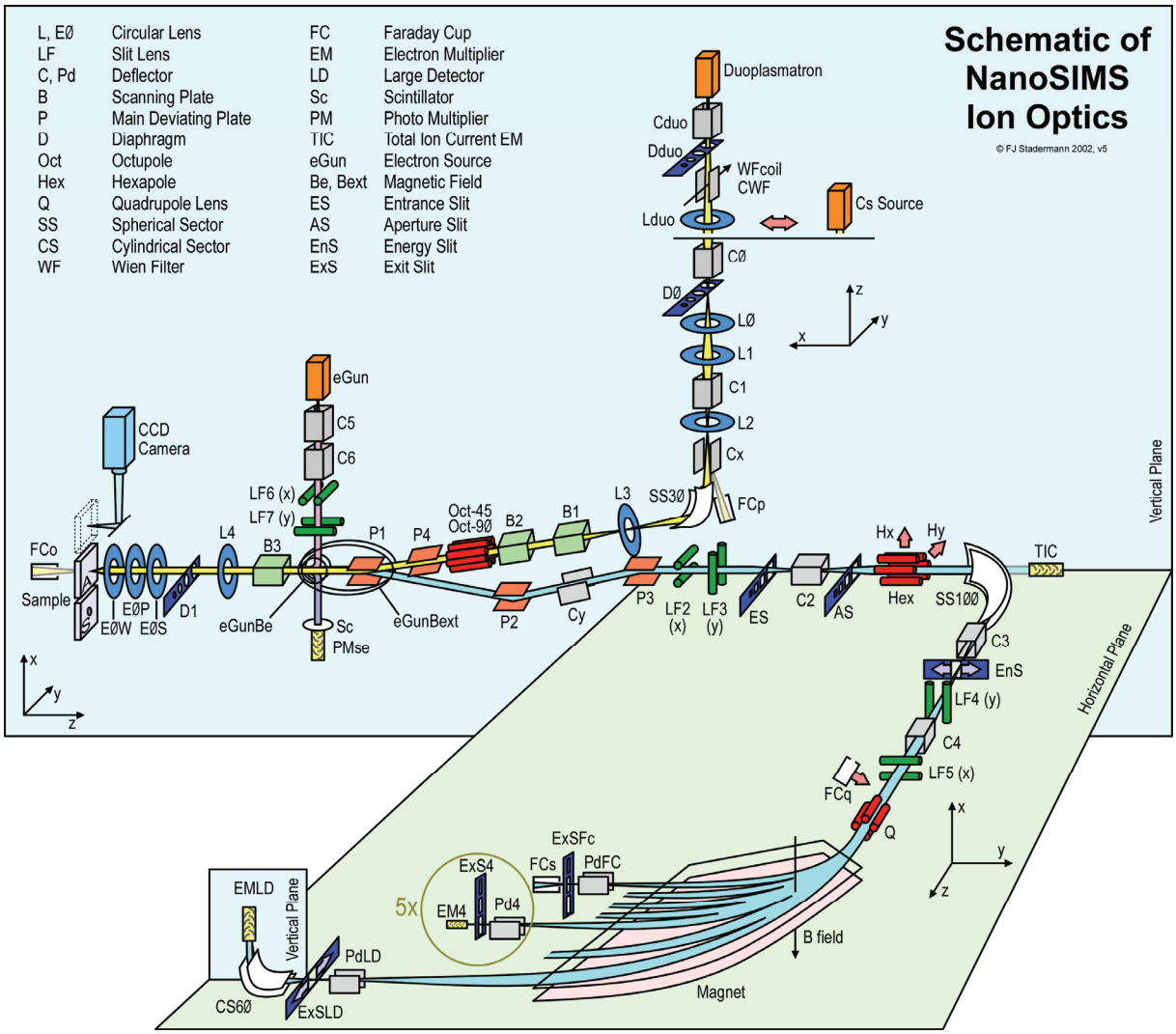

Figure 9: Schematic representation of the NanoSIMS. *Most notable legends are: Cs Source: Caesium primary ion source, Duoplasmatron: Duoplasmatron primary ion source; Sample, CCD: Charge-Coupled Device camera for optical observation of sample; eGun: electron gun; Primary column in yellow; Secondary column in blu; TIC: Total ion current detection; Electrostatic sector in gray; Magnet: Magnetic sector, Multi-detection at the exit of the magnet (Schematic by FJ Stadermann from Washington University, reproduced with the author's permission).*

The main components (Figure 9) of the NanoSIMS 50 are:

- A primary column with a primary caesium or oxygen ion source that enhances the useful yield of negative and positive secondary ions.
- An objective column where the same ion optic is used in a co-axial manner to focus the primary beam on the sample and to collect the secondary ions (Figure 6).
- An electron gun to flood the sample and neutralize positive charging to facilitate the analysis of insulators.

- A double focussing filter analyzer mass spectrometer consisting in an electrostatic sector and a magnetic sector with a focusing along the focal plane of the magnet. The transmission of the mass spectrometer is of 60% at a mass resolution $m/\Delta m = 4000$.
- Four moveable electron multipliers (EM) detectors and a fixed EM placed along the focal plane to acquire up to five masses simultaneously.

The 50 nm lateral resolution, combined with a high transmission at high mass separation opens up new areas of applications, especially in medical biology and life sciences, where high lateral resolution and high sensitivity are required. In comparison with X-Ray Fluorescence (about 1 micrometer of lateral resolution) and other techniques using radioactive isotopes, imaging by dynamic SIMS (dSIMS) offers new possibilities for biological research. At this scale it becomes possible to compare, in exactly the same subcellular compartments, the distribution of several molecules labelled with different stable isotopes (e.g. ^{15}N, ^{13}C, ^{2}H) or radioactive tracers.

I.B.1. Geographical distribution, price and use of the NanoSIMS

Table 3: Institutes equipped with a NanoSIMS and research fields.

Institution / Organization	Department	Location	Model	Dedicated to
Harvard Medical School	National Resource for Imaging Mass Spectrometry	Cambridge, Massachusetts, USA	NS 50 n°0 (prototype)	biology
University of Washington	Laboratory for Space Sciences	St Louis, Missouri, USA	NS 50 n°1	geochemistry, cosmochemistry
Institut Curie	Plateforme d'Imagerie Ionique	Paris, France	NS 50 n°2	biology
Max Planck Institut für Chemie (Otto Hahn Institut)	Particle Chemistry Department	Mainz, Germany	NS50 n°3	cosmochemistry
Centre de Recherche Public - Gabriel Lippmann	Department for the Science Analysis of Materials	Belvaux, Luxembourg	NS 50 n°4	material analysis (ceramics), biology
University of Tokyo	Ocean Research Institute	Tokyo, Japan	NS50	geochemistry
University of Oxford	Department of Materials	Oxford, UK	NS50	material analysis, biology
National Institute for Material Science		Tsukuba, Japan	NS50	material analysis (ceramics,semi-conductor)
ExxonMobil	N/A	New Jersey, USA	NS50	petrochemistry
University of California	Lawrence Livermore National Laboratory	Livermore, California, USA	NS50	material analysis, geochemistry, cosmochemistry, biology
National Aeronautics and Space Administration (NASA)	Astromaterials and Exploration Research Facility	Houston, Texas, USA	NS50L	geochemistry, cosmochemistry
Carnegie Institution of Washington	Department of Terrestrial Magnetism	Washington, Washington DC, USA	NS50L	geochemistry
Muséum National d'Histoire Naturelle	Laboratoire d'Étude de la Matière Extraterrestre	Paris, France	NS50	geochemistry, cosmochemistry, art
California Institute of Technology	Division of Geological and Planetary Sciences	Pasadena, California, USA	NS50L	geochemistry, cosmochemistry
Open University	Planetary and Space Sciences Research Institute	Milton Keynes, UK	NS50L	geochemistry, cosmochemistry
University of Western Australia	Centre for Microscopy, Characterisation and Analysis	Perth, Western Australia, Australia	NS50	material analysis, geochemistry, biology
University of Rennes	Observatoire National en Imagerie Scientifique		NS50	material analysis, geochemistry, biology
Physical Research Laboratory		Ahmedabad, India	NS50	geochemistry

Since the release of the NanoSIMS and until the beginning of this work in 2003, only Harvard Medical School, the university of Washington, the Institut Curie, the Centre de Recherche Public-Gabriel Lippmann and the Max Planck Institute were in the possession of a NanoSIMS 50. Despite the high acquisition costs (variable, around 2 million €), CAMECA has increased

their sales, particularly in the United States (7 total) and Europe (6 total). Surprisingly, only 5 NS50 are regularly used in the field of life sciences. Of those, currently only one is solely dedicated to fundamental research in biology (Institut Curie). Most groups have opted to develop service-based platforms, often termed "Ion Microscopy Platform", shifting back and forth between analytical services and research science. This may be partially explained by the fact that the know-how required to operate and maintain such an instrument is mainly found in material science laboratories in possession of previous SIMS models. While increased mass resolution to discern isotopes and increased lateral resolution are arguments clearly targeted towards life and earth sciences, the NS50 has found greater accordance in the fields of geo- and cosmochemistry. The NanoSIMS seems to be particularly well suited for the study of the elementary distribution of rare elements and their isotopes from terrestrial and cosmic minerals. Trace elements have been identified in igneous rock from the ocean floor in an effort to validate mantle melting models using NanoSIMS (Hellebrand, Snow et al. 2005). The study of variations in isotope ratios of mineral particles has helped in better defining solar system chronology and explaining the presence of presolar matter in primitive solar materials (Besmehn and Hoppe 2003; Floss, Stadermann et al. 2006; Hoppe 2006; Stadermann, Floss et al. 2006). The success of the NanoSIMS in this field of research has led CAMECA to develop slightly modified models of their instrument. The NS50LD, a hybrid model of the standard NS50, possesses a larger magnetic sector (radius of 650 mm instead of 550 mm) thus increasing mass separation between adjacent detectors. The NS50L is equipped with 2 supplementary detectors, totalling 7 electron multipliers. Similarly to the NS50LD, it is fitted with a larger magnetic sector. Optionally, it can be configured with 7 Farraday cups to measure the ion current of selected secondary ions. These modifications permit the parallel detection of large isotope families (e.g. ^{54}Fe, ^{56}Fe, ^{57}Fe, ^{60}Fe) (Mostefaoui, Lugmair et al. 2004) at the same time, reducing variations that may occur during sequential acquisitions.

Depth profiling

Dynamic SIMS is extensively used in semi-conductor industry to perform depth profiling of high-k dielectric used in gate materials, layer contaminant analysis and quantification of dopants with the use of standards. For these applications, where ultra-shallow depth profiling of uppermost layers may be required, the NanoSIMS is not well adapted as the sputtering at 16 keV cannot be easily modified. Several instruments (e.g. CAMECA SC Ultra) are capable of modulating the sputtering conditions such as the angle of incidence of primary ions, the primary ion beam energy and enhance secondary yield by gas flooding. Whereas they are not meant for imaging, they are more suited to depth profiling than the NanoSIMS.

I.B.2. Sample preparation

A variety of sample preparation techniques exists in microscopy. They involve a high degree of complexity and a high specificity to the sample, depending on the observation method. Nevertheless, similarities in the different methods of preparation are not uncommon, either for analytical methods performed under vacuum (e.g. TEM, SEM) or at atmospheric pressure (OM, CLSM).

A general sample preparation involves (i) a fixation step to cross-link proteins and lipids chemically or by cryofixation (Palade 1952; Sabatini, Bensch et al. 1963) to preserve the morphological integrity of the cellular and subcellular structures, (ii) an optional dehydration step to reduce the water content of the sample and (iii) an embedding into resin (OM, TEM, SEM) or paraffin (OM) to allow ulterior sectioning of soft tissues or cells.

When reviewing SIMS literature it becomes obvious that development of sample preparation protocols for ion microanalysis is still an ongoing process. Under the primary ion beam, a specimen is subject to conditions similar to TEM, such as ultra-high vacuum and high dose radiations. The similarities between TEM and SIMS analytical conditions are reflected in the sample preparation for SIMS that consists in the adaptation of electron microscopy procedures. In these protocols, fresh biological specimens are fixed, dehydrated, embedded into plastic resins and cut on an ultramicrotome.
A considerable effort has been invested into the development of sample preparation protocols compatible with SIMS. These procedures depend on the nature of the sample and the type of elements to be detected by the mass spectrometer. The following sections will enumerate several aspects of SIMS sample preparation.

B.2.1. Ion contamination

Eliminating potential ion contaminants during every step of the sample preparation to reduce the background in dSIMS analysis is crucial, especially when observing trace elements in the specimen. These contaminants may originate from specimen handling (e.g. metal tweezers), containers (e.g. glassware) or solutions (e.g. buffer solutions). Additionally, SIMS sample holders or residues from prior analysis may be the source of contamination, with sometimes unknown concentrations of trace elements (e.g. iron fraction in Cu blocs).

B.2.2. Fixation

The main purpose of fixation is to preserve the specimen in time, effectively taking a snapshot of the sample in a state that is as close as possible to its native live state. It involves blocking intracellular trafficking of organelles such as vesicles and structural features such as the cytoskeleton, generally immobilizing the translocation of any elements of the cells. As a result, the fixation prevents protein, lipids, nucleotides, and smaller cellular content from modification or movement. The type of fixation is dependant on the focus of the analysis and determines the entire sample preparation protocol. In the conventional chemical fixation, immobilization is a slow process performed by cross-linking agents. Cryofixation is a rapid fixation approach where the specimen is flash frozen (Quintana 1994). Combinations of both methods have been reported (Tokuyasu 1973; Armbruster, Carlemalm et al. 1982; Carlemalm, Garavito et al. 1982).

Chemical fixation

The main fixative used in TEM and SIMS is glutaraldehyde ($C_5H_8O_2$) at a 1.5-2.5% in a hypo-osmolar buffer. Introduced as a TEM fixative by Sabatini et al. (1963) in the early sixties, it cross-links proteins via its –CHO groups covalently binding protein amino groups (Hopwood 1967; Fraschini, Pellicciari et al. 1981; Kellenberger, Carlemalm et al. 1981). The drawback of glutaraldehyde over formaldehyde is the large size of the molecule, which slows down its penetration into the sample and the introduction of free aldehyde groups, which may react with antibodies and cause unspecific background labelling in the case of immunolabelling.

The outline of a standard protocol for SIMS fixation is shown in Table 4.

Table 4: A protocol for chemical sample preparation for SIMS analysis.

Fixation I	glutaraldehyde 4% in PBS 1X or sodium cacodylate 0.2M	1h
Washing	PBS 1X or sodium cacodylate 0.2M	10’
Fixation II	OsO4 1% PBS 1X or sodium cacodylate 0.2M	1h
Washing	PBS 1X or sodium cacodylate 0.2M	1h
Dehydration	ethanol 25%	10’
	ethanol 50%	10’
	ethanol 75%	10’
	ethanol 95%	10’
	4 x ethanol 100%	15’
	3 x propylene oxide 100%	15’
Infiltration	propylene oxide/ resin (v/v)	4h
	hydrophobic resin at 4°C	Overnight
Embedding	embed in fresh resin, subsequent stepwise increase of temperature to 65°C	48h

PBS binds polyvalent cations causing their precipitation. As an alternative for cation studies by SIMS, a slightly hypo-osmolar sodium cacodylate ($(CH_3)_2AsO_2Na$) buffer can be used. Also, HEPES ($C_8H_{18}N_2O_4S$, 4-(2-Hydroxyethyl) piperazine-1-ethanesulfonic acid), a tertiary amine heterocyclic buffer is an alternative to PBS as it does not react with polyvalent cations.

Imaging contrast in TEM is proportional to the atomic number (Z) of the elements in the sample (Carlemalm, Acetarin et al. 1982; Kellenberger, Carlemalm et al. 1986). As biological molecules consist mostly of atoms of low atomic weight (C, H, O, N, P and S), thin sections of biological material are counterstained by heavy metals salts such as uranium, lead and osmium, which are electron opaque. As SIMS measures ion distributions, such fixatives are not necessary for their contrasting abilities but they have proven to be very useful as secondary fixatives of lipids.

UHV sample preparation, especially for SIMS and TEM requires a very thorough dehydration by organic solvents such as ethanol or acetone to remove the free water from cells and replace

it by water insoluble embedding media. However, organic solvents may extract up to 95% of lipids, which may lead to sample shrinkage. The extraction of lipids can be reduced by a secondary fixation with osmium tetroxide (OsO_4) or uranyl acetate by mainly cross-linking unsaturated fatty acids. Since acetone takes up atmospheric humidity, ethanol is preferred as dehydration agent in case of animal cells. Acetone is better suited for the dehydration of plant cells as it penetrates more easily their cellulose-rich cell walls. Unlike acetone, ethanol is not directly miscible with resins and a linking agent (clearing agent) is required after dehydration. The most common clearing agent is propylene oxide (C_3H_6O, 2-epoxypropane).

When using solvents, as required during chemical fixation protocols, increase of membrane permeability followed by the diffusion of low mass biomolecules and elements, such as ions or neutrally charged particles, must be taken into consideration. If SIMS observation targets these constituents, cryogenic fixation may be advantageous.

Cryogenic sample preparation

In cryofixation the redistribution of soluble molecules is prevented by flash-freezing. This results in only limited alteration of the cellular constituents by rapidly arresting physiological processes and reducing the loss of soluble material by diffusion. Both the antigenic properties and the morphological structure of the sample are well preserved. Rapid freezing at ultra-low temperatures (< 123 K) favours the formation of vitreous ice instead of crystalline ice, which causes morphological damage. These conditions are only reached for thin layers, as biological samples act as temperature insulators and prevent the rapid freezing of deeper regions of the sample.
Cryofixation is usually achieved by (i) slam-freezing the sample on a precooled mirror-polished metal surface; (ii) by plunging the sample into nitrogen-cooled liquid propane or (iii) by high-pressure freezing.

In the rapid immersion freezing technique (plunge-freezing), the sample is projected into liquid cryogen, usually propane or ethane. Only the outer sample layer of around 10 µm is usable as the remaining layers are being damaged by ice crystal formation. This freezing method proved to be well suited for cell suspensions (suspended drop) and very small tissue samples (< 200 µm diameter).

In the freeze-slam technique, a tissue sample is frozen by contact with a mirror polished metal

block cooled by liquid nitrogen. The expected usable layer is approximately 20 µm thick. While the metal-mirror slamming procedure is not appropriated for cell suspensions, it is suitable for freezing pelleted cell suspensions. Furthermore, freeze-slamming does not require the use of an explosive and volatile cryogen. Hence, its use is more straightforward and safe than freeze-plunge.

A frozen-hydrated sample can be directly analysed on a TEM fitted with a cryogenic chamber. On dynamic SIMS, this type of chamber does not exist, and the sample needs to be further processed before analysis. The ice is exchanged by an organic solvent at low temperatures (-90°C) during a freeze-substitution process. The solvent, miscible with the embedding media, is progressively substituted by resin. The curing of the embedding media is performed by heat at 60°C or by UV light at -10°C. Our samples were cryosubstituted and cryoembedded using a freeze-substitution device, the LEICA EM-AFS. Table 5 outlines step-by-step a typical freeze-substitution process, which defines plateaus and temperature slopes for a gradient freeze-substitution.

Table 5: A protocol for cryogenic sample preparation for SIMS analysis.

Step	Reagent	Time [h]	Temp [°C]	Slope [°Ch^{-1}]
T1	Acetone	80	-90	
S1		6		+10
T2		4	-30	
S2		4		+5
T3		1	-10	
T1	Epon	48	60	

Modifications of this protocol might include change of solvents (e.g. methanol), infiltration into resin at low temperatures before embedding and use of different types of resin with modified polymerization properties.

B.2.3. Embedding

Resin embedding is the last step in sample preparation for TEM and SIMS. Its multiple roles are (i) to create an interstitial matrix to keep the sample from collapsing, (ii) to be electron transparent for TEM and (iii) to permit cutting by an ultramicrotome. Image quality is dependant on the homogeneity and stability of the embedding media under the impacting beam, which constitute primordial factors for the selection of proper resins. Unstable resins

may melt when subjected to high energy beams and are unfit for analysis. Popular resin preparations have been known for decades (Glauert, Glauert et al. 1956; Glauert and Glauert 1958; Finck 1960) and both Epon 812 (Fluka) and Araldite M (Sigma-Aldrich) were chosen for their homogeneity and beam stability properties,. These are hydrophobic epoxy resins whose drawback resides in their fast polymerisation and high viscosity at room temperature. For Araldite M the curing reaction is delayed at room temperature, allowing the freezing of pre-aliquoted resin at -20°C. In addition, the slightly lower viscosity of the epoxy M component bears better homogenization and degassing and produces less brittle resins that are easier to cut with the ultramicrotome. The high viscosity of these resins perturbs the homogenisation, increases the formation of air bubbles and thus requires thorough degassing before use. Badly degassed resins may contain microscopic air bubbles that are visible as artefacts by TEM and SIMS. Spurr, a low viscosity alternative to Epon 812, yields preparations of equal quality at reduced infiltration times. Reputed for its high toxicity, Spurr was only used for samples where infiltration was problematic with Epon 812 or Araldite M.

Hydrophobic plastic resins require a thorough dehydration with an organic solvent, which in turn enhances the extraction, mainly of lipids. As resins themselves are organic solvents, they further contribute to the extraction of lipids.

In opposition, hydrophilic acrylic resins tend to have a low viscosity, which favours their rapid penetration and diffusion in the sample, limiting their extraction effect. Another advantage of these resins is their high polarity that eases the rapid permeation by aqueous solution, as for instance antibody solutions in immuno-histochemical studies. As an example, the hydrophilic acrylic LR White resin is miscible with water (up to 10%) and does not require the complete dehydration of the sample. The cross-linking reaction can be initiated by heat (50°C for 24 hours), by exposure to UV light or by a chemical accelerator. The drawback of LR-White is its relative sensitivity to O_2, which inhibits polymerization. As a result, curing must be done under anaerobic conditions, e.g. in a vacuum oven, under N_2 or Ar, or in sealed gelatine capsules. In the case of vacuum polymerisation, the evaporation of the volatile components of the resin formulation should be avoided and vacuum should not exceed 200 mBar. Epon embedding procedures performed during this work included infiltration under vacuum at 100 mBar to favour the penetration of the resin into the sample.

A Leica Ultracut (UCT) ultramicrotome was used for resin sectioning and sections of 50 nm were prepared for TEM and sections of 200 nm to 400 nm for SIMS.

B.2.4. Sample mounting

NanoSIMS samples must be mounted on conductive or semi-conductive sample-holders, which are placed into a sample-carriage. NanoSIMS sample carriers, with a capacity of 8 sample holders, are inserted one at a time into the entry chamber. Pressure is then lowered to 10^{-4} Torr and samples are transferred into a storing chamber at 10^{-7} Torr with space for 8 carriages. Per carriage analysis is performed in the analysis chamber at 10^{-10} Torr, a vacuum achieved by turbo-molecular and ionic pumps.

At atmospheric pressure (760 Torr) there is an equilibrium between atmospheric humidity and sample water content. At very low pressure, the sample releases H_2O perturbing the chamber pressure and inducing prolonged equilibration times before UHV is attained again. Typically, samples are introduced the day before analysis for overnight degassing. Samples can be mounted either directly on sample holders or indirectly through various contraptions.

Direct mounting technique

Copper cylinders. Initially samples were deposited on mirror-polished homogenous copper cylinders. These cylinders are manufactured at the CRP-GL / SAM and polished manually to 0.1 µm rugosity. Cu cylinders tend to oxidize in contact with water from the section deposit provoking oxidation artefacts, which can be observed on the optical camera of the NanoSIMS and during ion microprobe analysis of oxygen based ions. As a result, steel sample holders are often preferred.

Steel cylinders. Mirror-polished steel cylinders have been manufactured by Gradel S.A. (Steinfort, Luxembourg) to 1 µm rugosity. Before use, additional polishing to 0.1 µm is required to eliminate striations caused by automated manufacturing. Steel cylinders are now the preferred sample holders whose advantages reside in their scratch resistance compared to Cu steel cylinders and their immunity to oxidation.

Indirect mounting technique

In the indirect mounting technique, samples deposited on different types of conductive support material, are cut with a diamond-tip or a ceramic-tip cutter to 2-6 mm^2 shards. A hollow copper ring is then placed on a glass slide, the sample shard being face-down at the bottom. The ring is filled to the brim with melted bismuth-based Wood alloy (melting point 69°C). Once the alloy is solid, the copper ring with the sample shard embedded in Wood can be easily detached from the glass slide and presents a flat surface to avoid local variations in the emission due to differential surface profiles during NanoSIMS analysis.

Currently used conductive support materials are:

Mirror polished semi-conductors. Indium phosphate slides and silicon slides (Plano Gmbh, Wetzlar, Germany) are excellent sample holders for SIMS. A further advantage of Si slides resides in its compatibility to cell culture, as adherent cell lines can grow directly on the sample holder. Further treatments (fixation, dehydration, embedding by resin film) can be performed by handling the Si slides.

Glass slides. Non-conductive sample-holders, such as OM glass slides, are not suitable without post-mounting metal-coating to lower localized charge discrepancies resulting in biased measurements. While this method reduces the detection yield of elements due to non-homogenous sample charging, its compatibility with OM before sputter-coating and SIMS analysis is a major advantage, in particular for parallel fluorescent and NanoSIMS imaging.

Cu mirror-polished to 1 µm. Cu foils of 18 µm, 35 µm, 70 µm and 105 µm were graciously provided by Circuitfoil S.A. (Wiltz, Luxembourg). Thin metallic foils present several advantages during sample preparation. Their size (provided as A4 foils) allows multiple deposits side by side and subsequent cutting of zones of interest as located by OM. Low thickness allows cutting using standard scissors. 70 µm and 105 µm have been found easy to handle during the embedding into the Wood alloy.

Electron microscopy (EM) grids. Sample holders allowing parallel EM and NanoSIMS analysis on the same sample were successfully used at the Laboratoire de Microscopie Ionique (Paris, Orsay). TEM analysis on samples deposited on EM grids helped to identify cellular features prior to SIMS analysis, which was performed on the same resin sections, on sample holders compatible with EM grids. Similar modified sample holders have been developed at the CRP-GL / SAM. These sample holders allow the precise sub-cellular localization of SIMS labels by overlaying EM images with NanoSIMS images. Alternatively, TEM grids can be embedded directly into copper rings using Wood alloy.

Coating of samples

The analysis of biological preparations tends to suffer from a local accumulation of charges due to the insulating nature of those samples. This so-called *charge effect* decreases the detection efficiency of secondary ions. Low conductivity is related to the possible insulating properties of the sample carrier (e.g. glass slides) and/or of the sample itself e.g. embedding material, surface size and thickness of sample. To avoid the charge effect, different sample carriers, thinner sectioning of samples as well as surface coating of samples with gold or palladium (Pd) have been tested. Charge effects are inexistent on resin section surfaces of less than 0.5 mm^2 and their metal coating did not substantially improve the secondary ion yield.

However, for sections above 0.5 mm^2, metal coating and electron flooding were sometimes required to counter the charging effects.

I.C. Review of current biological applications in dSIMS and NanoSIMS

In the last three decades, attempts to use SIMS in life sciences have been numerous and in several cases fruitful. A detailed reading of SIMS literature allowed the identification of two distinct strategies and interest groups. The first and most common strategy consists of a bottom up approach where the technique is on the lookout for applications. It is usually initiated by SIMS platforms fanning out for collaborations. The resulting publications have a pronounced technical orientation and are published in journals specialised in surface analysis (over 90% of dSIMS publications are published in "Applied Surface Science" (Elsevier B.V.). They usually discuss several distinct topics per publication and can be summarized as feasibility studies where the innovative use of the NanoSIMS is challenged.

Scientists from the fields of medicine or biology have adopted the second concept, a top-down strategy. Not as common, this approach relies on different techniques, including SIMS, to answer to a specific problem in life sciences. The ensuing studies target either broad life science journals (e.g. Nature, Cell, BioMed Central, Micron, Journal of Microscopy) or journals more related to the investigated topic. The following section describes several of the most notable applications performed using dynamic SIMS.

I.C.1. Cell biology

Imaging cell structures by SIMS is possible either by visualising native ions or by using isotopically labelled markers. While in some cases, such as in biomineralization studies, the distribution of native ions is the key to understanding microaggregate formation, most other applications rely on the use of labelled markers raised against the background of abundant elemental C, N, O and P ions. Candidate labels contain halogen atoms, stable isotopes and radioisotopes.

Galle demonstrated the utility of halogen-based nucleotide analogues such as bromodeoxyuridine (BrdU) and iodouridine (IdU) incorporated preferentially to DNA, or fluorouracil (5-FU) favouring RNA (Galle 1991). The halogens were detected as elemental ions $^{79}Br^-$, $^{19}F^-$ and $^{127}I^-$.

In recent studies, the existence of cation-chromosome interactions was confirmed by SIMS (Strick, Strissel et al. 2001; Strissel, Strick et al. 2004). While Ca^{2+}, Na^{2+} and K^+ seem to be required for chromosome condensation, the authors suggested a more specific role of Mg^{2+} in

maintaining chromatin structure. Where previous studies mapped the cellular distribution of physiological cations by indirect imaging techniques, SIMS allowed their direct visualisation and corroborated their essential role in chromosome condensation.

Modern SIMS instrumentation with their improved transmission, with their ability to better discern isotopes from their mass interferences and with the general availability on the market of readily labelled amino acids and nucleotides have strongly promoted the use of stable isotopes like ^{15}N, ^{13}C, ^{18}O for ion microscopy labelling. They allowed to image the turnover of proteins and fatty acids based on isotopically labelled nutritional precursors containing ^{13}C and ^{15}N stable isotopes, by comparing isotopic ratios of the recombined cyanide ions $^{12}C^{14}N$, $^{13}C^{14}N$, $^{12}C^{14}N$, $^{12}C^{15}N$ to their natural abundance (Lechene and Bonventre 2003; Peteranderl and Lechene 2004).

Stable isotopes ion microscopy seem to be well suited for the investigation of translocation and diffusion processes in thin organic films and was proposed as an alternative to fluorescence microscopy to investigate compositional differences of lipid bilayers and the dynamic rearrangements of the protein and lipid components in the plasma membrane (Galli Marxer, Kraft et al. 2005; Kraft, Fishel et al. 2006). Isotopically labelled lipids or proteins were raised from the phospholipidic membrane were observed using the ^{31}P secondary ions, while proteins were identified by the emitted $^{12}C^{14}N$ secondary ions. This method permitted the identification and quantification of the composition of microdomains present in this lipidic bilayer model. The considerable advantage of this novel approach lies in the direct following of molecules without the use of a grafted bulk fluorophore, which may modify membrane properties.

Ion microscopy provided the means to observe hair formation and elemental composition of hair features at ultrastructural level (Hallegot, Peteranderl et al. 2004). Oxygen rich regions were observed in the melanin granules of melanocytes, which may be generated by ultraviolet absorption by the melanin granules and subsequent release of oxygen radicals. Furthermore, a recent publication discriminated pheomelanin (rich in sulphur) from eumelanin (absent of sulphur) in B16 melanoma cells (Guerquin-Kern, Hillion et al. 2004).

I.C.2. Pharmacology

Boron neutron capture therapy (BNCT) is a new potential treatment for malignant brain tumour and melanomas. It is based on the neutron induced fission of ^{10}B resulting in unstable ^{11}B which decays to ^{7}Li and an α particle with a kinetic energy of 2.79 MeV. Several molecules are currently under investigation for the delivery of boron to tumour cells in the

brain. Main candidates are the amino acid derivatives boronophenylalanine-fructose (BPA-f) and sodium borocaptate (BSH). Boron delivery was investigated in glioblastoma cells, co-cultured with LLC-PK_1 epithelial cells or skin fibroblasts (Lorey, Morrison et al. 2001). *In vitro* glioblastoma cells showed an increased ^{10}B distribution mainly in the nucleus and the cytoplasm. However, this pattern of BPA-f and BSH was also found in epithelial cells and fibroblasts. SIMS microanalysis on an IMS 3f was used to localize a rat gliosarcoma and measure ratios between boron isotopes at the interface between tumour and healthy tissue (Smith, Chandra et al. 2001). In these histological studies, a gradient of ^{10}B suggested some degree of specificity of boron for the tumour. While the cell-type specific selectivity of boron remains controversial, SIMS proved to be an excellent technique to image the boron distribution directly and remains the method of choice for the study of the potential selectivity of boronated drugs.

Besides the localization of BPA-f and BSA, the distribution and accumulation patterns of several other anticancer drugs was determined by comparative SIMS and fluorescence microscopy (Guerquin-Kern, Coppey et al. 1997). In MCF7-P, a malignant human mammary cell line, the distribution kinetics were highly different for the structurally similar drugs pazelliptine or intoplicine. Pazelliptine translocated rapidly from the cytoplasm into the nucleolus. However, the drug was absent from the nucleus after 24 hours of incubation. As fluorescence emission of both drugs is reduced when bound to DNA, neither of them could be observed by fluorescence microscopy. On the other hand, SIMS images showed a progressive accumulation of intoplicine in the nucleus, confirming the usefulness of the technique as a complement to common fluorescence imaging in pharmacological studies.

N-2-diethylaminoethyl-4- iodobenzamide (BZA) (^{127}I-BZA), a candidate drug binding to melanoma cells targets both melanocytes and melanophages, was also studied by SIMS. An initial attempt to image I-BZA, through the stable isotope ^{127}I, was performed by Chehade et al. (1996). More recently, highly resolved imaging of ^{127}I-BZA and its radioisotope derivate ^{14}C-I-BZA bound to melanin granules of B16 melanoma cell colonies in lung tissue were obtained (Guerquin-Kern, Hillion et al. 2004; Chehade, de Labriolle-Vaylet et al. 2005), invalidating a model suggesting a binding to σ-receptor of the cell membrane (John, Bowen et al. 1993).

The role of calcium in the transport activity of the plasma membrane was assessed by measuring $^{44}Ca/^{40}Ca$ isotopic ratio variations in vitamin D deficient and vitamin D repleted chicken injected with the stable isotope ^{44}Ca (Chandra, Fullmer et al. 1990). Absorption of ^{44}Ca was shown to vary from 0.5 to 20 minutes. The stimulation of Ca absorption by vitamin

D in the intestine was confirmed by analyzing cryofrozen epithelial cells on a Cameca IMS-3f.

It is widely accepted that the ionic balance is impaired in malignant cells. Aberrant signal transduction, among others modifying Ca distribution, have been reported in human melanoma and ovarian cancer xenografts (Kohn, Sandeen et al. 1992). Direct imaging of calcium gradients in both malignant and healthy cells demonstrated the utility of SIMS. Furthermore, SIMS proved to be an invaluable tool to study the kinetics of Ca^{2+} entry into the cell (Chandra, Ausserer et al. 1992; Chandra, Fewtrell et al. 1994).

SIMS may also provide the means to study drug vectorization in pharmacology as has been shown in a recent study (Römer, Wu et al. 2006). Bacterial Shiga toxin and related toxins are composed of an A-subunit, which exhibits catalytic activities inducing cytotoxicity, and a non-covalently bound B-subunit, that acts as a transporter for the A-subunit. The B-subunit (STxB) has been demonstrated as a powerful vector for transporting attached peptides into cells (Johannes and Goud 1998; Johannes 2002). The STxB is known to transport to the endoplasmic reticulum via the Golgi apparatus through a retrograde route (Mallard, Antony et al. 1998). By using ^{15}N-enriched STxB, Römer et al. have proven that subcellular localization of an isotopic labelled vector can be visualized using NanoSIMS. STxB was shown to bind to the plasma membrane followed by internalization into the cell and accumulation in the Golgi region.

I.C.3. Toxicology

Toxic compounds can be categorized as elements, inorganic molecules, or more or less complex organic molecules. The information yielded by chemical microanalysis such as scanning ion microprobes and related techniques, e.g. electron probe x-ray microanalysis (EPMA), can be a valuable addition in the investigation of their metabolic pathways.

The accumulation of toxic lanthanide or actinide elements (group IIIA) in the lysosomes of the kidney convoluted proximal tubular cells, long thought to be the consequence of a dose-dependent pathological effect, has been proposed to be the result of a selective concentration (Berry 1996). Most analytical techniques, such as EPMA, rely on the administration of high doses for the subcellular localization of toxic element. The high sensitivity of the NanoSIMS permitted the localization of trace quantities of aluminium and indium in the proximal tubules of rats previously treated with these compounds. Indium and aluminium were both visible in the cytoplasm probably because of accumulation in the lysosomes, while indium was also observed in the nuclei. Both metals were found as precipitates in the tubular lumen. This

selective accumulation suggested a mechanism of concentration, precipitation and elimination as previously observed by EPMA after a high dose administration and confirmed by NanoSIMS at more realistic doses (Galle, Levi-Setti et al. 2004).

In a recent article, arsenic distribution was examined by NanoSIMS in human hair sections to investigate signs of As poisoning (Audinot, Schneider et al. 2004). Natural concentrations in the hair typically range between 0.1 – 1 ng/mg hair and As^- signals are homogenous throughout the hair cortex. Control hair exposed experimentally to arsenic salts showed a similar distribution pattern but with higher signal intensity. In contrast, hair from individuals who ingested arsenic over longer periods of time displayed a coarse speckled pattern of high doses of As in the medulla. Accumulation of As during hair growth may explain this pattern but years of treatment with products containing As may have similar effects. SIMS could be used to further study As incorporation in hair and could be crucial in the diagnostic of chronic arsenic poisoning e.g of historic figures.

Nitrogen oxides (NO_x) resulting from petrol combustion constitute one of the main air pollutants in industrialized countries and are thought to be an important cause of an increase in sensitivity to pollen allergens. Using SIMS, Lhuissier et al (2000) observed an accumulation of ^{15}N in the sporoderm and cytoplasm of birch and cockfoot pollen exposed to ^{15}NO. This application is particularly interesting because it relies on SIMS' unique ability to follow stable isotopic markers, applied to the field of environmental science. The low molecular mass nitrogen oxides could not have been traced by alternative techniques based on radioisotopes, as oxygen only possesses short half-life isotopes and as natural nitrogen radioisotopes do not exist.

I.C.4. Biomineralization

The high sensitivity and spatial resolution of SIMS have been particularly useful to analyse biomineralization processes and the chemical composition of the resulting microagglomerates.

In odontology, amelogenesis, e.g. formation of dental enamel, has been investigated by SIMS microanalysis (Chabala, Edward et al. 1988). The fluorine distribution (Lodding 1983), normalized against P (F / P ratio) of Ca (F / Ca ratio) has been studied to some extend, as the instrument is particularly well suited to detect minute traces of fluorine, the element possessing the highest ionisation yield τ_u.

The development of enamel goes through several phases: (i) during the pre-secretory phase pre-ameloblasts differentiate to ameloblasts; (ii) in the secretory phase, ameloblasts develop

the Tome's process, a structure responsible for enamel secretion; (iii) in the maturation phase ameloblasts undergo morphological changes and evacuate organic components from the dental matrix. During the development of dental matrices, the density of rod-like structures of hydroxyapatite increases. Chemical analysis of rat incisor enamel showed that inorganic ions (e.g. ^{31}P, ^{35}Cl) present a distinctive pattern and an increase in incorporation during enamel development (Lundgren, Persson et al. 1998). During maturation phase ^{12}C, ^{19}F, ^{23}Na and ^{39}K were resorbed by ameloblasts, gradually reducing these elements in the enamel matrix.

An ongoing study on hydroxyapatite agglomerates investigates the mineralization process in Madin-Darby Canine Kidney (MDCK) epithelial cells (Guerquin-Kern, Wu et al. 2005)**.** It shows evenly distributed phosphorus, sulphur and calcium oxide within the agglomerates. Carbon and cyanide ions accumulate specifically at the interface between tissue and agglomerate. This study also demonstrates a complementarity between high-resolution ion microprobe analysis and TEM imaging when SIMS sample holders compatible with TEM grids are used.

Quintana et al. (2006; 2007) analysed the sub-cellular localization of iron in senile plaques, neurons and glial cells from the hippocampus of patients suffering from Alzheimer disease (AD) and the thalamus of AD transgenic mice. A recent model incriminated the production of free radicals and their toxic effect to the existence of Fe agglomerates in the brain. SIMS ion maps, correlated to optical imaging and supplemented by TEM immunogold labelling of tau protein and β-amyloid, supported the hypothesis of an impaired ferritin, an iron binding protein, which could result in an accumulation of ferrous iron.

I.C.5. Radiotoxicology and nuclear medicine

Pierre Galle pioneered the notion of scanning ion microprobes as a tool for observing both stable isotopes and radioisotope distribution in tissues (Galle 1982; Hindie, Hallegot et al. 1988), determining its usefulness in nuclear medicine (Briancon, Jeusset et al. 1992). An ongoing study investigates the differential distribution of the iodine isotopes (^{127}I and ^{129}I) in the colloid of thyroid follicles. Due to high electron affinity and effective ionisation yield $\tau_{u,}$ iodine is an element of choice for SIMS analysis. To identify uptake patterns of exogenous iodine, young rats were injected with the isotope ^{129}I and sacrificed at predefined intervals. After fixation and embedding, thyroid sections were analysed by SIMS. As expected, the natural isotope ^{127}I was homogenously distributed in the colloid region throughout the thyroid while exogenous ^{129}I, given 6 hours earlier, was only found at the periphery of the colloid. This differential distribution may be of interest to better understand the risk of accidental

exposure to radioactivity.

I.D. Imaging techniques directly related to SIMS

While SIMS was the first technique to introduce the idea of imaging elemental species, its interest was limited to material science. Advances in molecular imaging using static SIMS and laser induced desorption and ionization (MALDI) paved the way for the microanalaytical imaging of organic ions of sufficient mass and complexity to be tied to their parent molecule. While not comparable to the detection capabilities of dynamic SIMS measuring eroded elemental ions, the sensitivity of these techniques has greatly improved and highly expressed proteins can be identified using these instruments. An interesting review by McDonnel and Heeren compares several mass spectrometers (e.g. NanoSIMS, TOF-SIMS, MALDI-TOF), their respective attributes, abilities, advantages and disadvantages in relation to ion imaging (McDonnell and Heeren 2007).

Furthermore, while TOF-SIMS and MALDI-TOF are akin to each other, the ion formation is inherently different. As a result, SIMS is usually better suited for the analysis of elemental and low mass molecular ions, that may be masked by the matrix signal in MALDI. On the other hand, soft ionization processes in TOF-SIMS yield larger molecular ions that are better suited for protein analysis (Garrison, Delcorte et al. 2003).

I.D.1. TOF-SIMS imaging

The need to access molecular information, obtained from a low dose primary ion beam sputtering secondary ions in the static regime, led to the development of the Time-of-flight SIMS instrument (TOF-SIMS). Pulses of primary ions, typically in the nanosecond range, are emitted by the primary ion source. The packets of ions resulting from the bombardment are extracted and accelerated to a given kinetic energy before entering the field-free zone of the tube-of-flight mass analyzer, where ions of different masses have different velocities, relative to their kinetic energy. The detector measures the time of flight of individual ions and deduces their masses. While SIMS is a destructive technique, erosion in TOF-SIMS is a slow process engaging one or two monolayers (1 nm) in a standard analysis. TOF-SIMS lateral resolution is usually in the sub-micron range (down to 500 nm) and sensitivity is highly dependant on ion size, with a better detection of low mass ions but depending on the surrounding chemical environment (matrix effect). The m/z ratio of TOF-SIMS is typically 500, a mass range much lower than MALDI-TOF.

I.D.2. MALDI-TOF imaging

Developed by Caprioli in the late nineties (Caprioli, Farmer et al. 1997; Todd, Schaaff et al. 2001), MALDI Imaging mass spectrometry is rapidly gaining attention in the life sciences, retaining spatial information of protein profiling by mass spectrometry on prefixed tissue samples. To avoid cocrystallisation of matrix with excess salts, tissue sections are desalted by thorough washing steps in solvent before matrix deposition on the sample (Caprioli, Farmer et al. 1997).

The lateral resolution of 25 μm is achieved on commercial settings and is directly related to the laser spot size. Higher lateral resolutions (10 μm) are only obtainable to the detriment of sensitivity, as smaller spot sizes cause less desorption of material.

The greater awareness and acceptance of MALDI-TOF Imaging compared to TOF-SIMS imaging in the biomedical sciences probably lies in the only minor modifications necessary to retrofit existing MALDI-TOF instruments used for proteomics to enable mass spectral imaging (generally, software upgrades are sufficient). Moreover, knowledge of MALDI and its role in proteomics is ubiquitous and the switch to MALDI imaging is easier and more comfortable to setup.

I.E. Confocal Microscopy

I.E.1. Introduction

The relative ergonomy of current confocal microscopes and the speed of acquisition explain their extensive use in life science laboratories during the last decade. Today confocal microscopy constitutes, together with widefield epi-fluorescence microscopy, the backbone of non-invasive biological imaging.

Widefield imaging is based on the illumination from a powerful xenon or mercury white-light source. The image of a sample is projected onto a collecting device (CCD) or directly on the eye by a sequence of magnifying lenses. Confocal microscopy, is an evolution of the conventional fluorescence microscope and was first developed by Marvin Minsky in the mid fifties and patented in 1957. Missing an intense light source to palliate the loss of intensity, the first confocal microscope setups went unnoticed by the scientific community. Inspired by the developments in laser technology occurring in the sixties, imaging of corneal endothelial cells on a confocal microscope equipped with a laser light source was proposed by Davidovits in the mid seventies (Davidovits and Egger 1973). The computational processing power for image reconstruction of confocal laser scanning microscopes (CLSM), available since the

1980s, was the crucial factor to the development of the technique. Today's CLSM based imaging exploits the fluorescence emitted by auto-fluorescent molecules or fluorescent tracers grafted to a molecule of interest. The technique is particularly well adapted to the observation of fluorescence emission due to its high sensitivity and ability to discriminate photons emitted from spatially distinct points (spatial filtering). Furthermore, the corroboration of fluorescence of spatially co-localized objects in a same optical section is facilitated by the reduction of background noise from adjacent layers.

I.E.2. Principles and Instrumentation

A schematic representation of a confocal laser scanning microscope configuration is depicted in Figure 10. The light source of a CLSM is typically an argon, xenon or neon laser which emits a beam of coherent light. The scan head, centerpiece of the confocal microscope, is responsible for applying a rasterized scan of the sample and for collecting emitted photons, which are reconstructed to an image. Two galvanometric mirror scanners move the light beam in a raster-like fashion on x and y lateral directions. In the descanning process, the resulting fluorescence emitted from the sample is restricted to a defined range of wavelength by a fluorescence emission filter. At the heart of a confocal microscope, the pinhole aperture spatially filters the transmitted photons before their detection by the photomultiplier tubes (PMTs), translating count registrations into relative intensities. Fluorescence emission occurring at locations above and below the focal plane of the objective is not confocal with the pinhole and projects Airy discs of increased diameter onto the pinhole, as opposed to in focus emission whose Airy disc diameter is condensed. As a result, only a fraction of out-of-focus fluorescence passes the pinhole aperture, hence drastically reducing the detection of non-focal signal. The pinhole diameter can be modulated by the operator, which modifies the optical section thickness.

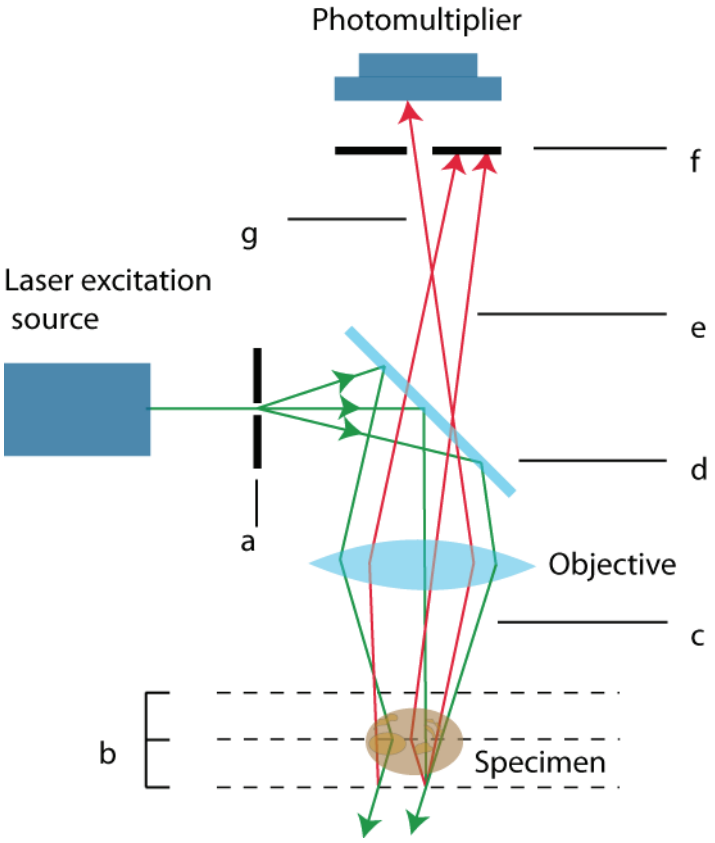

Figure 10: Schematic representation of a confocal laser scanning microscope. *(a) light source pinhole aperture, (b) focal planes, (c) excitation light ray, (d) dichromatic mirror, (e) out-of-focus fluorescence emission light ray, (f) detector pinhole aperture, (g) in-focus emission light ray.*

On modern confocal microscopes, a series of diffraction prisms and aperture slits in proximity to the PMTs allow the acquisition of emission fingerprinting in discrete wavelength bands. These acquisition profiles are followed by spectral unmixing, an algorithm which corrects spectral bleedthrough between different fluorescence spectra.

The work presented in this thesis was conducted on an inverted Zeiss Axiovert 200, fitted with an LSM 510 confocal head and a Zeiss META spectral imager.

Table 6 is a summary of the objectives available on the microscope.

Table 6: Optical objectives installed on the Zeiss LSM 510.

Magnification	Type	NA*	Working distance	Contrast	Immersion
x10	Plan NeoFluar	0.3	5.6 mm	-	-
x10	A-Plan	0.25	4.4 mm	PlasDIC	-
x20	Plan Neofluar	0.5	2 mm	DIC II	-
x20	LD A-Plan	0.3	4.3 mm	PlasDIC	-
x40	Plan Neofluar	1.3	0.2 mm	DIC III	oil
x63	Plan Apochromat	1.4	0.18 mm	DIC III	oil
x63	C-Apochromat	1.2	0.24 mm	DIC III	water

*NA numerical aperture

Table 7 summarizes the lasers present on the Zeiss LSM 510 and their respective excitation wavelengths.

Table 7: Laser lines available on the Zeiss LSM 510.

UV diode	**405 nm**					
Argon		**458 nm**	**476 nm**	**488 nm**	**514 nm**	
Hene1						**543 nm**
Hene2						**633 nm**

I.E.3. Resolution in optical microscopy

Optical imaging devices rely on the emission or transmission of photons by the specimen, either as transmitted light, reflected light or photoluminescence (e.g. phosphorescence and fluorescence). Imaging a light source condensed to a point results in the formation of an electromagnetic field in the image plane. The amplitude variations of the field, described by an amplitude point spread function (PSF), are characteristic of the optical system and its response to the specimen. While amplitude modulation cannot be directly visualised, instruments record images as digital representations of the closely related intensity point

spread functions (PSF). Light emitted from a specimen can be considered as originating from discrete sources below the resolution capabilities of an optical system. As a result, the images consist in partially overlapping PSFs and the resolution of the optical system is defined by its ability to discriminate between two close PSFs.

In a confocal microscope, optical resolution is also determined by the diameter of the pinhole which modulates the size of the Airy disc. As a consequence, for a pinhole of 1 Airy unit, the resolution can be described in the lateral plane xy as follows:

$$R_{xy} = \frac{0.46\lambda}{NA}$$

and in the axial planes xz and yz as follows:

$$R_{xz,yz} = \frac{1.44n\lambda}{NA^2}$$

I.E.4. Fluorescent probes

As mentioned previously, CLSM is well suited for the observation of either live or fixed samples. The ability of a CLSM, shared by all fluorescence microscopes, is to selectively target a fluorescent molecule by its excitation wavelength and to represent a contrasted signal corresponding to the emitted photons against a dark background. Fluorescence microscopy pervaded life sciences due to (i) its high detection sensitivity and high susceptibility to subtle changes in the surrounding chemical environment and (ii) to the use of fluorescent probes and chromophores designed to migrate to specific regions of a specimen.

Generally, fluorescent probes are classified according to their excitation and emission wavelengths, the size of the molecule, their chemical nature, and their ability to permeate membranes of living cells. While live staining is a very popular method to study biological processes on living material, it induces a phototoxic effect through the accumulation of cytotoxic compounds formed during the illumination of the sample (Hockberger et al. 1999 PNAS). The excitation of endogenous (or exogenous) fluorophores may lead to either the decay to a singlet state and photon emission or the decay to a long-lived reactive triplet states producing H_2O_2.

Highly antigen specific fluorescent probes result from the grafting of imunoglobulins (IgG or IgM) or Fab fragments to reactive esterized fluorophores (e.g. N-hydroxysuccinimide ester). Intracellular staining using these high molecular weight probes requires fixation and permeabilization of cells (see I.E.5).

I.E.5. General sample preparation considerations

Specific intra-cellular antigen site recognition through fluorescently labelled antibodies requires fixation before permeabilization of cellular membranes to antibodies by detergents. The most commonly used detergents are Triton X-100 (*t*-Octylphenoxypolyethoxyethanol) and saponin (Willingham, Yamada et al. 1978), a plant glycoside that interacts with cholesterol (Lucy and Glauert 1964). Saponin treated membranes allow the penetration of immunocytochemical markers into the cell. The gentler action of saponin has been shown to result in better preservation of membrane subcellular structure (Bohn 1978; Willingham, Yamada et al. 1978; Goldenthal, Hedman et al. 1985) and is preferred to Triton X-100 for electron microscopy applications. Due to a "washing out" effect of saponin treated membranes, the saponin permeabilization is reversible and each subsequent incubation step and washing step must contain saponin to avoid the closing of pores. Nevertheless, cholesterol free membranes such as the nuclear envelope or the mitochondrial membranes will not be permeabilized by saponin and alternative penetration agents must be considered for intra-organelle staining. Moreover, Triton X-100 remains an excellent choice for confocal microscopy where ultrastructural preservation of membranes is not such an important issue.

Numerous preparation procedures in the literature account for the nature of the sample type (cell, tissue,…), the analytical method of choice (CLSM, OM…) and the observed target (fluorescent probes, gold probes, precipitates). Immunofluorescence (IF) is probably one of the most challenging and most used techniques in modern fluorescence imaging, and has been used extensively during this thesis. It is based on the conjugation of a fluorescent molecule to a monoclonal or polyclonal antibody specific for a target protein and is commonly used in a one-step or a two-step incubation procedure.

In the **one-step procedure** (Figure 11), the specimen is fixed using a low-strength fixative (e.g. methanol, formaldehyde), followed by an optional permeabilization by a detergent. The sample is then preincubated with a blocking solution (e.g. protein rich serum), binding to accessible sample epitopes to reduce background fluorescence caused by unspecific binding of the fluorescent antibodies. Finally, the sample is incubated with a fluorescently labelled monoclonal primary antibody. These primary antibodies present a higher affinity for the studied antigen and compete with the non-specifically bound proteins from the blocking solution.

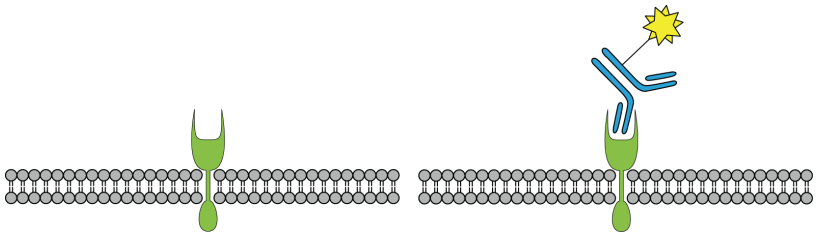

Figure 11: One-step immunolabelling procedure. *No amplification of fluorescence signal.*

The **two-step procedure** (Figure 12) is performed on a fixed, optionally permeabilized sample. Pre-incubation with a blocking solution is mandatory, as background fluorescence is usually higher than in the one-step procedure. During the first incubation, a non-labelled primary monoclonal antibody binds specifically to an antigen. In a second incubation, an isotype-specific fluorescently labelled secondary antibody binds to the primary antibody. Several secondary antibodies may bind to the heavy chain of the same primary antibody and amplify the signal. Low represented antigens, which were under the detection limit in the one-step procedure, profit from this signal amplification and might become detectable. A drawback of this procedure is an increase of background signal caused by unbound secondary antibodies.

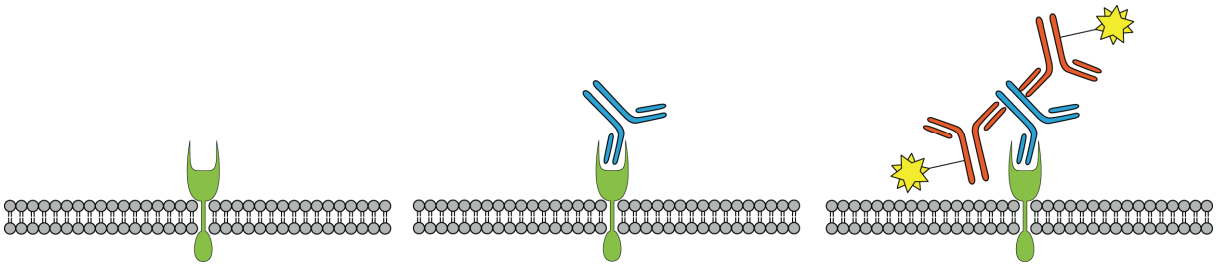

Figure 12: Two-step immunolabelling procedure. *Amplification of fluorescence signal.*

Both procedures require intensive washing to reduce background due to non-specifically bound labelled antibodies and to wash out unbound fluorescent labels (excess DAPI or antibodies). The most commonly used fixative is formaldehyde, which does not cross-link protein sites as thoroughly and thus preserves antigen sites unlike glutaraldehyde-based fixatives.

I.E.6. Advantages and disadvantages of confocal microscopy

Confocal microscopy is inherently non-invasive and imaging can be performed on both living or fixed tissues and cell suspensions. In conventional widefield microscopy, the secondary fluorescence is emitted throughout the volume of excitation, thus effectively hiding features in the objective focal plane. In a CLSM, the presence of a pinhole aperture of adaptive diameter modulates the depth of field. This feature, along with the focusing of a coherent

laser beam, permits the optical slicing and collection of serial sections of typically 0.9 µm with a 1.4 NA 63X objective by modification of the focal plane. The optical sectioning can be performed on specimens of up to 50 µm thickness. Furthermore, the diversion of out of focus information results in a glare effect characteristic of widefield microscopy, which degrades the resolution. Finally, recent confocal microscopes capable of spectral imaging are able to acquire and reconstruct volume projection of time-resolved processes in fluorescent specimen at varying wavelength (emission fingerprinting) over a defined time (timelapse).

Several drawbacks of confocal microscopes have to be addressed. In widefield epi-fluorescence, the arc-discharge lamps are either helium based (HBO) or xenon based (XBO). Arc lamp irradiance spectra cover the whole light spectrum and are used to excite most available fluorophores. In CLSM, the number of possible excitation wavelengths is limited by the number of available lasers, which reduces the number of candidate probes for excitation and fluorescent emission.

Bi-photon and multi-photon excitation fluorescence microscopy are currently under close investigation and may represent the future of confocal microscopy. A pulsed laser emits at a wavelength (e.g. 1000 nm), which is a factor of the excitation wavelength of a fluorophore. The fluorophore simultaneously absorbs several photons from the source, and the excitation energy is equivalent to the sum of the absorbed energies of all the photons. Furthermore, multiphoton imaging only excites fluorophores in the plane of the optical section being imaged. Consequently, fluorophores in the bulk of the specimen are not excited, considerably reducing the photo generation of toxic products in the sample. An important drawback of multi-photon microscopy is the slow acquisition speed harbouring imaging rates of 0.1 frames/s to 2 frames/s (Kim, Buehler et al. 1999), in comparison to classical high speed confocal microscopy fitted with high sensitivity cameras capable of recording live processes at 120 frames/s (e.g. Zeiss LSM Live sonfocal system or Nipkow spinning disc confocal from Leica).

I.F. Electron microscopy

I.F.1. Introduction

Transmission electron microscopes (TEMs) are mainly used to observe submicroscopic structure, composition and properties of a specimen. It has led to significant discoveries in most if not all areas of modern life sciences and can be considered, with optical microscopes, as the most useful tool in cytology and histology. Antibodies coupling to metallic beads,

visible on TEM, afforded immunospecific site recognition and high resolution imaging, further increasing the usefulness of the technique. Besides life sciences, TEM continues to have significant impact in material science, geology and chemistry.

I.F.2. Principles and Instrumentation

The first prototype of a TEM was build more than seven decades ago (Knoll and Ruska 1932). This significant discovery was rewarded by the attribution of the Nobel prize in 1986 for life-long achievements in the field of electron optics (Haguenau, Hawkes et al. 2003).

Its principle, close to widefield microscopes, revolves around an electron source (cathode) emitting a high voltage electron beam (50 - 200 keV). Electrons are accelerated and focused by a sequence of magnetic lenses before passing through a thin sample. Contrast is obtained by scattered electrons detected by i) a phosphorescent plate, ii) a photographic plate or iii) a charge-coupled device (CCD) camera. Modern TEMs usually possess a combination of these detection methods.

The scattering (deviation) of electrons is proportional to the elemental electron density and is directly related to the image contrast. Figure 13 is a schematic representation of a TEM.

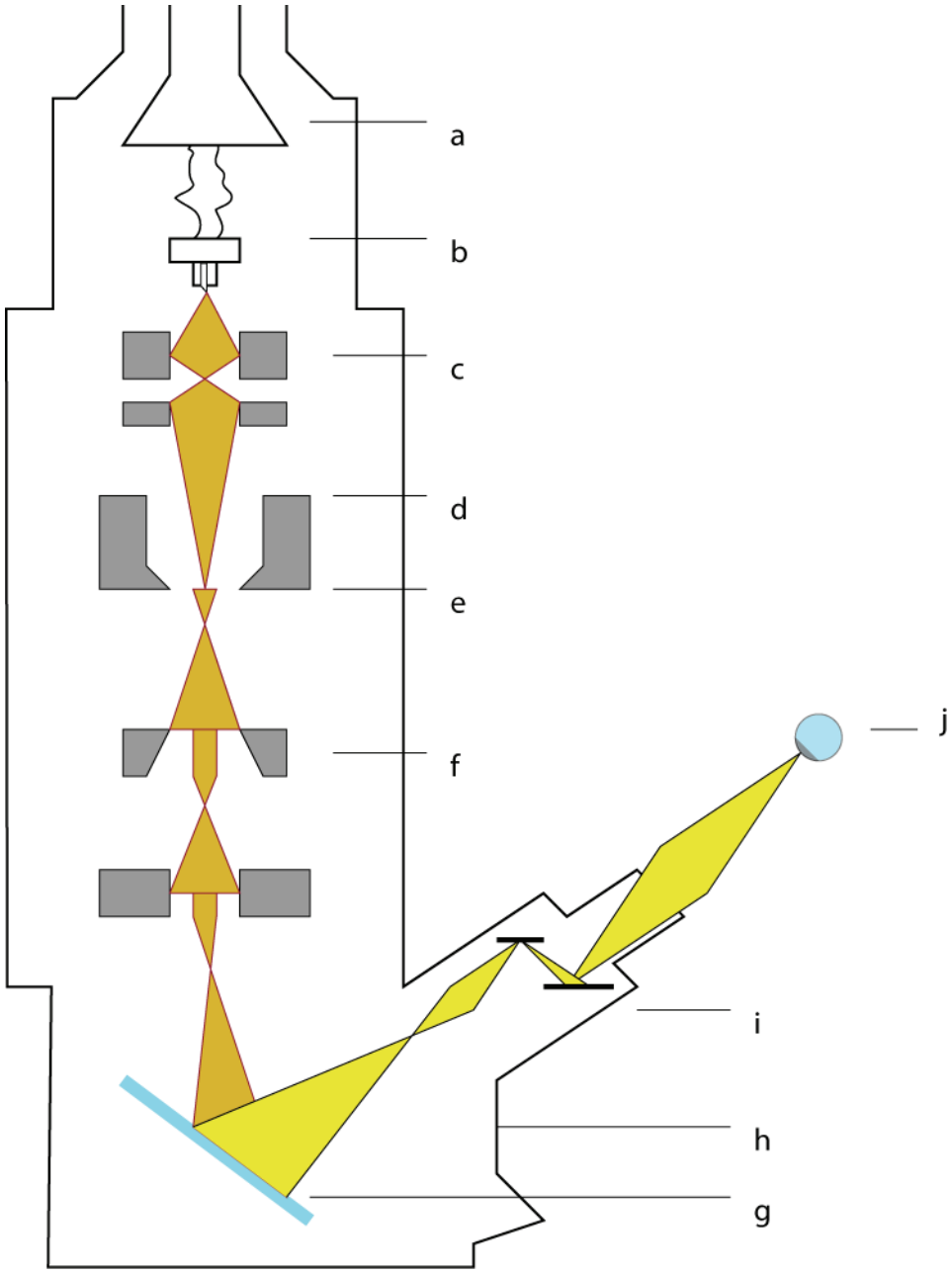

Figure 13: Schematic representation of a TEM, *(a) isolator, (b) source of electrons, (c) condenser lens, (d) objective, (e) sample, (f) projector lens, (g) fluorescent plate / photographic plate, (h) camera, (i) magnifying binoculars, (j) viewer.*

I.F.3. Instruments related to TEM

Over the years, many variations of electron microscopes have found their way into laboratories.

The Scanning Electron Microscope (SEM) emits a finely focused electron beam deflected laterally by scanning coils in the objective lens to raster scan the sample. Secondary electrons emitted from the surface of the sample are detected and reconstructed into an image. The maximum achievable lateral resolution is under 1 nm. Not only are the basic principles of this technique close to SIMS (primary electron/ion source, secondary electron/ion emission), but

the detection of emitted X-rays on electron impact in energy dispersive X-ray spectroscopy (SEM EDS/EDX) can also be used for the chemical characterization at lateral resolutions of 1-10 nm. SEM EDS/EDX is limited to the detection of elements ranging from Boron to Uranium, without discrimination of their isotopes. In the last decade, the environmental SEM (ESEM), a new generation of SEM, has become popular. On such an instrument, analysis is performed at 10-50 Torr in a gaseous atmosphere allowing samples to remain in a hydrated state, therefore it is particularly well suited to the analysis of biological samples in a live state (Nelson 1988).

The Scanning Transmission Electron Microscope (STEM) is a hybrid between TEM and SEM. As in SEM, a focused electron beam is raster scanned on the sample and transmitted electrons are recorded. Chemical mapping analysis can be performed using STEM fitted with EDS/EDX or EELS (Electron Energy Loss Spectroscopy). STEM has been successfully used in biology on numerous occasions (Crewe, Wall et al. 1970; Leapman, Gallant et al. 1997; Gilbert, Beales et al. 2005).

The *High Resolution Transmission Electron Microscope (HRTEM)*, is based on the imaging of interferences of the electron wave with itself and measures the phase component of the electron wave, giving the technique the name of electron phase contrast imaging. HRTEM relies on software algorithms with chromatic aberration correctors to achieve atomic scale resolutions of 0.5 Å.

I.F.4. Resolution in electron microscopy

The single most considerable feature of a TEM is its tremendous increase in resolving power compared to optical microscopes, which are inherently limited by the wavelength of visible light. The de Broglie hypothesis states that

$$\lambda = \frac{h}{p} \quad (1)$$

with $p = m \times v$ where $h = 6.626*10^{-34}$ Js, defining the wave/particle duality relating particle momentum (m× v) and wavelength (λ). Introducing Einstein's theorem

$$E = mc^2 \quad (2)$$

with E the energy of a photon and c = 300.00 m/s into de Broglie equation the wavelength of a photon can be described as:

$$\lambda = \frac{hc}{E} \quad (3)$$

As mentioned in "Resolution in optical microscopy" (I.E.3), the resolution in an optical system is further limited by diffraction patterns of two contiguous Airy discs and in the visible light spectrum (at 400 nm) the maximum resolution is around 200 nm.

A similar approach is used to describe the wavelength of an electron, which is obtained through the equation of the kinetic energy of a particle:

$$E = \frac{1}{2}mv^2 = \frac{p^2}{2m} \quad (4)$$

where v is the velocity of the particle and m its mass. We can rewrite the relation as:

$$p = \sqrt{2mE} \quad (5)$$

By inserting (5) into (1) we obtain:

$$\lambda = \frac{h}{\sqrt{2mE}} \quad (6)$$

Through the use of an electron source, the wavelength can be modulated by varying the electric charge to achieve an increased resolution of 0.2 nm, a thousand times superior to the resolution of an optical system (200 nm).

I.F.5. General sample preparation considerations

Standard TEM analysis requires a sample thickness of 50 to 100 nm. Thicker samples are electron opaque, as only a minute fraction of electrons is transmitted, and thus are unfit for analysis. TEM and dynamic SIMS sample preparation was addressed in I.B.2.

The analysis of the samples presented in this thesis was performed either on a Hitachi H7500 or on a Hitachi H6000.

I.G. Matrix Assisted Laser Desorption Ionization – Time of flight (MALDI-TOF)

I.G.1. Introduction

MALDI (Karas and Hillenkamp 1988; Hillenkamp, Karas et al. 1991) is an analytical method suited to the identification of proteins, peptides, oligonucleotides and oligosaccharides. As the technique is robust and relatively permissive to buffers and contaminants, it is widely distributed and together with electrospray ionization mass spectrometers (ESI-MS), it is the most important tool in proteomics. Moreover, peptide sequences or protein post-translational modifications (PTMs) are accessible through MALDI. Whereas protein identifications are based on correlation between measured peptide mass spectra and known sequences from

protein databases, *de novo* sequencing, without prior knowledge of amino acid sequence is also possible.

I.G.2. Principle and Instrumentation

Similarly to SIMS instruments, MALDI mass spectrometers may be fitted with mass analyzers of different types, typically TOF tubes, quadrupoles, magnetic sectors and Fourier transform ion cyclotrons. The numerous combinations between ion sources, mass analyzers and detector components are outside the scope of this work and covered extensively in the literature (Aebersold and Mann 2003). The instrument used during this thesis was a Bruker Ultraflex I (Bruker, Leipzig, Germany), a mass spectrometer with a reflector TOF mass analyzer. The basic principle of this instrument will be addressed in the following paragraphs.

In MALDI-TOF, the concept of matrix is fundamentally different from TOF-SIMS. A UV laser, commonly a nitrogen laser at 337 nm, targets a matrix cocrystallized to the analytes. At laser impact, both components are vaporised into the gas phase. At this stage, an energy transfer (proton transfer), termed desorption, occurs from the matrix to the analyte. Extraction and acceleration of ions is performed by electronic lenses.

In the linear mode, ions enter the field-free zone of the tube-of-flight mass analyzer where ions of different mass-to-charge (m/z) ratios have different velocities and maintain their respective kinetic energy. In other words, TOF analyzers separate ions according to their m/z ratio, with heavy ions drifting more slowly in the tube than light ions. The TOF in the tube is measured for individual ions by time-sensitive detectors and deducted to their m/z ratio. As MALDI is considered a soft ionization method, it generates predominantly singly charged (z=1), mostly unfragmented molecular ions, and their m/z ratio can be considered equivalent to their mass.

In the reflectron mode of a reflector TOF mass analyzer, at the exit of the field-free zone, ions are subjected to an electrical field gradient. Ions of identical mass travel in the tube with a broad energy distribution, thus penetrating differently into the field gradient before being reflected, and resulting in the compensation of the energy dispersion of reflected ions in a population of same mass. Consequently, the mass resolution of the instrument is improved. Additionally, the reflectron may be used to separate ions that are generated by post-source decay (PSD). Those metastable parent ions spontaneously decay in the drift tube to a series of daughter ions of inferior masses.

While in linear mode the resulting ions retain the velocity of the parent ion and arrive at the same time on the linear detector, in the reflectron mode ions of different kinetic energy and

mass, but same velocity, are reflected differently and hit the reflector detectors at different times. Therefore, the reflectron can be used to separate parent ions from their daughter ions issued from PSD (Figure 14).

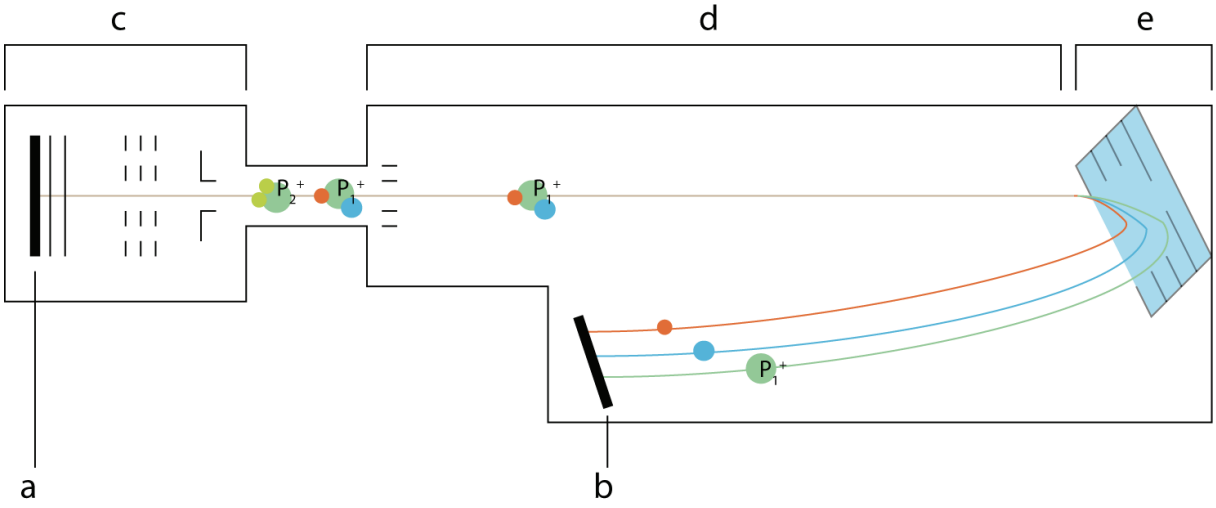

Figure 14: Principle of PSD and reflectron, *(a) target plate, (b) reflector detector, (c) source and ion selection, (d) drift region, (e) reflector/linear detector.*

Probably the most common application of MALDI mass spectrometry is peptide sequencing using tandem MS (MS/MS). This technique relies on the ability to select one parent ion, provoke its decay, e.g. by a higher energy contribution from the laser ("laser induced decay") or through collision induced decay in a collision cell, where ions are forced to collide with a gas, commonly argon or helium. In MALDI, peptides decay consists mostly in peptide backbone fragmentation and sidechain fragmentation. A nomenclature for bond breakage has been proposed (Roepstorff and Fohlman 1984; Johnson and Biemann 1989; Rouse, Yu et al. 1995), which takes into account peptide bonds susceptible to break during MALDI ionization and post source decay (Figure 15).

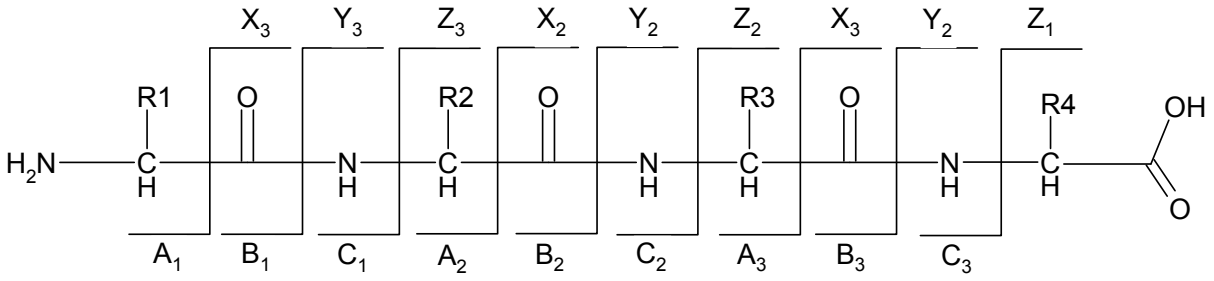

Figure 15: Susceptible peptide backbone cleavage sites. *For each amino acid residue six main fragment ions are possible. A, B and C ions retain their charge ion on the N-terminal fragment. X, Y and Z retain their charge on the C-terminal fragment.*

During MALDI peptide sequencing, peptide fragments of different masses are grouped together by series (A,B,C and X,Y,Z) using combinatorial analysis to obtain several, usually incomplete, amino acid sequences. Protein identification is carried out by mapping mass lists

of potential sequences against known sequence databases for the best match. Protein sequence databases are collections of mass lists obtained by digesting purified proteins with a given enzyme.

I.G.3. General sample preparation considerations

Large peptides cannot be directly identified by MS and have to be fragmented by tryptic digestion before analysis. The proteolytic activity of Trypsin cleaves peptides on the carboxyl side of arginine (R) and lysine (K) aminoacids. The resulting MS spectrum, termed "peptide mass fingerprint" or PMF is often precursor to MS/MS for protein identification.
While large sized proteins may need enzymatic digestion, it implies an increase of complexity of the sample. Simplification of peptide mixes is provided by liquid chromatography coupled to MS (LC-MS) where peptides are prefractionated by chromatography prior to mass spectral analysis (Hunt, Henderson et al. 1992).

I.H. Scope of the thesis

This thesis is aimed at investigating the utility and the need of the CAMECA NanoSIMS ion microprobe in life science research and to define methods, both preparative and analytical, to improve secondary ion mass spectrometry imaging. The limited knowledge of the behaviour of biological samples under a primary ion beam impedes the identification of tissue and cellular features and requires supplementary confirmation by complementary techniques. Abiding to the experience gained in the course of the thesis, several applications are proposed in the areas of trace metal detection, phagocytosis and protein localization.

Chapter II is not a study *per s*e. However, it describes the development of several utilities for the conversion and processing of SIMS image data files and the extraction of acquisition parameters. Image processing includes several algorithms for ratiometric data analysis. Furthermore, the use of an algorithm to normalize image intensities to improve heterogeneously implanted images is proposed. Finally, the development of a similar software utility for the analysis of confocal images is presented.

The objective of the first study (Chapter III) was to address shortcomings in NanoSIMS imaging, generally due to insufficient understanding of the underlying physical processes involved in primary ion implantation. A first step involved the characterisation of implantation artefacts, both through theoretical computer models and experimental data, that

lead to poor secondary ions yields and thus to images of spuriously distributed intensity. In a second step, best practice analytical approaches to improve secondary ion emission were defined, involving a better timed implantation at potentially higher intensity. Finally, an alternative solution was proposed involving pre-implantation on another SIMS instrument. This strategy had the advantage of resulting in a gain of time by homogenous large surface pre-implantation, eliminating the need for regional implantation on the NanoSIMS.

The second study (Chapter IV) aimed at evaluating and improving sample preparation of cells and tissues for NanoSIMS microanalysis, characterised by ultra high vacuum and stability of the sample under the ion beam. Several approaches were investigated, which can be considered as adaptations from transmission electron microscopy. These preparations were compared to optical microscopy protocols for pathology, based on paraffin-embedded tissue samples deposited on glass slides, and to TEM protocols. Ion micrographs obtained by SIMS were compared to imaging techniques such as optical microscopy and electron microscopy. A first example of SIMS labelling using a halogen-based marker was given.

The third study (Chapter V) built on the experience gained in tissue processing for SIMS imaging from the preceding chapters to support the use of highly resolutive NanoSIMS analysis for trace metal detection in lichens.

The fourth study (Chapter VI) introduced the concept of metabolic labelling in SIMS using stable isotopes. The study of the uptake and processing of fully labelled bacteria by human monocytes was proposed as a potential application of SIMS. The incorporation of the label provided as a stable nitrogen isotope in the culture media of bacteria was assessed by two different methods. The first method, based on MALDI-TOF mass spectrometry, determined the incorporation of the label at the proteome level by targeting an abundant bacteria protein. A second method, using a ratiometric analysis of the stable isotopes of nitrogen measured by SIMS, determined the total incorporation of the labelled isotope by the bacteria. Finally, the bacterial phagocytosis was followed by SIMS and the protein turnover was evaluated for several subcellular organelles.

In the fifth study (Chapter VII), the isotope labelling was further refined, ultimately leading to the development of a $^{13}C^{15}N$ labelled antibody directed against the viral nucleoprotein of the measles virus. Several experiments were devised to characterise the chronology of a measles

infection and to investigate the formation of aggregates of both human MxA and viral nucleoprotein in a monocytic cell line. Aggregates were studied in SIMS by stably labelled amino-acid pulsing and immunolabelling using the previously mentioned antibody. To our knowledge, this is the first reported immunolabelling experiment in SIMS imaging. The SIMS study of the formation of aggregates was complemented by confocal microscopy.

Due to the nature of Chapter II, oriented towards software development, the form of narration was different from the following chapters. It describes the main developmental difficulties, presents the algorithms integrated in the software and mentions the implemented features.
Chapter III, IV, V, VI and VII are each constituted of the sections "Introduction", "Material & Methods", "Results" and "Discussion", treating separately each application. A general discussion draws the most noteworthy conclusions from the preceding chapters and includes an outlook on further developments and the future role of SIMS in life sciences.

Published:

Pirrotte, P., Guerquin-Kern JL., et al. (2006). Secondary Ion Mass Spectrometry in Life Sciences. In: Biophotonics for Life Sciences and Medecine. Eds: M. Faupel, P. Smigielski, A. Brandenburg and J. Fontaine, Fontis Media

Manuscripts in preparation:

Based on Chapter III:

Pirrotte, P., Audinot, J.N., Migeon H.N., Muller, C.P. Implantation on NanoSIMS 50 : Relevance for the analysis of biological samples.

Based on Chapter V:

Pirrotte, P., Azevedo-Rodrigues, S., Fernandez-Salegui, A.B., Audinot, J.N., Migeon, H.N., Muller, C.P. NanoSIMS imaging of trace metals in lichens.

Based on Chapter VI and VII:

Pirrotte, P., Revets, D., Kremer, J., Fack, F., Audinot, J.N., Migeon, H.N., Muller, C.P. Metabolic labelling using stable isotopes on NanoSIMS. Potential applications in life sciences.

Chapter II Software Development

II.A. Development of an image analysis software package for Cameca NanoSIMS images

II.A.1. Introduction

The recent breakthrough of ion microscopy coupled with the still small user community has resulted in a shortage of generally available tools for SIMS data analysis, especially for image treatment. Most of these utilities are developed internally in each SIMS platform and rarely shared. Furthermore, basic image treatments are usually performed by the acquisition software on the instrument and converted into more common file formats, such as the lossless Tagged Image File (TIFF), the Portable Network Graphics (PNG) (ISO/IEC IS 15948:2004) or the lossy Joint Photographic Experts Group (JPEG, ISO/IEC IS 10918-1, ITU-T T.81).

Regular work with SIMS ion maps identified the need for tools more adapted to the visualisation of these images, to be compatible with depth stacks and to offer isotopic ratio calculation capabilities.

The few utilities freely available are mostly incomplete, not up-to-date and lack scripting abilities for batch analysis. The program *ImConvert* was developed by Cameca, running solely on Microsoft Windows operating systems, which opens and converts SIMS image acquisition maps to various common formats. Its post-treatment functions are very limited. Look-up tables (LUT) can be applied to image maps and the pixel intensity can be distributed against a logarithmic or a linear scale. ImConvert extracts basic acquisition parameters only and, although it is closed source, binaries of the program are available on demand at Cameca.

Doug Benson has developed the *NRIMS analysis module* (Benson 2007) for the National Resource for Imaging Mass Spectrometry (Harvard Medical School). It is a plugin for the ImageJ image analysis framework, thus profiting from the vast library of image analysis plugins available for ImageJ. It offers several ratio calculation methods for isotopic images, most notably the HSI (Hue Saturation Intensity) method. In its current version (January 2007), a few measurement tool features were integrated into the plugin. While the source code is freely available, to date no statement has been issued on the licensing scheme.

Through the regular use of these tools, the need for batch analysis and file format conversion became obvious. A new software utility, which would combine these features, would be useful.

II.A.2. Developmental notes

Complete metadata extraction: During NanoSIMS ion map acquisitions, most instrumental parameters are recorded as metadata alongside image description inside the Cameca image file format. The image analysis software developed during this thesis was based on the most recent file format definitions available (version 5, graciously provided by Cameca) and was designed to extract the totality of the information stored inside these files (over 200 instrumental parameters). An option to export these parameters to the human legible Extensible Markup Language (XML) data representation was also included.

Cross-platform usability: While IBM PC compatible hardware, running the Microsoft Windows operating system, is the most widespread, alternative operating systems like Apple Macintosh OS or Unix flavours are commonly found in the scientific community. To address the largest user community, the object oriented Java programming language (Sun Microsystems) was chosen to develop the utility. Java is a compiler language where human readable source code, grouped into classes, is compiled into a machine-readable binary format. Java binary classes are run in a Java Virtual Machine (JVM), which plays the role of an interface between the application and the underlying operating system and its hardware. As JVMs are available for most platforms, a compiled Java application runs on many different operating systems ("compile once, run anywhere"). The first JVM was released by Sun Microsystems in 1995, and ever since the language was submitted to a continuous user reviewed process termed "Java Community Process", which led to alternative implementations, both free and commercial, of the JVM specifications. The primary JVM targeted by the application was the standard Sun Java Virtual Machine version 1.4.2 (Merlin release, specification JSR 59).

A major drawback of the use of Java is the speed decrease, caused by the added abstraction layer of the JVM, which acts as a virtual hardware interface when compared to machine dependant programming languages (e.g. C, C++). This drawback is nevertheless compensated by modern hardware with recent chipsets and fast access times to random access memory and hard drives.

Integration into an image-processing framework: ImageJ is an image-processing application targeted to the scientific community and developed by Wayne Rasband at the Research Services Branch of the National Institute of Mental Health (NIMH, Bethesda, U.S.A.), a department of the National Institute of Health (NIH,U.S.A.). While its predecessor NIH Image was only available on the Apple Macintosh platform, ImageJ is written in Java

and thus runs on most operating systems. ImageJ's interface is based on the Advanced Windows Toolkit (AWT) from the Java Foundation Classes.

The large number of processing plugins available for the ImageJ application motivated the choice of ImageJ, also taken by Doug Benson for the development of the NRIMS plugin. A macro language for batch processing and the functional extension of ImageJ is integrated into the framework, with several hundreds of pre-defined macros available. Furthermore, the community around ImageJ development is dynamic, and comprises scientists from many fields, from biology and medicine to geology and industrial engineers, resulting in many implementations of signal processing algorithms. Finally, ImageJ is released under the public domain, and the source code is fully available for review and modifications without any limitations.

An open-source licensing model: The NanoSIMS user community being very small, the development of an application tailored to the analysis of NanoSIMS image data cannot target a large public. To avoid any potential deadlocks that could have occurred with an application limited to selected SIMS platforms, a more open distribution scheme was chosen. The application was initially released under the Creative Commons Attribution-NonCommercial-NoDerivs 2.5 license. Following releases were licensed under version 2 of the GNU General Public license (Foundation). Both licenses required the public release of the source code, and while the CC license does not allow derivations of the work, the GPL encourages the dissemination and the modification of the source code.

Isotopic ratio calculation: By isotopically enriching the sample, semi-quantitative analysis can be performed on SIMS by measuring isotopic ratios and comparing these to their natural abundance. The application should implement standard ratio measurement and more advanced algorithms based on a HSI representation of ion maps.

To further increase the range of use of the application, the development of the utility was separated into a reader module (codec) and an analysis module (ImageJ plugin). The codec, called *SIMSReaderImageIOPlugin*, uses the ImageIO API distributed with most JVMs (javax.imageio.ImageIO package) to read both images and series of images (stacks) as collections of java.awt.BufferedImage, and extract and represent metadata in hierarchical memory structures. The resulting codec can be distributed on any Java enabled platform and used to open NanoSIMS images. By providing the codec to the JVM, existing applications, whose image loading mechanisms use ImageIO, are automatically extended to recognize the Cameca Image format. *SIMSReaderImageIOPlugin* is independent of the ImageJ imaging framework.

The ImageJ plugin, called SIMSToolbox, is a wrapper to the *SIMSReaderImageIOPlugin* codec comprising a Swing graphical user interface (GUI) to represent 16 bit grayscale ion maps (e.g. counts are represented using 2^{16} = 65536 discrete values) in an ImageJ window (class:ij.gui.ImageWindow for a standard image and class:ij.gui.ImageStack for a stack) Metadata are represented in a tree structure (class:javax.swing.JTree), with additional search functions. The complete metadata tree can be exported to XML for further treatment in other applications. Metadata comprises analyzed mass name (as a character String, e.g. 31P) for each detector, exact mass as set during acquisition (as a decimal value, e.g. 30.9834), settings for entry and exit slits, potential measured at various lenses (e.g. L0, L1), among others.

Ratio images are usually represented as either monochrome images, intensity projections or pseudocolor hues (Poenie, Alderton et al. 1986; Tsien and Harootunian 1990). Two ratio calculation modes, the standard ratio mode and the HSI ratio mode, were integrated into the SIMSToolbox. Both modes of ratio representation yield inconsequential values for regions where intensities of both $I_{iso1}(x,y)$ and $I_{iso2}(x,y)$ are close to 0. To avoid these artefactual ratio values, both iso1 and iso2 images can be thresholded to a cut-off value. Pixel values of ratio intensities are set to predefined background values (usually intensity 0, black) if iso1 or iso2 pixel intensities are below the threshold.
To calculate a *standard ratio* between two isotopic images iso1 and iso2 (typically $^{12}C^{15}N$ versus $^{12}C^{15}N$), the following equation is used by SIMSToolbox:

$$R(x,y) = \frac{I_{iso1}(x,y)}{I_{iso2}(x,y)} \times b$$

Where for each pixel at pixel positions x and y, R(x,y) is the resulting ratio intensity counts, $I_{iso1}(x,y)$ the intensity of iso1 and $I_{iso2}(x,y)$ the intensity counts of iso2. The constant b depends on the bit depth of the resulting ratio image to scale up the values to bit range.

The ratio calculation method devised by Tsien, Harootunian and Poenie (often referred as either *Tsien-Poenie ratio* or *HSI ratio*) depicts the images using a spectrum lookup table with a homogenous hue arrangement. HSI is a non-linear transformation of the RGB (red, green, blue) colour space (Smith 1978) (Figure 16A). In the HSI model, the colour gamut is formed of the three components hue, saturation and intensity which describe colours in familiar terms (hue: pure colour; saturation: purity of colour, vibrancy; intensity: brightness of colour). Blue,

generally known as a cold colour, is mapped to low ratio intensities, while high ratio values are mapped to red or pink (Figure 16B).

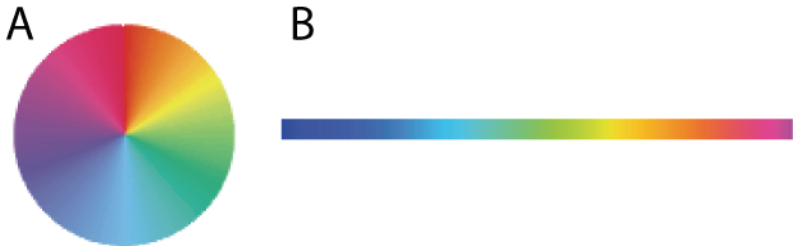

Figure 16: Representation of the Hue, Saturation and Intensity colour gradient. *(A) HSI colour wheel, colours are defined by polar coordinates, (B) linear HSI gamut.*

Conversion between HSI and RGB colour space is provided by the following equations:

$$Hue = \frac{\frac{1}{2}\left((R-G)+(R-B)\right)}{\sqrt{(R-G)^2+(R-B)\times(G-B)}} \quad (1)$$

$$Saturation = \frac{\left(\max(R,G,B)-\min(R,G,B)\right)}{\max(R,G,B)} \quad (2)$$

$$Intensity = \frac{R+G+B}{3} \quad (3)$$

In case of ratio calculation, the hue is described as follows:

$$Hue(x,y) = R(x,y)\frac{I_{iso1}(x,y)}{I_{iso2}(x,y)} + B \quad (4)$$

Both a(x,y) and b are used to scale up the values to the bit range. For the processing of SIMS ratios Doug Benson rewrote equation (4) to take account of minimal and maximal ratio values (Benson and Lechene 2005; Benson 2007):

$$Hue(x,y) = \frac{R(x,y)-R_{\min}}{R_{\max}-R_{\min}} \quad (5)$$

The intensity is described as either:

$$Intensity(x,y) = \max\left(I_{iso1}(x,y), I_{iso2}(x,y)\right) \quad (6)$$

$$\text{or } Intensity(x,y) = \min\left(I_{iso1}(x,y), I_{iso2}(x,y)\right) \quad (7)$$

$$\text{or } Intensity(x,y) = \frac{\left(I_{iso1}(x,y)+I_{iso2}(x,y)\right)}{2} \quad (8)$$

$$\text{or } Intensity(x,y) = I_{iso1}(x,y)^2 + I_{iso2}(x,y)^2 \quad (9)$$

As computer displays only represent colours defined in the RGB colour space, the values for hue, saturation (constant) and intensity are converted into RGB triplets as follows:

$$\mathrm{Re}\,d(x,y) = Hue_R(x,y)\times Intensity(x,y) \quad (10)$$

$$Blue(x,y) = Hue_B(x,y) \times Intensity(x,y) \quad (11)$$

$$Green(x,y) = Hue_G(x,y) \times Intensity(x,y) \quad (12)$$

Using a HSI palette, the Tsien-Poenie ratio images visually enhance variations recorded on the large dynamic range of SIMS images. Small regions of interest (ROI), of a few pixels only, with high ratio (pink), stand out against a low ratio (blue) background.

Figure 17 and Figure 18 depict the graphical user interface of SIMSToolbox.

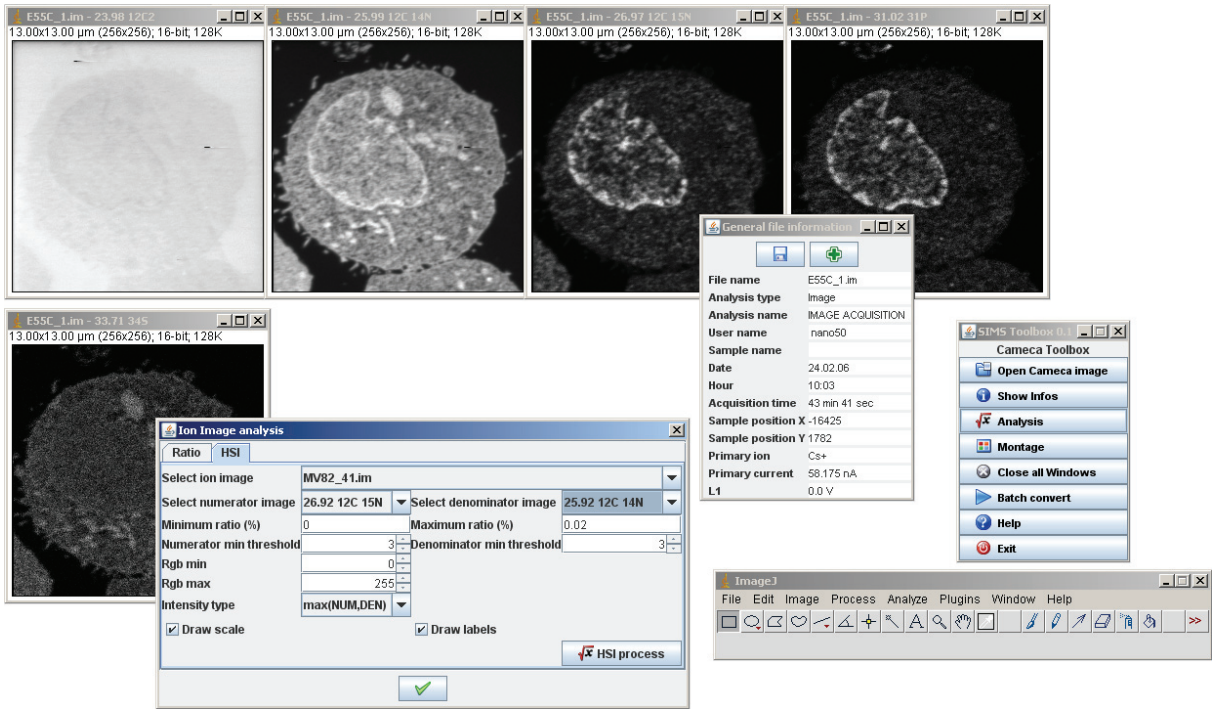

Figure 17: SIMSToolbox interface in ImageJ. Ratio graphical user interface and info screen.

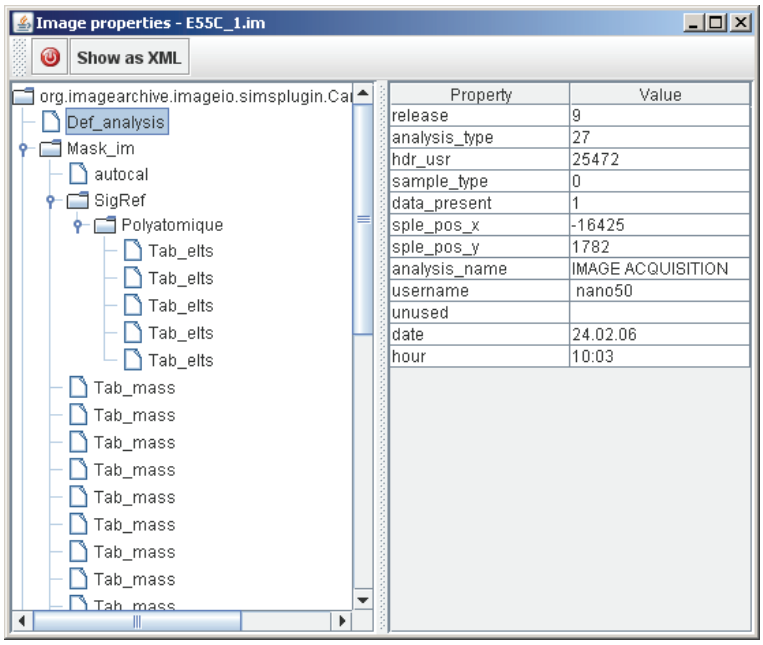

Figure 18: SIMSToolbox Metadata tree representation, with the XML export option.

Public release and Documentation

Both plugins are available as binaries and source code. Installation and user documentation is available at the download site and on the ImageJ documentation wiki.

SIMSReaderImageIOPlugin is available at

http://imagejdocu.tudor.lu/Members/ppirrotte/simsreaderimageioplugin

SIMSToolbox is available at

http://imagejdocu.tudor.lu/Members/ppirrotte/sims_toolbox/

II.B. Enhancement of SIMS images

Digital images obtained by SIMS exhibit various analytical artifacts that prevent proper post-acquisition data processing. Images from new generation SIMS, such as NanoSIMS, are especially prone to aberrations. Those are mostly due to the prototype nature of the instrument, which also reduces the throughput of images per acquisition session. As a SIMS analysis involves an implantation of several minutes to reach the dynamic state of secondary emission, only 10 to 15 images are generated per day of analysis, it is therefore particularly important to reduce these artifacts to improve the throughput of the instrument.

Most of the artifacts result either from background noise or from heterogeneous implantation, and a method to prevent the formation of implantation artifacts, based on the pre-implantation of primary ions in the sample on an IMS-6f, is proposed in Chapter III.

An adequate use of post-acquisition image enhancement may improve otherwise unusable SIMS data. The most common algorithm used to remove background was based on homogenously *thresholding* the image. The HSI images provided by the algorithm presented in II.A were obtained after a variable thresholding, usually a subtraction of 1-3 counts/pixel, of both isotope ion micrographs before the calculation of the HSI ratio.

Another image enhancement performed on SIMS images suffering from implantation artifacts is *histogram matching* (Gonzalez, Woods et al. 2004). When observing the intensity histogram of such images, an orientation in the intensity distribution can be observed. This is exemplified for Figure 19A and its intensity histogram Figure 19B. A standard processing algorithm would involve an equalization of the histogram, by spreading the levels of intensity of the image over a wider range of the intensity scale. This normative transformation does not always yield good results (Figure 19C and Figure 19D).

With an *a prior*" knowledge of what result is to be expected from the processing, a non linear transformation may drastically improve the quality of images, with an orientation of both highly concentrated dark pixels (low ion counts/pixel) and lowly concentrated bright pixels

(high ion counts/pixel), resulting from an inhomogeneous implantation. Histograms of these images are essentially bimodal, with a mode at the origin and another mode in the high-end range. By matching these histograms against a bimodal Gaussian function, images are improved further than with standard histogram equalization (Figure 19E and Figure 19F). Cellular features inside the green frame of Figure 19E are the most notably enhanced by this transformation. The image processing presented in this section was performed with Matlab R2007B (The MathWorks, MA, USA) using the algorithm presented by Gonzalez et al (2004).

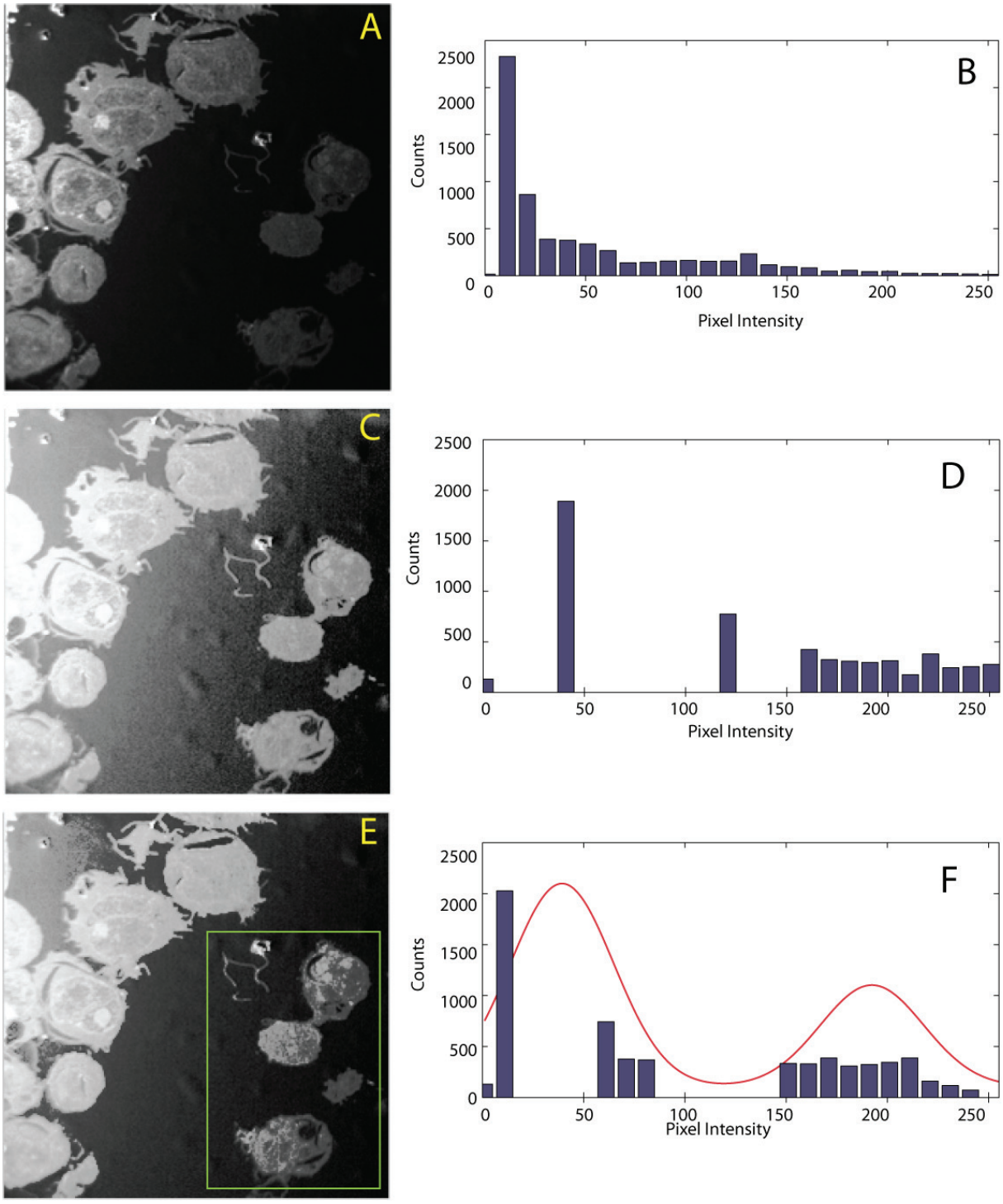

Figure 19: Inhomogeneously implanted Ion micrographs and their histograms. Enhancement by histogram matching algorithms. *(A) NanoSIMS image ($^{12}C^{14}N^-$) with implantation artefacts. Bottom-right corner is badly contrasted. Top-left corner is well implanted. (B) Intensity histogram of A. (C) Same image, normalized by a linear transformation ("standard histogram equalisation"). (D) Intensity histogram of C. (E) Same image, normalized by a bimodal transformation of its intensity distribution. Features of cells in the green frame are more contrasted. (F) Intensity histogram of E. Bimodal gaussian in red (First median = 0.15, First standard deviation = 0.10, Second median = 0.75, Second standard deviation = 0.10, Floor = 1, First amplitude = 0.50, Second amplitude = 0.002). Histograms obtained with Matlab R2007B (The Mathworks, MA, USA)*

II.C. Development of an image analysis software package for Zeiss LSM510 confocal images

As from 2003, I decided to further the development of the LSMReader, a Java application that provided support in ImageJ for LSM510 confocal images, and which was initiated by Yannick Kremmpp and Jérôme Mutterer. The reasons for using Java and the ImageJ framework have been developed in II.5.2. To separate the decoding capabilities of the plugin from the analysis modules, I entirely rewrote the LSMReader and developed a new application, termed LSMToolbox, based on the same reader codec, to include several options for confocal image processing. The features of the LSMToolbox include: macro awareness to allow scripting and batch processing of images, and support for LZW compressed confocal images. Furthermore, the application is compatible with 8, 12 and 16 bit images and image stacks (depth: z-stacks, time: t-stacks and lambda: λ-stacks). Image manipulations include image stamping (including depth, time and spectral data). Image stacks can be visualised in HyperVolume_Browser, developed by me, or Image5D (Walter, Tellerb et al. 2006), which is based on HyperVolume_Browser. Channel merging, fusion and LUT mapping are supported. The LSMToolbox extracts most of the data included in the Zeiss file format version 4.0 and presents them in a similar fashion than the SIMSToolbox. Figure 20 depicts the graphical user interface of LSMToolbox.

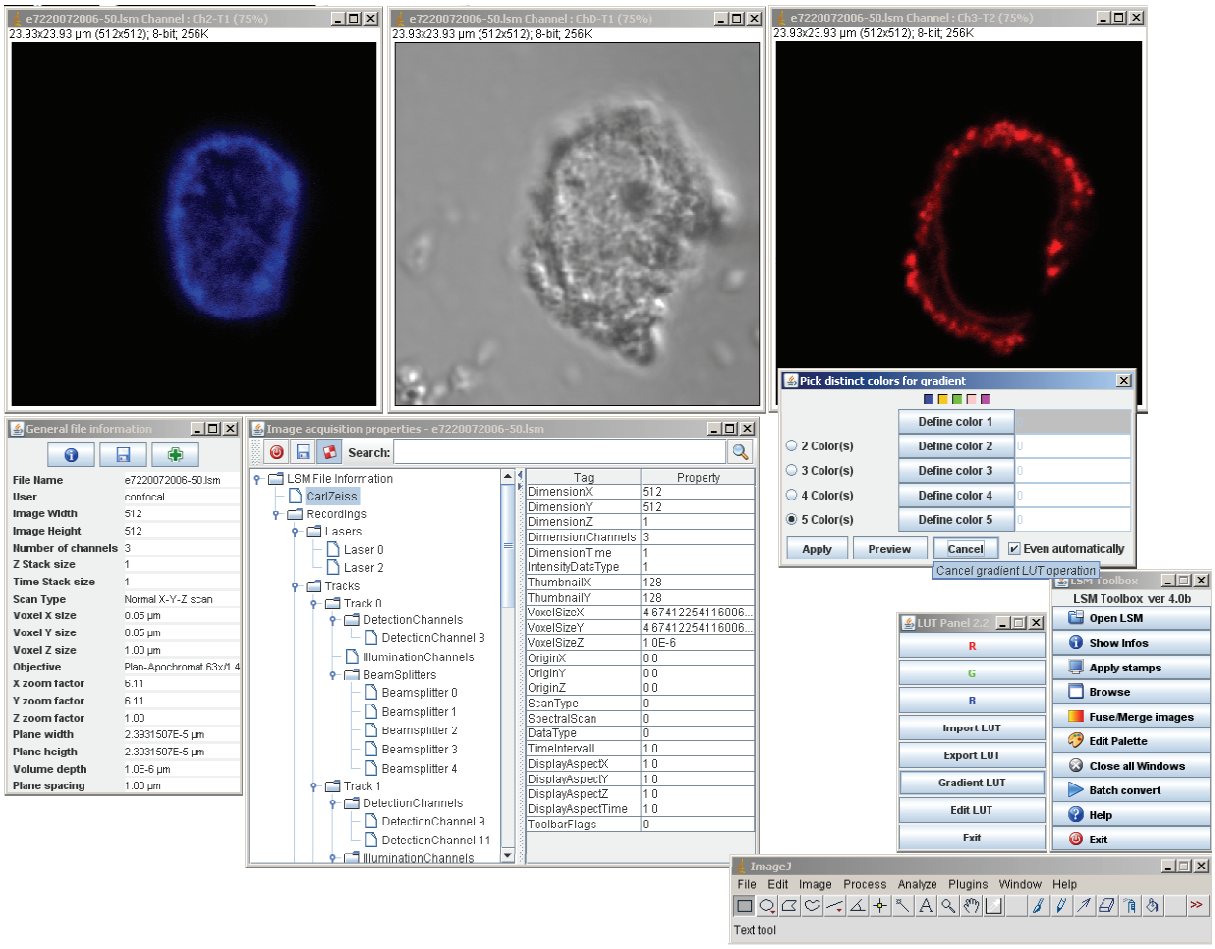

Figure 20: LSMToolbox interface in ImageJ, with info screen, metadata tree representation and the Lut_Panel gradient window.

Public release and Documentation

Both plugins are available as binaries and source code. Installation and user documentation are available at the download site and on the ImageJ documentation wiki.

LSMReader is available at

http://imagejdocu.tudor.lu/Members/ppirrotte/lsm_reader/

LSMToobox is available at

http://imagejdocu.tudor.lu/Members/ppirrotte/lsmtoolbox

Additionally, other plugins developed during this thesis are:

Lut_Panel is available at

http://imagejdocu.tudor.lu/Members/ppirrotte/lut_panel/

and HyperVolume_Browser is available at

http://imagejdocu.tudor.lu/Members/ppirrotte/hypervolume_browser/

II.D. Discussion

During the first year of this thesis, images acquired on the NanoSIMS ion microprobe were processed with Cameca's *ImConvert* software. In the following years, the ImageJ plugin *SIMSToolbox* and the codec *SIMSReaderImageIOPlugin* were used to extract SIMS images and associated metadata. Its algorithm for the HSI ratio calculation of isotopic image data was adapted from Doug Benson's ImageJ module, whereas other features such as total metadata extraction and batch analysis are attributes unique to *SIMSToolbox*. Ratiometric analysis using HSI was particularly useful to enhance the visual perception of a localised isotopic enrichment and was extensively used to process the image data obtained in Chapter VI and Chapter VII, where a localised excess of ^{15}N due to a differential integration of the isotope was emphasized by applying a HSI colour range to a ratio image of $^{12}C^{15}N^-/^{12}C^{14}N^-$. Furthermore, the implemented algorithm thresholded the ion images before the ratiometric calculation to reduce the background noise and generally improve the signal-to-noise ratio of detected ions. Both the codec and the ImageJ plugin were presented at *the First ImageJ User and Developer Conference* (poster presentation: Pirrotte, Audinot et al. 2006). Several laboratories have expressed their interest in the software, and it is used for the processing of their NanoSIMS acquisition files.

The histogram matching algorithm described in II.B was applied to enhance features in poorly contrasted images This algorithm is presented as a post-acquisition processing solution to enhance images suffering from an insufficient primary ion implantation. In parallel, experimental improvements to reduce implantation artifacts at acquisition were investigated and are presented in Chapter III.

In complex transformations, such as histogram matching, the intensity distribution is altered in relation to the histogram of the input image. Therefore, even transformations on isotope images of a same element such as $^{12}C^{14}N^-$ and $^{12}C^{15}N^-$ are decoupled and the resulting transformed images are not fit for quantification through ratiometric analysis.

However, the use of this algorithm notably increased the number of usable images resulting from a NanoSIMS acquisition session and helped in qualitatively determining cellular features otherwise masked by a differential contrast caused by insufficient implantation. The implementation of this algorithm into the *SIMSToolbox* application is planned.

The *LSMToolbox* and its reduced version the *LSMReader*, both developed during this thesis, have encountered a considerable success with reports of installation in several hundreds of laboratories in more than 40 different countries. In the latest months, numerous articles have

referenced the use of the plugin in various fields of applications (Smets, Caplanusi et al. 2004; Baron, Caplanusi et al. 2005; Fournel, Wieckowski et al. 2005; Kim, Liu et al. 2007; Klumpp, Lacerda et al. 2007). This keen interest has resulted in the bundling of the small footprint LSMReader in current releases of ImageJ in order to implement confocal image treatment functionality. Furthermore, the package was integrated in a client/server application developed for archiving of confocal images (Pirrotte and Mutterer 2004).

Chapter III Implantation on NanoSIMS

Relevance for the analysis of biological samples

Manuscript in preparation: Pirrotte, P., Audinot, JN., Migeon HN., Muller, CP. Implantation on NanoSIMS 50 : Relevance for the analysis of biological samples

III.A. Introduction

Primary ion bombardment and secondary ion formation in SIMS are currently under close scrutiny to better comprehend these processes, (Solomko, Verstraete et al. 2006). Particularly primary ion implantation and its influence on secondary ion emission remains a core subject in dynamic SIMS literature (Gnaser 1995; Mazarov, Samartsev et al. 2006; Tuleta 2006; Wittmaack 2006).

By modulating the primary ion dose, two secondary emission regimes can be highlighted. While SIMS is generally considered a destructive technique, in the static regime, with a primary ion fluence (dose) of under 10^{13} atoms/cm^2, less than the equivalent of one atomic layer is sputtered during the analysis. The operation of a SIMS instrument in the static regime provides elemental and molecular information from the uppermost layers of the specimen. In static SIMS, less than 1% of the sample surface is pulverised, highly reducing the probability of a subsequent primary ion impact at a previously analysed spot, resulting in low fragmentation during early analysis (Benninghoven 1969; Benninghoven, Rüdenauer et al. 1987). However, the probability to analyse a previously analysed spot area increases with time, and fragmentation events are more frequent in late analysis. In the dynamic regime, the fluence is higher by several orders of magnitude than in the static regime (approximately 10^{17} atoms/cm^2) and the pulverization of the sample surface is close to 100%. The increased rate of bombardment of the sample increases the effect of surface erosion causing the analyzed surface to continuously move down into the bulk material. The stress induced at the impact of primary ions on the sample surface favors chemical bond breakage, promoting the emission of secondary ions of elemental origin. These ions may recombine *in situ* or at the sample surface, generating cluster ions such as MCs^+, or the biologically relevant cluster ions $^{12}C_2$ and $^{12}C^{14}N^-$ (Gao 1988). The enhanced sputtering rate increases detection event accumulation, resulting in an improved sensitivity (ppb to ppm) and permitting the profiling of variations of elemental composition in relation to depth.

Dynamic SIMS instruments are not restricted to elemental depth profiling as they also allow the elemental mapping with high sensitivity in the SIMS imaging mode. However, quantitative determination of ion concentrations is challenged by factors such as implantation and chemical environment. While the related physical processes involved during primary ion implantation are largely understood and quantification of induced secondary ion species in homogenous matrices correspond to predictive ionisation models, the increasing complexity of the surrounding chemical environment complicates the modelling of secondary ion

emission. This matrix effect (Yu 1986) is an aggravating factor in the study of biological matrices, where elemental composition, concentration, homogeneity and chemical bonding are unknown parameters. The importance of the matrix effect, inducing strong variability in the secondary ion yield obtained from organic samples, has only marginally been studied for biological samples (Chandra, Ausserer et al. 1987).

Approaches to enhance the secondary ion yield, directly related to an increase of sensitivity of the method, are currently under investigation. Fuoco et al. (2001) quantified the secondary yield increase in polymethylmetacylate layers using an SF_5^+ primary ion cluster source While these findings open the way to technical improvements of current SIMS instruments, this study concentrates on the characterisation of Cs^+ implantation on biological samples for image analysis. Experience has shown that SIMS ion map acquisitions are often started during the early onset of the dynamic regime or during the intermediate state between static and dynamic regimes, leading to uneven or incomplete surface implantation as shown in Figure 21. An oriented distribution of the pixel intensities, linked to the detection events of $^{12}C^{14}N^-$, is visible. Such a phenomenon is typical of images with a differential implantation of Cs^+ primary ions, occurring when an image acquisition is performed at the limit of the implantation crater. In the upper left corner, the duration of the primary ion implantation was t, while in the lower right corner the duration of implantation was t', with ($t' < t$).

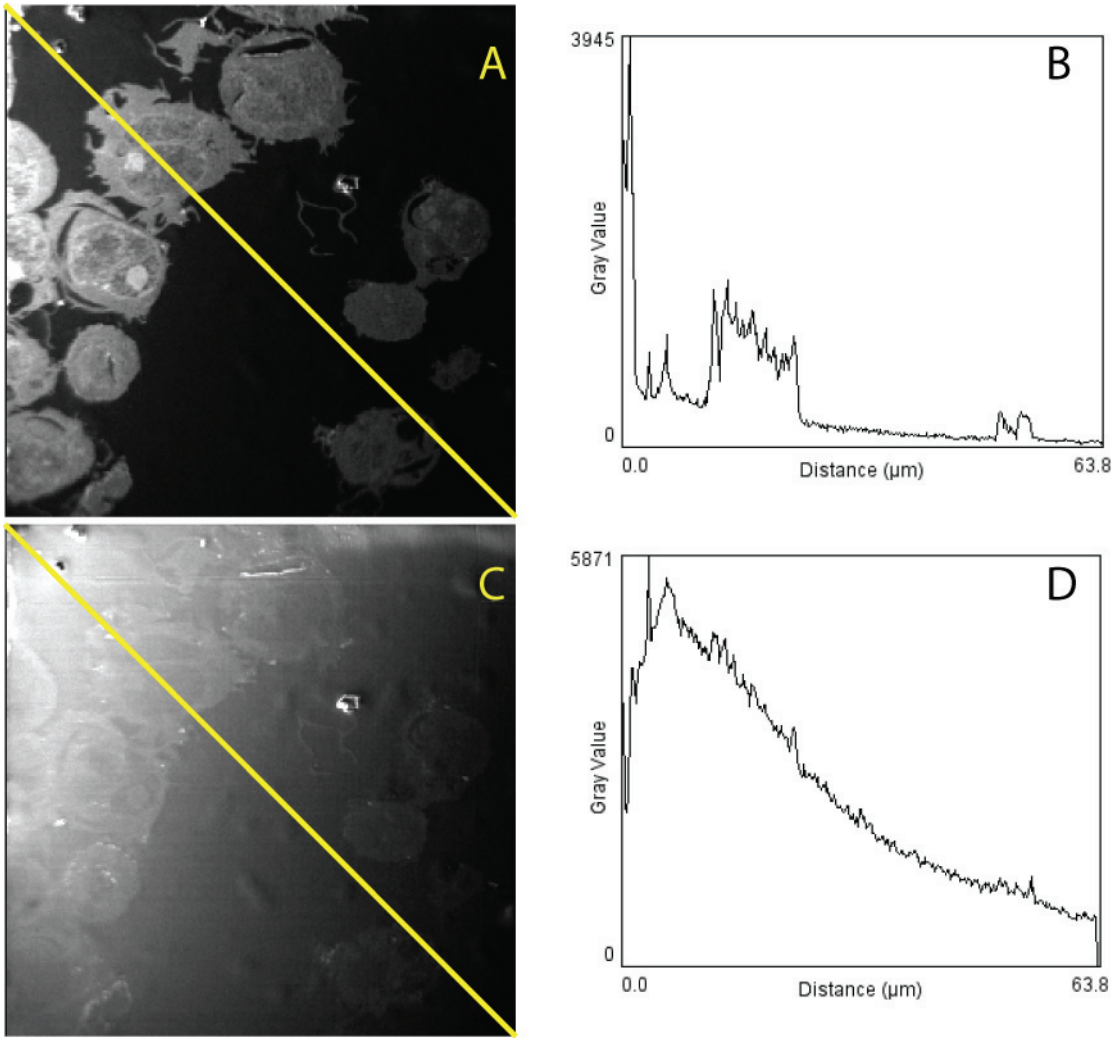

Figure 21: Inhomogeneously implanted images and their intensity profiles. *(A) $^{12}C^{14}N^-$ ion micrograph. (B) An intensity line profile from the top-left corner of the image to the right-bottom corner results in a slope due to heterogeneous implantation. This phenomenon is more pronounced on the $^{12}C^-$ ion micrograph (C) and its intensity profile (D).*

Recently, the NanoSIMS, an ion microprobe combining the sensitivity of SIMS to high resolution mapping of elemental ions, was introduced (Slodzian, Daigne et al. 1991; Hillion, Daigne et al. 1993; Krein, Audinot et al. 2007). With the high lateral resolution of 50 nm, implantation artefacts are more obvious on images generated by this instrument. A better characterisation of the implantation process and a standardisation of analytical procedures may result in a reduction of these artefacts and lead to improved secondary ion yields.

III.B. Material and Methods

III.B.1. Computer simulation of Cs^+ implantation

Computer simulations were used to determine the optimal Cs concentration in order to compare the experimental results to the model used to describe ion emission from organic

(and biological) surfaces. For this purpose, the simulation code TRIDYN was used (Moller and Eckstein 1984; Moller, Eckstein et al. 1988). TRIDYN is based on TRIM from the SRIM package (*Stopping and Range of Ions in Matter,* www.srim.org) (Ziegler 1977-1985; Biersack and Haggmark 1980; Biersack and Eckstein 1984), which simulates ion irradiation of amorphous targets in the binary collision approximation by using the Monte Carlo method, where thermal dependent processes like diffusion and segregation are ignored. While TRIM allows only the simulation of a pure static system (each ion impact happens on a non-irradiated target), TRIDYN simulates the evolution of the system with the primary ion fluence giving access to the system composition and sputtering parameters in the equilibrium regime. The comparison between simulation and experimental results will be performed in this intermediate state. For this study, it is especially useful to reproduce the Cs concentration with respect to the ion and neutral Cs fluence and to get hold of this concentration in the intermediate regime.

The simulation conditions were chosen to be identical to the experimental conditions used during NanoSIMS acquisition. Primary ion bombardment of Cs^+ was carried out with an impact energy of 16 keV and an incidence angle of 0° (normal to the surface) onto a homogenous epoxy resin. The epoxy resin contained the following elements, defined in atomic fractions: 47.5% H, 45% C and 7.5% O.

An additional computer simulation, using the same experimental conditions, was conducted using the TRIM simulation code. As opposed to TRIDYN, TRIM does not take into account the pulverisation of material occurring at primary ion beam impact. As a result, it does not accurately model the erosion process involved in SIMS. The penetration of primary ions in the sample, however, is well modelled by TRIM, which motivated its use in this study.

III.B.2. Sample preparation

Resin embedded cell suspensions

The human premonocytic cell line THP-1 was cultured in RPMI-1640 (Gibco BRL, Rockville, U.S.A.), harvested and prepared following standard electron microscopy protocols. Cells were washed twice in PBS 1X, pH 7.2 (Gibco BRL, Rockville, U.S.A.) and fixed for 1 hour at room temperature in glutaraldehyde 2.5% (Electron Microscopy Sciences, Hatfield, U.S.A.). After two washing steps in PBS, cells were post-fixed in 1% osmium tetroxide (Fluka Chemie, Buchs, Switzerland) and dehydrated in a series of ethanol steps. Clearing was performed by two subsequent steps in propylene oxide 100% followed by overnight infiltration in intermediate solvent combinations of propylene oxide and the embedding

medium Epon 812 (Fluka Chemie, Buchs, Switzerland). Cells were then centrifuged into a pellet in fresh resin following the Luft formulation (Luft 1961) to obtain a sufficient cell density before curing for 48 hours at 60°C at 100 mg Hg.

Resin embedded kidney

Kidneys from a 6 week old balb/c mouse were obtained by dissection, freed of adhering tissues, cut into 2-3 mm^3 blocks, washed in PBS and fixed overnight in 2.5% glutaraldehyde at 4°C. Post-fixation occurred in 1% osmium tetroxide for 1 hour followed by dehydration in a graded series of ethanol. Tissue clearing was performed in 100% propylene oxide, followed by overnight infiltration in intermediate solvent combinations of propylene oxide and Epon 812. Samples were then infiltrated in fresh resin for 2 hours on a rotator and cured for 48 hours at 60°C and 100 mm Hg. This protocol, used in previous works, yielded fine structural preservation of kidney tissue and was chosen as a standard SIMS preparation protocol for other animal tissues.

III.B.3. Analytical conditions

On the NanoSIMS 50, implantation was performed with the Cs^+ primary ion source on surface areas from 10 µm x 10 µm, 20 µm x 20 µm, 30 µm x 30 µm, 40 µm x 40 µm to 75 µm x 75 µm and intensities on the sample of 160 pA, 2 nA or 8 nA. Living organisms are constituted of mainly low Z elements: carbon, hydrogen, nitrogen, oxygen, phosphorus and, to a lesser degree, sulphur. Mono or diatomic ions of these elements generate a contrasted SIMS image that corresponds to the morphology of the cell. As all biomolecules are composed of carbon atoms, only certain classes of molecules may generate a specific signal, which is raised against the resin background (essentially an organic polymer), and results in a contrasted image. The resin emits high amounts of ^{12}C and $^{12}C_2$ ions, as well as the cluster ion $^{12}C^{-14}N^-$. Carbon-nitrogen rich regions generate recombined $^{12}C^{14}N^-$ ions, good for the localisation of proteins. Stable isotopes of sulphur, found in the amino acids Cysteine and Methionine, as well as in structural and membrane bound (acidic polysaccharides) biomolecules, may also serve to determine protein distribution. The mapping of phosphor ions is commonly used to identify nuclear DNA, RNA and phospholipids essentially found in membranes.

The emission of a selection of biologically relevant ion types ($^{12}C^-$, $^{12}C_2^-$, $^{12}C^{14}N^-$, $^{31}P^-$, ^{32}S) was recorded simultaneously using electron multiplier detectors, effectively obtaining a depth profile of the resin sections. In order to avoid premature ageing of the electron multipliers by intensities above 10^{17} counts/s, secondary ion emission was limited by entry and exit slits.

The ion image maps were realized using a Cs^+ primary ion beam with a current of 0.8 pA. Negative secondary ion signals for ^{12}C, $^{12}C_2^-$, $^{12}C^{14}N^-$, ^{31}P and ^{32}S were measured simultaneously.

III.B.4. Preimplantation

Wide area preimplantation was performed using the Cs^+ beam of an IMS-6f on resins sections containing organic material. A surface of 500 µm x 500 µm was implanted with a dose of $2x10^{17}$ atoms/cm^2, a dose at which the dynamic regime was expected to be reached.

A vacuum suitcase, shown in Figure 22, was developed at the CRP-GL/SAM for the purpose of transporting and transferring samples under ultra-high vacuum conditions (10^{-8} to 10^{-10} Torr) between a series of instruments for surface analysis (Microlab Auger/XPS, IMS-6f, CMS, NanoSIMS 50).

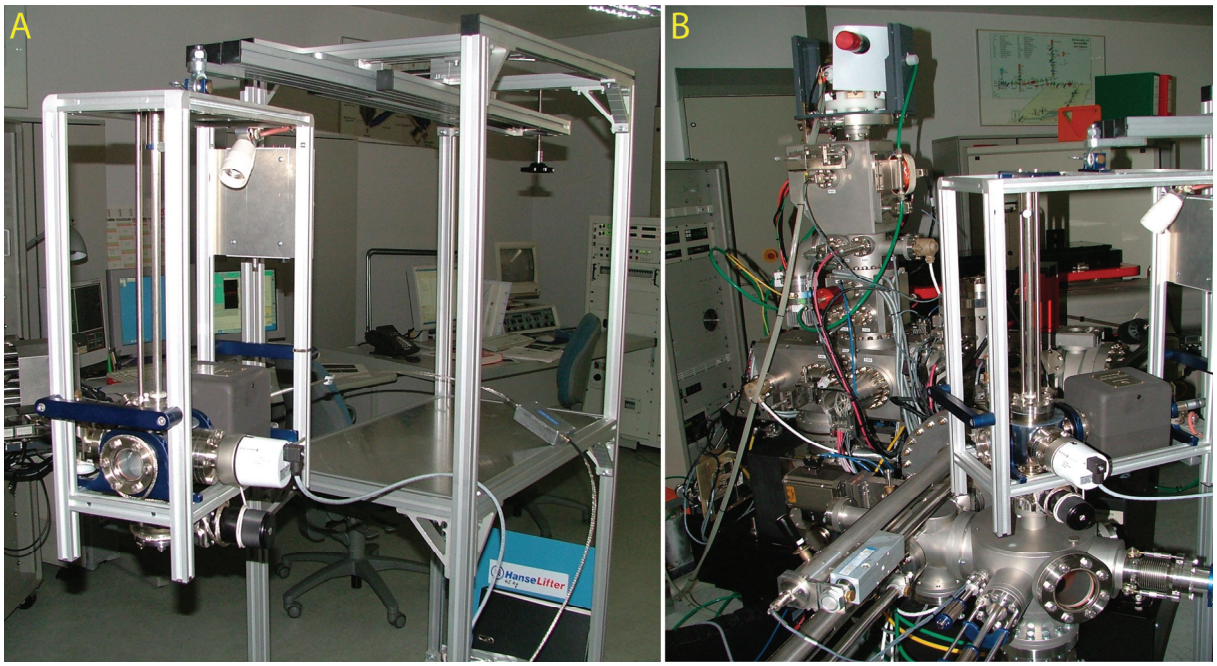

Figure 22: Vacuum transfer suitcase. *(A) on the trolley lifter (B) on the NanoSIMS*

Each of these spectrometers underwent adaptations to allow the docking of the suitcase and the vacuum transfer of samples, using universal sample holders manufactured for this purpose. This configuration avoids oxygen contamination and the subsequent modifications of the surface of the samples, provoked by the oxidation of the implanted highly reactive Cs.

After preimplantation on the IMS-6f, samples were either vacuum transferred to the NanoSIMS using the vacuum suitcase or subjected to an intermediary passage to atmospheric pressure, before immediate reintroduction into the NanoSIMS. To reduce caesium oxidation, samples that underwent atmospheric passage were first transferred into a nitrogen atmosphere to equilibrate the caesium on the sample surface.

III.C. Results

III.C.1. Computer simulation of Cs^+ implantation

Modelled by TRIM, Figure 23A shows the penetration depth of implanted primary Cs^+ ions, and the distribution following an inverse cone, termed implantation cone, caused by the atomic collisions, which deflects the primary ions from their incident trajectory. In this model, caesium ions penetrate up to a depth of 400 Å (40 nm) into the sample. Figure 23B shows that the primary ions have a Gaussian distribution, with a peak at 254 Å (25.4 nm) where most caesium is situated. Interestingly, in the first few nm, Cs is almost absent.

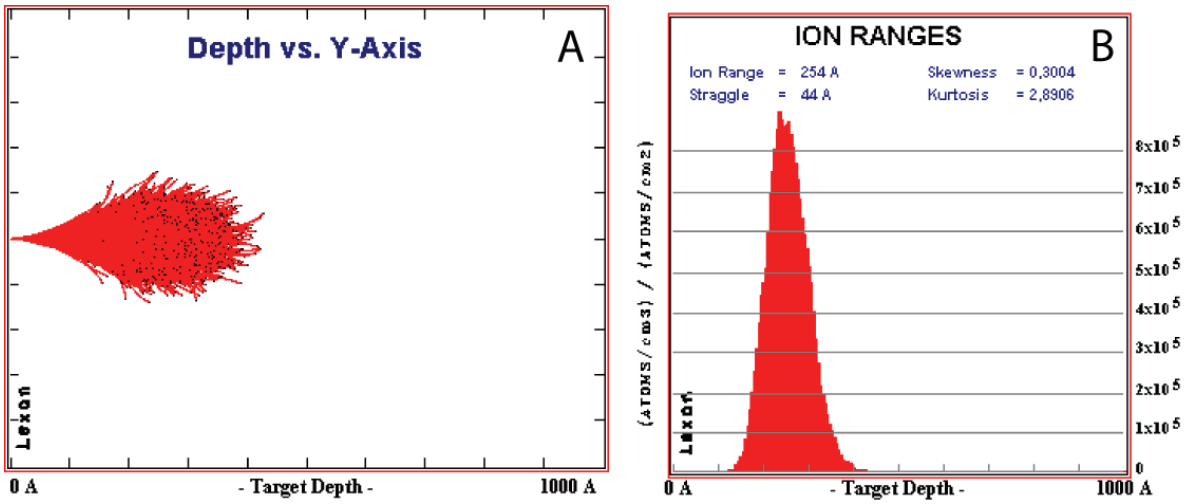

Figure 23: SRIM modelling principle. *Represents the penetration depth of implanted Caesium ions (A) and the Gaussian distribution of primary ions (B).*

The TRIDYN model takes the pulverisation of bulk matter by the primary ion beam into account. At the onset of the implantation, the Cs^+ follows a Gaussian distribution in the sample (Figure 24, in green), agreeing with the TRIM model (Figure 23B). During the erosion of the bulk material, the Gaussian of Cs^+ moves from the upper layers down into the sample (Figure 24B, Gaussians in blue). The emission of Cs as secondary ions corresponds to the integration of all the Gaussians in Figure 24, represented by the red curve. In the model, the first Gaussian presents a higher intensity. This is supposed to be related to an increased Cs^+ concentration in the first layers. As the erosion is triggered by a specific dose in the sample, in the first moments of the implantation no secondary emission of Cs^+ occurs and Cs^+ is accumulated. Once the dynamic regime is reached, each implanted Cs^+ ions results in the secondary emission of Cs^+. As a result, the concentration of Cs^+ is higher in the first layers at the onset of the modelling experiment.

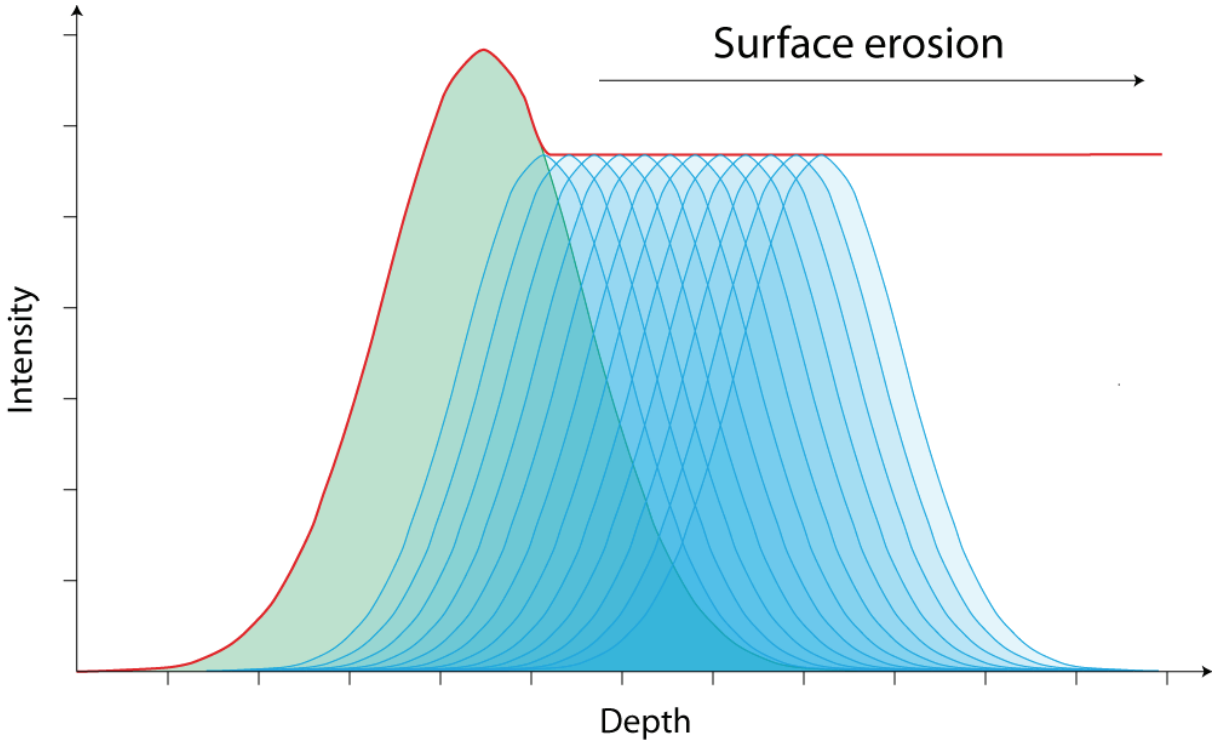

Figure 24: TRIDYN modelling principle. *Represents the intensity of emitted secondary Cs^+ ions in relation to the depth. The first Gaussian (in green) represents the initially implanted Cs^+ primary ions. Unlike TRIM, TRIDYN takes into account the pulverisation of the sample by the primary ion beam. During the erosion effect, the Gaussian moves down into the sample (subsequent Gaussians, in blue). The resulting depth profile for an ion corresponds to the integral of all the Gaussians (in red).*

The modelled data shown in Figure 25 represents the erosion of the sample (in Å) in relation to the implanted Cs^+ dose (in atoms/cm^2). In the early phase of a high energy caesium implantation, 400 Å (40 nm) of the sample are eroded. At a dose of approximately $8x10^{16}$ atoms/cm^2, the implantation of Cs^+ shifts from erosion to an increase in sample volume of 300 Å (30 nm).

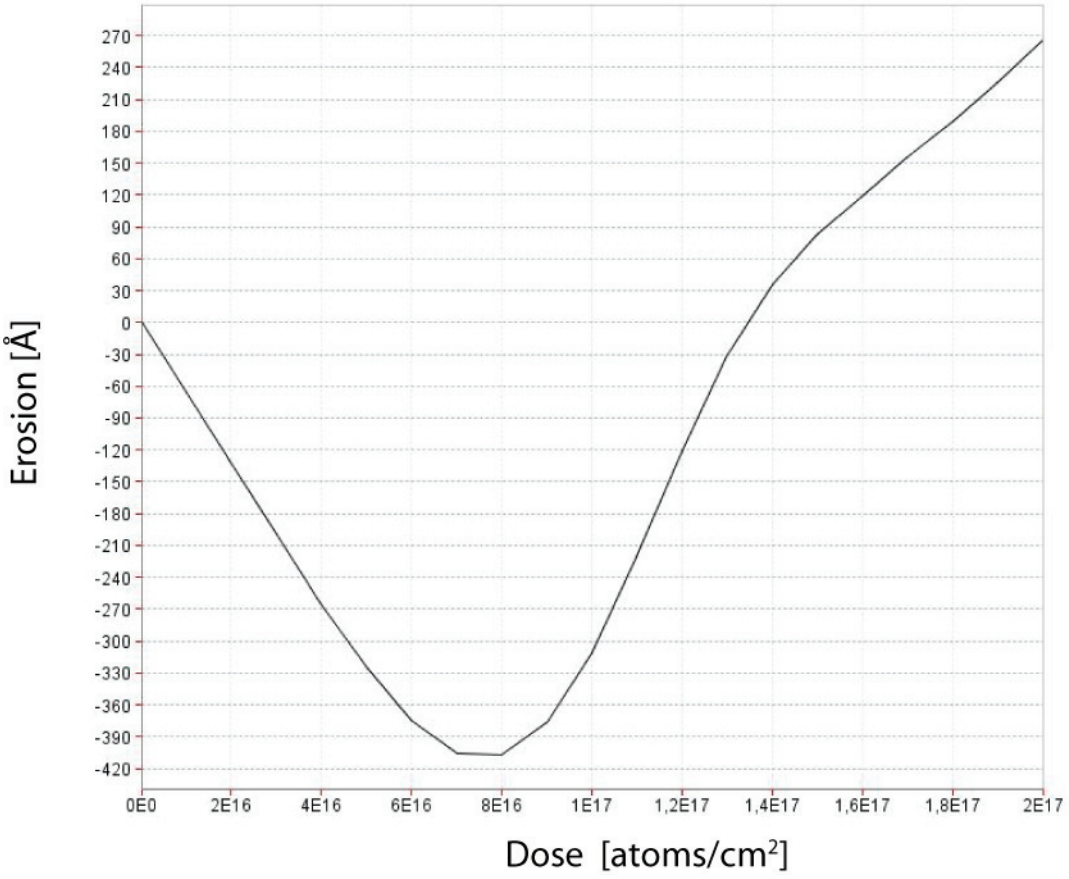

Figure 25: Erosion versus Dose modelled using TRIDYN, *for a Cs^+ primary ion beam impacting at 16 keV with an incident angle of 0° on a homogenous epoxy resin.*

Figure 26 shows the progression of the concentration of Cs, H, C and O (in atomic fractions) in relation to the implanted Cs^+ dose (in atoms/cm^2). While at the onset of the modelling, Cs was absent from the sample (0%, concentrations are expressed as atomic fractions), the implantation increased the Cs concentration in the sample to a peak value of 24% at a dose of 10^{17} atoms/cm^2 before decreasing and stabilizing at a plateau value of 18%. Albeit less pronounced than for Cs, the progression of C was similar. The content of O in the epoxy resin is low, and the concentration remained stable throughout the modelling experiment. While the decrease of H cannot readily be explained, a possible explanation could be the existence of a yet unknown desorption process of H before its stabilization at a concentration of 18%.

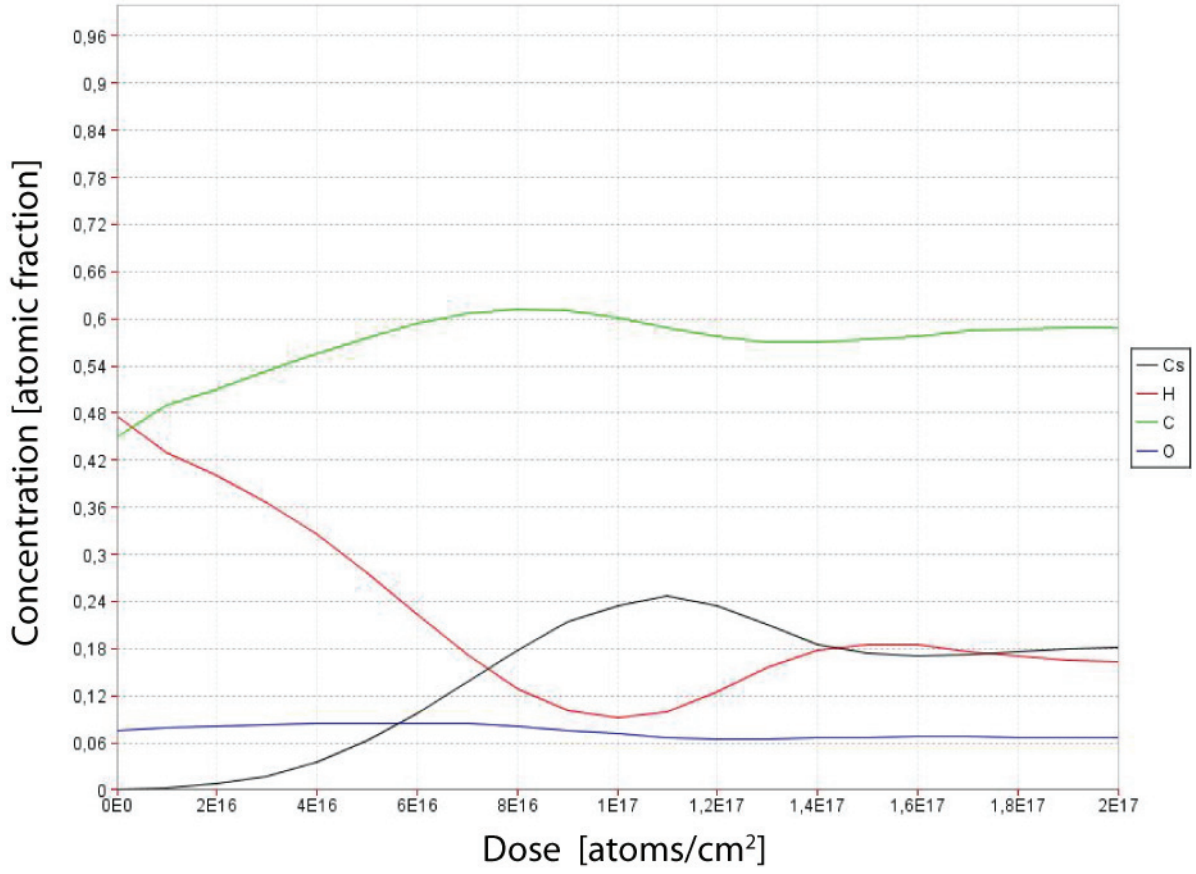

Figure 26: Concentration (in atomic fractions) versus Dose (in atoms/cm^2) modelled using TRIDYN, *for a Cs^+ primary ion beam impacting at 16 keV with an incident angle of 0° on a homogenous epoxy resin.*

Figure 27 describes the secondary emission yield, expressed as the ratio of the sum of secondary ions emitted over the sum of incident primary ions, versus the implanted Cs^+ dose, expressed in atoms/cm^2. The yields of Cs, C and H oscillated at the transition from the static regime to the dynamic regime where they stabilized at a dose between $1x10^{17}$ and $2x10^{17}$ atoms/cm^2. The dynamic regime was reached at a secondary emission yield of 1, where for each incident Cs^+ ion, a secondary Cs^+ ion was emitted. The oscillation observed for all modelled elements probably corresponded to the higher concentrations of Cs^+ in the first layers, promoting the secondary ions of other elemental ions such as C, and to a lesser degree O. Consistently with Figure 26, H varied more drastically, especially at low implantation doses, comforting the hypothetical existence of a rapid H desorption process, which may be due to a higher lability of H atoms. Both Cs and C increased at 10^{17}atoms/cm^2, with the C yield rising slightly earlier than Cs. In comparison, H increased later, at $1.6x10^{17}$atoms/cm^2. The progression of the individual ions was identical to those described in the modelling of concentration versus dose (Figure 26). Similarly, oxygen variations remained low during the modelling experiment.

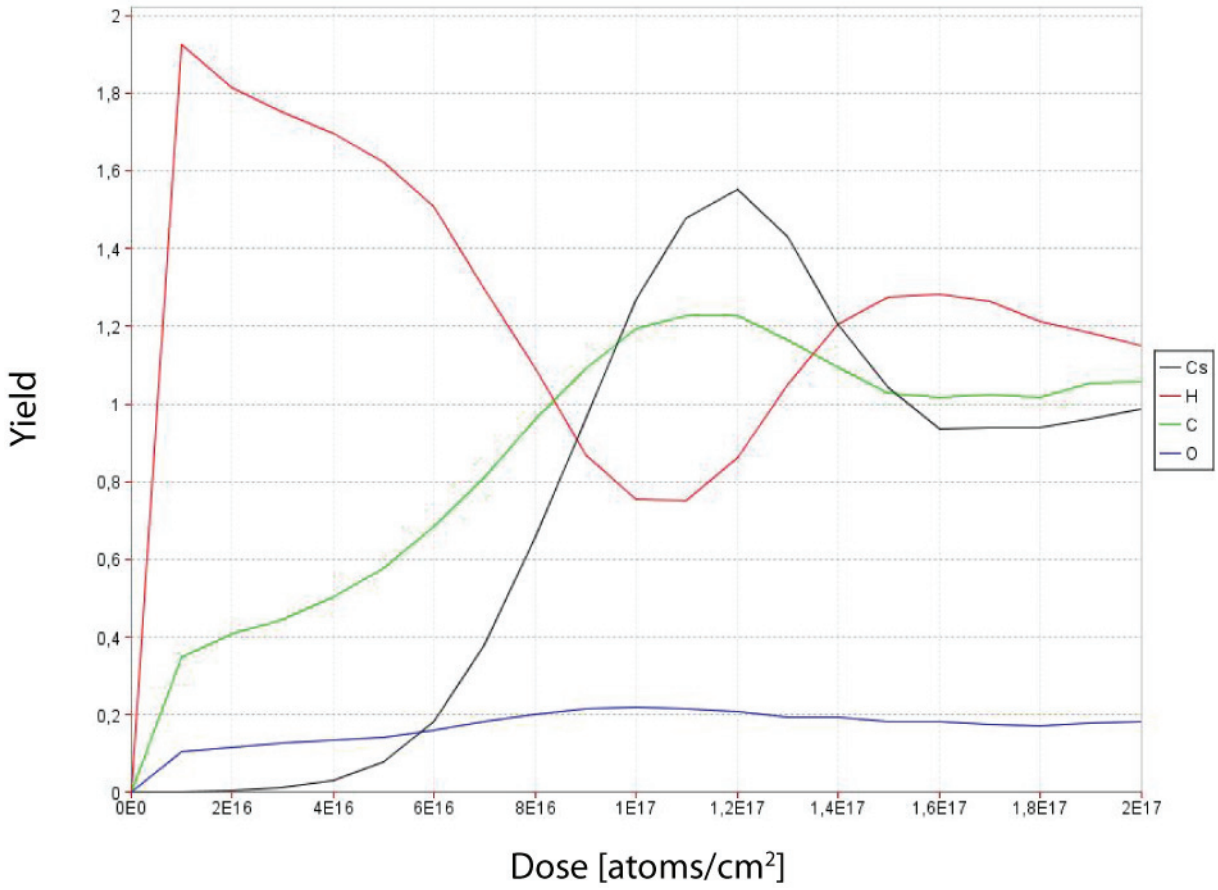

Figure 27: Secondary emission Yield (ratio of secondary ions emitted over incident Cs+ primary ions) versus Dose (in atoms/cm^2) using TRIDYN.

III.C.2. Dose variation and its effect on imaging

Caesium implantation of resin embedded THP-1 cells, on a surface of 30 µm x 30 µm at a primary ion current of 160 pA, was aborted at 300 s, 700 s and 1500 s. The ion images recorded for the elemental ions ^{12}C, ^{31}P and ^{32}S and the cluster ions $^{12}C_2$ and $^{12}C^{14}N$ are presented in Figure 28. At 300 s of implantation, all the detected carbon based ions showed sufficient counts to be raised from the general detector background. Only the cluster ion $^{12}C^{14}N$ gave a contrasted image discriminating intracellular features, like the nucleus with a finely delimited nuclear membrane. While phosphor signal remained above the background noise, the detection values situated around 10 counts/s did not yield a sufficiently differentiated image. For this short implantation time, no relevant sulphur signals could be measured. After an implantation of 700 s, all studied ions were emitted adequately. The cellular and nuclear membranes, as well as the nucleoli, are well defined on the ^{12}C, $^{12}C^{14}N$ and the ^{31}P ion maps. Especially ^{12}C and ^{32}S signals benefited from an increased implantation time of 1500 s, while contrast was not greatly enhanced for the $^{12}C^{14}N$ and ^{31}P ion maps.

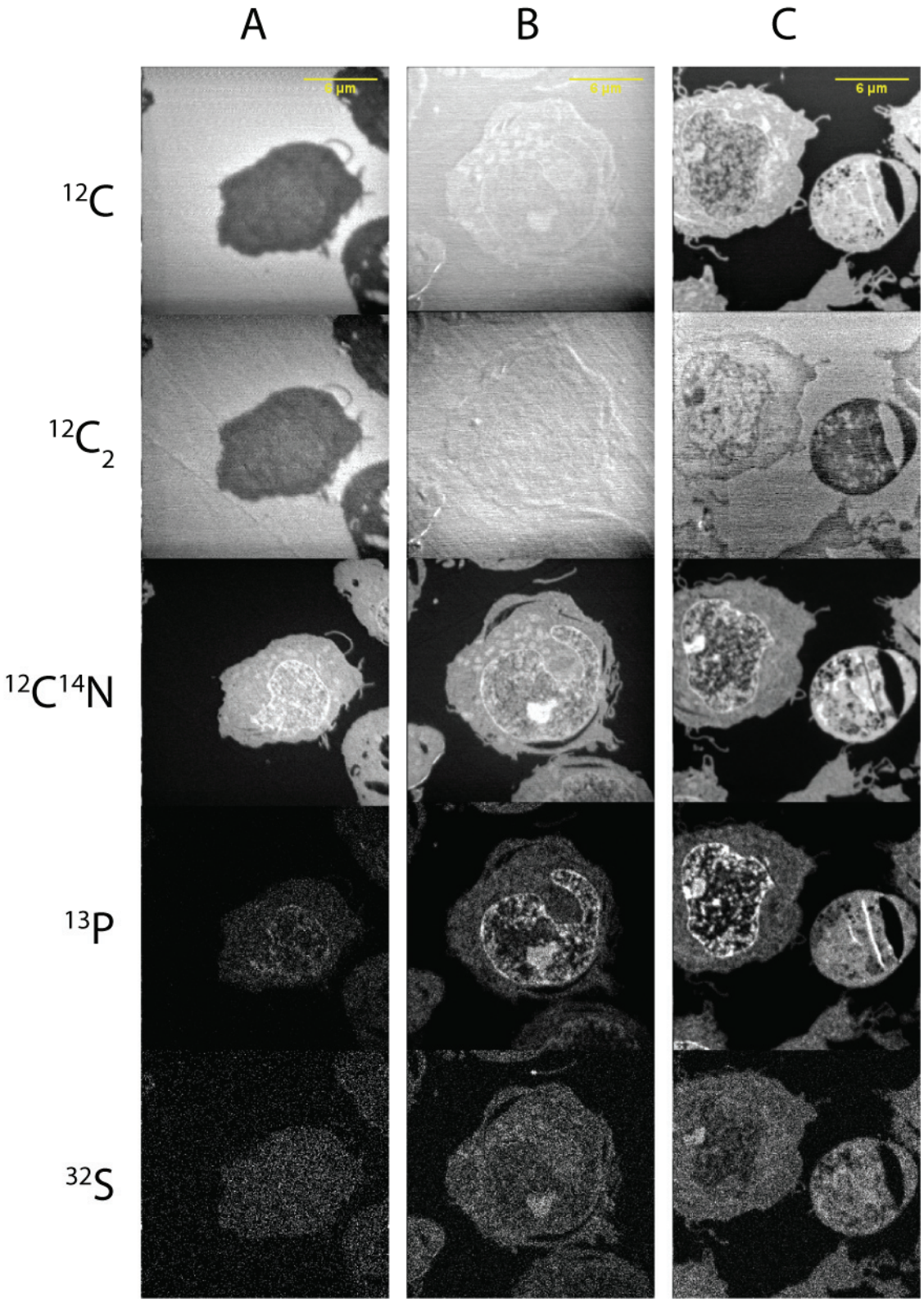

Figure 28: Ion maps of THP-1 cells (20 µm x 20 µm) after varying implantation times. *Images are arranged in columns after an 160 pA implantation of 300 s (A) after an implantation of 160 pA for 700 s (B) after an implantation of 160 pA of 1500 s (C).*

A depth profile analysis of these elements was acquired on an identical surface and sample type (Figure 29). At 300 s, ^{12}C, $^{12}C_2$ and $^{12}C^{14}N$ emissions were between 10^4 and 10^5 counts/s,

while ^{31}P and ^{32}S emissions were low. At 700 s, the dynamic regime was almost reached and ^{31}P and ^{32}S could be clearly separated from the background. At 1500 s, secondary ion emission was steady for all ions.

These results confirm the general trend reported in the literature of an optimal secondary emission in the dynamic regime, for a fluence situated around $1x10^{17}$ ions/cm^2 (Benninghoven, Rüdenauer et al. 1987).

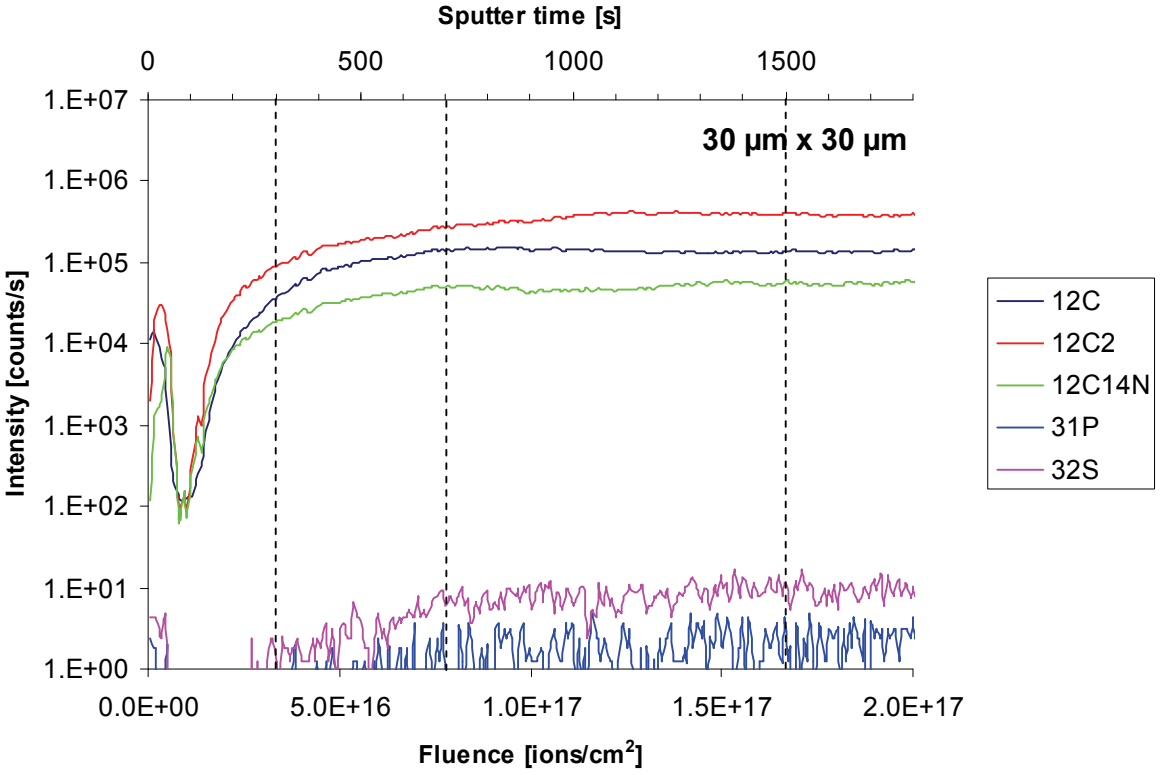

Figure 29: Depth profile (30 µm x 30 µm, 160 pA) of a THP-1 cell suspension embedded in epoxy resin.

III.C.3. The dynamic regime as a function of the implanted dose: Relationship to the surface

Depth profiles on surfaces of varying size were performed on both tissue and cell samples. The sizes ranged from 10 µm x 10 µm to 60 µm x 60 µm (Figure 30). The dynamic regime was reached approximately after 10^{17} atoms/cm^2 of Cs^+ were implanted in the sample and could be observed for the biologically relevant ions that plateaued at that dose. This also confirmed the necessity to implant at least 10^{17} atoms/cm^2 to obtain the optimum secondary emission mentioned in III.C.3 and observed in Figure 29. However, for larger areas and for a fixed primary ion beam of 160 pA, the time to reach the plateau increased (Figure 30). The linear relation between implantation dose and surface is depicted in Figure 31, for all

observed ions. Interestingly, the plateau is not reached at the same time and dose for each ion types, and secondary emission of ^{31}P and ^{32}S seems to lag slightly as compared to ^{12}C (observed in Figure 30 and Figure 31). Variations in secondary emission could be observed in a same sample, as well as between sample types. However, the general trend of the progression of secondary emission in relation to surface size was identical between the two sample types.

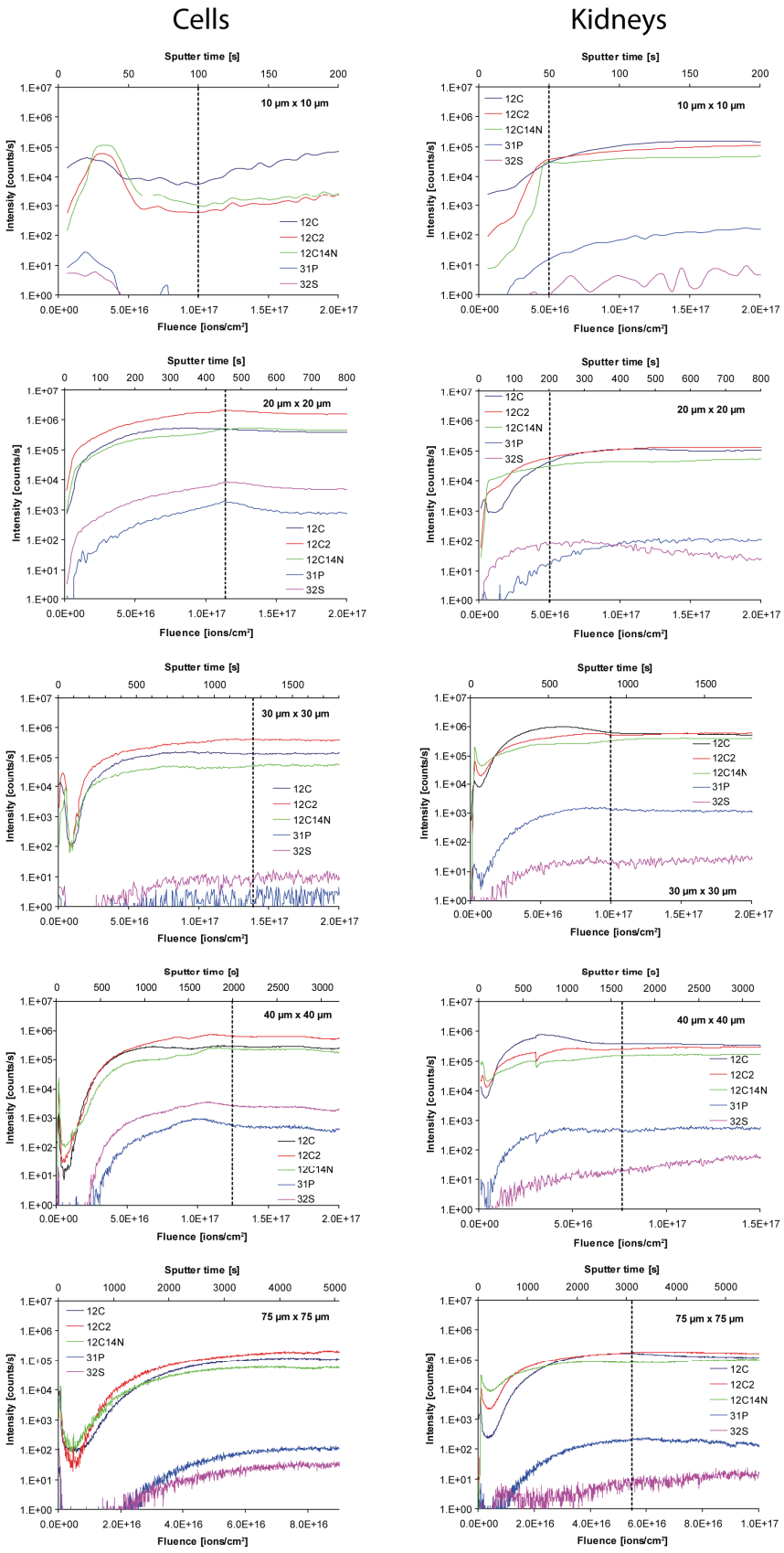

Figure 30: Depth profiles of a selection of biologically relevant ions at increasing surfaces, in cells and kidneys. *The dotted lines represent the dose at which secondary emission of $^{12}C^{14}N^-$ ions reached plateau values. Due to the length of the acquisition of 75 µm x 75 µm depth profiles, these were stopped before reaching 10^{17} atoms/cm^2. However, the*

progression of the ion curves clearly shows that plateau values are reached at similar doses independently of the implanted area size.

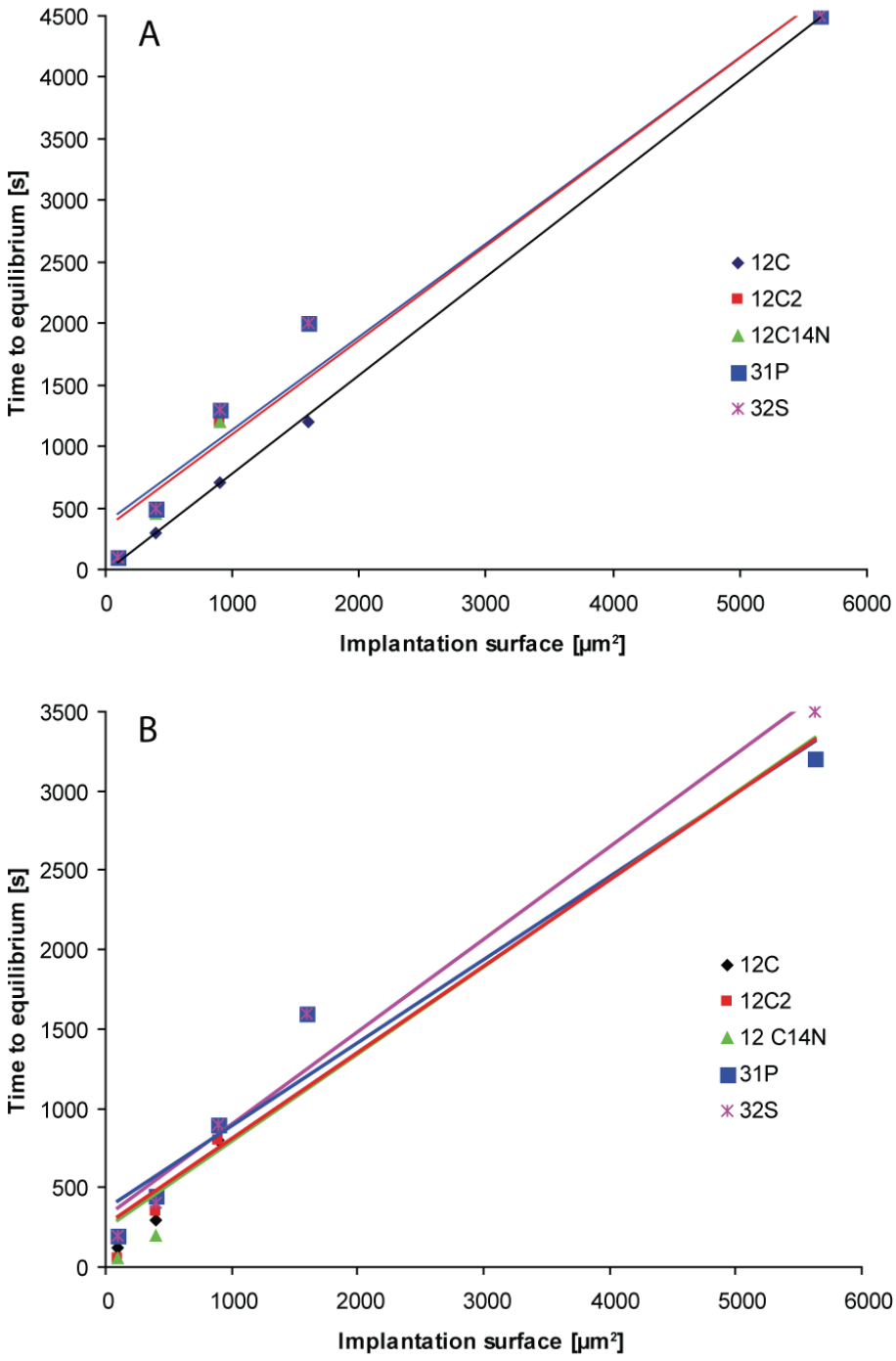

Figure 31: Time to reach the equilibrium, plotted versus the implantation surface. *(A) embedded THP-1 cells. $R^2(^{12}C) = 0.9996$, $R^2(^{12}C_2) = 0.9692$, $R^2(^{12}C^{14}N) = 0.9692$, $R^2(^{31}P) = 0.9667$, $R^2(^{32}S) = 0.9692$; (B) embedded kidney. $R^2(^{12}C) = 0.9513$, $R^2(^{12}C_2) = 0.9492$, $R^2(^{12}C^{14}N) = 0.9387$, $R^2(^{31}P) = 0.9591$, $R^2(^{32}S) = 0.9735$; For both profiles an implantation at s primary ion current of 160 pA was performed on a surface of 30 µm x 30 µm.*

III.C.4. Variation of implantation primary ion beam current

At a primary ion beam intensity of 2 nA on cell inclusions, secondary emission plateaued at a dose ranging between $0.75x10^{17}$ and $1.25x10^{17}$ ions/cm^2, while sputter time increased with implantation surface (40 µm x 40 µm, plateau at $1.26x10^{17}$ ions/cm^2, 170 s; 60 µm x 60 µm, plateau at $1.01x10^{17}$ ions/cm^2, 308 s; 75 µm x 75 µm, plateau at $1.01x10^{17}$ ions/cm^2, 544 s). Secondary ion imaging performed on the implantation zone resulted in well-conserved regions at implantation intensities of 160 pA and 2 nA (160 pA, not shown as similar to Figure 28; 2 nA shown in Figure 32).

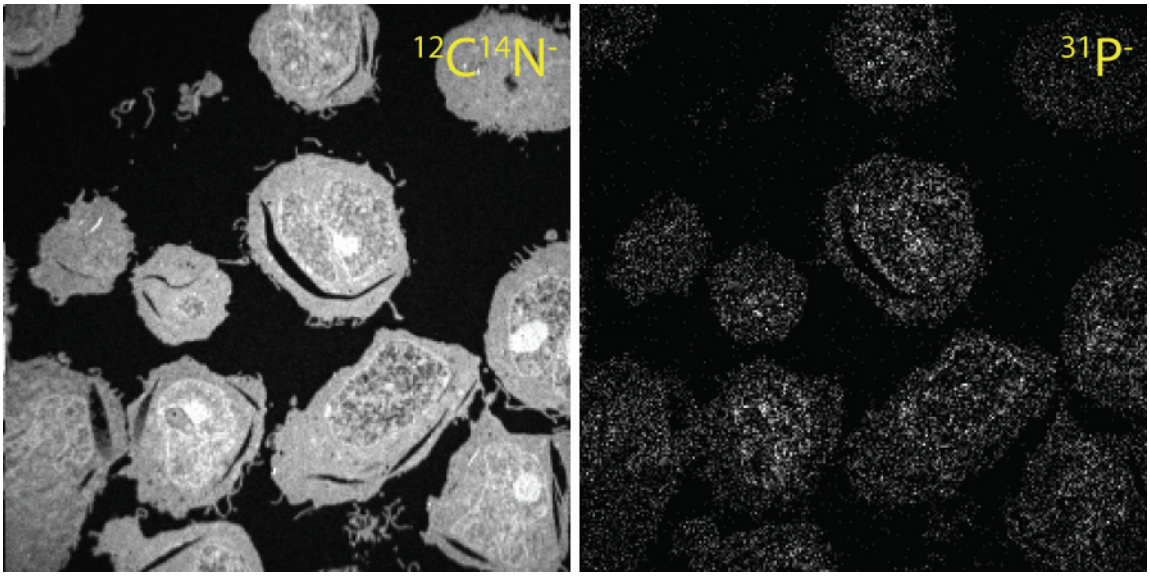

Figure 32: Ion micrographs of cells after 2 nA implantation. *Images are of good quality after a Cs^+ implantation at a primary ion current of 2 nA (acquisition at 10 ms/pixel).*

Implantation at 8 nA resulted in unusable images due to highly variable surface profiles. The formation of these features may be due to a heterogeneous density of the probe at high primary ion current, causing variations in secondary ion yield on the irradiated sample surface. Furthermore, at high primary ion current, the duration required for a proper implantation was reduced to several seconds. The slightest deviation in the duration of implantation caused the formation of holes in the thin resin sections.

III.C.5. Secondary ion emission after pre-implantation on the IMS-6f

After the initial implantation of $2x10^{17}$ ions/cm^2 on the IMS-6f, depth profiling analysis of the tissue resin sections by NanoSIMS showed that the dynamic regime had already been reached and the secondary ion emission remained steady at plateau values identical to those obtained in the dynamic regime of NanoSIMS implanted samples (Figure 33). Moreover, no notable difference in secondary ion emission was recorded between samples transferred at 10^-

^{7} Torr, using the vacuum cassette, and samples that transited at atmospheric pressure. Similar profiles were obtained for cell embeddings.

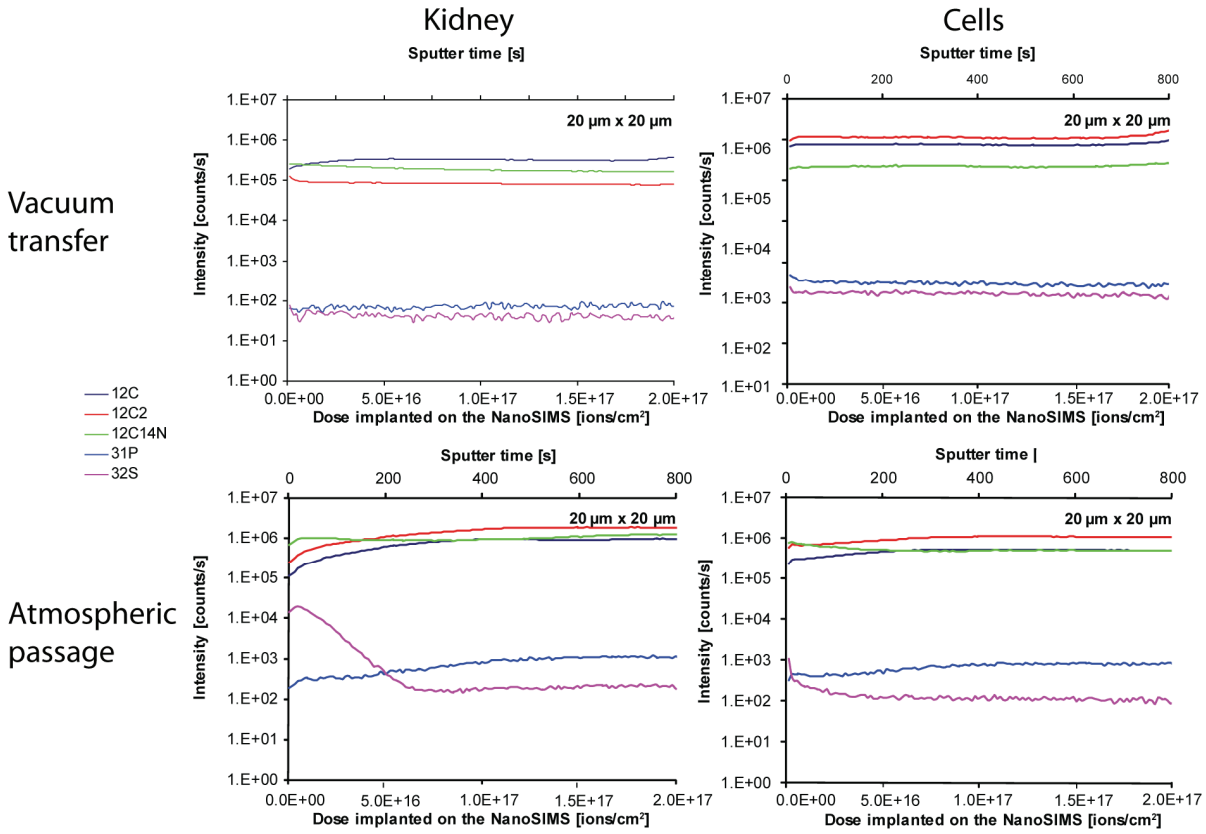

Figure 33: Depth profile analysis of pre-implanted resin embedded mouse kidney on NanoSIMS. *(160 pA, 20 µm x 20 µm), after pre-implantation on the IMS-6f of a Caesium dose of 2x10^{17} atoms/cm^{2}. Transfer from the IMS-6f to the NanoSIMS with the vacuum transfer suitcase at 10^{-7} Torr (upper graphs) or with an intermediary transit at atmospheric pressure. Profiles were similar for cells and tissue preparations (lower graphs).*

Ion micrographs performed after the pre-implantation procedure showed no alterations on the IMS-6f or transfer to the NanoSIMS on the corresponding ion maps (Figure 34, only tissue specimens shown). The quality of the acquisitions was excellent, and secondary ion emission was optimal, resulting in well contrasted images for all the observed ions.

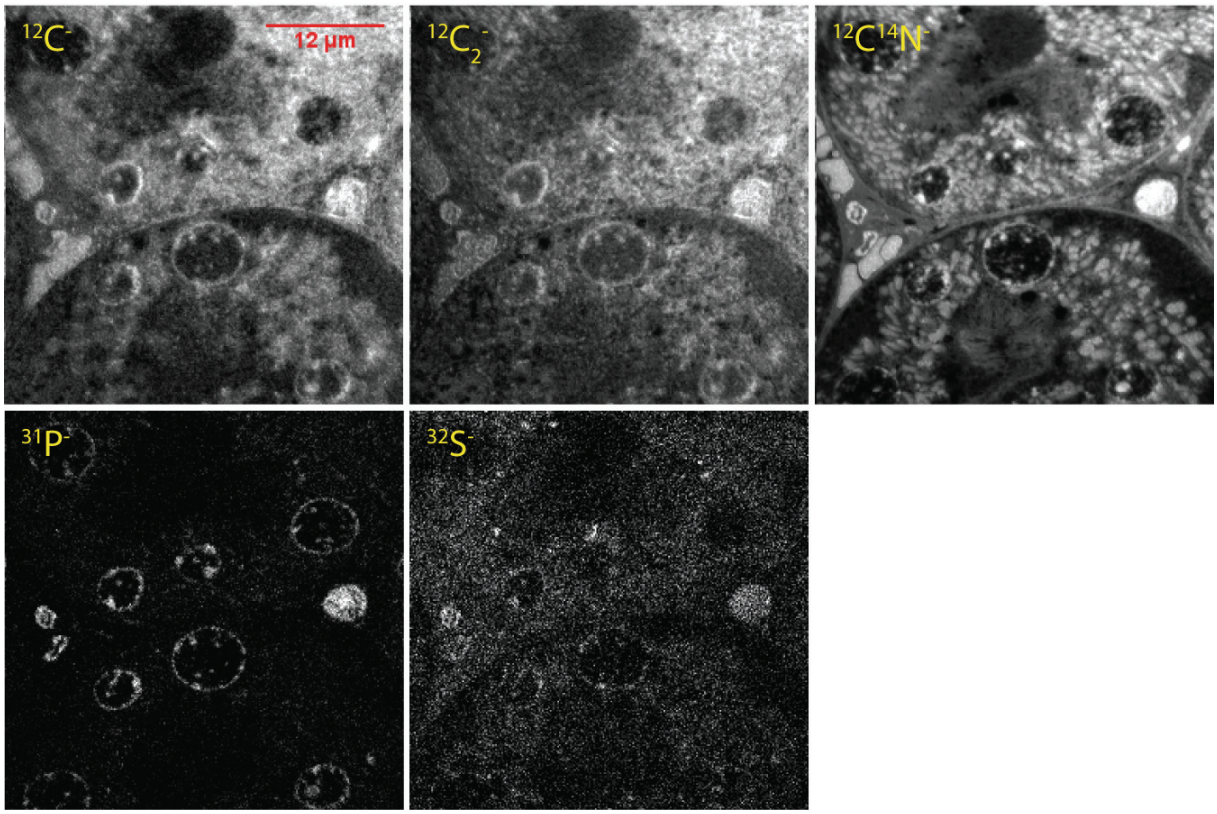

Figure 34: Kidney sample, implantation on the IMS-6f, vacuum suitcase transfer to the NanoSIMS. *40 µm x 40 µm, 256 pixel x 256 pixel, 40 ms/pixel.*

III.D. Discussion

This study investigated ways to improve the analytical conditions of NanoSIMS image acquisition of organic samples. The study focused on the characterisation of primary ion implantation and its effect on the secondary ion emission during analysis of cells and tissues. Several modifications to standardize acquisition protocols with respect to the duration of implantation increased the daily throughput of properly implanted samples.

The results showed an optimal secondary emission when a concentration of 10^{17} atoms/cm^2 of implanted Cs^+ ions had been reached on the sample surface, corresponding to the onset of the dynamic regime of secondary emission. As the concentration of Cs^+ in the sample correlated with the implantation area, the analysis of larger areas required either longer implantation times or higher primary ion intensities. At an increased primary ion current from 160 pA to 2 nA, the dynamic regime was reached approximately ten times faster, drastically reducing implantation times. However, primary ion currents above 2 nA resulted in a differential erosion of the sample, forming topological features on the sample surface.

Carbon/nitrogen rich environments, such as cells or tissues embedded in epoxy resins, emit the elemental or cluster ions ($^{12}C^-$, $^{12}C_2^-$ and $^{12}C^{14}N^-$) in sufficient amounts to generate

meaningful contrast during ion imaging. In the analysis of biological samples, such ion micrographs are related to proteins and lipid membranes and the features depicted within the image are largely consistent with TEM micrographs. Implantations below 10^{17} atoms/cm^2 resulted in suboptimal secondary emission, and poor signal (detected as counts/s). Especially the imaging of $^{31}P^-$ and $^{32}S^-$ were poorly contrasted at low Cs^+ concentration.

Similarly, secondary ion emission profiles were observed for cells and tissues. Therefore, secondary emission of so-called *structural ions,* such as those observed in this study, is not sample specific and does not require particular adaptations to the analytical conditions. However, in subsequent depth profiles of the same sample type small variations were recorded in the secondary ion emission, especially for the elemental ions ^{31}P and ^{32}S. Generally, the detection of secondary emission of these elements was low, with several hundreds of counts/s, and profiling trough phosphorus or sulphur rich regions (such as nuclei) had a measurable impact on the detection of these ions, causing noticeable variations in their depth profiles.

These results were confirmed by the computer simulations on TRIDYN, which revealed unstable emission of secondary ions below 10^{17} atoms/s. Shortly before the regime was reached, an increase in emitted secondary Cs^+ ions was be observed on the model and confirmed experimentally. This increase was recorded for the atomic fraction of Cs^+ in the TRIDYN model, and in the depth profiles of Cs^+, and may be explained by an accumulation of Cs^+ at high concentration in the first atomic layers (6-8 nm) of the sample, at the onset of the analysis when almost no erosion by secondary ion emission occurs. The implantation of Cs^+ by the primary ion beam follows a Gaussian distribution. Cs^+ is implanted in the same layers until the dynamic regime is reached. As a result, the introduction of additional matter into a semi-elastic sample such as an epoxy resin causes a slight dilation, which explains the negative erosion depth in Figure 25. Once the dynamic regime is reached, this phenomenon is suspended and the concentration of Cs^+ remains stable at 10^{17} atoms/cm^2, while the primary beam erodes successive layers into the sample.

Furthermore, the increase in Cs^+ also explains the slight increase of secondary emission of other ions, observed in the TRIDYN model and in the experimental results, before reaching the dynamic equilibrium. The higher Cs^+ concentration in the first layers implanted by the primary ions may promote the secondary emission of the other analysed ions (Benninghoven, Rüdenauer et al. 1987).

Pre-implantation of the sample on an IMS-6f is described as an alternative method to reach the required concentration of Cs^+ in the sample, for analysis in the dynamic regime. It

presents the advantage of homogenously implanting large areas in a short time period. When analysed on the NanoSIMS, the sample is already saturated in Cs^+ and ion imaging can immediately be performed.

Developed to preserve the sample from alterations provoked by the reaction of the implanted caesium with ambient oxygen, the vacuum transfer suitcase was compared to transfer at atmospheric pressure. No notable difference was recorded these two methods. The routing of the sample through a nitrogen atmosphere, before its contact with ambient air at atmospheric pressure, could be sufficient to prevent alterations due to the reactive Cs^+ species. As nitrogen saturates surface Cs^+, it can be deduced that it is mainly the primary ions implanted near to the surface that are responsible of surface modifications when reacting with oxygen.

To circumvent the time-consuming vacuum suitcase procedure, the transfer through atmospheric pressure following the method described above is advisable. Because implanted caesium remains in the sample for several weeks, the following procedure, spanning over more than one day, is proposed. On the eve of the day of analysis, the samples are pre-implanted on an IMS-6f, or equivalent. They are then transferred to the NanoSIMS and left to equilibrate overnight in the sample chamber at 10^{-7} Torr. The samples are then transferred and analysed, without the implantation requirement. Practice has shown that preimplantion of samples increases the amount of acquisitions per day by at least 50%. The larger size of the area pre-implanted on the IMS-6f is an additional advantage of this method, compared to the high-intensity implantation, as it reduces the probability of analysing a sample close to a transition area between implanted and non-implanted, which is the cause of most of the observed implantation artefacts in NanoSIMS imaging.

Chapter IV Investigation of general imaging procedures on NanoSIMS

IV.A. Introduction

In order to assess the imaging capabilities of NanoSIMS for various cell and tissue types, several sample preparation protocols were tested, and the best practice analytical conditions for selected biological specimens were determined. To this date, various sample preparation procedures for ion microprobe imaging are still under investigation (Levi-Setti 1988; Sod, Crooker et al. 1990; Chandra and Morrison 1992; Mony and Larras-Regard 1997; Takaya, Okabe et al. 2003; Dickinson, Heard et al. 2006; Grovenor, Smart et al. 2006; Lechene, Hillion et al. 2006). Moreover, improvements to simplify the sample handling are proposed regularly, as for instance the direct analysis of resin blocks without ultramicrotome sectioning (Hallegot, Audinot et al. 2006). The following preparations are adaptations to ion microprobe analysis including chemical fixation protocols and cryo-preparation of cells and tissues. Futhermore, tissue sections embedded in paraffin, a technique commonly used for pathological observation by optical microscopy, were evaluated as an alternative sample preparation technique for NanoSIMS. A SIMS nuclear labelling technique using the thymidine analogue 5-bromo-2'-deoxyuridine (BrdU) was investigated in an attempt to gain better knowledge of labelling in high resolution SIMS. The BrdU staining technique was introduced by Galle in the early nineties and used by Levi-Setti to determine the correspondence of BrdU stained chromosomal maps to Giemsa band stained caryotypes (Galle 1991; Levi-Setti, Chabala et al. 1994; Levi-Setti, Chabala et al. 1997). Labelling using both halogen atoms and stable isotopes is further evaluated in chapter VI and VII.

IV.B. Materials and Methods

IV.B.1. Sample preparation of murine lung, kidney and peyer patches for ion microprobe analysis

Lung, kidney and Peyer patches were dissected from 4 weeks old male balb/c mice, washed three times in 0.2 M sodium cacodylate buffer pH 7.2, cut to 1 mm^3 sections and fixed overnight in glutaraldehyde 2.5% in buffer at 4°C. After an additional wash in cacodylate buffer, the tissues were post-fixed in 1% osmium tetroxide (Fluka, Germany) sodium cacodylate buffer for 1 hour. Excess fixative was washed out in sodium cacodylate buffer. The specimens were dehydrated in a series of graded ethanol solutions each time for 10 minutes (once in 50% ethanol, twice in 75% ethanol, twice in 95% ethanol and three times in 100% ethanol). Following this, the sections were cleared twice in 100% propylene oxide for

10 minutes. The specimens were infiltrated for 2 hours in a solution of 70% propylene oxide and 30% Epon 812 epoxy resin (Fluka, Germany), followed by 2 hours in a solution of 30% propylene oxide and 70% epoxy resin. Infiltration in resin was conducted in 100% epoxy resin for 12 hours. After exchanging the resin with fresh embedding media, curing was performed at 200 mBar, first at 40°C for 2 hours, then at 65°C for 48 hours. Resin blocks were cut on a Leica UCT ultramicrotome into thin sections of 200 nm, mounted onto SIMS steel sample holders and observed on the NanoSIMS.

Additionally, kidney tissues were washed in phosphate buffer saline at pH 7.2, immersed in 10% formaldehyde fixative in PBS at 4°C overnight. The samples were washed twice in double distilled water for five minutes. Dehydration was performed in a graded series of ethanol solutions at 50%, 75%, 85%, 90%, 95% and 100% ethanol, each step for 15 minutes. The samples were then cleared twice in 100% xylene for 10 minutes, and transferred in a solution of xylene:paraffin (1:1), for 30 minutes at 60°C. Finally, the samples were immersed in fresh embedding medium at 58°C and allowed to cool down. Paraffin sections were obtained using a microtome (1 µm thick) and deposited on 18 µm thick copper foils (Circuitfoil S.A., Wiltz, Luxembourg). The foils were embedded with Wood alloy into copper ring sample holders and observed on NanoSIMS.

IV.B.2. Sample preparation of rat brain and spinal cord for ion microprobe analysis

Rats that were 12 weeks old were perfused transcardially with 500 ml of 1% glutaraldehyde / 1% formaldehyde / 0.1 mM $CaCl_2$ in PBS pH 7.2. Cerebrum, cerebellum and spinal cord were excised, postfixed 18 hours at 4°C with 2.5% glutaraldehyde in PBS and rinsed twice with PBS. Cells were then post-fixed for 1 hour in 1% OsO_4, washed twice in double distilled water and dehydrated in a graded series of ethanol solutions (50%, 75%, 2 X 95% and 2 X 100% ethanol, each for 10 minutes). After clearing twice in 100% propylene oxide for 10 minutes, samples were infiltrated first in a solution of Araldite 502 and propylene oxide (1:1) for 2 hours, then in pure Araldite 502 (Electron Microscopy Sciences, Fort Washington, U.S.A.) for 12 hours, before embedding in fresh resin at 60°C for 24 hours. Thin sections of 100 nm were cut on a Leica UCT ultramicrotome, and deposited on 18 µm thick copper foils The foils were embedded with Wood alloy into copper ring sample holders and observed on NanoSIMS. Several resin sections were deposited on glass slides and stained with 0.02% methylene blue.

IV.B.3. Sample preparation for nuclear labelling of metaphase arrested cells using BrdU

THP-1 cells were cultured in RPMI-1640 with Hepes (Gibco/Invitrogen, Belgium) supplemented with 2 mM L-glutamine and adjusted to contain 25 mM glucose, 1 mM sodium pyruvate, 0.05 mM 2-mercaptoethanol, 50 U/L disodic penicillin G and 10 g/L Streptomycin (Cambrex, Belgium). Additionally, BrdU (Sigma-Aldrich, Germany) at 0.4 µg/mL was added to the medium and the cells were incubated for 24 hours. 10^7 cells were resuspended in 9 mL BrdU supplemented RPMI medium, and arrested in metaphase by adding 1 mL of Colcemid (Sigma-Aldrich, Germany) at 10 µg/mL. The cells were incubated for 45 minutes, harvested and washed twice in 0.05 M sodium cacodylate buffer at pH 7.4. A primary fixation was performed in 2.5% glutaraldehyde buffer for 1 hour, washed again in buffer and post-fixed for 1 hour in 1% OsO_4 (Fluka, Germany) PBS. After two washes in PBS, cells were transferred into a graded series of ethanol solutions (50% ethanol for 5 minutes, 75% ethanol for 10 minutes, twice in 95% ethanol for 10 minutes, twice in 100% ethanol for 10 minutes). Subsequently, the cells were cleared in 100% propylene oxide (Fluka) for 15 minutes, followed by an infiltration of 1 hour in a solution of 50% propylene oxide and 50% Epon 812 epoxy resin (Fluka, Germany). Infiltration in pure resin was realised for 12 hours. After exchanging the resin by fresh embedding media, curing was done at 200 mBar, first at 40°C for 2 hours and then at 65 °C for 48 hours. Resin blocks were cut on a Leica UCT ultramicrotome into thin sections of 300 nm that were mounted onto steel sample holders and observed on the NanoSIMS.

IV.C. Results

A major difficulty in SIMS imaging comes from the ion distribution not being directly related to optical images. Nevertheless, the SIMS can be operated in TIC - total ion current - mode, measuring the total secondary ion current of all the masses. TIC images give an approximate view, without mass discrimination of sample features, allowing a lateral orientation within the sample before the mass resolved analysis. In TIC mode, care must be taken not to relate to topological features that may not be visible under the specific ion detection mode.

The NS50 is equipped with an optical camera with provides some orientation on the sample holder and helps in positioning the ion beam spot for chemical microanalysis. Light reflected on the mirror polished sample holder forms an image of the sample, which is recorded by the camera. As opposed to transmitted light microscopy, this configuration does not resolve features inside the sample well, and usually, only the transition between resin sections and

specimen holder could be observed. Most often, the optical camera was not helpful in assessing the general quality of the sample and the microprobe analysis was preceded by staining of the sections with either toluidine blue or methylene blue, and observation on a Leica DMIL II optical microscope.

IV.C.1. Ion microprobe analysis of Peyer patches

Gut-associated lymphoid tissue (GALT) consists of specialised immune cells, such as intraepithelial lymphocytes (IEL), antigen-presenting epithelial cells such as lamina propria lymphocytes (LPL), dendritic cells and macrophages (Mayer 2000). While the general function of the gut immune system is to protect the tissue from gut antigens, follicular organisational units called Peyer's patches, mainly found in the ileum, play a major role in the immune response to gut lumen antigens. The epithelial M-cells above the Peyer's patches possess selective transepithelial transport capabilities of antigens or microorganisms. The mucus produced by goblet cells, which covers gut epithelial cells, is absent from M-cells, favouring the transcytosis of antigens to the underlying Peyer's patches composed of B-lymphocytes and antigen-presenting cells. The previous description describes the humoral response of B-lymphocytes, the activation and proliferation of CD8+ cytotoxic cells and CD4+ helper T cells, and constitutes the immunological responses of the GALT to harmful antigens.

The ion micrograph on Figure 35 illustrates the GALT of the terminal ileum. Lymphocytes, characterised by their small and compact size, are visible both on $^{12}C^{14}N^-$ and $^{31}P^-$ ion maps due to the high secondary ion emission arising from their nuclei. On the other hand, membranes, rich in phosphorus, are not clearly delimited. While the intensity of nuclei of M-cells is low, their nucleoli can be distinguished. Several round shapes with hypersignals of $^{12}C^{14}N^-$ and absent of $^{31}P^-$ correspond to inclusion bodies (McMahon, Glassner et al. 2006) migrating via vesicular transport in the M-cells. This is particularly visible in the close-up of several M-cells in Figure 35C and Figure 35D.

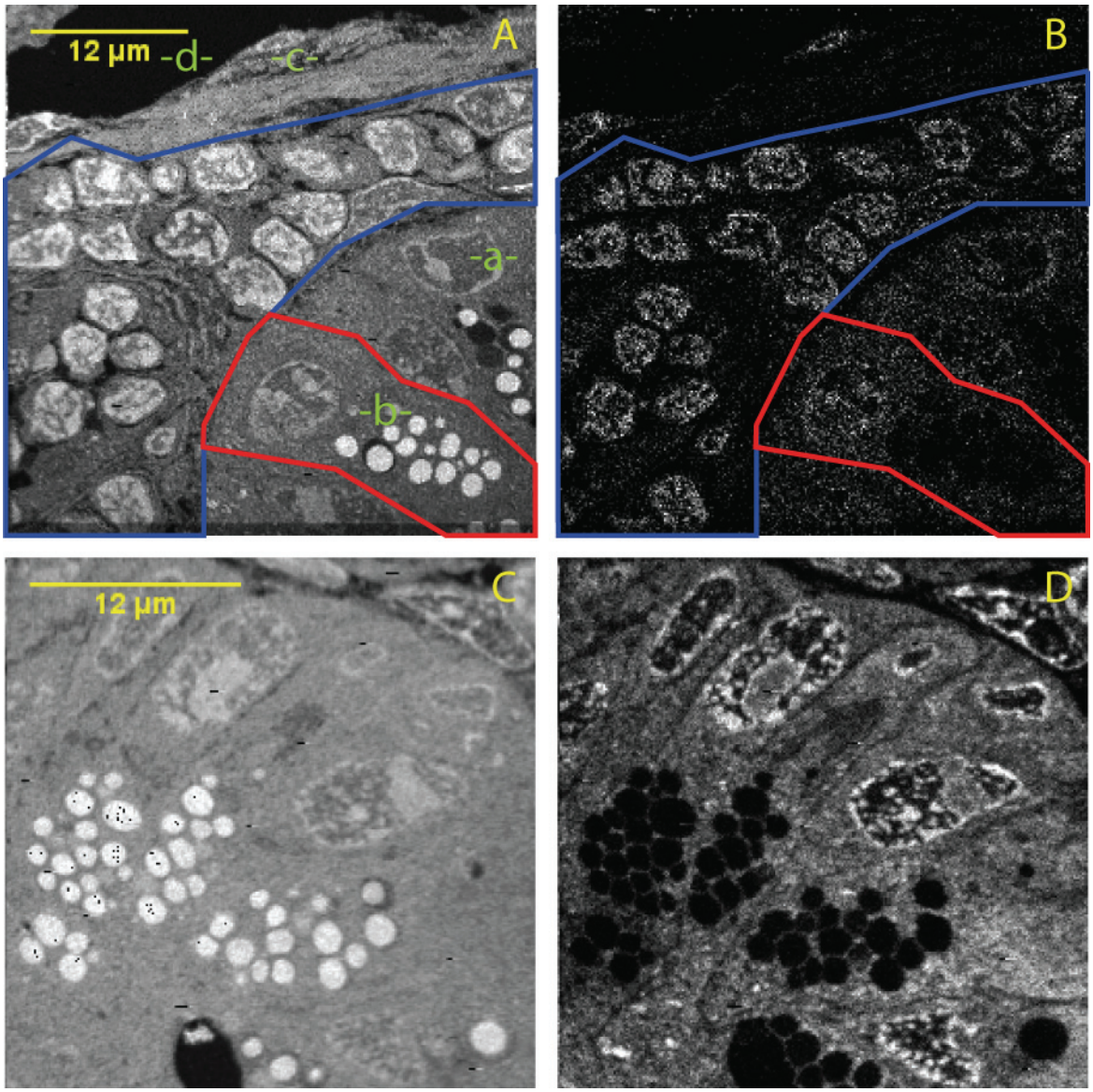

Figure 35: Ion micrograph of murine Peyer patches. *Cs^+ impact energy 16 keV, 256 pixels x 256 pixels (A, B) $^{12}C^{14}N^-$ and $^{31}P^-$ micrographs (32.9 nA, 60 ms/pixel, L1 = 6714.0 V). Outline of M-cell in red. Lymphocyte population in blue. -a- nucleus of M-cell, -b- inclusion bodies, -c- gut epithelium, -d- gut lumen (C, D) $^{12}C^{14}N^-$ and $^{31}P^-$ micrographs (85.4 nA, 90 ms/pixel). A close-up of M-cells shows similarly distributed inclusion bodies in the cell, rich in cyanide ions and poor in phosphorus.*

IV.C.2. Ion microprobe analysis of murine lung

The lung bronchioles are organised in alveoli separated by alveolar septal junctions. The main cell types found in these junctions are type I and type II pneumocytes, alveolar macrophages, fibroblasts and capillaries. Type II granular pneumocytes are cuboidal cells that produce and secrete lung surfactant. Figure 36 shows a T shaped alveolar septum surrounded by alveolar lumen. The nuclei of several cells could be distinguished in the septum. The elongated shape of these cells may identify them as a type I pneumocyte, responsible for gas exchange in the alveoli (Figure 36A, green arrows). Interestingly, some $^{12}C^{14}N^-$ hypersignals did not show

corresponding $^{31}P^-$ hypersignals. Considering both that lung tissue is strongly irrigated and that these structures dwell in proximity of type I pneumocytes, they may be related to capillaries (Figure 36A, red arrows). Some features such as round aggregates or vesicles of a diameter of approximately 1 µm could not be clearly identified by ion microprobe imaging.

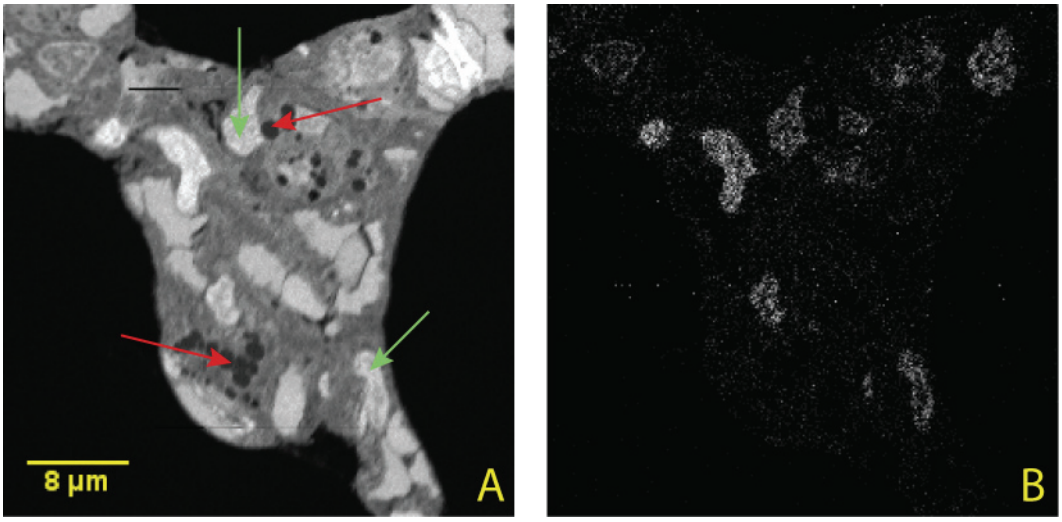

Figure 36: Ion micrograph of murine lung tissue. *Potential type I pneumocytes are marked by green arrows. Capillaries are marked by red arrows. (A) $^{12}C^{14}N^-$, (B) $^{31}P^-$; Cs^+ impact energy 16 keV, primary current 29.50 nA, 256 pixels x 256 pixels, 15 ms/pixel.*

IV.C.3. Ion microprobe analysis of murine kidney

Figure 37A and Figure 37B depict a section through a nephron, the functional unit of a kidney. Centrally positioned is a renal tubule of 12 µm in diameter. The relatively small size of the central lumen point to an intermediate tubule, which is part of the Henle loop. In the image, larger structures corresponded to proximal tubules. Several nuclei emitted a dense $^{31}P^-$ signal. Both basal lamina and membranes were well defined. Figure 37C and Figure 37D corresponded to a formaldehyde fixed mouse nephron section embedded in paraffin. While the general shape of the tubule was determined on the cyanide ion micrographs, with cuboid cells and nuclei visible with $^{12}C^{14}N^-$ and $^{31}P^-$, the image quality was inferior to glutaraldehyde fixed resin embedded sections. This is accentuated on the $^{12}C^{14}N^-$ image, where an impression of surface features becomes visible, typical of the analysis of non-flat surfaces.

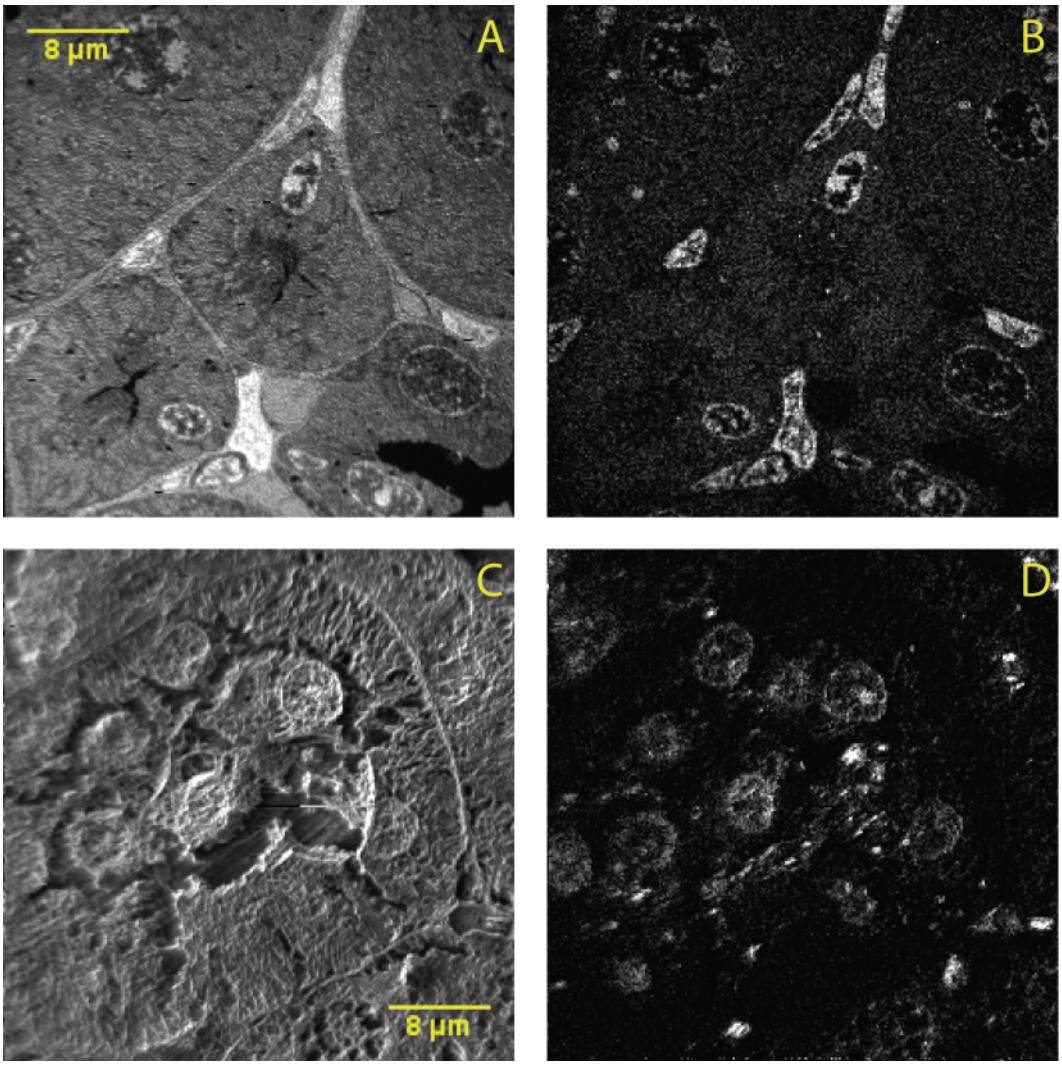

Figure 37: Ion micrograph of murine kidney tissue. *Cs^+ impact energy 16 keV, 256 pixels x 256 pixels. (A, C) $^{12}C^{14}N^-$, (B, D) $^{31}P^-$. (A, B) glutaraldehyde fixation, dehydration and embedding following a standard SIMS protocol, (37.5 nA, 90 ms/pixel). (C, D) formaldehyde fixation, dehydration and paraffin embedding following a standard OM protocol, (49,7 nA, 20 ms/pixel).*

IV.C.4. Ion microprobe analysis of rat cerebellum and spinal cord

A methylene stained mouse cerebellum is depicted in Figure 38. Variations in staining density allowed the identification of the stratum molecular from the stratum granulosum. Purkinje cells were situated at the interface between both stratii. The tissue was strongly vascularised (Figure 38A, in green). Figure 38B shows a transversal section through the dorsal lobe of the spinal cord of a rat. A capillary, constituted of a single epithelial cell, with a lumen of 1.5 µm diameter was visible. The lower cell, with a large nucleus but without clearly delimited plasma membrane corresponded to an oligodendrocyte, responsible for the myelin sheath formation around neurons. The upper nucleated cell was probably the soma (cell body) of a neuron, where a synapse with synaptic vesicles could be distinguished. Surrounding those

cells, a multitude of myelinized axons was present, identified by their overlapping phospholipid layers. As both the osmium tetroxide and the uranyle acetate treatment fixed phospholipid membranes, myelin sheaths are particularly electron dense on EM. The high number of myelinized neurons is typical of white matter in the central nervous system.

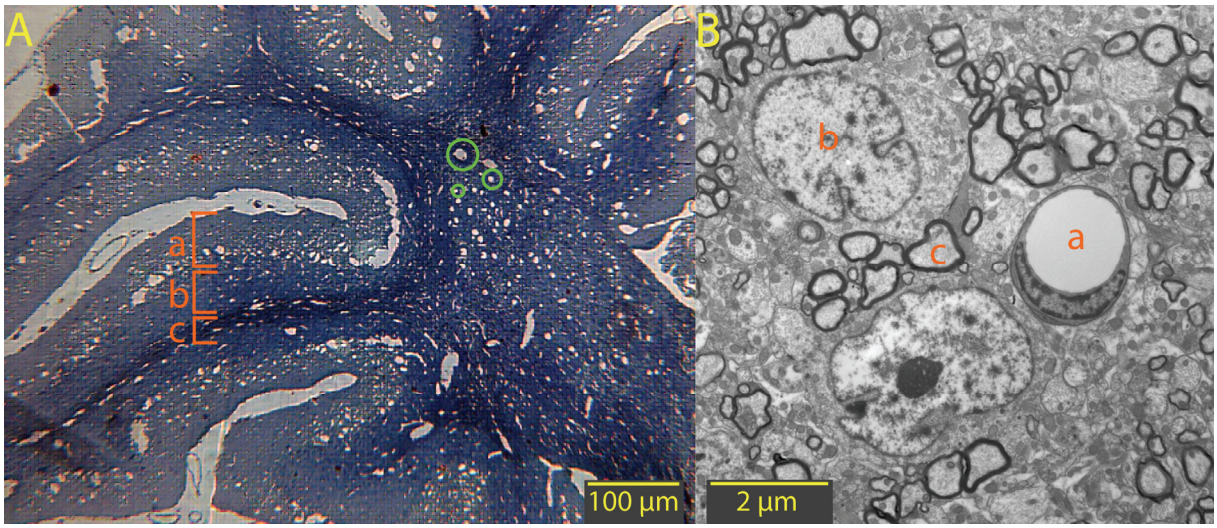

Figure 38: Rat cerebellum. *(A) Optical microscope image stained by methylene blue 0.02%, magnified 400X. (a) Stratum moleculare, (b) Purkinje cells, (c) Stratum granulosum and white matter. Capillaries in green. (B) Transmission electron micrograph of rat spinal cord, 7100 kV, magnified 7000X. (a) capillary, (b) oligodendrocyte, (c) myelinized axon, (d) synapse.*

The identification of nervous tissue on NanoSIMS ion micrographs was not as obvious. Nevertheless, visual similarities are illustrated on Figure 39 and Figure 41. Several erythrocytes were visible in the lumen of a blood vessel on the $^{12}C^{14}N^-$ ion image. Mouse erythrocytes have no nucleus and lack DNA; therefore, $^{31}P^-$ signal of the erythrocytes is very low. However, the nucleus of the epithelial cell of the capillary is clearly delimited against the lower phosphorus background. Generally, cell nuclei emit high amounts of $^{31}P^-$, and substructures inside the nucleus are visible. Emission of $^{12}C^{14}N^-$ was homogenous, and did not yield sufficient contrast for a clear image.

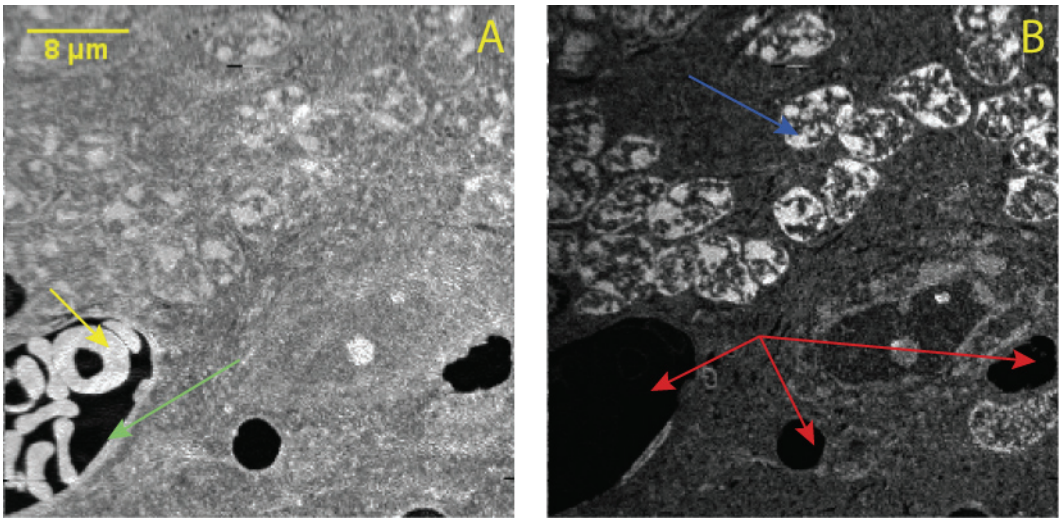

Figure 39: Ion distribution maps of mouse cerebellum. *Erythrocytes (yellow arrow) can be found in the lumen of a capillary (red arrows). The nucleus of a capillary epithelial cell is marked by a green arrow. Nuclei are denoted by a blue arrow. (A) $^{12}C^{14}N^-$, (B) $^{31}P^-$. Cs^+ impact energy 16 keV, primary current 91.3 nA, 256 pixels x 256 pixels, 20 ms/pixel.*

Figure 41 shows that $^{16}O^-$, used as an additional ion, yields contrasted images with a sufficient secondary emission. Myelin is constituted of the myelin basic protein (MBP) (Eylar, Brostoff et al. 1971), the myelin oligodendrocyte glycoprotein (MOG) (Roth, Malfroy et al. 1995), the proteolipid protein (PLP) (Lees, Chao et al. 1983) and the phospholipids galactocerebroside (Figure 40) and sphingomyelin. It was the oxygen rich phospholipid galactocerebroside that was visualised both with $^{16}O^-$ and $^{31}P^-$. Plasma membranes were visible neither in Figure 41 nor in Figure 42.

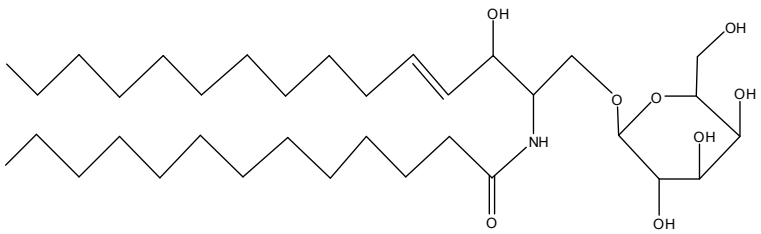

Figure 40: Galactocereboside.

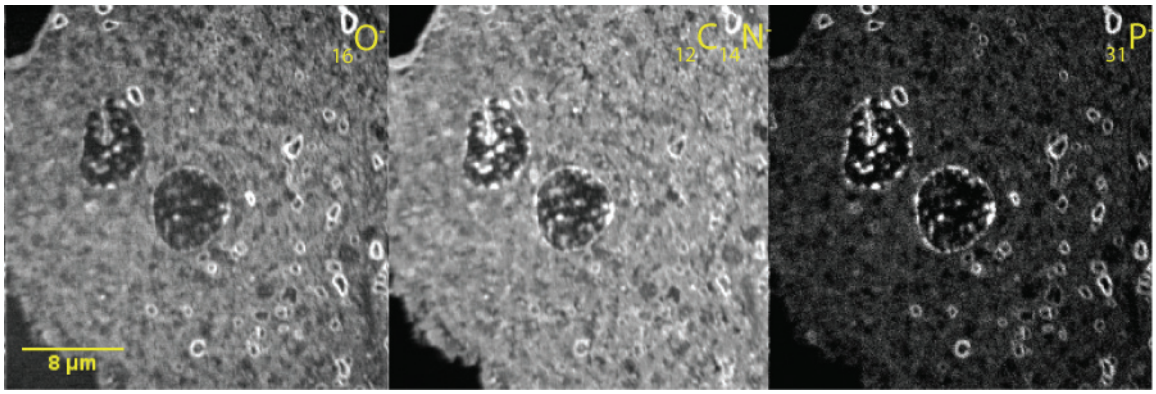

Figure 41: Ion distribution maps of mouse cerebellum. *Cs^+ impact energy 16 keV, primary current 32.3 nA, 256 pixels x 256 pixels, 40 ms/pixel. Nuclei of cells are clearly delimited. Small round structures of 1 µm correspond to myelinized axons.*

The choice to observe other ions besides $^{12}C^{14}N^-$ is even clearer in Figure 42 where $^{31}P^-$ yielded the most contrasted image. Besides round nuclei, oblong myelinized structures were observed. Interestingly, nuclei did not present high secondary emission yields for $^{32}S^-$. On the other hand, the condensed state and the structural stabilization function of myelin proteins such as MBP point to high number of sulphur bonds (Galiano, Andrieux et al. 2006), as confirmed by the sulphur ion micrographs.

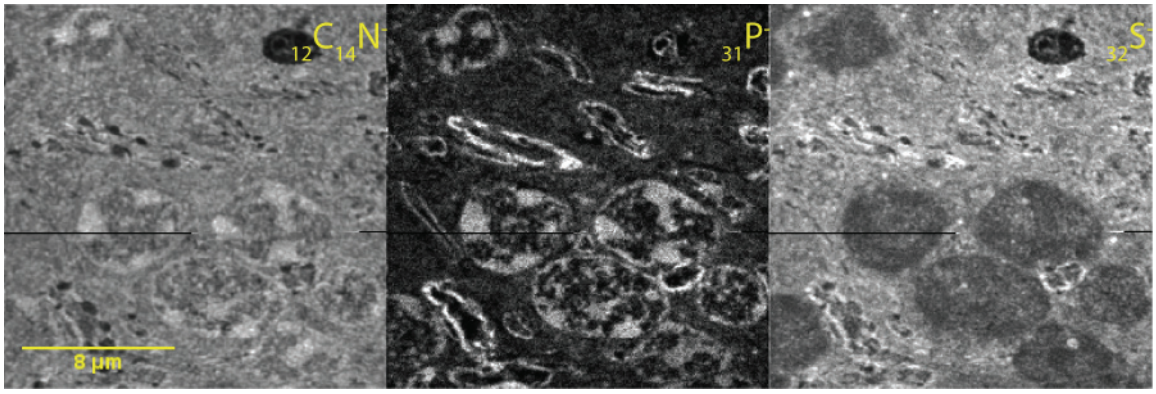

Figure 42: Ion distribution maps of spinal cord. *Cs^+ impact energy 16 keV, primary current 56.7 nA, 256 pixels x 256 pixels, 40 ms/pixel.*

IV.C.5. Ion microprobe analysis of BrdU labelled metaphase arrested cells

Bromide possesses two stable isotopes, at 79 and 81 a.m.u and their natural abundances are almost equivalent (50.69% and 49.31% respectively). To avoid interferences of the ion PO_3^- at mass 79, the Br isotope with mass 81 was selected for NanoSIMS analysis.

Figure 43 depicts a single cell arrested in metaphase. Hypersignals of cyanide, phosphorus and bromide, were visible as elongated shapes centrally located inside the cell, which corresponded to the chromosomes. Their compacted nature was due to the high concentration

of $^{12}C^{14}N^-$, $^{31}P^-$ and $^{81}Br^-$ inside the microvolume of analysis, and explained the high intensity (expressed as counts/pixel) in an image pixel. Concurrent with the absence of nucleus in metaphase, no nuclear membrane was distinguished in the $^{31}P^-$ ion map. Several small round features speckled the cytoplasm, emitting $^{12}C^{14}N^-$ ions. While presence of $^{81}Br^-$ in these structures would have identified them as mitochondria by bromide staining of their mitochondrial DNA, the sole emission of cyanide ions identified them as lysosomes, which was consistent with previous findings (Berry 1996). As the three ions were detected simultaneously, a perfect superimposition of images was possible and is illustrated in Figure 43, for the bromide ion map overlaid on the cyanide ion map. An overlay of the phosphorus ion map on the cyanide ion map would have yielded a perfect superimposition as well (data not shown).

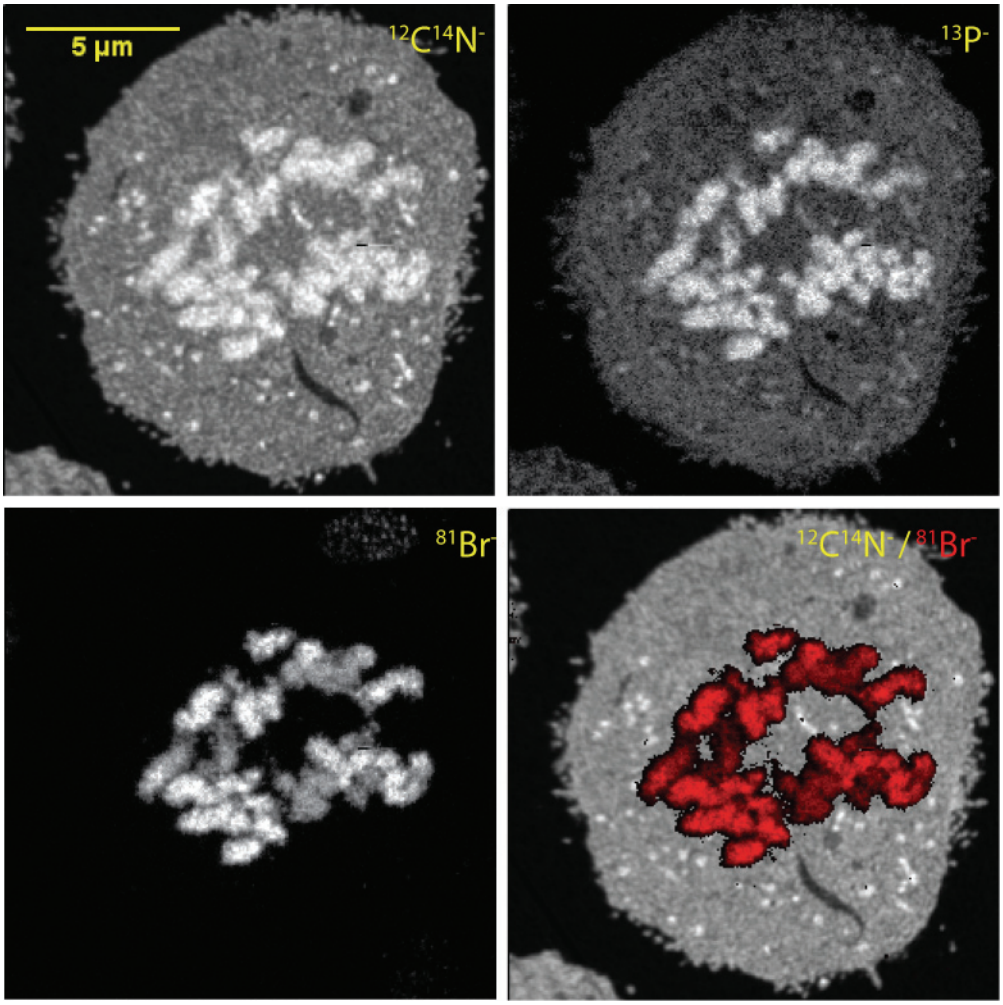

Figure 43: Ion distribution maps of a metaphase arrested cell. *Ions of interest are $^{12}C^{14}N^-$, $^{31}P^-$ and $^{81}Br^-$. Cs^+ impact energy 16 keV, primary current 97.8 nA, 256 pixels x 256 pixels, 20 ms/pixel. Chromosomes emit strongly in the three maps. An overlay of the cyanide ion with Br^- (in red) shows the perfect superimposition of bromide hypersignals with the cyanide ions. $^{31}P^-$ would perfectly superimpose with the cyanide ions (data not shown).*

IV.D. Discussion

The difficulty to identify tissue structures and orientation in ion micrographs without comparative observations by OM is a known experimental reality. Causes for these difficulties are primarily the lack of experience in relating elemental or small cluster ions to cellular features and the limited field-of-view (FOV) range available in SIMS.

In SIMS imaging, the mapping of specific ions cannot always be directly related to optical images. Nevertheless, the NanoSIMS can be operated in total ion current mode (TIC), measuring the total secondary ion current resulting from the population of all emitted secondary ions before mass separation by the analyzer. Such TIC images give an approximate view, without mass discrimination of sample features allowing a lateral orientation within the sample before the mass resolved analysis. The images obtained in this mode should not be related to topological features, as these images may not reflect the distribution of a specific ion in the ion detection mode. Although cellular features sometimes emit strongly for a specific ion and highly contrast the resulting TIC images, these features may not necessarily appear on micrographs of other ions.

On the NanoSIMS, imaging FOVs range from 10 µm x 10 µm to 80 µm x 80 µm, complicating morphological observations of biological specimens. While technically lower FOVs are possible on the NanoSIMS, their use is limited by the lateral resolution of the instrument (50 nm for the Cs^+ primary ion beam) which is a hindrance to obtain better-resolved images. At FOVs above 80 µm x 80 µm, image distortions due to lens aberrations occur. Thus, the working range of the NanoSIMS is disadvantageous to the analysis of tissues, where observation over large areas of the sample might be required. However, tissues with characteristic features such as brain, kidney, Peyer's patches, liver or lung, easily identified. The use of thin copper sheets as sample holders, a method proposed in IV.B.2, has allowed the distribution of serial sections and large tissues over a sizeable area. These conductive foils were cut to size to fit in the copper rings only after positioning the resin sections, improving the handling of large samples.

Surface erosion of samples has proven not to be an alternative to ultra-microtome sectioning, as the erosion was irregular and depended on the local chemical composition of the sample. The ensuing increase in sample topology causes variations in the ion extraction field, which leads to erroneous ion counts and artefacts.

Our successful observation of bromide at high resolution encouraged the use of BrdU as a DNA specific label in further applications (see Chapter VI).

Chapter V NanoSIMS imaging of trace metals in lichens

Manuscript in preparation: Pirrotte, P., Azevedo-Rodrigues, S., Fernandez-Salegui, AB., Audinot, JN., Migeon, HN., Muller, CP. NanoSIMS imaging of trace metals in lichens.

V.A. Introduction

Lichens are symbiotic associations between a fungus (mycobiont) and a green algae and/or a cyanobacterium (photobiont). The mycobiont is usually obligated to this symbiosis, while the photobiont can be found as a single, independent organism.

The lichen used in this study, *Evernia prusnastri* (L.) Ach., has a fruticulose structure with a dorsiventraly arranged thallus. It is mostly composed of fungal hyphae with a lower and an upper cortex (corresponding to the lower and upper surface, respectively) built of cell-like compartments of densely packed hyphae. Between the upper and lower cortex is the medulla, which is composed of lax network of hyphae. In the upper part of the medulla, is located an algal layer intermixed with fungal hyphae.

For years, lichens have been used as bioindicators of atmospheric pollution through studies on their biodiversity and effects of atmospheric pollutants on their physiology (Nimis, Castello et al. 1990; Bennett and Wetmore 1999; Asta, Erhardt et al. 2002).

The effects of atmospheric pollution on lichen ultrastructure have been demonstrated for SO_2 (Holopainen and Karenlampi 1984), CO_2 and O_3 (Balaguer, Valladares et al. 1996), through fumigations of lichen thalli. This relationship was also demonstrated for lichens collected in sites near atmospheric pollution sources, emitting SO_2 along with other elements, including heavy metals (Tarhanen, Poikolainen et al. 2000).

Recent studies attempted to identify the relationship between sources of heavy metal pollution, such as industrial Cr and Cd emissions, and the lichen physiology and cellular ultrastructure (Sanita Di Toppi, Musetti et al. 2004; Sanita Di Toppi, Musetti et al. 2005), by immersion-spiking lichen thalli in highly concentrated salt solutions of trace elements. Biomonitoring studies performed on lichens involve the exposure of a lichen, from few days up to several months, to a variety of environmental compounds in the field. Modelling by immersion-spiking can be seen as an approximation to assess the effects of atmospheric pollution on lichen physiology and ultra structure.

Elemental distribution on lichens transplanted to polluted sites has been assessed by Macro-PIXE (Macro-Particle induced X-ray emission) and Micro-PIXE (Clark, Mangelson et al. 1999; Budka, Przybylowicz et al. 2002). PIXE measurements allow the examination of heavy metal distribution patterns in different lichen layers. The spatial resolution of the method is 1 mm, which allowed to determine the elemental distribution in the in the upper and lower cortices, algal layer, medulla and rhizines, while the elemental retention by ultrastructural components could not clearly be determined. Several studies have assessed the suitability of

the lichen *Evernia prunastri* for biomonitoring atmospheric pollutants (Conti, Tudino et al. 2004; Gaio-Oliveira, Dahlman et al. 2005). Compositional studies by Inductively Coupled Plasma Mass Spectrometry (ICP-MS) have been performed on several lichen species on a broad range of pollutants (Pino, Alimonti et al. 2007). In collaboration with the University of Aveiro (Portugal) and the University of León (Spain), this study aimed to correlate the quantitative elemental composition obtained by ICP-MS to their localisation obtained by NanoSIMS. Furthermore, ion microprobe analysis was used to identify fungal and algal structures involved in heavy metal retention, potentially leading to ultrastructural changes that may affect the lichen physiology.

V.B. Materials and Methods

E. prunastri was employed to study trace element deposition in the province of Léon, Spain, by the University of León. Samples of this lichen were transplanted from an area free of atmospheric pollutants to different sites with suspected industrial pollution, and two specific sites within the city of Léon, to monitor pollution in these areas over time. Special care was taken to select thalli of the same size corresponding to the same stage of development (Conti, Tudino et al. 2004). After 6 months, the thalli were analyzed by ICP-MS for the following trace elements: Co, Cu, Cd, Ba, Mn, Zn, Ni, Al, S, Ca. Table 8 shows the elemental composition of *E. prunastri* thalli in ppm or ppb for four sites: (i) Candanedo, control location, without known sources of atmospheric pollution, (ii) La Pola de Gordon, in proximity of a tunnel construction site (iii) Michaisa and Quevedo in the city of Léon. The quantification the selected trace elements was obtained by A. B. Fernández-Salegui and A. Terrón (Department of Biodiversity and Environmental Management, University of León).

Table 8: ICP-MS analysis of *E. prunastri* thalli.

Samples	Co (ppb)	Cu (ppm)	Cd (ppb)	Ba (ppm)	Mn (ppm)	Ni (ppm)	Al (ppm)	S (ppm)	Ca (ppm)	Zn (ppm)
Candanedo	67	1.67	75.8	8.36	196	0.82	220	502	5340	12.4
P. Gordon	1853	6.56	97	46	185	6.86	9481	2190	38500	30.7
Michaisa	634	30.7	156	40	303	3.13	1369	4620	12700	109
Quevedo	398	27.9	118	20.5	168	1.98	911	3110	11900	41

Due to the long fixation protocols for NanoSIMS, only the Quevedo sample was prepared for ion microprobe imaging. The following lichen sample preparation consists in variations from common lichen preparation protocols for electron microscopy (Gloser 2002). Samples were rehydrated overnight to facilitate the infiltration of the fixative and avoid structural damage

due to the mechanical stress during the cryofixation. To avoid a relocation of ions that would occur in a chemical sample preparation, the samples were cryofixed by metal mirror freeze-slamming on a copper bloc cooled by liquid nitrogen using the Leica MM80. A subsequent cold fixation was performed at -90°C for 4 hours in a 2.5% glutaraldehyde PBS solution. Substitution was carried out in a Leica AFS freeze substitution device, in ethanol 100% following the substitution steps outlined in Table 9.

Table 9: Cryofixation of lichen tissue.

Solvent	Time [h]	Temp [°C]	Slope [°Ch^{-1}]
Ethanol	72	-90	
	25		+5
	1	-40	
	1		+20

The sample was washed with fresh ethanol 24 times for 5 minutes each, followed by two steps in 100% propylene oxide for 20 minutes. Resin infiltration was carried out over 3 days, with fresh Epon 812 exchange every 12 hours. The samples were embedded in flat and conical moulds in the epoxy resin. Resin sections were deposited on TEM grids, stained with 1% uranyl acetate and observed on TEM (Hitachi H6500) to identify lichen thalli structures. The ions maps for $^{12}C^{14}N$, ^{16}O, ^{31}P, ^{63}Cu and ^{65}Cu, $^{27}Al^{16}O$, $^{64}Zn^{16}O$ were then acquired on the NanoSIMS. As Al and Zn do not emit negative secondary ions under the caesium beam, the analysis using the duoplasmatron mode should have been performed. However, as the resolution capacity of the duplasmatron beam is inferior to the one of the caesium beam, the negatively emitted molecular clusters ZnO and AlO were observed using the caesium beam to conserve the resolution.

V.C. Results

Figure 44 depicts the ultrastructure of *E. prunastri* thallus as seen by electron microscopy. A general instability of the resin sections resulted in the formation of holes during the observation. Several algal cells were visible, identified by their dense cytoplasm, the thick electron permissive cellulose membrane, chloroplast thylakoids and by wide ovoid structures inside the chloroplasts that resulted from the accumulation of starch grains (Figure 44A). Several smaller cells were positioned around the algal cells, notably above the upper left cell magnified in Figure 44B. They corresponded to fungal cells, confirming the symbiotic

relationship between fungal and algal cells (Scheidegger and Schroeter 1995; Nash 1996; Gaio-Oliveira, Dahlman et al. 2005). Figure 44C shows another algal cell, surrounded by fungal cells. Figure 44D is a closer view inside an algal cell. The plasma membranes were detached from the cellulose membrane, an artefact potentially induced by the preparation and observed for several cells. These artefacts may also find their origin in the long desiccation period to which the lichens were subjected after sample collection and prior to rehydration and analysis.

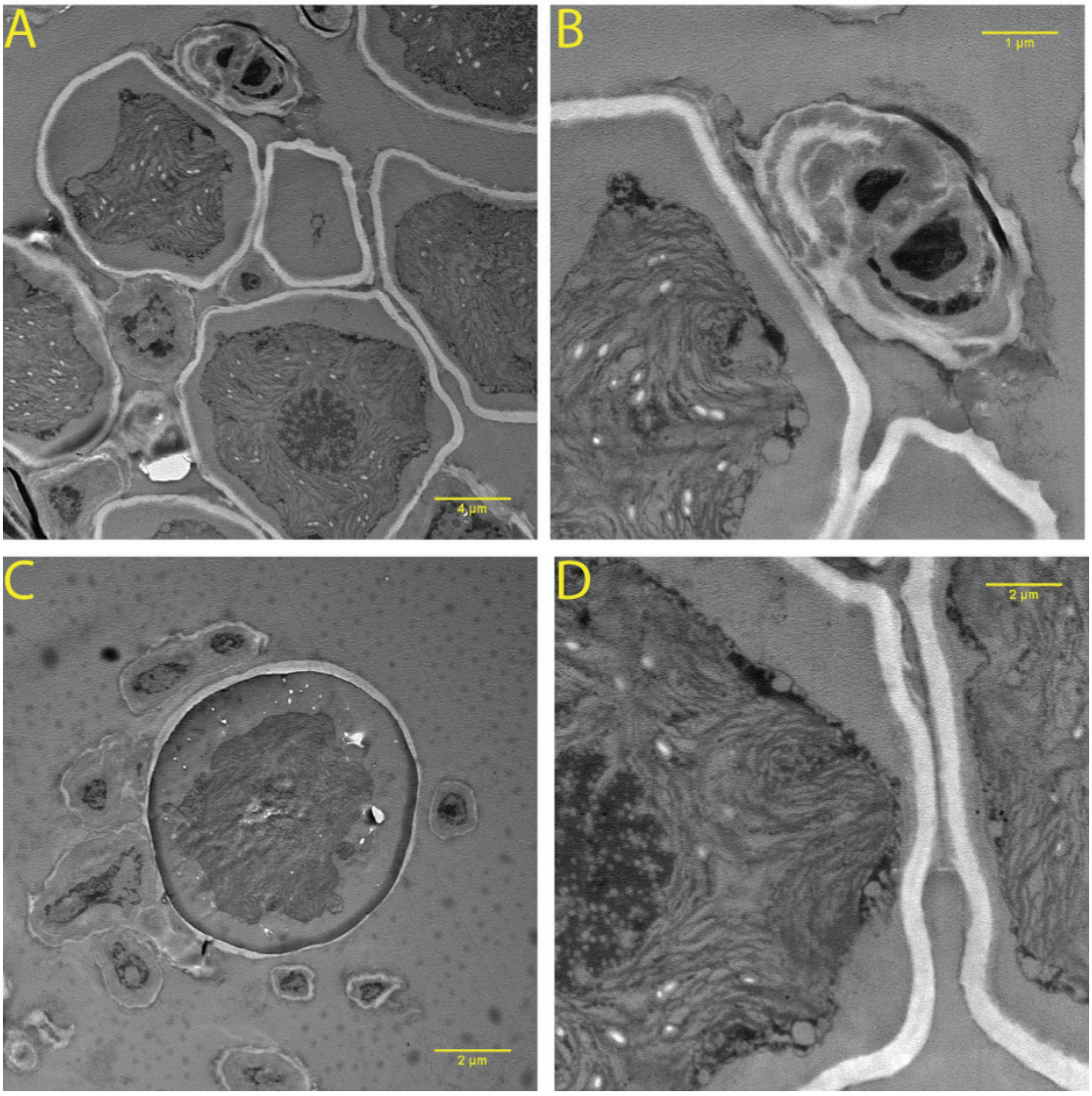

Figure 44: The lichen *E. prunastri* observed on TEM. *(a) photobiont in the upper cortex, (b) interface between algal and fungal cells, (c) photobiont surrounded by mycobiont in the medulla, (d) interface between two algal cells.*

Figure 45 displays SIMS ion micrographs acquired on the sections previously observed with TEM. The round cells corresponding to the photobiont (green arrows, identified on toluidin stained sections by optical microscopy) were situated below a tight fungal layer (Figure 45A, framed in red). Several fungal cells were in contact with the algal cells (blue arrows). The

photobiont presented an accumulation of Cu at the level of its cellulose membrane, which was not verified for the fungal cells, below the tight outer layer (Figure 45A, ^{63}Cu and ^{65}Cu micrographs). Counts for both ^{63}Cu and ^{65}Cu were low, ranging between 5 counts/pixel and 15 counts/pixel, and the distribution was more clear on ^{65}Cu micrographs than on ^{63}Cu micrographs. The tight fungal layer itself exhibited a strong signal for all the ion species. This was attributed to the formation of holes in the resin section during primary ion implantation, which resulted in artefactual measurements. Figure 45B shows an algal cell, with a localised distribution of ^{27}Al and ^{64}Zn in the cellulose membrane. A similar distribution of these elements was observed in the algal cells of Figure 45C. Artefactual holes, encircled in red, were clearly discriminated as they strongly emitted for all the analysed ions. The localisation of both ZnO and AlO metal-based molecular clusters was possible due to the ubiquitous presence of $^{16}O^-$ in the sample.

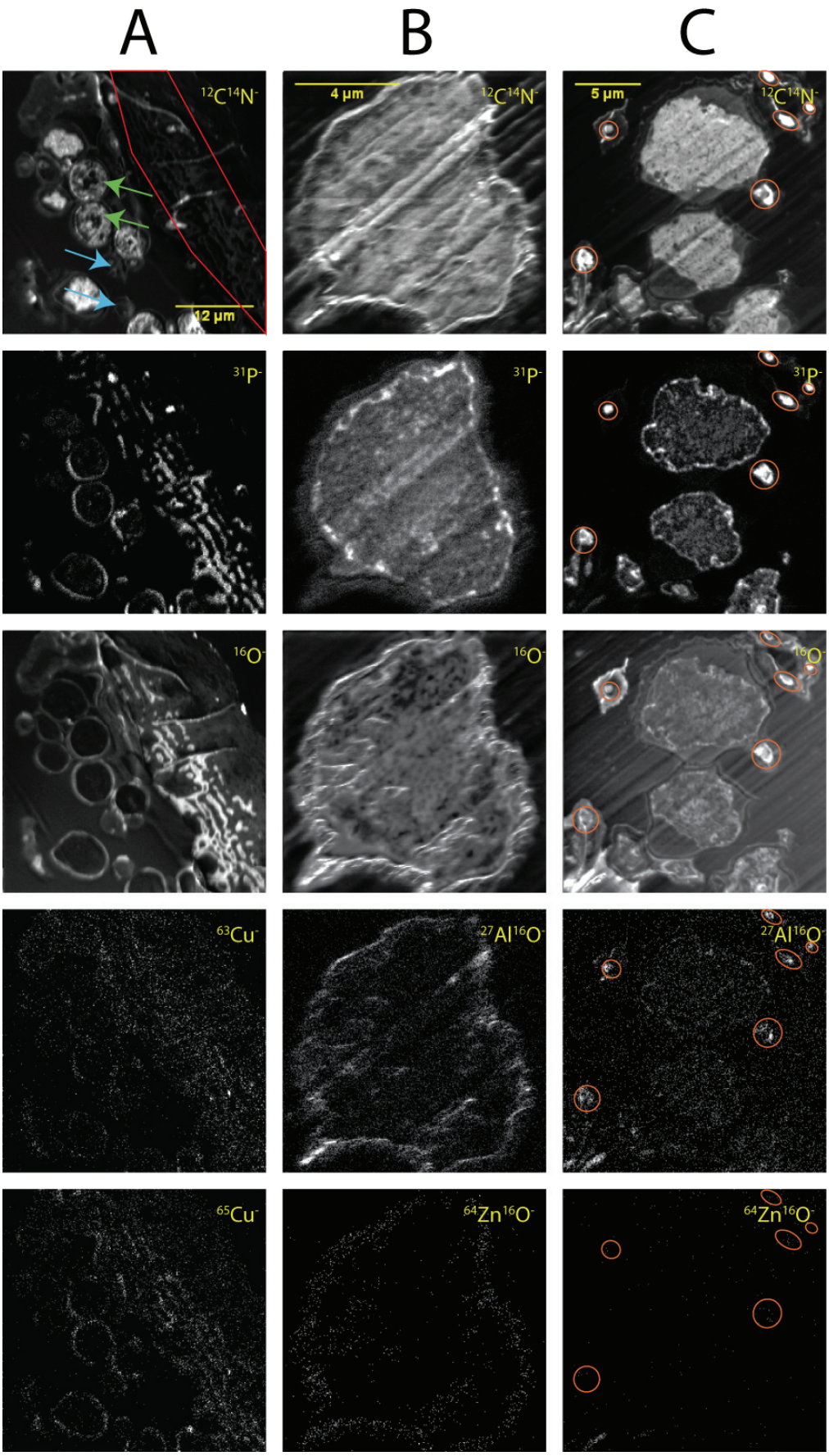
A
B
C
$^{12}C^{14}N^-$
12 µm
4 µm
5 µm
$^{31}P^-$
$^{16}O^-$
$^{63}Cu^-$
$^{27}Al^{16}O^-$
$^{65}Cu^-$
$^{64}Zn^{16}O^-$

Figure 45: Lichen upper cortex and underlying algal layer. *(A) Upper cortex (in red), algal cells (green arrows), fungal cells (blue arrows); (B) algal cell (C) algal cells; artefactual holes in the resin encircled in orange*

V.D. Discussion

During both SIMS and TEM analysis, the samples were subjected to stringent conditions that resulted in artefacts such as holes and tears in the resin sections. These artefacts caused by the ion beam (or the electron beam, respectively) are formed progressively and are usually the consequence of an incomplete infiltration of the resin in the sample. In order to improve the penetration of the resin into the cryofixed samples, several approaches were investigated. Neither prolonged infiltration times nor vacuum infiltration improved the quality of the preparations. High pressure freezing of lichen thalli was explored as an alternative to standard cryogenic preparation protocols, but yielded qualitatively inferior samples. To better understand the repeated failure to produce correctly prepared tissues by cryofixation, a better revision of lichen literature was undertaken. Lichen high-resolution imaging is scarce, probably due to the difficulty of thalli preparation. Resin infiltration in loosely organised lichen species, such as *E. prunastri*, is thought to be burdened at regions interfacing algal and fungal cells. Although this information was not formally described in the literature, it was a recurring topic in scientific community imaging lichen ultrastructure (personal communication: C. Ascaso). Electron micrographs of algal cells of *E. prunastri* showed shrinking of the plasma membrane and of the cytoplasm and their detachment from the cell walls. Similar shrinking of algal cells of *E. prunastri* was described elsewhere, confirming the difficulty of preparation of this lichen (Millanes, Fontaniella et al. 2004).

Under such sub-optimal conditions, the analysis of trace metals has to be considered with precaution. The presence of holes in the sample may generate artefactual signals, usually over several, if not all, ion detectors. The selection of suitable sections by TEM, before ion microprobe analysis, was a crucial step to identify these artefacts and avoid their processing as a significant signal.

The elemental detection of Cu, Zn and Al was generally low, with only several counts/pixel. It has been reported that elemental concentrations inside thalli increases with age (Senhou, Chouak et al. 2002), consistently with longer exposure periods. Thus, using older parts of the thalli that possess higher concentrations of trace elements would have been advantageous to improve detection by SIMS. However, trace metal composition in younger parts of the thalli reflect better recent pollution events (latest months). As this was the study's purpose, only young marginal lobes of the thalli were selected for sample preparation and analysis.

The localisation of the referred metal elements was determined at an unprecedented resolution by NanoSIMS. Cu, Zn and Al were mostly accumulated around cellulose membranes of algal cells. Generally, imaging of ^{65}Cu (69.2%) generated slightly better contrasts, which can be related to its higher abundance when compared to its isotope ^{63}Cu (30.8%).

In a previous study, mullite particles ($3Al_2O_3.2\text{-}SiO_2$) were observed in the upper cortex (Ayrault, Clochiatti et al. 2007). These particles were not observed by NanoSIMS analysis which might have been caused by a poor preservation of the upper cortex during cryofixation. The previous study also reported a homogenous presence of Zn in the upper cortex and the underlying algal layer of *E. prunastri*, with a decreasing concentration in the medulla. This Zn distribution may not be the result of unspecific accumulation and an active role in various biological processes has been suggested for the metal (Cuny 1999).

A recent study on *Evernia prunastri* and *Xanthoria parietina* revealed the presence of urease in the algal cell walls (Millanes, Fontaniella et al. 2004). This enzyme, which is thought to be related to the binding of fungal lectins on the surface of algal cells (Molina, Muniz et al. 1993), was stained according to Gomori (Gomori 1952). This cytochemical method is based on the precipitation of cobalt salts in contact with the enzyme, and the subsequent observation of cobalt deposits by TEM. It could be hypothesised that the presence of proteases such as urease in the algal cell walls may be involved in the accumulation of trace metals such as Cu, Zn or Al.

This study revealed that NanoSIMS is a valuable tool in identifying subcellular compartments involved in the retention of trace elements and is of particular interest in biomonitoring studies. However, the data obtained by SIMS have only a qualitative value and must be complemented by other techniques, such as ICP-MS, to determine elemental concentrations in the sample. Such an approach, combining quantitative ion measurements with qualitative image mapping, has been recently reported for the study of Fe variations in cosmological dust particles (Dauphas and Rouxel 2006).

Chapter VI Following the phagocytosis of a metabolically labelled antigen by NanoSIMS

Manuscript in preparation: Pirrotte, P., Revets, D., Kremer, J., Fack, F., Audinot, JN., Migeon, HN., Muller, CP. Metabolic labelling using stable isotopes on NanoSIMS. Potential applications in life sciences. (Chapter VI and VII)

VI.A. Introduction

Antigen presenting cells (APCs) play a pivotal role in specific immune responses against pathogens and in the processes of self from non-self discrimination. They are found mainly in peripheral tissues, where they ingest particles, microorganisms and other antigens that are processed and presented to T cells. While non-specific internalization is based on phagocytosis, specific internalization relies on receptor-mediated uptake of antigens. Once ingested, antigens are taken up into phagosomal vesicles. These vesicles fuse with lysosomes that release enzymes resulting in the digestion of the ingested antigens in the phagosome.

Macrophages and monocytes are important agents in the defence against pathogens. Common antigens such as lipopolysaccharides (LPS) are recognized by their receptors, which target evolutionary conserved motifs (PAMP, pathogen-associated molecular patterns). At least three families of receptors are known to bind to LPS: (i) CD14, co-acting with TLR-4 or TLR-2, (ii) macrophage scavenger receptors (iii) and CD11/CD18 integrins. Therefore, the non-adherent THP-1 cell line (Tsuchiya, Yamabe et al. 1980) (ATCC TIB-202), a monoblastic cell line from a patient with acute myeloid leukaemia was chosen to investigate antigen uptake and processing. THP-1 cells closely resemble human monocytes and can be differentiated, by retinoids, 1,23-dihydroxyvitamin D or phorbol myristate acetate (PMA), to adherent macrophage-like cells expressing CD11, CD14, TLR-2 and TLR-4.

In order to follow the uptake of an antigen and visualize its intracellular processing on SIMS, the bacteria *Escherichia coli,* fully isotopically labelled with ^{15}N, was developed as a model. ^{15}N is an element with an excellent ion yield when observed as the molecular ion $^{12}C^{15}N$ on dSIMS. *E. coli* are rod-shaped (1 µm x 0.3 µm) gram-negative bacteria found in the intestinal tract of mammals as part of the enteric flora. Gram-negative bacteria contain the endotoxin and mitogen lipopolysaccharide as a major cell-wall constituent (Fenton and Golenbock 1998; Medzhitov and Janeway 2000). As a result, *E. coli* presents antigenic properties useful to the study of antigen uptake by APCs and their processing during innate or adaptive immune responses. The *E. coli* strain used in this study was susceptible to infection by M13 bacteriophages (Zacher, Stock et al. 1980).

VI.B. Materials and Methods:

VI.B.1. ^{15}N / BrdU labelling of E. coli

Bacteria were prepared for SIMS analysis by double metabolic labelling. The isotope ^{15}N was introduced into *E. coli* using a culture medium based on the M9 minimal medium

supplemented with an ^{15}N ammonium salt ($^{15}NH_4Cl$) as the only nitrogen source. Additionally, the medium was labelled with 5-bromo-2'-deoxyuridine (BrdU), a thymidine analogue which is preferentially incorporated into the double helix of DNA during its neosynthesis.

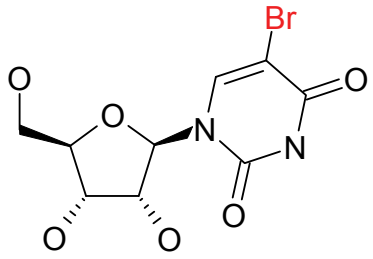

Figure 46: 5'-bromo-2-deoxyuridine (BrdU).

While BrdU induced toxic effects at high doses (above 1 µM range), at low concentrations (20 - 200 nM) the bacteria remained viable. A control colony of *E. coli* was grown in non-labelled M9 minimum medium.

Table 10: M9 minimal medium composition. For labelling purposes, $^{14}N_4HCl$ was replaced by $^{15}N_4HCl$.

Na_2HPO_4	0.2M
KH_2PO_4	0.1M
Tetracycline	20mg/L
Thiamine (vit B1)	0.5µg/L
$CaCl_2$	0.14mM
$MgSO_4 \cdot 7H_2O$	1mM
NaCl	42mM
NH_4Cl	93mM
BrdU	200nM
Glycerol	20%

To optimize the ^{15}N enrichment of the cultures, two subsequent inoculations of labelled bacteria were performed in fresh-labelled M9 medium.

VI.B.2. Fitc fluorescent labelling of E. coli

E. coli grown in non-labelled M9 minimum medium were washed twice in PBS 0.5X pH 7.2, fixed in 70% ethanol for 20 minutes and washed in 0.2 M ammonium bicarbonate buffer (pH 9.2), all steps at 4 °C. Bacteria were then incubated with light shaking for 12 hours at room

temperature and in the dark, with 250 µg of Fitc fluorochrome per 10^9 bacteria. The formulation of the incubation medium was as follows: Fitc 250 mg/L, 130 mM DMSO in 0.2 M ammonium bicarbonate buffer (pH 9.2). After fluorochrome conjugation, the bacteria were washed twice in ammonium bicarbonate buffer, once in PBS for 8 hours with light stirring and once with PBS / 2 mM EDTA. Finally, bacteria were resuspended in PBS.

VI.B.3. Assessment of the ^{15}N labelling efficiency of E. coli by MALDI-TOF mass spectrometry

Soluble proteins in the bacterial culture supernatant were concentrated by polyethylenegylcol /NaCl (PEG/NaCl) precipitation, in order to evaluate the efficiency of ^{15}N incorporation by MALDI mass spectrometry. For labelled and unlabelled cultures of *E. coli*, an adaptation of a virion purification procedure was carried out (Wickner 1975). Bacteria were centrifuged (4500 g for 10 minutes at 4°C) and resuspended in fresh medium. Cultures were supplemented to 16% of the final volume with 3.3 M PEG-NaCl (PEG-8000, Union Carbide Corporation, PA) and shaken for 8 hours at 4 °C. After 1 hour of centrifugation at 4500 g, 4°C, the supernatant was transferred to clean tubes. The supernatant was then filtered using 0.2 M ABC with a series of centrifugal steps at a 100 kDa cut-off (Millipore Amicon Centricon, Billerica, MA). The retentate was incubated with membrane lysis buffer (2 M urea, 2 M thiourea, 4% CHAPS, pH 8.5) for 30 minutes at room temperature. Proteins from the retentate were then precipitated by addition of 8 volumes of acetone for 1 hour at -20°C. After a progressive centrifugation up to 4500 g, the supernatant was discarded and the pellet was washed with 90% acetone at -20°C and centrifuged again at 4500 g for 30 minutes. The pellet was solubilised in 50 mM ABC at 4 °C. Trypsin at 25 ng/µL (Sigma-Aldrich, St. Louis, MO) and 13 µL of 50 mM ABC were added to 7 µL of sample, which was digested at 37°C for 8 hours (pH 7.8). The enzymatic activity of the trypsin was then stopped by lowering the pH to 2 by adding trifluoroacetic acid (TFA) to 1% final concentration. Finally, the sample was clarified using a reverse phase C18 column (Millipore ZipTip, Billerica, MA). Positive ion MALDI-TOF mass spectrometry was performed on the tryptic digests using a Bruker Daltonics ULTRAFLEX TOF/TOF equipped with a 337 nm, 50 Hz N_2 laser of 100 µJ. The crystal matrix, HCCA/DHB from Bruker Daltonics (Leipzig, Germany) was prepared as follows: 7 mg/mL HCCA, 1.2 mg/mL DHB in a 1:1 solution of acetonitrile and ddH_2O in 0.1% TFA. A 0.5 µL volume from each sample and matrix solutions were mixed directly on the stainless steel probe and allowed to dry (10 min). Spectra were recorded in the reflectron mode and the resulting data were analyzed using the Biotools software supplied by Bruker

Daltonics. The instrument was calibrated using a synthetic mixture of peptides solution in ddH_2O (Peptide Calibration Standard II, Bruker Daltonics, Leipzig, Germany). The HCCA/DHB matrix profits from the ionisation improvement by HCCA of low molecular weight molecules (< 2500 Da) (Cohen and Chait 1996) and by DHB of hydrophobic peptides (Kussmann, Lassing et al. 1997; Yao, Scott et al. 1998; Land and Kinsel 2001).

Liquid chromatography separation was performed on the Agilent 1100 series, equipped with a binary capillary pump and a UV cell (internal volume 80 nL, path length 6 mm). Peptides resulting from the tryptic digest were separated on a reversed phase Zorbax SB-C18 (length 15 cm, diameter 300 µm, bead diameter 5 µm, pore size 300 Å). The column was kept at 25 °C in a column heater. Samples (injected volume 2 µL) were eluted using a gradient from 5% ACN in 0.08% TFA to 95% ACN in 0.12% TFA. The flow rate was 3.5 µL/min at a collection rate of 30 s/fraction. The solvent gradient applied during the chromatography run is indicated in Figure 47. Peptides were detected at 214 nm absorbance. Aromatic cycles were detected at 280 nm absorbance.

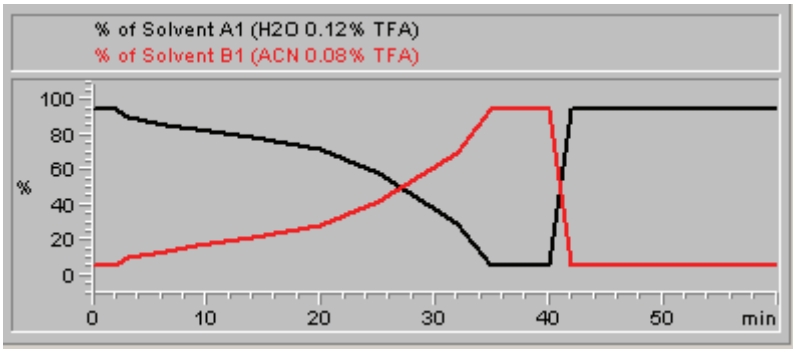

Figure 47: Solvent gradient applied to the peptide separation by HPLC.

Peptides resulting from the tryptic digestion, before and after a capillary liquid chromatography purification step, were analysed by MALDI-TOF/TOF (MS/MS). Tryptic peptides were analysed in TOF mode for protein identification and in TOF/TOF mode to estimate the isotopic labelling at peptide and amino acid levels. Eluate fractions of 2 µL were directly spotted on a MALDI target. After addition of matrix (HCCA/DHB mixture) the peptide content of the fractions was analysed by MALDI-MS/MS.

VI.B.4. Assessment of the THP-1 phagocyte function by flow cytometry

The phagocytosis of *E. coli* by the THP-1 cell line was assessed by flow cytometry. Both THP-1 differentiation to macrophages by phorbol myristate acetate (PMA) and bacteria opsonisation were investigated as ways to increase phagocytic events. Opsonins are proteins, generally antibodies or complement molecules, which bind to antigens. As both antigens and

target receptors on the phagocyte are negatively charged, coating of the antigen by opsonins decreases charge repulsion and increases the phagocytic efficiency. Furthermore, opsonised antigens may be selectively recognised by target receptors and elicit an increased expression of complement molecules by neighbouring phagocytes. In this study, undiluted human serum from a healthy donor was used as an opsonising agent.

Bacteria at $2.5x10^5$/µL were resuspended in PBS/GA (PBS, 0.5% BSA, 5.6 mM glucose at pH 7.4). THP-1 cells were differentiated for 48 hours with 100 nM PMA, collected in PBS/EDTA (PBS, 0.02% EDTA at pH 7.4) and adjusted to $1.25x10^4$ cells/µL in PBS/GA. A volume of 40 µL Sornes buffer (PBS, 0.5% BSA, 5.6 mM glucose, 0.9 mM $CaCl_2 \cdot 2H_2O$, 0.5 mM $MgSO_4 \cdot 7H_2O$ at pH 7.4) was added to 20 µL of the bacteria solution and 20 µL of human serum. The control sample without opsonins consisted of 20 µL of bacteria and 60 µL of Sornes buffer. Both samples were first incubated for 7.5 minutes at 37°C, then incubated with 20 µL of cells for another 7.5 minutes at 37°C, before adding 400 µL of ice cold PBS/EDTA. The ratio bacteria to cells was 1:20 ($5x10^6$ bacteria for $2.5x10^5$ cells). The cells were mixed with 100 µL of FACS buffer (PBS, BSA 1%, 150 mM sodium azide) and analysed on a Coulter Elite flow cytometer. Post-acquisition analysis was done using WinMDI version 2.8 (The Scripps Research Institute, La Jolla, CA).

As an additional control of phagocyte activity, $5x10^5$ THP-1 cells were incubated for 10 minutes with Fitc conjugated bacteria at a ratio of 1:20 (cell:bacteria), washed twice in PBS and fixed in 4% formaldehyde/PBS. Cells were washed twice in PBS and observed in mounting medium (90% glycerol, 1% ascorbic acid, PBS) under a Leica DMIL fluorescence microscope.

VI.B.5. Assessment of the ^{15}N labelling efficiency of E. coli by NanoSIMS. Imaging of THP-1 phagocytic activity.

THP-1 cells were grown in RPMI-1640 with Hepes (Gibco/Invitrogen, Belgium) supplemented with 2 mM L-glutamine and adjusted to contain 25 mM glucose, 1 mM sodium pyruvate, 0.05 mM 2-mercaptoethanol, 50 U/L disodic penicillin G and 10 g/L Streptomycin. To observe the induction of THP-1 cells into macrophage-like cells, these were differentiated for 48 hours with 100 nM PMA (Sigma-Aldrich, Germany). At time point t = 0, batches of 10^7 cells were incubated with metabolically labelled bacteria at a ratio of 1:20 (cell:bacteria) and harvested at t = 0, t = 15 minutes, t = 30 minutes and t = 5 hours. Cells were harvested, washed twice in PBS 1X pH 7.2, fixed in 2.5% glutaraldehyde/PBS for 8 hours at 4°C, washed again in PBS and post-fixed for 1 hour in 1% OsO_4/PBS (Fluka, Germany). After two

washes in PBS, cells were transferred into a graded series of ethanol solutions (50% ethanol for 5 minutes, 75% ethanol for 10 minutes, twice in 95% ethanol for 10 minutes, twice in 100% ethanol for 10 minutes). Subsequently, the cells were cleared twice in 100% propylene oxide (Fluka) for 15 minutes, followed by an infiltration of 2 hours in a solution of 70% propylene oxide, 30% Epon 812 epoxy resin (Fluka, Germany) and 2 hours in a solution of 30% propylene oxide, 70% epoxy resin. Infiltration in resin was conducted in 100% epoxy resin for 12 hours. After exchanging the resin with fresh embedding media, curing was performed at 200 mBar, first at 40 °C for 2 hours and then at 65 °C for 48 hours. Resin blocks were cut on a Leica UCT ultramicrotome into thin sections of 300 nm that were mounted onto steel sample holders and observed on the NanoSIMS.

VI.C. Results

VI.C.1. Assessment of the phagocyte function of THP-1 by flow cytometry

The frequency of untreated THP-1 cells that phagocyted *E. coli* was 48.1%. Interestingly, PMA treatment of THP-1 cells decreased their phagocytic activity (43.2% positive cells). Furthermore, the effect of opsonins on PMA stimulated cells did not improve their phagocytic activity compared to unstimulated cells (47% positive cells), while opsonin treatment without PMA stimulation elicited an increase of 15% of phagocyting THP-1 cells (63.7% positive cells*)* (

Table **11**, Figure 48).The high phagocytic activity of untreated THP-1 was deemed sufficient for imaging and motivated the choice neither to stimulate THP-1 cells with PMA nor to opsonise bacteria in further experiments.

Table 11: Phagocyte function of THP-1 cells by flow cytometry.

Sample	% positive
THP negative control	0
THP Bact~Fitc	48.1
THP Bact~Fitc PMA	43.2
THP Bact~Fitc PMA opsonin	47
THP Bact~Fitc opsonin	63.7

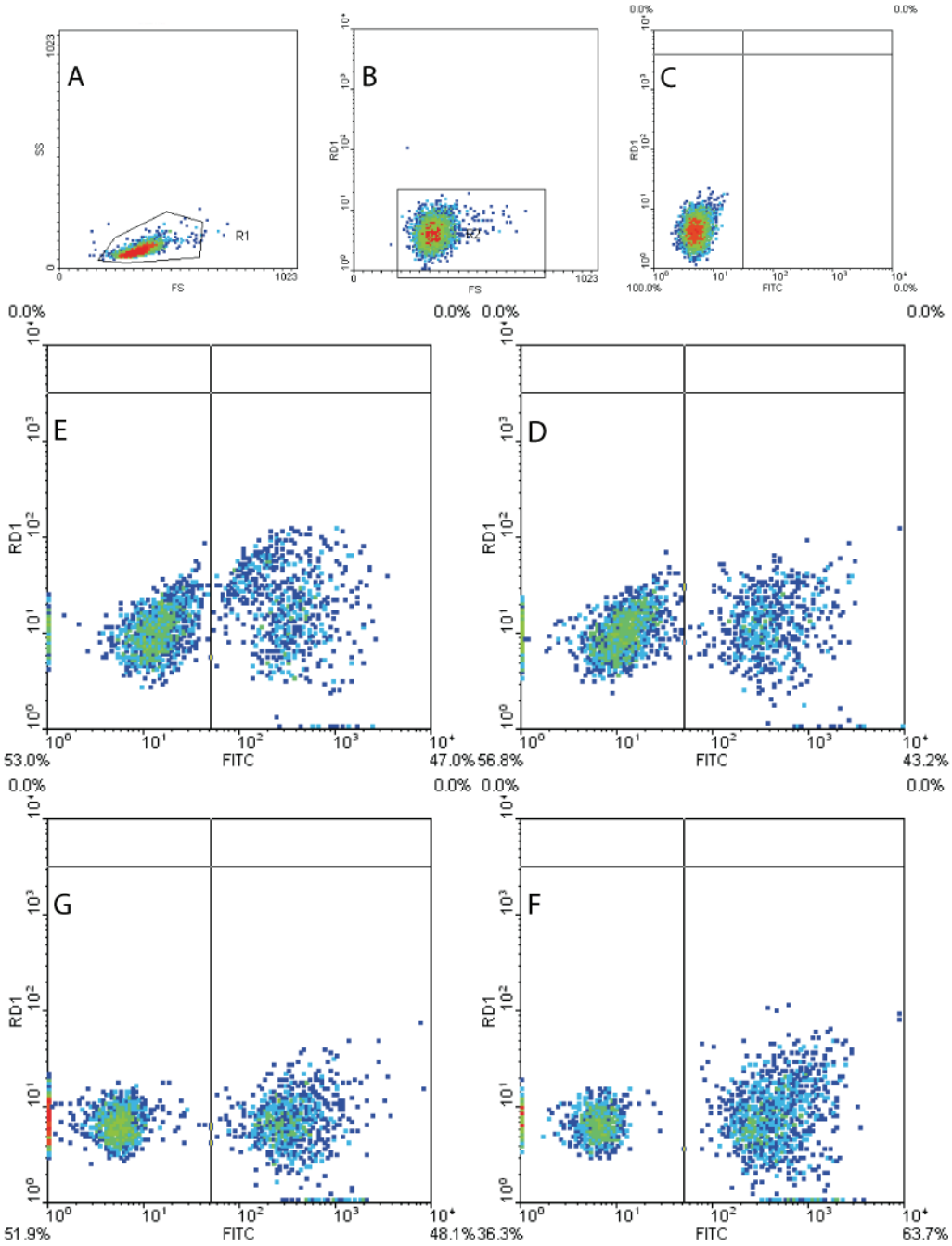

Figure 48: Flow cytometry assay of the phagocytic activity of THP-1. *(A) gating forward scatter versus sideward scatter, (B) gating forward scatter versus RD1 (C) gating Fitc versus RD1, (D) THP Bact~Fitc, (E) THP Bact~Fitc PMA, (F) THP Bact~Fitc, PMA opsonin, (G) THP Bact~Fitc opsonin.*

The observation on the fluorescence microscope of formaldehyde fixed cells further confirms that approximately half of the THP-1 cells phagocyted the fluorescently labelled *E. coli* (Figure 49).

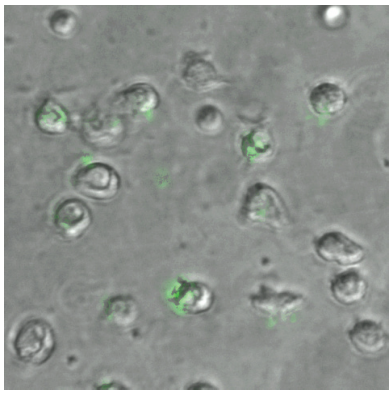

Figure 49: Uptake of Fitc conjugated *E. coli* by THP-1 cells.

VI.C.2. Assessment of the ^{15}N labelling efficiency of E. coli by MALDI-TOF mass spectrometry

In order to determine the incorporation of the stable nitrogen isotope ^{15}N, a soluble protein found in the culture supernatant had to be identified. While the mass profile of a tryptic digest did not yield any PMF that allowed for unambiguous protein identification, several intense mass peaks hinted to the presence of one or more abundant proteins (Figure 50).

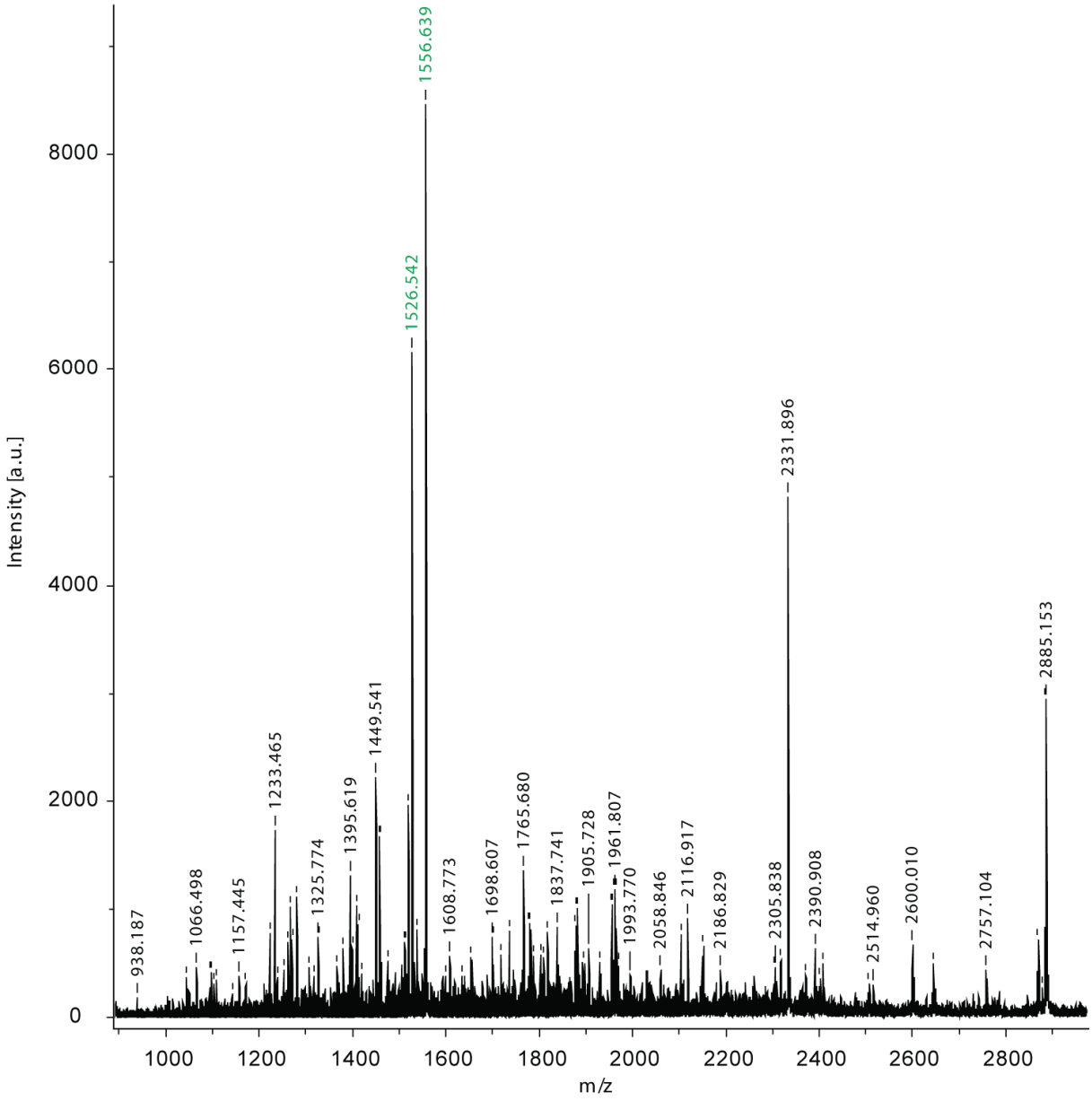

Figure 50: Tryptic peptides of a precipitated non-labelled protein fraction analysed by MALDI-TOF. *The abundant ion species of mass 1526 and 1556 were selected for MS/MS analysis (in green).*

Peptides in the non-labelled sample corresponding to mass 1526 and mass 1556, hereafter mentioned as peptide 1 and peptide 2 respectively, were further characterised in a post-source decay spectrum of their metastable daughter ions to yield sequence information of the parent

peptides. Peptides 1 and 2 corresponded to the bacterial protein periplasmic dipeptide transport protein precursor (Accession Nr: NP_756223). Figure 51 shows the MS/MS analysis of peptide 1 from the non-labelled sample.

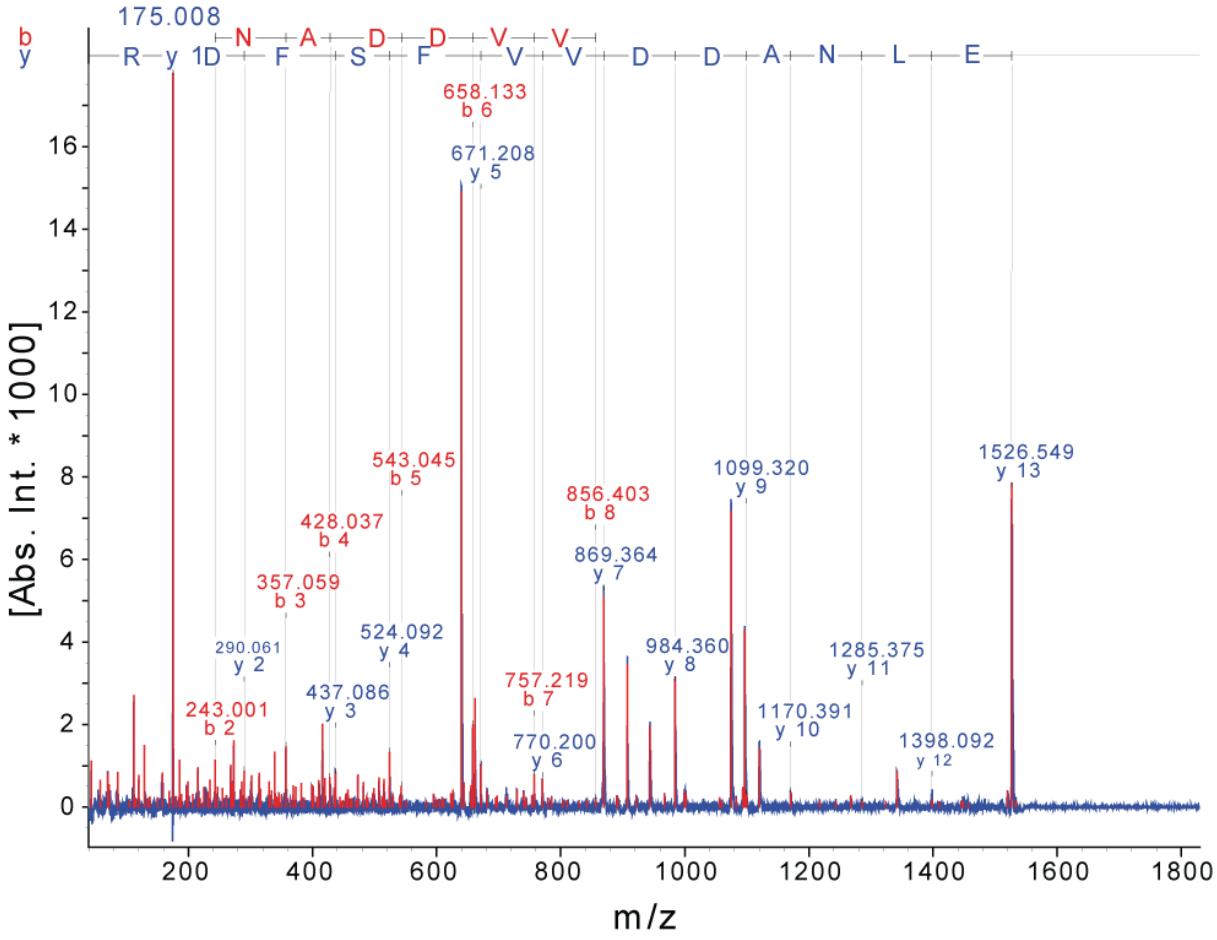

	E	L	N	A	D	D	V	V	F	S	F	D	R	Glu	Leu	Asn	Ala	Asp	Asp	Val	Val	Phe	Ser	Phe	Asp	Arg
Ion	1	2	3	4	5	6	7	8	9	10	11	12	13	1	2	3	4	5	6	7	8	9	10	11	12	13
a	E	L	N	A	D	D	V	V	F	S	F	D	R	102.055	215.139	329.182	400.219	515.246	630.273	729.341	828.410	975.478	1062.510	1209.579	1324.606	1480.707
b	E	L	N	A	D	D	V	V	F	S	F	D	R	130.050	243.134	357.177	428.214	543.241	658.268	757.336	856.405	1003.473	1090.505	1237.574	1352.600	1508.702
y	E	L	N	A	D	D	V	V	F	S	F	D	R	175.118	290.145	437.214	524.246	671.314	770.383	869.451	984.478	1099.505	1170.542	1284.585	1397.669	1526.712

Figure 51: MS/MS analysis of peptide 1 derived from ^{14}N proteins. *Identification of the sequence of peptide 1 by MALDI-TOF/TOF analysis. A complete "y" ion series could be observed for this peptide, partially confirmed by the detection of "b" and "a" ions.*

The ^{15}N incorporation in peptide 1 and peptide 2 could be observed in the PMF of the tryptic digestions derived from labelled and non-labelled cultures (Figure 52). The mass spectra of the ^{14}N and ^{15}N samples showed that peptide 1 with a molecular weight (MW) of 1526 is nearly absent in the ^{15}N spectrum, whereas a peptide with a MW of 1543 appears. The peptide 2 with a MW of 1556 in the ^{14}N spectrum seems to be replaced by a peptide of a MW of 1573 in the ^{15}N spectrum. Thus, the peptide MS spectra appeared to be shifted by 17 m/z units in the ^{15}N spectrum compared to the non-labelled sample.

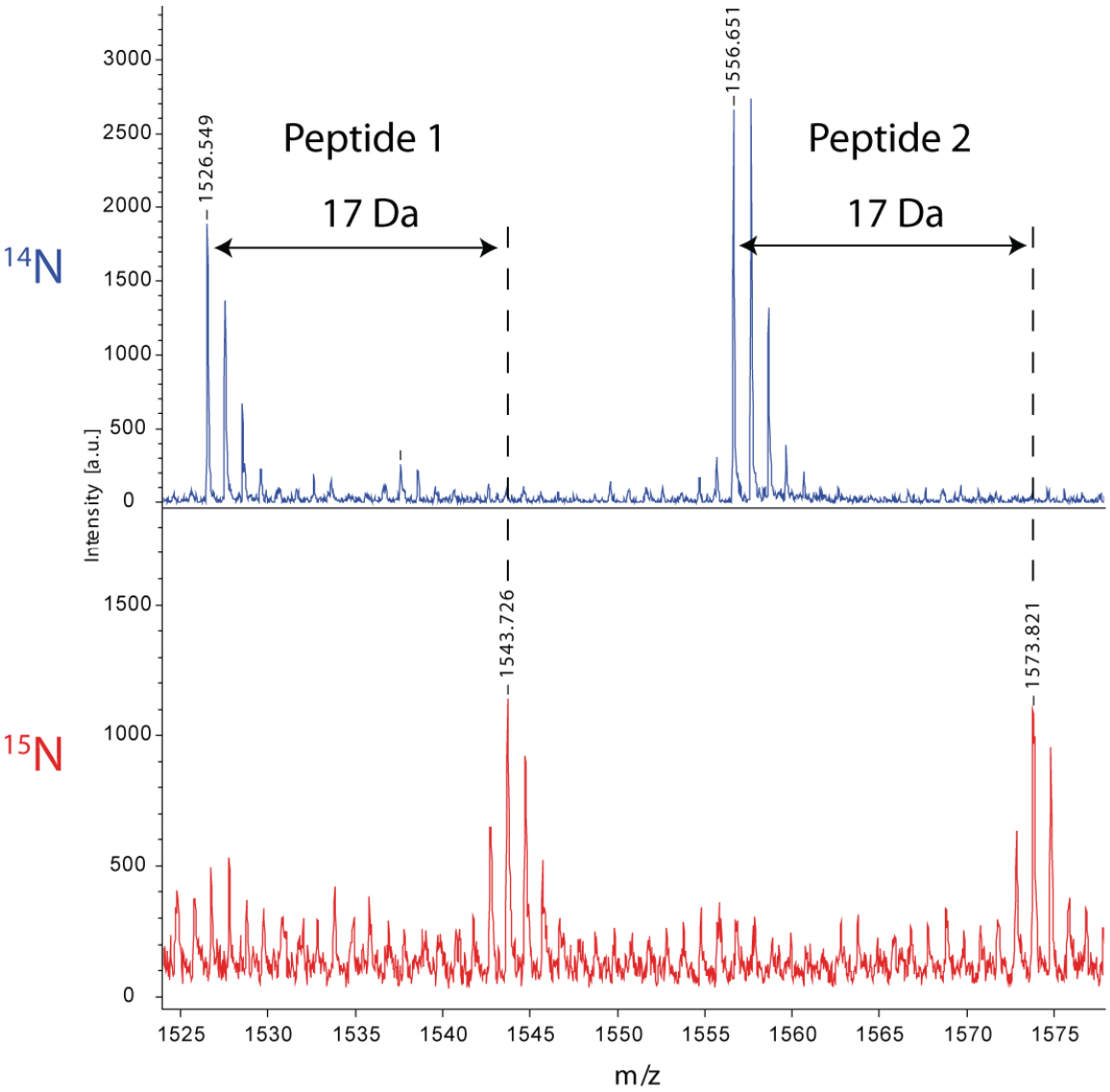

Figure 52: MALDI TOF spectra of tryptic peptides 1 and 2, derived from ^{14}N and ^{15}N cultures. *Tryptic peptides were spotted in HCCA/DHB matrix and analysed in reflectron mode. Peptides 1 and 2 identified in the ^{14}N spectra and peptides are shifted by 17 mass units (isotopic peaks shaded black) in the proteins derived from the ^{15}N culture.*

To confirm that the mass-shifted peptides corresponded to peptide 1 and 2 differing only by ^{15}N, a mix of the tryptic digests from the labelled and non-labelled cultures were separated by reverse phase chromatography. The chromatography fractions revealed clearly resolved peptide peaks (Figure 53).

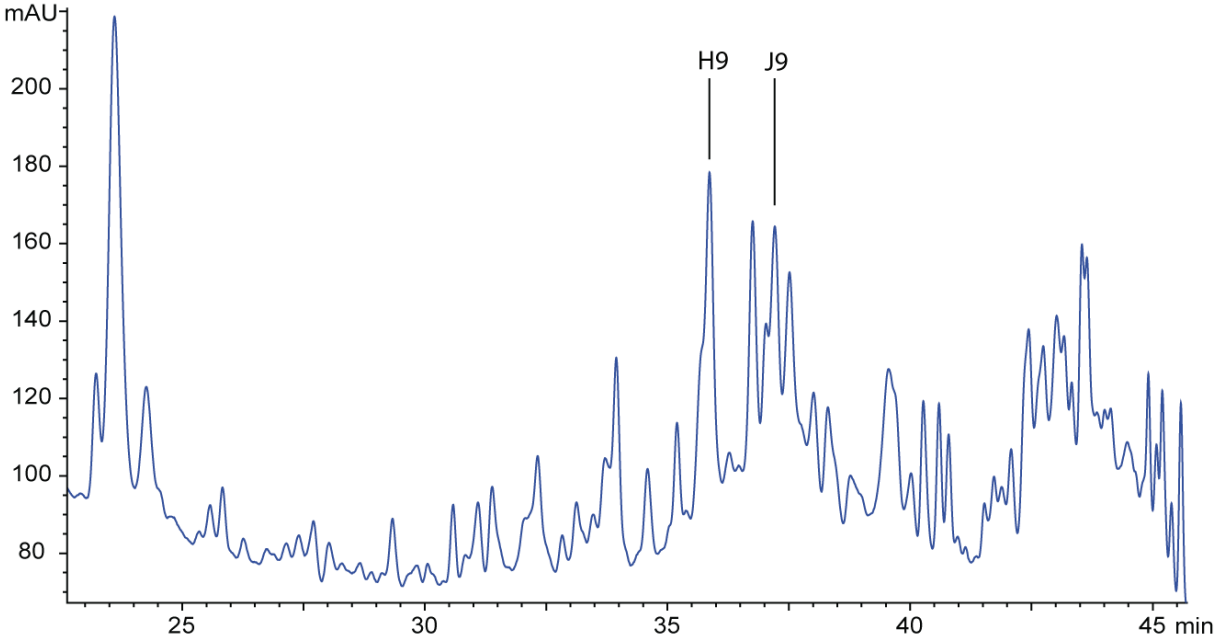

Figure 53: Chromatographic fractionation at 214 nm absorbance of tryptic peptides derived from ^{14}N and ^{15}N labelled proteins. *A mix of tryptic peptides derived from ^{14}N and ^{15}N proteins was separated by reverse chromatography on a capillary column (Zorbax C18, 300 µm diameter, 150 mm). The eluate was fractionated (2 µl) and directly spotted on a MALDI target for mass spectrometric identification of the peptides. Fractions containing the co-eluted peptides of interest are indicated as H9 and J9.*

During the MALDI-TOF analysis of the resulting fractions, fraction H9 was found to contain two co-eluted peptides of masses 1526 and 1543. The fraction J9 contained two co-eluted peptides of mass 1556 and 1573. The co-elution of these masses showed that the physicochemical properties of the corresponding peptides are identical in reverse phase chromatography, and differ only by the amount of ^{15}N. In other words, H9 corresponds to peptide 1 and J9 to peptide 2.

The MS/MS analysis of both low and high molecular weight peptides confirmed that they had identical sequences. The results of the LC-MALDI-MS/MS analysis of the co-eluted peptides, summarized in Table 12, demonstrate that the observed mass shift of 17 Da is due to the incorporation of ^{15}N in all the positions of the backbone and side chains of the two peptides.

Table 12: Amino acid sequences of peptide 1 and peptide 2. *Mass differences (ΔM) of labelled and non-labelled peptides.*

Peptide	AA sequence	Mass (^{14}N)	Mass (^{15}N)	ΔM (^{15}N - ^{14}N)	Elementary composition	HPLC fraction
1	ELNADDVVFSFDR	1526	1543	17	$C_{67}N_{17}O_{24}H_{99}$	H9
2	IVTYEWGEYLKR	1556	1573	17	$C_{74}N_{17}O_{20}H_{109}$	J9

The sequence of the peptides combined with the "y" ion spectrum allowed to evaluate the ^{15}N labelling at the amino acid level. The C-terminal arginine (R) was observed as a strong y1 ion in the MS/MS spectrum of the non-labelled sample used for sequence identification, whilst in the ^{15}N-labelled sample, the incorporation of four ^{15}N atoms increased the mass by 4 mass units corresponding to a fully labelled arginine (Figure 54).

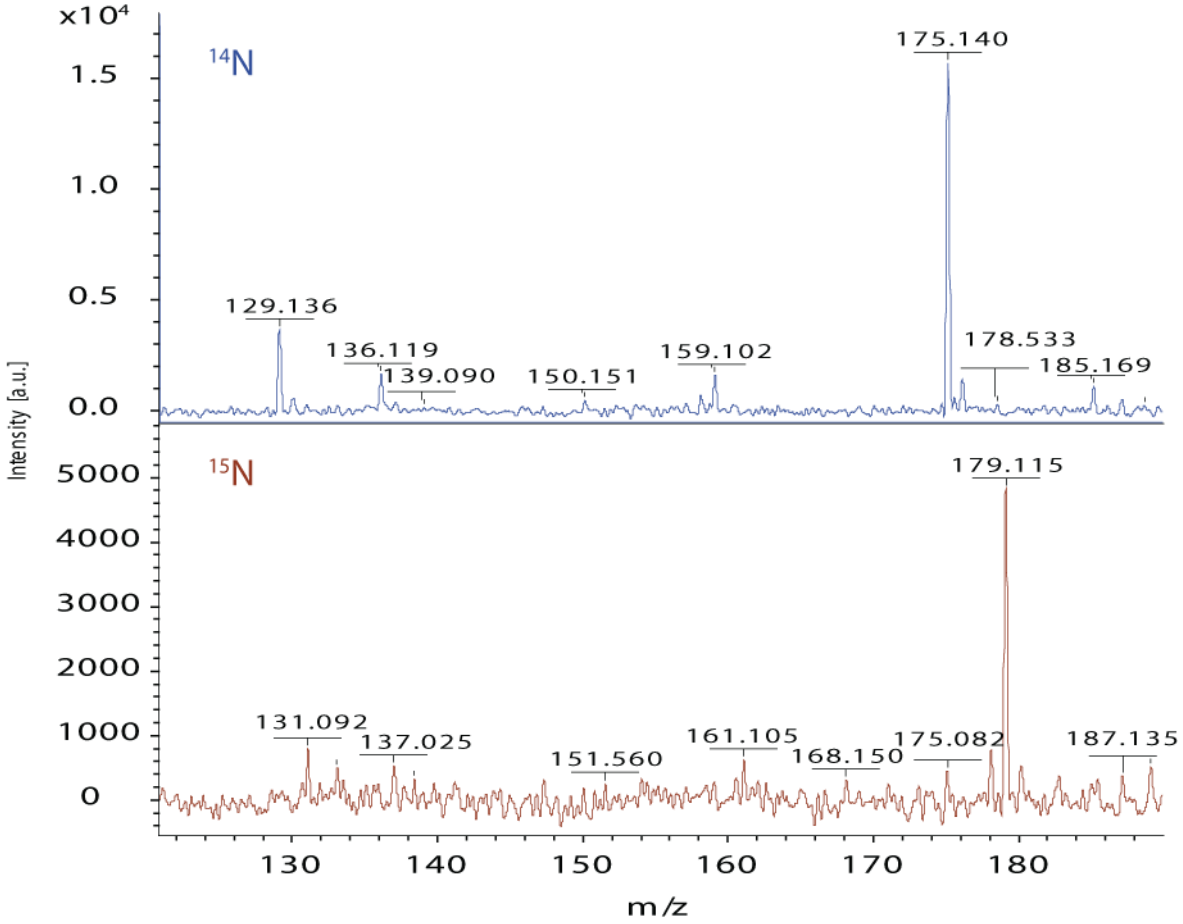

Figure 54: Isotopic labelling of arginine. *The comparison of the MS/MS spectra of the ^{14}N (upper panel) and ^{15}N sample (lower panel) shows that the y1 ion, which is observed under normal growth conditions (m/z 175) is only present at trace level after metabolic labelling. In the sample derived from the $_{15}N$ medium, the four nitrogen atoms of arginine were replaced by the heavy isotope, yielding an y1 ion of m/z 179.*

VI.C.3. Assessment of the ^{15}N labelling efficiency of E. coli by NanoSIMS. Imaging of THP-1 phagocytic activity.

Determination of the labelling efficiency of E. coli by NanoSIMS

Bacteria labelled with ^{15}N / BrdU were observed as the secondary ions $^{12}C^{15}N$ and ^{79}Br by NanoSIMS (Figure 55). BrdU signals were generally low (60-70 counts). Figure 55A and Figure 55B were acquired simultaneously, followed by Figure 55C and Figure 55D. This led to a change in sample depth because of sputtering, which may explain the increase of ^{79}Br

signal in Figure 55D compared to Figure 55B. Figure 55D shows deeper layers of the bacteria where, in this case, potentially more DNA is located.

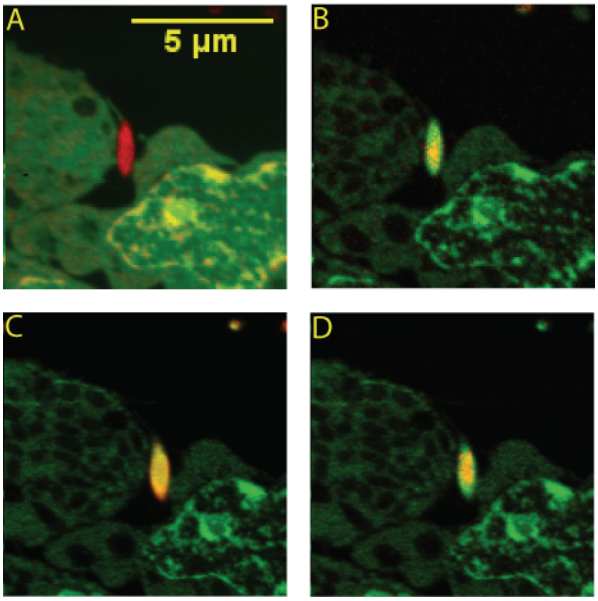

Figure 55: ^{15}N bacteria mixed in a 1:20 ratio with THP-1, observed on SIMS. *(A) ^{31}P in red, $^{12}C^{14}N^-$ in green; (B) $^{12}C^{14}N^-$ in green, $^{79}Br^-$ in yellow; (C) $^{12}C^{15}N^-$ in yellow, ^{31}P in green; (D) $^{79}Br^-$ in yellow, ^{31}P in green. Cs^+ impact energy 16 keV, primary current 39.6 nA, 128 pixels x 128 pixels, 20 ms/pixel.*

By calculating the ratio $^{12}C^{15}N^-$ / $^{12}C^{14}N^-$ for a given sample surface, a mean of ^{15}N incorporation by the bacteria was obtained. In order to do this, we measured the $^{12}C^{14}N^-$ and $^{12}C^{15}N^-$ ions for labelled bacteria ingested by THP-1. Using the NIH ImageJ image-processing toolbox, regions of interests (ROI) of 10 pixels x 10 pixels (0.22 μm^2) were defined for the two ion types as seen in Figure 56 that shows a THP-1 cell phagocyting at t = 0 minutes.

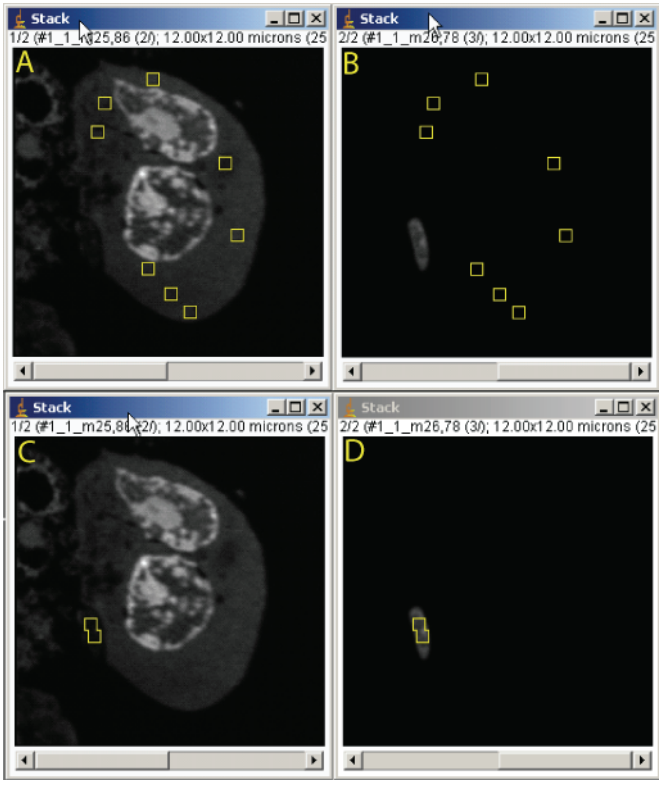

Figure 56: Ingestion of a ^{15}N labelled *E. coli* by THP-1 (t = 5 minutes). *Selected ROIs in yellow, 10 pixels x 10 pixels, 0.22 µm^2. (A) $^{12}C^{14}N^-$ ion distribution map, ROIs in the cytoplasm; (B) $^{12}C^{15}N^-$ ion distribution map, ROIs in the cytoplasm; (C) $^{12}C^{14}N^-$ ion distribution map, ROIs in the bacteria; (D) $^{12}C^{15}N^-$ ion distribution map, ROIs in the bacteria.*

Table 3 shows the mean counts of ^{14}N and ^{15}N, integrated on the surface of the ROIs of the cell cytoplasm or of the labelled bacteria. In the cell the percentage of ^{15}N was 0.4%, which roughly corresponds to the natural isotopic distribution of 0.37%. In the labelled bacteria, the percentage was 77.2%, which amounts to almost 200 fold enrichment of ^{15}N compared to the natural abundance of this isotope. This enrichment was obtained after two subsequent inoculations of bacteria in ^{15}N enriched media.

Table 13: $^{15}N/^{14}N$ ratio for ROIs defining cells and bacteria.

	Mean ^{14}N	**Mean ^{15}N**	**%^{14}N**	**% ^{15}N**
Cell	331.4	1.392	99.58172	0.418279
Bacteria	154.825	524.54	22.78966	77.21034

Imaging of E. coli uptake and processing by NanoSIMS.

PMA induced differentiation of THP-1 cells to macrophage-like cells is shown in Figure 46. After 48 hours, the typically round cytoskeleton of monocytes rearranged to an irregular digitated shape. Incorporated bacteria after 15 minutes of incubation are shown in red.

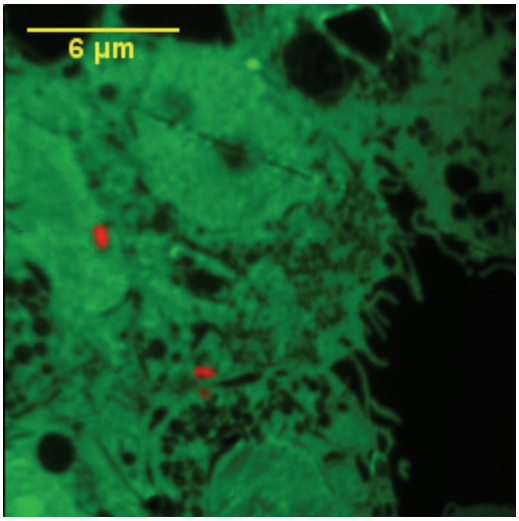

Figure 57: NanoSIMS ion micrograph of PMA induced THP-1. *Macrophage-like THP-1 cells changed shape ($^{12}C^{14}N$, green). They incorporated several bacteria ($^{12}C^{15}N$, red). Cs^+ impact energy 16keV, primary current 39.6 nA, 128 pixels x 128 pixels, 20 ms/pixel.*

Figure 58 shows the different stages of uptake and processing of ^{15}N labelled bacteria by non-differentiated THP-1 cells. In late phases of ingestion, protein turnover can be followed through the conversion of the isotopic measurements of $^{12}C^{14}N^-$ (e.g. Figure 58E) and $^{12}C^{15}N^-$ (e.g. Figure 58G) into the isotopic ratio $^{12}C^{15}N^-$ / $^{12}C^{14}N^-$ in HSI colour space, which provided the possibility to enhance high $^{12}C^{15}N^-$ counts from the label, while reducing low $^{12}C^{15}N^-$ counts due to background (e.g. Figure 58H) using the software developed in chapter II.

Labelled bacteria were only present on the membrane of cells fixed immediately after the inoculation, as it can be observed in Figure 58A (t = 0 minutes). The formation of cytoplasmic extensions (in green, above and below the bacteria) to engulf the targeted bacteria (in red) are visible. The HSI ratio image in Figure 58B shows the incorporation of several bacteria at an early stage of the phagocytosis (t = 15 minutes). While not very contrasted, the nucleus and the nucleolus can be distinguished. The large ^{15}N rich regions possess an intensely labelled centre and a gradient distribution around the edges. Aside from these ^{15}N rich regions, the cytoplasm of the cell presents a low homogenous distribution of ^{15}N corresponding to the natural abundance of ^{15}N. While a similar gradient distribution can also be observed 30 minutes after the inoculation (Figure 58C), several hypersignals of ^{15}N can be observed throughout the cytoplasm and inside the nucleus. Using the $^{31}P^-$ ion distribution the nucleus

can be identified by its large and dense structure in the overlay image, Figure 58D (in blue). In the same image, the chromatin can be observed inside the nucleus as small structures of highly concentrated $^{31}P^-$. Five hours after the inoculation, the overall protein turnover was measured in the cytoplasm where the $^{12}C^{15}N/^{12}C^{14}N$ ratio was 1%, which corresponds to a 2.5X increase of incorporated ^{15}N, caused by a high accumulation of newly synthesized proteins. In the nucleus, the protein turnover assessed by the $^{12}C^{15}N/^{12}C^{14}N$ ratio was 6%. Figure 58E and Figure 58F show the $^{12}C^{14}N$ and the $^{12}C^{14}N$ ion micrograph, respectively. Interestingly, in Figure 58G, several regions of the cytoplasm, notably above the nucleus, were devoid of ^{15}N.

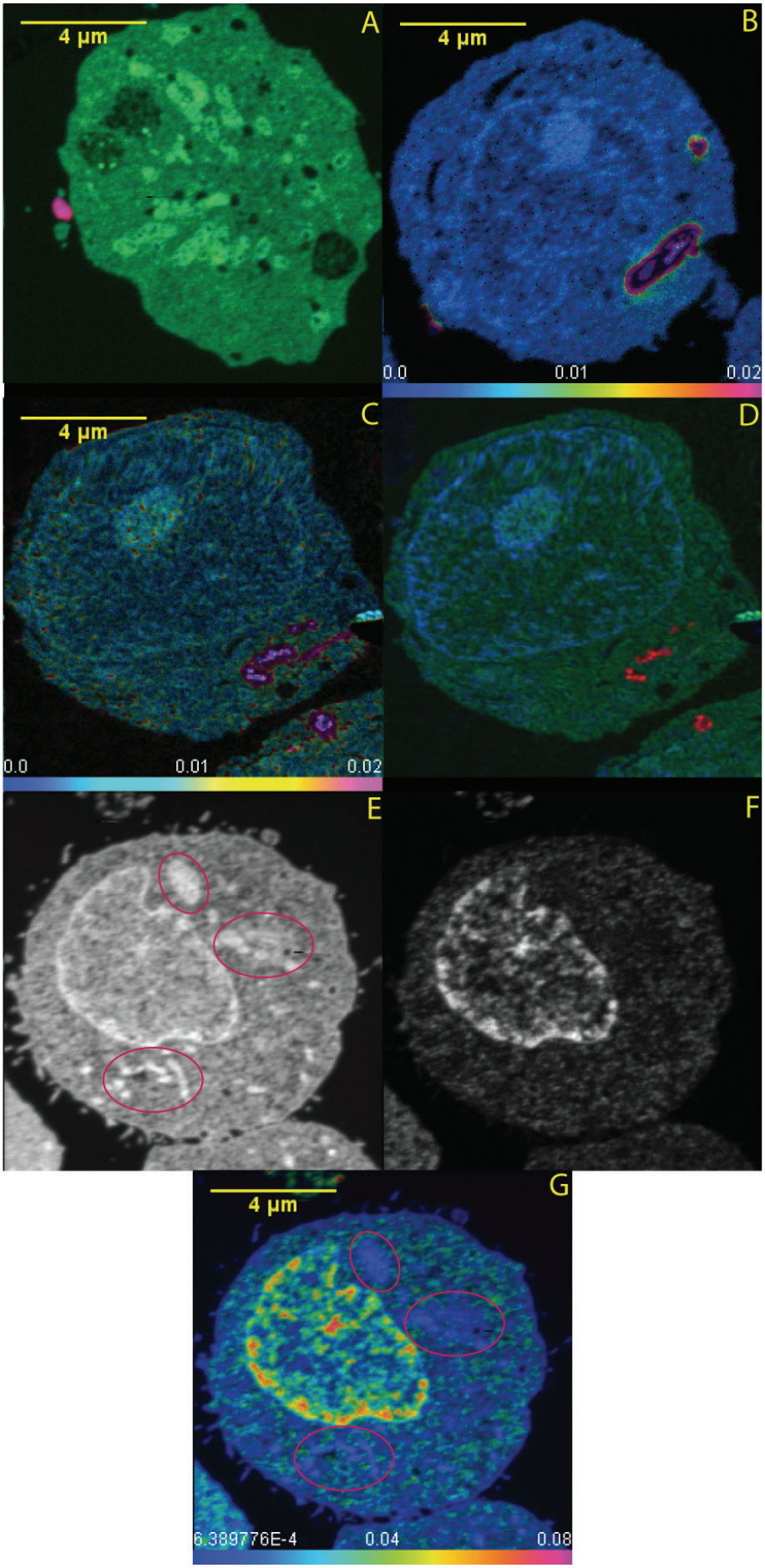
A
4 µm
B
4 µm
0.0
0.01
0.02
C
4 µm
0.0
0.01
0.02
D
E
F
G
4 µm
6.389776E-4
0.04
0.08

Figure 58: NanoSIMS ion micrograph of protein turnover, resulting from ingestion of ^{15}N labelled bacteria by non-differentiated THP-1 cells. *(A) t = 0 minutes (61.4 nA, 40 ms/pixel). Overlay with $^{12}C^{14}N$ in green and $^{12}C^{15}N$ in red (46.1 nA, 40 ms/pixel). (B) t = 15 minutes. HSI ratio $^{12}C^{15}N/^{12}C^{14}N$. (C) t = 30 minutes (37.1 nA, L1 = 6714 V, 40 ms/pixel). HSI ratio $^{12}C^{15}N$ / $^{12}C^{14}N$. (D) t = 30 minutes. Overlay with $^{12}C^{14}N$ in green, $^{12}C^{15}N$ in red and ^{31}P in blue. (E, F, G) t = 5 hours (58.2 nA, 40 ms/pixel); (E) $^{12}C^{14}N$ ion distribution (F) $^{12}C^{15}N$ ion distribution (G) t = 5 hours. HSI ratio $^{12}C^{15}N$ / $^{12}C^{14}N$. The ratio $^{12}C^{15}N$ / $^{12}C^{14}N$ is above 1% in the cytoplasm. In the nucleus hypersignals with a $^{12}C^{15}N$ / $^{12}C^{14}N$ ratio above 6% correspond to the sites of protein assembly.*

VI.D. Discussion

Both MALDI-TOF and SIMS analysis have shown that the ^{15}N metabolic labelling of bacteria using a ^{15}N enriched minimal medium was highly efficient. Both methods complemented each other by introducing two separate notions of labelling efficiency that allowed a quality control of the antigen labelling. The MALDI-TOF allowed to monitor the incorporation of the label at the amino acid level, for a particular peptide sequence, and to determine the number of nitrogen atoms that were replaced by the stable isotope. To reduce the risk of observing a biased incorporation of ^{15}N that occurs in protein with a low turnover, the ubiquitous, highly expressed dipeptide binding protein (DBP) was chosen as a model to study the labelling of *E. coli*. However, the MALDI-TOF analysis only revealed the ^{15}N incorporation in two tryptic peptides from the DBP, while NanoSIMS ratiometric imaging of bacteria, prior to ingestion and degradation, informed on the general labelling efficiency. The metabolic ^{15}N labelling was by nature not restricted to proteins and peptides alone, as the use of $^{15}NH_4Cl$ as a nitrogen source in the medium indiscriminately labelled all the nitrogen constituents of the bacteria, such as lipids, DNA, and glycocalyx.

It is generally known that antigens processed inside phagolysosomes result from the fusion of phagosomes with lysosomal vesicles (see extensive review Ramachandra, Chu et al. 1999). In our study, the antigen model *E. coli* was progressively processed by round structures that most certainly correspond to phagosomal vesicles (Figure 58). Products, such as amino acid and lipids, resulting from the antigen digestion by enzymes and toxic peroxides have the possibility to diffuse, which explains the ^{15}N gradient as is illustrated in Figure 58B and Figure 58C.

To increase the probability of observing phagocytosis in a field of view of a 40 µm x 40 µm NanoSIMS image, the inoculation ratio cell:bacteria was 1:20. The phagocytosis monitored by flow cytometry showed that after 7.5 minutes approximately 50% of THP-1 cells had phagocyted at least one bacteria. After 15 minutes, more than one bacterium was ingested by the cell was shown in Figure 58B. This phenomenon was emphasized over 5 hours and

explains the multitude of highly intense ^{15}N regions. Repeated inoculations over longer periods seem to cause strong accumulation of newly synthesized material in the nucleus, especially around the nuclear membrane and in the nucleolus.

The aim of this study was to verify the usability of NanoSIMS to follow the uptake and processing of antigens and to identify organelles involved in the phagocytosis, by the novel method of stable isotope labelling. However, it became clear that this type of studies needed to be complemented by TEM observations, to unequivocally identify, on the same resin sections, the organelles implicated in the processing of the antigens and to recognize e.g. the structure characterised by a low protein turnover above the nucleus as shown in Figure 58G.

The successful use of a labelled nitrogen source in a minimal culture medium, to induce total labelling of cellular content, makes it a viable approach in future studies and it is further developed in Chapter VII for the labelling of peptides.

Chapter VII Metabolic pulse labelling and immunolabelling in a viral study using NanoSIMS

Manuscript in preparation: Pirrotte, P., Revets, D., Kremer, J., Fack, F., Audinot, JN., Migeon, HN., Muller, CP. Metabolic labelling using stable isotopes on NanoSIMS. Potential applications in life sciences. (Chapter VI and VII)

VII.A. Introduction

Human MxA protein belongs to the dynamin-like GTPases (Staeheli, Pitossi et al. 1993) and plays an important role in transport processes, such as endocytosis (Urrutia, Henley et al. 1997) and intracellular vesicle transport (Rothman, Raymond et al. 1990). It presents an antiviral activity against a variety of RNA viruses: orthomyxoviruses (Pavlovic, Haller et al. 1992; Frese, Kochs et al. 1995; Pavlovic, Arzet et al. 1995) ; rhabdoviruses (Pavlovic, Zurcher et al. 1990) ; paramyxoviruses (Schnorr, Schneider-Schaulies et al. 1993; Schneider-Schaulies, Schneider-Schaulies et al. 1994; Zhao, De et al. 1996) ; and bunyaviruses (Frese, Kochs et al. 1996; Kanerva, Melen et al. 1996).

MxA protein is induced exclusively by type I (α / γ / β) interferons (Simon, Fah et al. 1991) and has been shown to accumulate in the cytoplasm of cells (Staeheli, Dreiding et al. 1985; Aebi, Fah et al. 1989). While the precise mechanism resulting in the antiviral activity of MxA is unknown, aggregation of MxA with viral nucleoproteins (NP) followed by sequestration in organelles (endoplasmic reticulum, golgi) or in perinuclear complexes has been reported for various viruses (Kochs and Haller 1999; Kochs, Janzen et al. 2002). The progressive formation of MxA / NP aggregates results from recruitment of both MxA and NP from the available cellular protein pool and is probably responsible for a depletion of unbound NP. As free NP becomes unavailable, viral capsid formation is inhibited resulting in the antiviral effect described above.

In order to study the putative formation of MxA / NP complexes in measles virus infected THP-1 cells by NanoSIMS and confocal microscopy, several sets of experiments were devised. The ability of NanoSIMS to discern minute variations in the relative abundance of the natural isotope ^{15}N was investigated, using a method based on metabolic pulse labelling with fully ^{15}N labelled lysine. Using the same amino acid, a labelled antibody against viral NP was produced. The incorporation of ^{15}N was characterized by MALDI-TOF analysis and an immunolabelling experiment for NanoSIMS was developed.

VII.B. Materials and Methods

VII.B.1. Timeline of a MV infection

A time pointhad to be determined where the majority of THP-1 cells were alive, and infected, and the MxA expression was notably increased. Therefore, a flow cytometry assay was devised to measure viral Hemagglutinin (H) expressed on the cellular membrane of infected

cells. In the same experiment, cell viability was determined with propidium iodide staining (Sigma-Aldrich, Germany). Furthermore, MxA expression was quantified by RT-PCR.

B.1.1. Flow cytometry assay

THP-1 cells were cultured in RPMI-1640 with Hepes (Gibco/Invitrogen, Belgium) supplemented with 2 mM L-glutamine and adjusted to contain, 25 mM glucose, 1 mM sodium pyruvate, 0.05 mM 2-mercaptoethanol, 50 U/L disodic penicillin G and 10 g/L streptomycin (Cambrex, Belgium). 10^6 cells were inoculated with MV (Schwarz vaccine strain) at a multiplicity of infection (MOI) of 1. A second sample, with the same amount of cells, was mock inoculated with Vero slam supernatant. At several time points (t = 1, 3, 6, 12, 18, 24, 36, 48, 60, 72 and 96 hours), cells were collected, pelleted and washed in FACS buffer (PBS, 1% BSA, 0.1% sodium azide). Cells were than split into two samples of MV infected (tube 1 and 2) and two samples of mock infected (tube 3 and 4), each sample being resuspended in 100 µL of FACS medium. To one tube of each sample type (tube 2 and 4), 1 µL of anti-MV negative human serum was added, mixed thoroughly, and the samples incubated for 15 minutes at 4°C. A monoclonal antibody anti-H conjugated to Fitc was added to the solution, which was further incubated for 15 minutes at 4°C. Cells were washed in FACS medium, resuspended in FACS fixation medium (25 µg/mL propidium iodide, 1% formaldehyde/PBS) and analysed on a Coulter Epics Elite flow cytometer.

B.1.2. mRNA quantification

RNA extraction

Total RNA was extracted from $5x10^5$ infected and non-infected THP-1 cells, using a commercial RNA purification kit (RNeasy Mini Kit, Qiagen, Germany). In summary, the cells were first lysed and homogenized in the presence of a highly denaturing guanidine-thiocyanate–containing buffer. Ethanol was added to the cell lysate, to provide appropriate conditions for the binding of RNA on a silica-based membrane, which is integrated in the RNeasy Mini spin columns. Contaminating DNA was digested on the column with DNase I (30 Kunitz units per sample). Other contaminants were washed out using two buffers supplied in the purification kit. The RNA was then eluted in 60 µl of ddH_2O.

Reverse transcription

The extracted RNA was reverse transcribed to obtain cDNA of all mRNAs expressed in the infected and non-infected cells. Therefore, 5 µl of purified RNA were mixed with 5 µl (50 ng/µl) of oligonucleotides (Random Primers, Invitrogen, Bertrange), 1 µl of 10 mM dNTP

mix (Invitrogen) and 1 µl of sterile distilled water. After 5 min incubation at 65°C, this first mix was chilled on ice. A second mix, including 4 µl of 5x First strand buffer (Invitrogen), 1 µl 0.1 M DTT (Invitrogen, Belgium), 1 µl (40 U/µl) of an RNase Inhibitor (RNAse OUT, Invitrogen), 1 µl (200 U/µl) of Reverse Transcriptase (Superscript III, Invitrogen) and 1 µl of sterile distilled water, was then added to the first mix. Reverse transcription was performed for 5 min at 25°C, followed by 80 min at 50°C.

Quantitative PCR

MxA mRNA expression was quantified using a commercial TaqMan Gene expression assay (Applied Biosystems, USA) and the universal FastPCR mastermix (Applied Biosystems, USA).

MV NP mRNA expression was quantified using an in-house TaqMan® assay. Therefore, the corresponding primers (MVN sense 5'-CCCTGAGGGATTCAACATGATTCT-3'; MVN antisense 5'-ATCCACCTTCTTAGCTCCGAATC-3') and TaqMan probe (Fam-5'-TCTTGCTCGCAAAGGCGGTTACGG-3'-BHQ1) were added to the universal FastPCR mastermix. The cycling conditions for both MxA and MV NP PCR were as follows: 20 s at 95°C followed by 40 cycles of 95°C for 3 s and 60°C for 30 s. Two housekeeping genes, beta-actin and GAPDH, were quantified using SYBR Green assays. Therefore 1 µl of cDNA was mixed with 14.65 µl of sterile distilled water, 2.5 µl of a 10x PCR buffer (Invitrogen), 1 µl of 50 mM $MgCl_2$ solution (Invitrogen), 0.5 µl of 10 mM dNTP mix, 0.25 µl of 100x SYBR Green solution (Clare Chemical Research), 0.1 µl (5 U/µl) of Taq Polymerase (Platinum Taq, Invitrogen) and 0.5 µl (50 µM) of both sense (beta actin: 5'-GGCCACGGCTGCTTC-3'; GAPDH: 5'-GAAGGTGAAGGTCGGAGTC-3') and antisense (beta actin: 5'-GTTGGCGTACAGGTCTTTGC-3'; GAPDH: 5'-GAAGATGGTGATGGGATTTC-3) primers (Eurogentec). The cycling PCR conditions were as follows: 1 min 30 s at 95°C followed by 35 cycles of 95°C for 30 s, 60°C for 1 min and 72°C for 1 min. The relative amount of MxA mRNA at different timepoints, following the infection was determined using the delta-delta Ct method (Fink, Seeger et al. 1998).

VII.B.2. Immunofluorescence assay

Teflon coated multiwell glass slides (MP Biomedicals, France) were cleaned with ethanol/ether (v/v) and film coated with 4 µL/well of poly-L-Lysine at 0.01% (mol. wt. > 300 kDa). In each well, $5x10^4$ cells are deposited and let to attach for 20 minutes at room temperature. The excess medium was washed three times in PBS, followed by a fixation step in 3% formaldehyde/PBS for 20 minutes. After three consecutive washes in PBS, the

remaining free aldehyde was quenched with 50 mM NH_4Cl/PBS for 10 minutes. The samples were washed again three times in PBS and cells were permeated with a 0.1 % Triton X-100 (polyethylene glycol p-(1,1,3,3-tetramethylbutyl)-phenyl ether, Sigma-Aldrich) PBS solution for 5 minutes. After three washing steps in PBS, blocking of unspecific antigen sites was performed in a blocking solution (5% bovine serum albumine (BSA, Sigma-Aldrich), 0.1% cold water fish skin gelatin (Sigma-Aldrich), 5% normal goat serum (Interchim, France), PBS) for 30 minutes. The unbound proteins of the blocking solution were removed by three washing steps of 5 minutes each in 0.1% BSA/PBS. The cells were incubated overnight at 4°C with mouse monoclonal anti-NP IgG antibody, mouse monoclonal anti-MxA IgG and mouse monoclonal anti-HA IgG in a solution of 0.1% BSA. The anti-HA antibody and the anti-MxA antibody were directly labelled with DyLight-547 (Cy3 equivalent dye, excitation at 553 nm, emission at 569 nm) and DyeLight 647 (Cy5 equivalent dye, excitation at 652 nm, emission at 673 nm) (Pierce Biotechnology, Rockford, USA), respectively, using the protocol of the manufacturer. The anti-HA antibody was also conjugated to Fitc following a standard Fitc-DMSO conjugation protocol for antibodies (Current protocols in Immunology). On the following day, the cells were washed during six steps of ten minutes each in 0.1% BSA/PBS and incubated for 4 hours at room temperature in the secondary antibody solution, containing mouse anti-chicken IgG conjugated with Alexa 488 (excitation at 488 nm, emission at 520) (Invitrogen) in 0.1% BSA/PBS. Cells were then washed six times in 0.1% BSA/PBS for 10 minutes and incubated in a solution of 300 nM 4', 6-diamidino-2-phenylindole (DAPI, Sigma-Aldrich) in 0.1% BSA/PBS for 5 minutes. The excess fluorochrome was removed by three washes in 0.1% BSA/PBS. Finally, the slides were mounted in mounting medium (PBS, 1% wt/vol ascorbic acid, 90% vol/vol glycerol) and sealed with nail varnish.

For better determination of the number of infected cells, some samples were processed using a variation of the incubation protocol described above. The primary antibody mix was exchanged in favour of an antibody directed against the viral HA protein. This antibody was directly labelled with DyLight-547 using the protocol of the manufacturer. Immunolabelling of HA protein using this antibody did not require further revealing by a secondary incubation step.

Imaging was performed on a Zeiss LSM 510 confocal microscope fitted with a META detector.

VII.B.3. Stable isotope pulse labelling of MV infected THP-1 cells

THP-1 cells were grown in RPMI-1640 with Hepes (Gibco/Invitrogen, Belgium) supplemented with 2 mM L-glutamine and adjusted to contain, 25 mM glucose, 1 mM sodium pyruvate, 0.05 mM 2-mercaptoethanol, 50 U/L disodic penicillin G and 10 g/L streptomycin (Cambrex, Belgium). This medium is hereafter termed THP-1 medium. For each sample, $6x10^6$ THP cells were infected with MV (Edmonston vaccine strain) at a MOI of 1 or mock infected with Vero Slam culture supernatant (t = 0) and incubated for 1 hour at 37°C. Cells were then spun down, resuspended in THP-1 medium and cultured in 6-well plates. At t = 20 hours, cells were pulse-labelled for a duration t' = 15 minutes, t' = 30 minutes or t' = 60 minutes with THP-1 medium supplemented with 200 mg/L fully labelled $^{13}C_6{}^{15}N_2$ L-Lysine (Isotec, Germany). The concentration of labelled L-lysine was added in a 5 times excess compared to the non-labelled L-lysine present in RPMI-1640. After the stable isotope pulse, the cells were washed and cultured in non-labelled THP-1 medium until t = 24 hours.

To prepare the samples for NanoSIMS imaging, cells were harvested, washed twice in PBS, fixed in 2.5% glutaraldehyde/PBS for 8 hours at 4°C, washed again in PBS and post-fixed for 1 hour in 1% OsO_4/PBS (Fluka, Germany). After two washes in PBS, the cells were transferred into a graded series of ethanol (50% ethanol for 5 minutes, 75% ethanol for 10 minutes, twice in 95% ethanol for 10 minutes, twice in 100% ethanol for 10 minutes). Subsequently, the cells were cleared twice in 100% propylene oxide (Fluka), followed by an infiltration of 2 hours in a solution of 70% propylene oxide and 30% Epon 812 epoxy resin, (Fluka) and another 2 hours in a solution of 30% propylene oxide and 70% epoxy resin. Infiltration in resin was conducted in 100% epoxy resin for 12 hours. After exchanging the resin with fresh embedding media, curing was performed at 200 mBar, first at 40°C for 2 hours, then at 65°C for 48 hours. Resin blocks were cut on a Leica UCT ultramicrotome into thin sections of 300 nm that were mounted onto steel sample holders and observed on the NanoSIMS.

VII.B.4. Stable isotope labelling of an antibody directed against a viral protein.

Metabolic labelling of antibodies

Murine monoclonal antibodies were derived from the culture supernatant of a hybridoma cell line secreting antibodies directed against measles NP. The hybridoma cell line was produced and described in previous works (Fournier, Ammerlaan et al. 1996; Fournier 1997).

The cell line was adapted to serum free HL-1 cell culture medium (Cambrex, Belgium) over 4 weeks, with an exchange of fresh medium every two days. After the adaptation period, cells were incubated in fresh HL-1 medium supplemented with 200 mg/L of fully doubly labelled $^{13}C_6{}^{15}N_2$ L-Lysine. Care was taken to remain below 20% dead cells in culture. After 5 days, cells were spun down for 15 minutes at 2000 g. The supernatant was passed through a 0.45 µm microfilter (Millipore, Billerica, MA) to remove cellular debris.

Protein G purification

The NP antibody was purified from the supernatant by Protein G affinity chromatography. The protein G resin (Sepharose 4 Fast Flow, Amersham) was rinsed and packed into a 3.5 cm column, following the manufacturer's instructions. Supernatant was diluted with an equal volume of loading buffer (10 mM sodium phosphate buffer, 2 M NaCl, 0.5 M EDTA pH 7.0). The diluted supernatant was injected into the column in a flowing stream of loading buffer. Reinoculation of unbound fractions in a closed circuit maximized the number of bound proteins on the column. Bound antibodies were then eluted from the column with 0.1 M glycine at pH 2.7 (Sigma-Aldrich). Eluted samples were neutralized with 1 M Tris buffer (Sigma-Aldrich). The concentration of the purified ^{15}N labelled antibody, hereafter called 15N-NP, was estimated using the photometric absorbance method at 280 nm and an extinction coefficient of $\mathcal{E}_{percent}$ = 14 (Babul and Stellwagen 1969). The antibody concentration was adjusted to 1 mg/mL.

Tryptic digestion and liquid chromatography separation

Twenty picomoles of labelled and non-labelled antibody were digested at 37°C in a trypsin solution (Roche, Germany) with 50 mM NH_4HCO_3 at pH 7.8 for 8 hours in a 1:50 (trypsin:antibody) ratio. The enzymatic activity of the trypsin was stopped by lowering the pH to 2 with the addition of trifluoroacetic acid (TFA) to 1% final concentration. Two picomoles of each sample were clarified using a reverse phase C18 (Millipore ZipTip, Billerica, MA). Positive ion MALDI-TOF mass spectrometry was performed on the digested antibody using a Bruker Daltonics ULTRAFLEX TOF/TOF, equipped with a 337 nm, 50 Hz N_2 laser of 100 µJ. The crystal matrix, HCCA/DHB from Bruker Daltonics (Leipzig, Germany) was prepared as follows: 7 mg/mL HCCA, 1.2 mg/mL DHB, 0.1% TFA in a 1:1 ddH_2O/acetonitrile solution. Sample and 0.5 µL matrix solutions were mixed directly on the stainless steel probe and allowed to dry (10 min) at room temperature. Spectra were recorded in the reflectron mode and the resulting data were analyzed using the Biotools software supplied by Bruker Daltonics. The instrument was calibrated using a digested BSA solution in ddH_2O (Bruker

Daltonics, Leipzig, Germany) solution in ddH_2O. The data collected was used as a protein mass fingerprint to confirm the validity of the approach before LC-MALDI.

HPLC separation was performed on a Agilent 1100 equipped with a binary capillary pump and a UV cell (internal volume 80 nL, path length 6 mm). Peptides resulting from the tryptic digest of the antibody were separated on a reversed-phase Zorbax SB-C18 (length 15 cm, diameter 300 µm, bead diameter 5 µm, pore size 300 Å). The column was kept at 25 °C in a column heater. Samples (injected volume 2 µL) were eluted using a gradient from 5% ACN in 0.08% TFA to 95% ACN in 0.12% TFA. The flow rate was 3.5 µL/min at a collection rate of 30 s/fraction. The solvent gradient applied during the chromatography run is indicated in Figure 47. Peptides were detected at 214 nm absorbance. Aromatic cycles were detected at 280 nm absorbance.

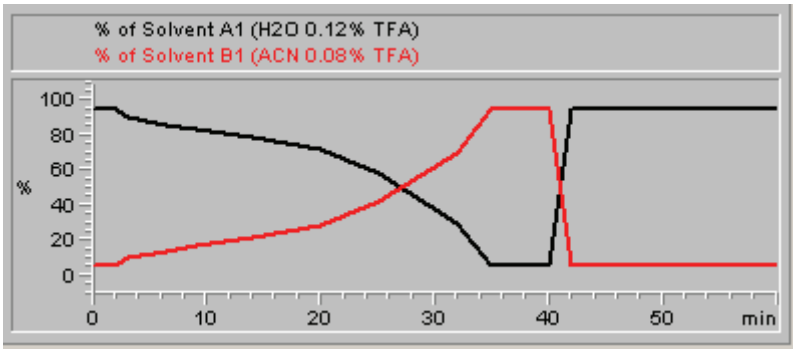

Figure 59: Solvent gradient applied to the peptide separation by HPLC.

Peptides resulting from the tryptic digestion of the antibodies, before and after a capillary liquid chromatography purification step, were analysed by MALDI-TOF/TOF. Tryptic peptides were analysed in TOF mode for protein identification at the peptide level and in TOF/TOF mode to estimate the isotopic labelling of the NP antibodies at the amino acid level.

VII.B.5. Immunolabelling assay by NanoSIMS

THP-1 cells were grown in RPMI-1640 with Hepes supplemented with 2 mM L-glutamine and adjusted to contain 25 mM glucose, 1 mM sodium pyruvate, 0.05 mM 2-mercaptoethanol, 50 U/L disodic penicillin G and 10g/L streptomycin. For each sample, $4x10^6$ THP-1 cells were inoculated with MV (Edmonston vaccine strain) at a MOI of 1 or mock inoculated with Vero Slam culture supernatant and incubated for 24 hours at 37 °C. Cells were harvested, washed in PBS and pre-fixed in a solution with 0.1% glutaraldehyde and 4% paraformaldehyde in PBS for 20 minutes. After three washed in PBS, aldehyde functions were saturated with NH_4Cl for 10 minutes and the sample was washed again three times in buffer. Permeation was performed with 0.1% Triton/PBS for 10 minutes, followed by three

additional washes in buffer. The sample was then incubated for 30 minutes with a blocking solution (PBS, 5% acetylated BSA (Aurion, The Netherlands), 0.1% cold water fish skin gelatin (CWFSG, Sigma-Aldrich), 5% normal goat serum (NGS, Interchim)) before being incubated with the antibody 15N-NP (1:1000 dilution of a 1 mg/mL antibody solution). Excess antibody was washed out in six consecutive washes in 0.1% acetylated BSA/PBS before fixing the sample with 2.5% glutaraldehyde for 1 hour. Post-fixation was performed in 1% OsO_4/PBS (Fluka, Germany). Cells were dehydrated in a graded series of ethanol (50% ethanol for 5 minutes, 75% ethanol for 10 minutes, twice in 95% ethanol for 10 minutes, twice in 100% ethanol for 10 minutes). Subsequently, the cells were cleared twice in 100% propylene oxide (Fluka), followed by an infiltration of 2 hours in a solution of 70% propylene oxide, 30% Epon 812 epoxy resin (Fluka), and 2 hours in a solution of 30% propylene oxide, 70% epoxy resin. Infiltration in resin was performed in 100% epoxy resin for 12 hours. After exchanging the resin with fresh embedding media, curing was performed at 200 mBar, first at 40 °C for 2 hours, then at 65 °C for 48 hours. Resin blocks were cut on a Leica UCT ultramicrotome into thin sections of 300 nm that were mounted onto steel sample holders and observed on the NanoSIMS. Several 1 µL drops of 15N-NP were deposited alongside the resin sections on the steel sample holders as positive controls.

VII.C. Results

VII.C.1. Timeline of a MV infection

C.1.1. Flow cytometry assay

Figure 60 represents the expression of HA in a population of THP-1 cells. 18 hours after inoculation with MV, 45.5% of the cell population was HA positive. After 24 hours, almost 93.4% of THP-1 cells were positive for HA.

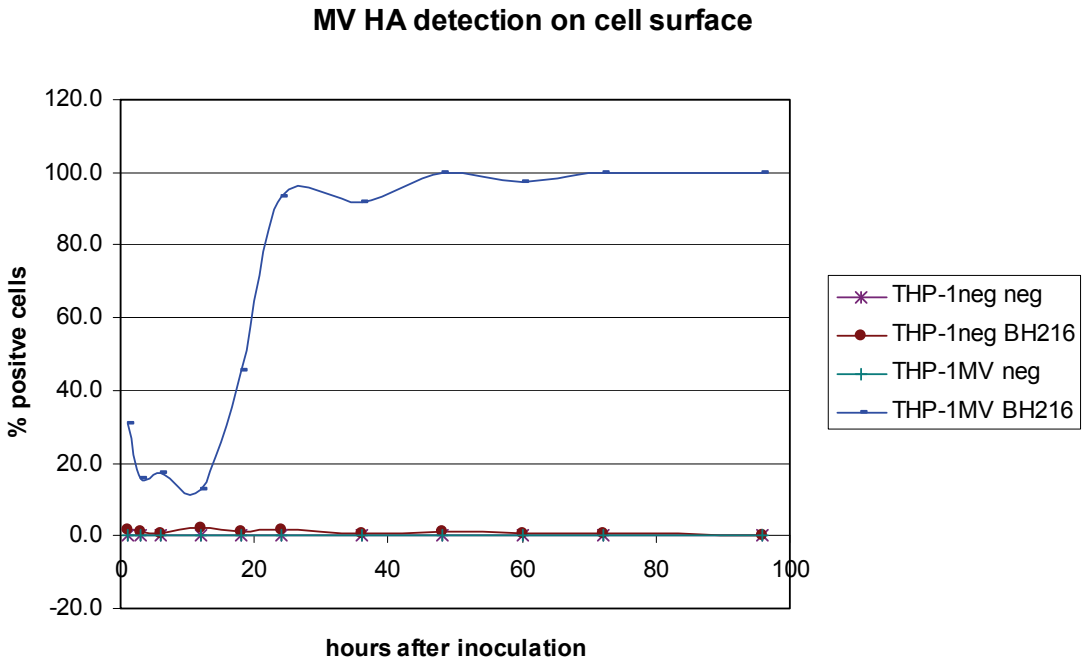

Figure 60: Detection of HA in MV infected THP-1 cells by flow cytometry.

In the same experiment, propidium iodide staining allowed to determine the morbidity of the infected cells. Until 24 hours after inoculation, cell death was below 5%. However, after 24 hours morbidity increased drastically and reached 90% at 96 hours. As expected, morbidity in healthy cells was below 5% during the whole experiment.

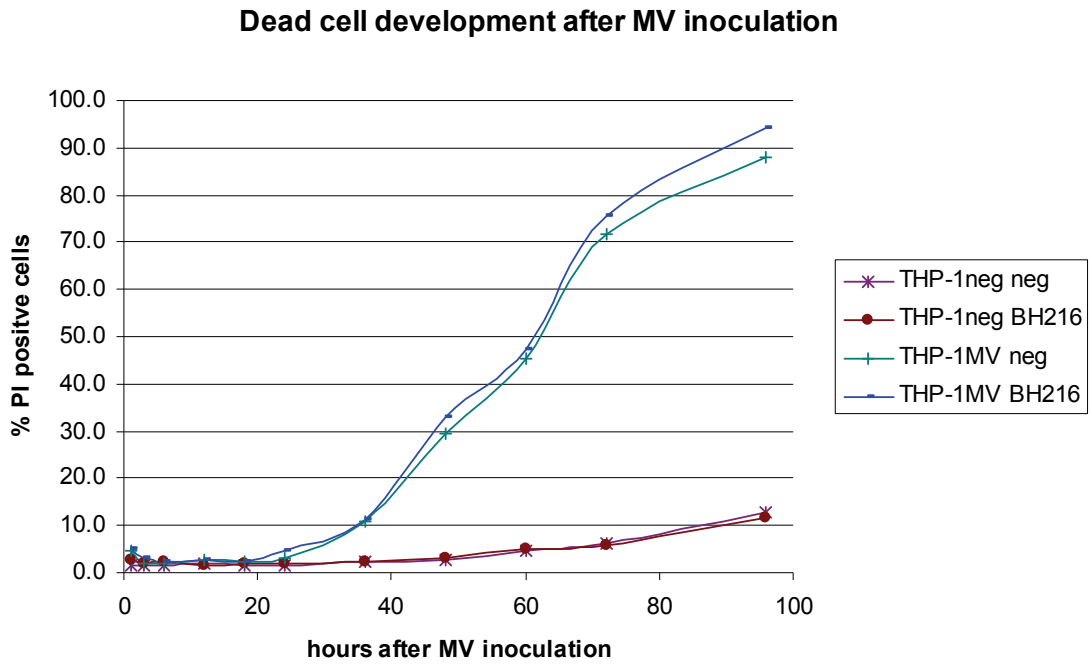

Figure 61: Progression of cell death during an MV infection of THP-1 cells by flow cytometry.

C.1.2. mRNA quantification

The mRNA quantification showed an increase in the expression of viral NP messenger RNA several hours after inoculation (Figure 62). Between 0 and 6 hours, the viral NP levels were still low, a latency in the infection which corresponded to the taking over of the host cell machinery. After 6 hours, viral NP mRNA was expressed. Between 18 and 24 hours, the levels of NP mRNA reached a first peak and a second peak was reached around 60 hours of infection. The first peak corresponded probably to the first wave of infected cells with a release of newly formed MV. This would be in accordance with the second peak at t = 60 hours which would correspond to a second wave of infection and production of an increased number of viral NP.

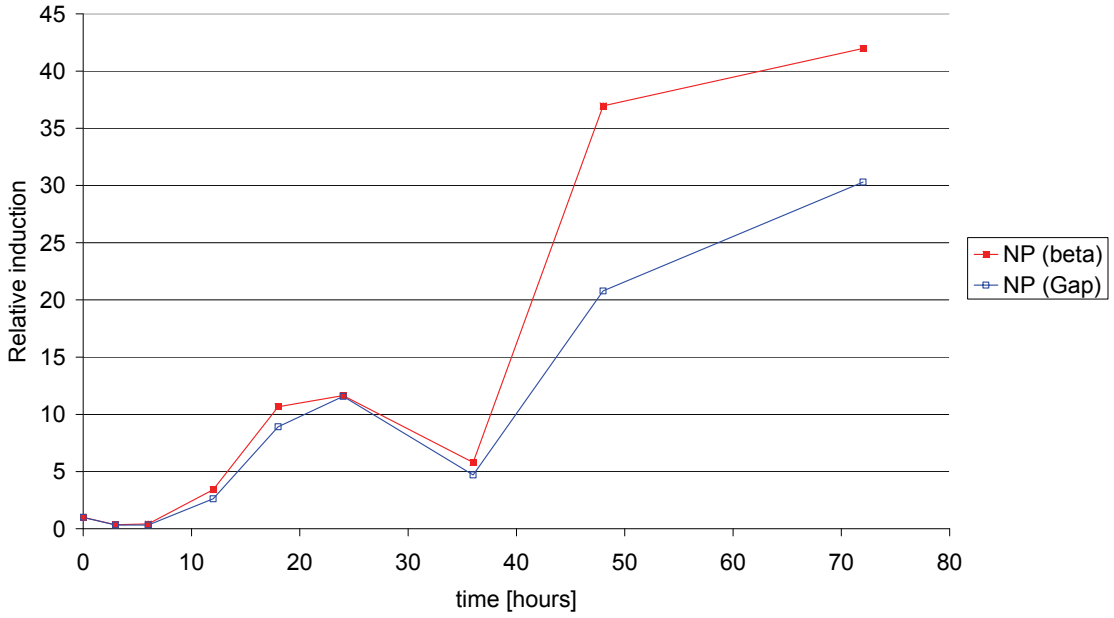

Figure 62: mRNA quantification of viral NP. *normalized against the housekeeping genes GAPDH (Gap) and beta-actin (beta).*

Human MxA mRNA was notably increased 6 hours after the inoculation. MxA expression levels reached a peak at 24 hours after infection, with a 350 fold increase relative to 0 hours (Figure 63).

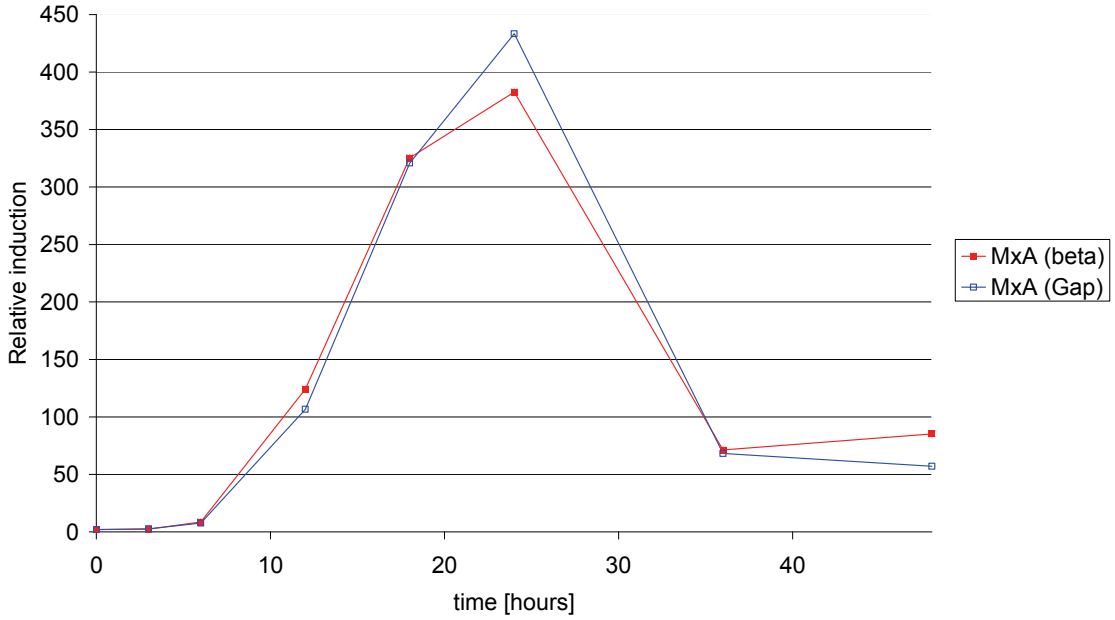

Figure 63: mRNA quantification of host cell MxA. *Normalized against the housekeeping genes GAPDH (Gap) and beta-actine (beta).*

The preceding flow cytometry results motivated the selection of a window between 20 and 24 hours after inoculation for optical microscopy and SIMS observations of infected cells. During this period, the majority of cells were infected, as determined by HA expression on the membrane. Furthermore, in this timeframe MxA expression was increased 350 fold and NP reached its highest levels during the first wave of infection.

VII.C.2. Immunofluorescence assay

During MV infection, the envelope of the virus fuses with the membrane of the host cell (Kerdiles, Sellin et al. 2006). The viral glycoprotein HA, present in the viral bilipidic envelope, is involved in the binding of the virus to the cell. After the fusion of the virus with the host cell, HA remains on the cell membrane at the location of viral entry. Later in the viral cycle, the virus induces a ubiquitous production of HA on the cellular membrane. As a result, the protein is a good marker to determine the stage of infection of a cell. Figure 64A shows a stitched view of THP-1 cells 24 hours after inoculation with MV virus. Cells are shown at various stages of infection, with several cells expressing large amounts of HA while other cells only present one or two viral entry points, observed as hotspots of HA on the cellular membrane. Nevertheless, the infection rate was high, confirming the results obtained by flow

cytometry in C.1.1. Figure 64B shows a cell at a late stage of infection, ubiquitously expressing HA on its membrane.

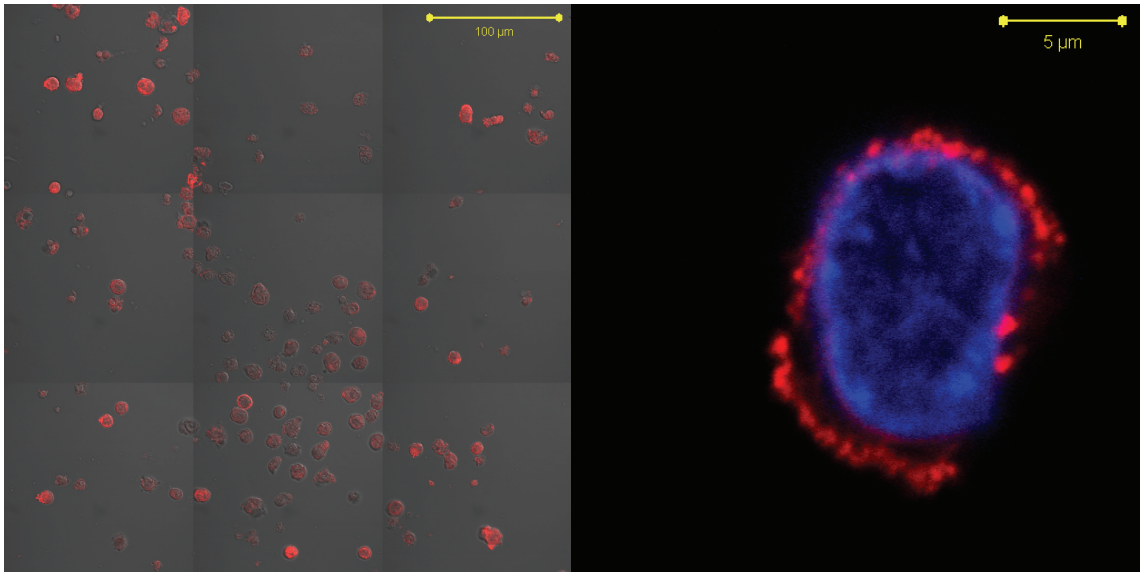

Figure 64: Measles infected THP-1 cells 24 hours after inoculation (HA & DAPI stain). *(A) The majority of cells were infected, but differences in expression of HA protein were observed. (B) Late stage of infection of a THP-1 cell. Anti-HA antibody (red). DAPI nuclear staining (blue).*

Figure 65 reveals the distribution of NP, HA and MxA in an MV infected THP-1 cell culture. Similar distribution patterns of HA could be observed in Figure 65B, 24 hours after inoculation. Some of the cells that strongly expressed HA also contained NP aggregates, probably related to sites of viral capsid assembly (Figure 65C). However, while MxA expression was highly cell-dependant, and the distribution inside a cell was homogenous, it could not be related to the expression of either HA or NP. No NP aggregates or potential colocalization of MxA with NP was observed. Infected cells secrete anti-viral factors such as type I IFN, which upregulate the expression of MxA (Kochs, Trost et al. 1998). High amounts of MxA are not necessarily the hallmark of infected cells, but may relate to healthy neighbouring cells activated by IFN.

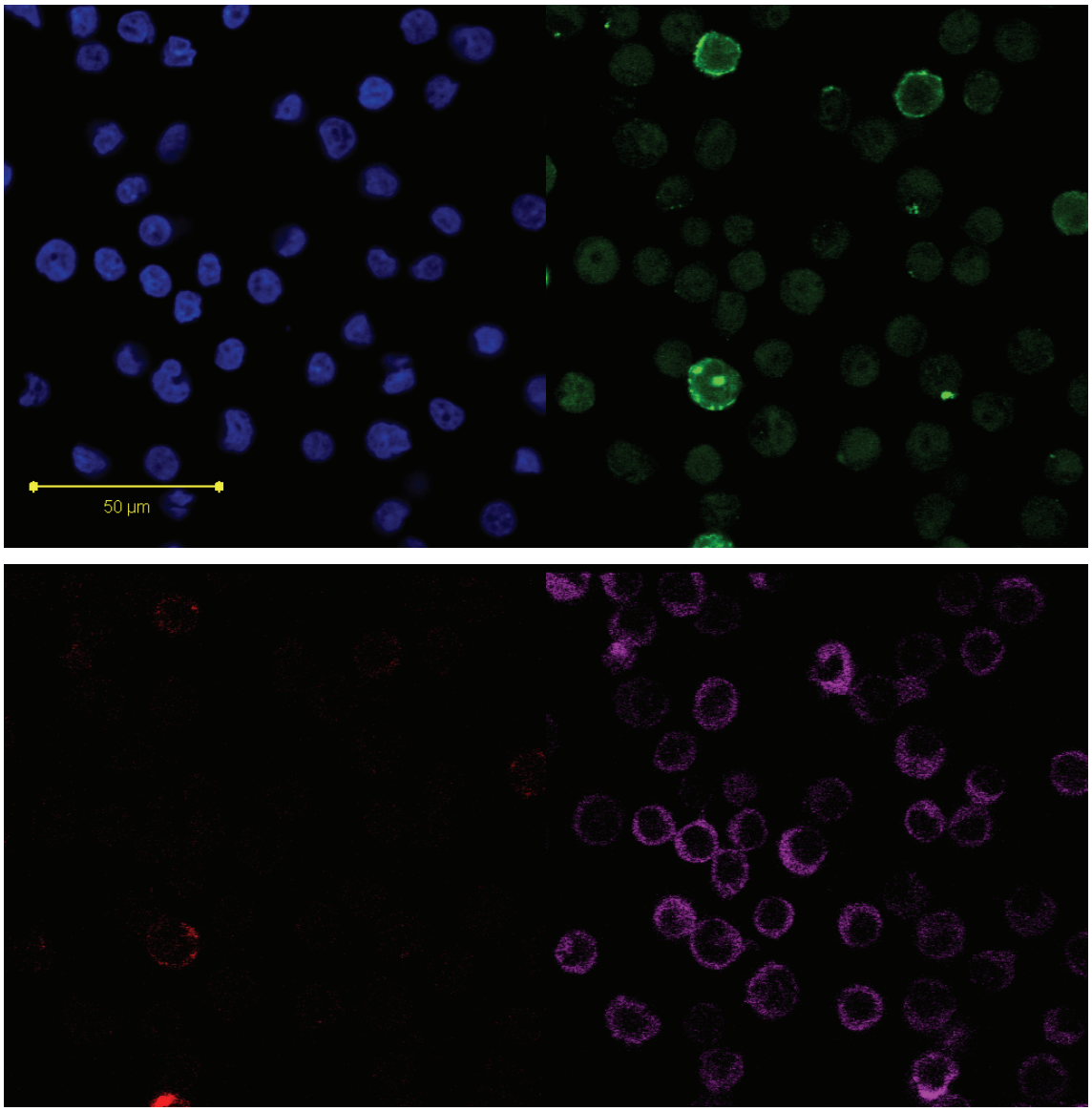

Figure 65: Measles infected THP-1 cells 24 hours after inoculation (HA, DAPI, NP & MxA stain). *(A) DAPI nuclear stain (B) Anti-HA antibody revealed several strongly infected THP-1 cells. Points of entry of the virus was visible. (C) Anti-NP antibody staining. Cells expressing HA on the plasma membrane showed aggregates of NP. (D) Anti-MxA antibody staining. No clear aggregate formation of MxA. Heterogeneous labelling intensity in the culture.*

VII.C.3. Stable isotope pulse labelling of MV infected THP-1 cells.

An alternative approach to visualise protein aggregates was given by pulse labelling and observation of the incorporation of ^{15}N labelled amino acids in an infected culture (HSI image, Figure 66). After a Lys-$^{13}C_6{}^{15}N_2$ pulse of 15 minutes, differences in labelling intensities of cellular compartments became visible. In the Mock infected cells, ^{15}N was heterogeneously accumulated in the cytoplasm close to the nucleus (Figure 66A). For MV infected cells, the ^{15}N was more generalised, but with a stronger intensity in the nucleoli (Figure 66B). For mock infected cells at t = 30 minutes (Figure 66C), ^{15}N incorporation in the

nucleoli could be described at levels similar to those found in Figure 66B, with a weak cytoplasmic distribution with only some regions with higher intensities. For a pulse of the same duration, infected cells showed a strong protein turnover throughout the cell, with an accentuated incorporation in the nuclei and on different sites along the nuclear membrane (Figure 66D). This trend was confirmed for MV infected cells for a pulse of 60 minutes (Figure 66E). In the cytoplasm of infected cells, several regions showed intense protein turnover rates. Unfortunately, images from mock infected cells at t = 60 minutes could not be processed due to a corrupted acquisition file.

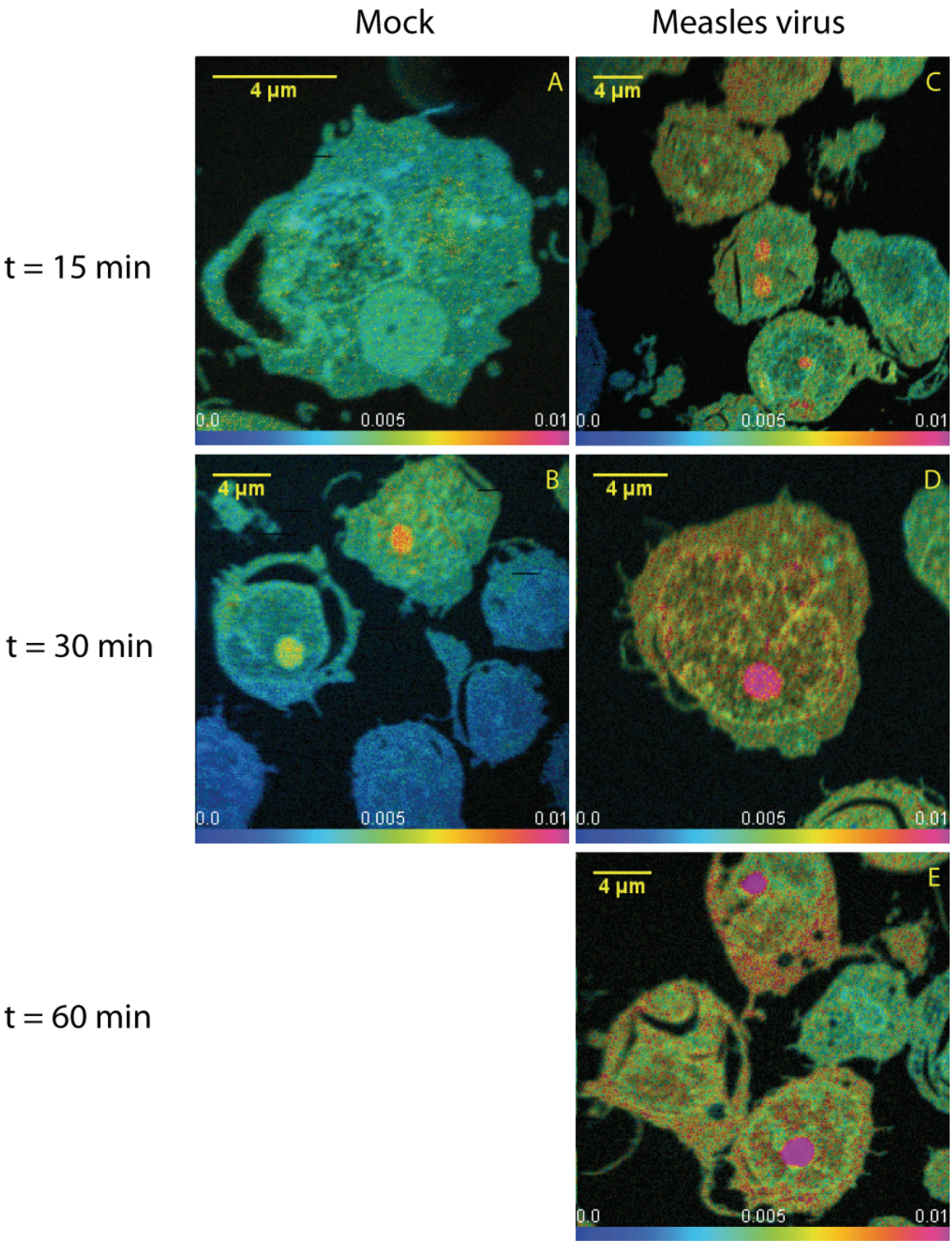

Figure 66: HSI ion micrographs ($^{12}C^{15}N$ / $^{12}C^{14}N$) Mock or MV infected THP-1 pulsed with ^{15}N for a duration t'. *Cs^+ impact energy 16 keV, 256 x 256 pixels. (A) Mock infection, t = 15 minutes (48.0 nA, 40 ms/pixel) ; (B) Mock infection, t = 30 minutes (52.3 nA, 40ms/pixel, L1 = 857 V) ; (C) MV infection, t= 15 minutes (48.3 nA, 40 ms/pixel) ; (D) MV infection, t = 30 minutes (48.6 nA, 40 ms/pixel) ; (E) MV infection, t = 60 minutes (48.6 nA, 40 ms/pixel).*

VII.C.4. Stable isotope labelling of an antibody directed against a viral protein

Only the incorporation of ^{15}N yielded interesting observable results on the NanoSIMS. However, the antibody was effectively double-labelled with two ^{15}N and six ^{13}C per lysine. Consequently, for each incorporated labelled lysine a supplementary mass shift of 8 Da was expected.

A MALDI-TOF analysis in the linear mode of intact non-labelled anti-NP antibody showed two peaks (Figure 67). The peak at 75527 Da represents the doubly charged antibody (z = +2). The monocharged antibody is identified by the peak at 151283 Da, corresponding to the 150 kDa theoretical molecular weight of an IgG antibody. At this molecular weight, the resolution of the MALDI-TOF operating in linear mode (with no reflectron) is dramatically reduced and it may explain the mass divergence of 229 Da between the monocharged and the extrapolated mass of the doubly charged antibody when brought to z = 1.

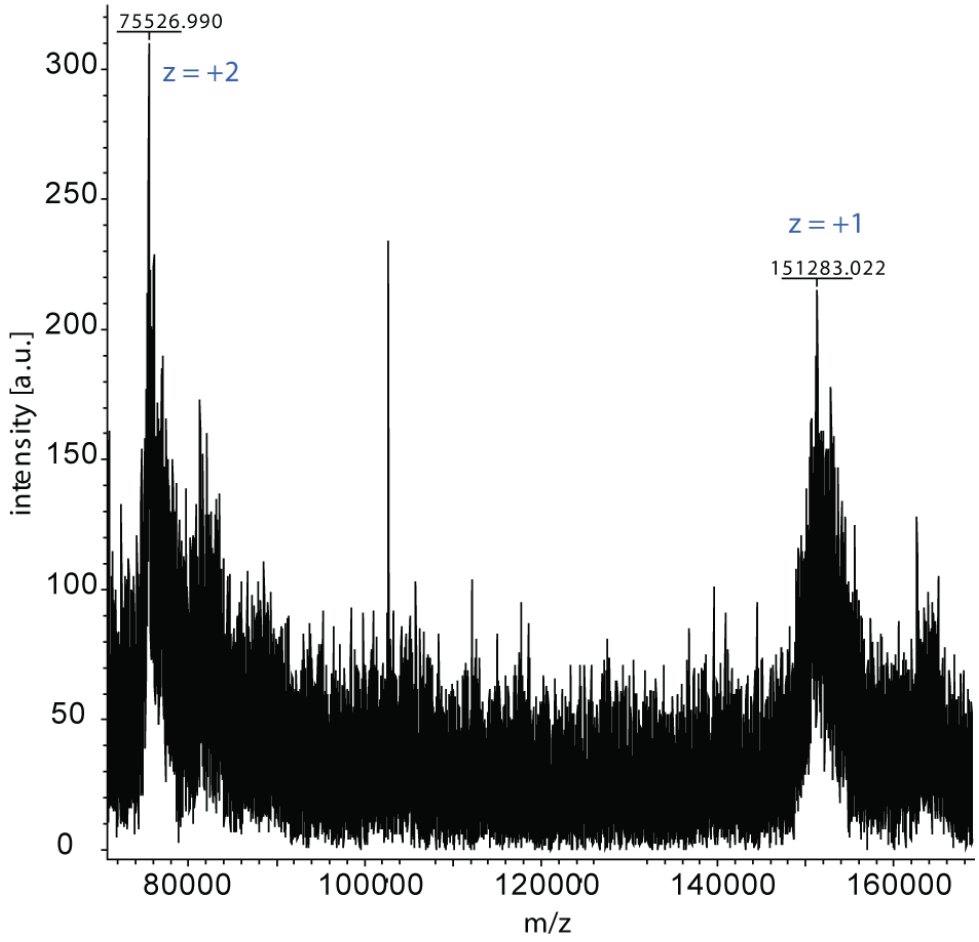

Figure 67: Intact mass analysis of non-labelled anti-NP antibody by MALDI-TOF in the linear mode.

The non-labelled anti-NP antibody was analysed and the spectra of the tryptic digest were processed by Bruker Biotools. A database search in Matrix Science Mascot identified the PMF of the Ig-κ chain, a well-conserved sub-fragment of an IgG antibody. The peak mass list that led to the identification of the Ig-κ chain is framed (Figure 68).

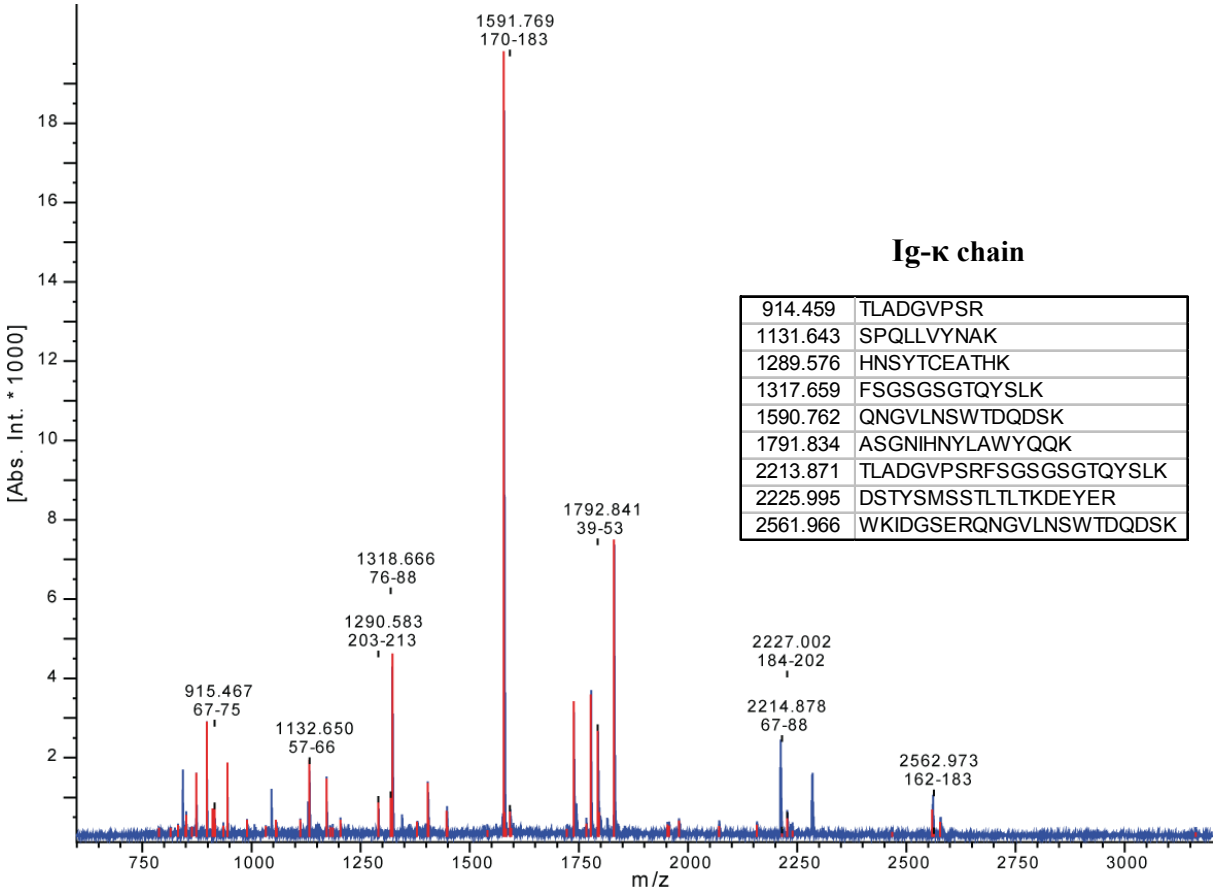

Figure 68: Analysis of non-labelled anti-NP antibody by MALDI-TOF. *The PMF corresponds to the Ig-κ chain. In blue, the mass spectrum obtained by Bruker FlexAnalysis. Red peaks are used for the Mascot database request. Peaks belonging to the PMF of Ig-κ chain are mass annotated.*

Peptides originating from the tryptic digest of the non-labelled anti-NP antibody were separated by liquid chromatography, as shown by well-resolved peaks in the chromatogram at 214 nm (Figure 69A). Each eluted fraction contained, most of the time, only one or two peptides, identified by MS, with a terminal lysine or arginine (Figure 69B). Furthermore, the mass resolving capacity of MALDI-TOF in the reflectron mode discerned the isotopic distribution of the peptide, as illustrated in Figure 69C.

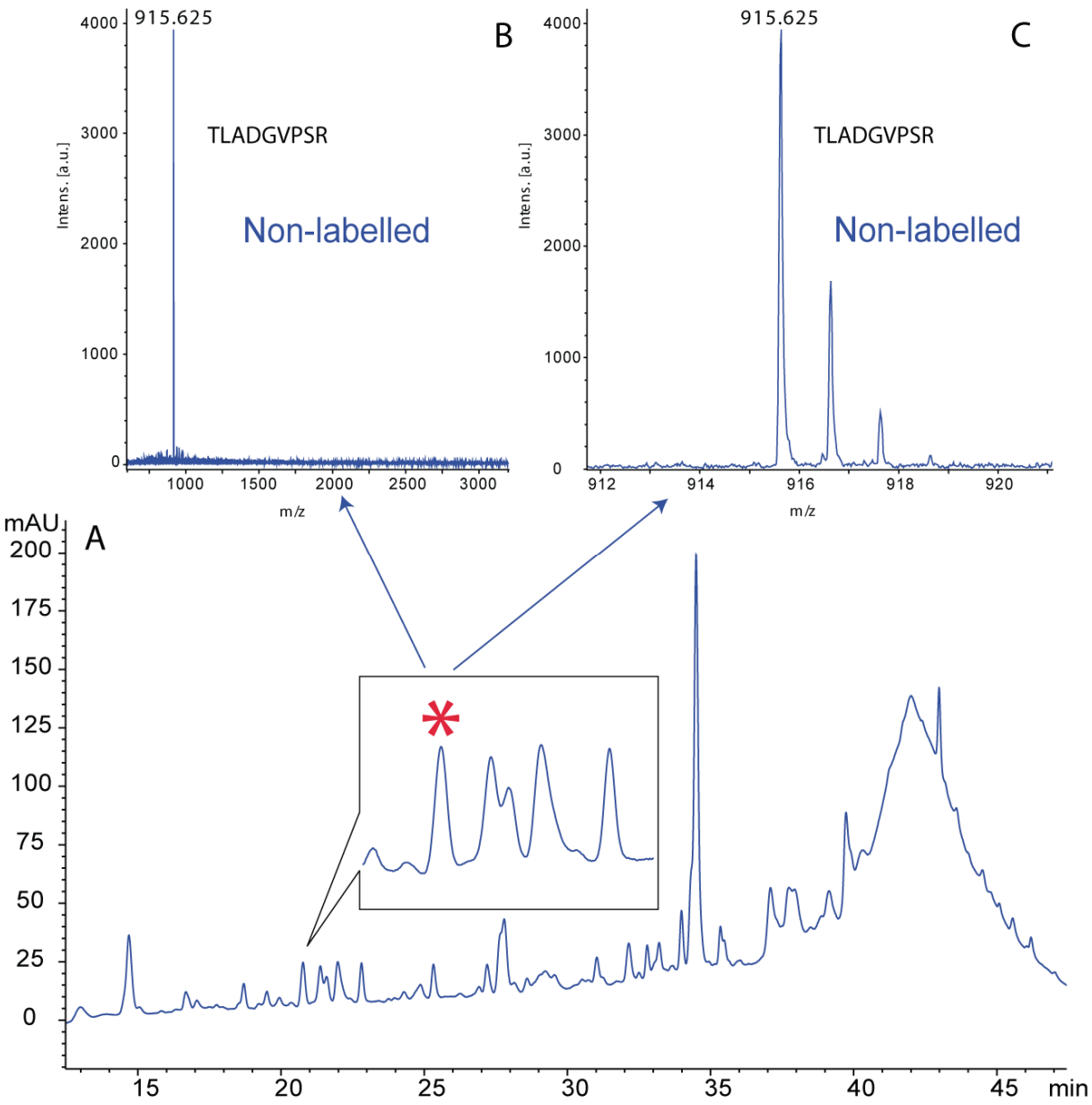

Figure 69: Confirmation of the identification of non-labelled anti-NP antibody tryptic digest by LC-MS and MS/MS. *(A) chromatogram at 214 nm absorbance of the tryptic peptide separated by LC. The MS spectrum of the fraction marked by a star is shown in (B). The fraction contains a single eluted peptide. (C) Spectrum shows a mass resolution sufficient to isolate the isotopes of an individual peptide.*

The tryptic digests of non-labelled and isotopically labelled antibodies, separated by liquid chromatography, were analysed by MALDI-TOF. Figure 70 shows the spectra of two peptides with the sequences SPQLLVYNAK and ASGNIHNYLAWYQQK. In both cases, an expected shift of 8 Da was observed between the non-labelled and the labelled peptide. Moreover, while in the non-labelled fraction only one peptide was represented with an internal isotopic distribution, in the labelled fraction two distinct peptides could be identified (e.g. 1132 and 1140 respectively 1792 and 1800). Both correspond to the same peptide that co-eluted. While the predominant rightmost peptide corresponded to the labelled material, the

leftmost peptide corresponded to the remaining non-labelled peptides inside the labelled sample. The mass shift between labelled and non-labelled peptides is explained by the replacement of the single lysine (K) by a lysine containing two ^{15}N and six ^{13}C atoms, resulting in an increase in mass of 8 Da. It should be noted that while the internal isotopic distribution of a peptide resulted in sequential peaks, a shift of 8 Da is sufficient to distinguish a labelled peptide, having incorporated a labelled lysine, from a non-labelled peptide.

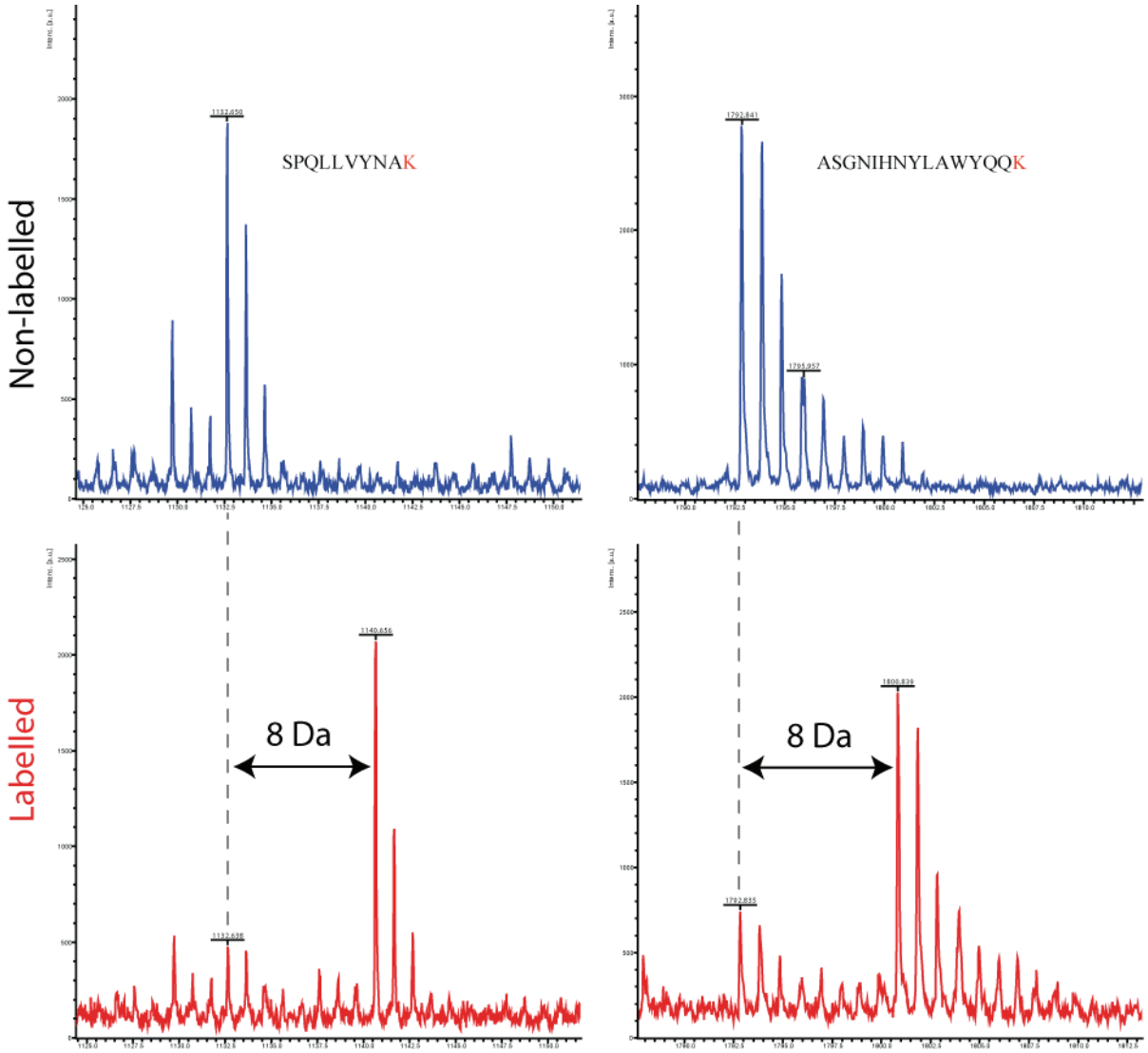

Figure 70: Both labelled and non-labelled tryptic digests of anti-NP antibodies have been separated by liquid chromatography. *(A, B) shows two peptides at masses 1132 and 1792. (C, D) in a labelled fraction, the labelled peptides are preponderant (at masses 1140 and 1800). The remaining non-labelled peptide was co-eluted and corresponds to the leftmost peak distribution. A mass shift of 8 Da is visible between the labelled and non-labelled peptide.*

The chromatographic separation and subsequent MALDI-TOF analysis of a mixture of tryptic digests of labelled and non-labelled antibodies are shown in Figure 71. The superimposition of chromatograms of non-labelled peptide (Figure 71A, blue) and labelled peptide (Figure

71A, red), at an absorbance of 214 nm, illustrates the co-elution of peptides in a same fraction due to their identical physicochemical properties. In a non-labelled sample, only one peak was distinguished, which corresponded to the peptide sequence SPQLLVYNAK (Figure 71B). In the mixture, both non-labelled and labelled peptides of sequence SPQLLVYNAK co-eluted and were present in the same fraction, separated by a mass shift of 8 Da due to the dual isotope composition of the labelled lysine.

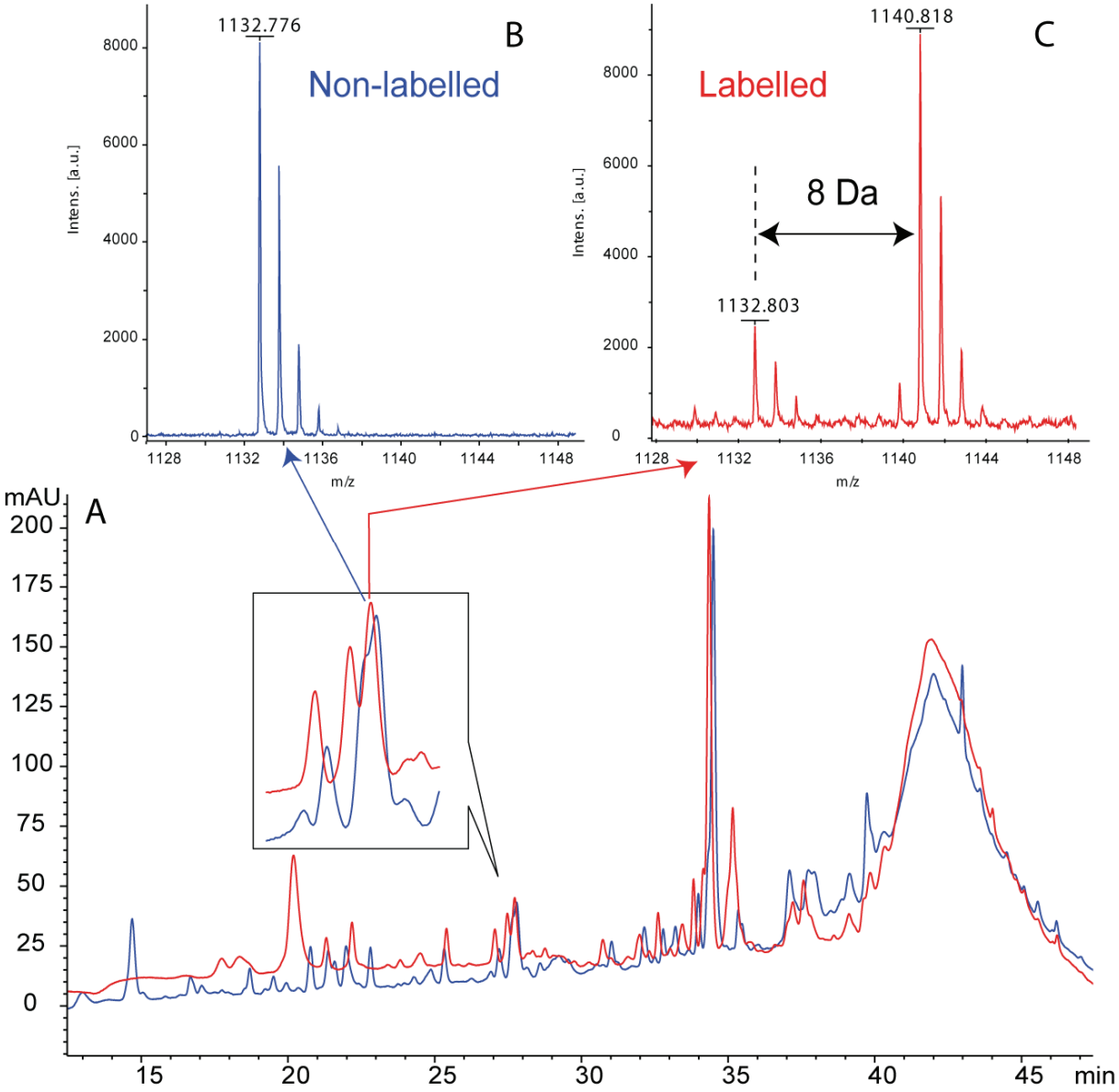

Figure 71: Correspondence between HPLC chromatogram and MS spectrum for labelled and non-labelled peptides. *(A) Retention times of labelled (blue) and non-labelled (red) tryptic peptides at 214 nm. (B) In a separation of non-labelled material, only one peptide was eluted (MS spectrum). (C) Mixture of ^{15}N labelled and non-labelled tryptic digests, separated by liquid chromatography. The labelled and non-labelled peptides co-eluted (MS spectrum).*

VII.C.5. Immunolabelling assay by NanoSIMS

The incorporation of ^{15}N in the 15N-NP antibody was confirmed by deposits of labelled and unlabelled 15N-NP antibody on the sample holder (Figure 72). A 2.5 fold increase in ^{15}N was found (natural abundance of ^{15}N = 0.37%, labelling peaks at 1%) for the labelled antibody.

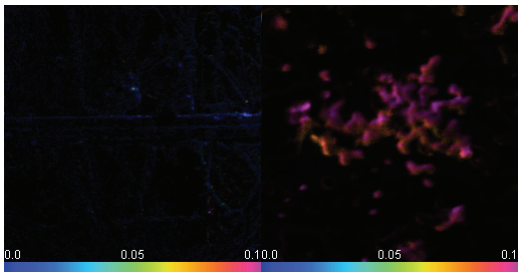

Figure 72: Confirmation of the incorporation of the isotopic label by NanoSIMS. *$^{12}C^{15}N/^{12}C^{14}N$ HSI ratio of 1 µL deposit of a 1mg/mL solution diluted 1:1000. (A) unlabelled anti-NP antibody, (B) $^{13}C_6{}^{14}N_2$ labelled anti-NP antibody solution.*

In a NanoSIMS immunolabelling experiment, the ^{15}N labelled anti-NP antibody was exclusively localised outside of the cytoplasm. The nuclear membrane was delimited by a slightly lower incorporation of ^{15}N relative to its natural abundance. The ^{15}N enrichment from the labelled antibody was observable as increase relative to the natural ^{15}N abundance (raised from the background) and its distribution hinted to an heterogeneous accumulation seen as aggregates in three different regions.

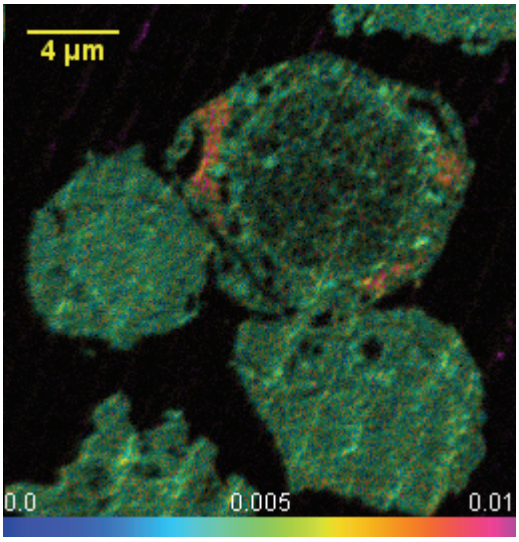

Figure 73: Immunolabelling by isotopically labelled antibody, visualized on NanoSIMS. *$^{12}C^{15}N/^{12}C^{14}N$ HSI ratio of measles infected THP-1 cells, incubated with $^{13}C_6{}^{14}N_2$ labelled anti-NP. Cs^+ impact energy 16 keV, primary current 39.7 nA, 256 pixels x 256 pixels, 40 ms/pixel.*

VII.D. Discussion

This study aimed at investigating the protein aggregate formation following a MV infection of THP-1 cells, by combining microanalytical imaging techniques, such as NanoSIMS and Immunofluorescence, by means of flow cytometry and optical microscopy. A first set of experiments was designed to investigate using confocal microscopy, the hypothetical co-localization of viral NP with human MxA, reported for other RNA viruses such as orthomyxoviruses and paramyxoviruses. The production of MxA was upregulated after MV infection, and corresponded to the production cycle of both viral proteins NP and HA. While no co-aggregation of human MxA with the viral NP was observed, several NP aggregates were identified by immunolabelling, which corresponded to the viral assembly sites. In an attempt to better characterise the aggregate formation a NanoSIMS study of similarly infected cells was performed. As expected for a viral cell infection, which hijacks the host cell machinery for the production of viral proteins for the virus replication, the protein turnover measured by the incorporation of ^{15}N was accentuated in infected cells. Mock-infected cells showed mostly a homogeneous increase of protein turnover over time, with only several hotspots in the cytoplasm, although some regions with high concentrations of ^{15}N could be seen even after short ^{15}N pulses. In the case of infected cells, a strong incorporation of ^{15}N may be explained by the increased production rate and the recruitment of ribosomes to cope for the increased transcription activity caused by the viral infection. Longer pulses also stained the nucleolus of healthy cells with a normal transcription and cell activities, as expected. Attempts to detect the ^{13}C isotope from the $^{13}C_6{}^{15}N_2$ lysine amino acid were not conclusive, a potential explanation being the natural abundance of ^{13}C (1%) almost three times higher than ^{15}N (0.37%) and the ubiquity of carbon.

The MALDI-TOF results confirmed the incorporation of isotopically labelled lysine in anti-NP antibody. Additionally, by observing the ^{15}N enrichment, induced by the specific binding of the antibody to NP in NP rich regions, it was shown that immunolabelling studies by NanoSIMS were shown to be possible. The data obtained in the SIMS experiment confirmed both the distribution described by optical fluorescence data in VII.C.2 and the potential aggregates observed after pulse labelling in VII.C.3. This is the first report of an immunolabelling study using a stably labelled isotope in SIMS analysis.

Chapter VIII General Discussion

The title of this thesis, *"Biological applications of the NanoSIMS",* introduces two distinct premises. First, it implies a certain novelty of a technique called NanoSIMS. Also, it implies the concept of NanoSIMS as a technique new to the field of life sciences, and whose propensity to yield interesting results requires investigation. This last chapter will attempt to argument these premises, in a typical instrumental approach on the lookout for potential applications in an unknown field. It will also briefly present the studies of the previous chapters, put them into perspective and rate the worth of NanoSIMS for the imaging of biological samples.

The novelty of SIMS and NanoSIMS

Whether SIMS is new or not is debatable. It has been mentioned previously that the technique was known for decades and that instruments based on it were present in analytical material science labs. It is reputed as a sturdy and robust technique for chemical microanalysis, with widespread knowledge of its capabilities and limitations. Most importantly, the interpretation of SIMS data either as static SIMS mass spectra, dynamic SIMS depth profiles or ion micrographs is well defined in analytical material science laboratories. On the other hand, the release of the NanoSIMS is a clear sign that the SIMS community is interested in sharing their technique outside their circle. This trend is confirmed by the characteristics harboured by this instrument, well suited for the isotopic discrimination of ions of low masses, representative of organic samples. Furthermore, its capability for high-resolution imaging clearly targets the segment of biological imaging and is coupled by an aggressive marketing stance to seduce the larger community of the life scientists.

However, the recent introduction of the NanoSIMS ion microprobe in life sciences poses several problems. The prototypal nature and the resulting price tag of around 2 million Euros is prohibitive to a large-scale dissemination of the instrument. The NanoSIMS involved in this work, and located in an analytical material science laboratory, was the fourth ion microprobe of its kind delivered worldwide. With a long-standing experience of dynamic and static SIMS, the laboratory was well qualified for the operation of a NanoSIMS. Notwithstanding, knowledge of the peculiar specificities of NanoSIMS was absent and had first to be gained. Although not officially being labelled as prototype, the downtime of the NanoSIMS in the five years since its acquisition was approximately 160 days/year. These were either due to lengthy maintenance operations or caused by instrumental instabilities of varying origins and severity. While the handling of the ion microprobe became more streamlined with the gain of experience, only a slim improvement in the acquisition throughput could be recorded over

time, which further confirms the early state of development of high resolution SIMS. Likewise, the instability of the acquisition software corroborated the impression that the NanoSIMS was not yet ready. Such difficulties are not common in the field of life sciences today and most techniques rely on high throughput analysis executed on robust devices. Whereas life sciences laboratories are usually focused on fundamental research, done by post-doctoral researchers and students, analytical laboratories are confronted with applied sciences, more the province of engineers. This is reflected both in their approach to a scientific question and in the instruments themselves, which commonly undergo in-house modifications to suit more specific needs. In this, the NanoSIMS is not an exception and joint-venture projects between industry and academia investigate the feasibility of further adaptations, such as the replacement of the oxygen source with a more resolved gallium source or the fitting of an electron microscope onto the ion microprobe.

As has been discussed in this thesis, the NanoSIMS holds many features of interest to biology. However, it is a device built by engineers with mostly a material science background and this is reflected in the analysis of biological samples of a more complex nature than the usually analysed materials. A typical life science approach to gain statistically meaningful data through repeated experiments is jeopardized by the low number of daily image acquisitions and their overall poor reproducibility.

Besides instrumental difficulties involved with the use of a novel technique, an added obstacle was the paucity of available experimental SIMS data on biological samples, as well as the scarcity of NanoSIMS publications specifically addressed to life sciences.

However, a sure sign that life science is on the rise in SIMS is supported by the fact that the pioneering work in dynamic SIMS of several life science groups, such as Levi Setti's and Chandra's, has lately been gratified by an entire conference session for life sciences in the biennial SIMS symposium (e.g. SIMS XV, 12.9-16.9 2005, Manchester, UK and SIMS XVI, 29.10-2.11 2007, Kanazawa, JP).

Developments and Applications

During this thesis, one of the most challenging tasks has been to adapt sample preparation protocols taking into account the variety of samples, ranging from cell suspension, adherent cells and both animal and plant tissues, and analyse them by NanoSIMS in an exploratory series of experiments. The screening process for optimal candidates in the search for applications required sample-by-sample adaptations to assess the sample quality after chemical fixation, or after alternative cryogenic fixation techniques such as plunge freeze and

slam freeze followed by cryosubstitution. This is an ongoing topic in the SIMS community, which aims at limiting the diffusion of small ions while preserving the morphological integrity of cells and tissues (Chandra and Morrison 1988; Hallegot, Girod et al. 1990; Chandra and Morrison 1992; Mony and Larras-Regard 1997; Dickinson, Heard et al. 2006; Grovenor, Smart et al. 2006). When the diffusion of small ions was not an issue, for example during the analysis of bound or sequestered molecules, chemical procedures were preferred as these preparations are less time-consuming and not subject to restrictions such as the limited usable sample depth in cryogenic preparations. While most specimens bore well either chemical or cryogenic sample preparations, some specimens were particularly difficult to adapt for SIMS analysis, irrespective of the preparation method. Specimens such as cell suspensions and animal tissues (e.g. kidney, lung : presented in Chapter III, Chapter IV, Chapter VI and Chapter VII) were of excellent quality and features (tissue morphology, cellular ultrastructure, e.g. organelles such nuclei) and could be identified to a varying extent. Other samples such as lichens (Chapter V) gave suboptimal results with both sample preparation methods, but identification of tissue features was difficult.

The lack of practice in the critical interpretation of ion micrographs for biological samples is a common problem and complementary observations, using other imaging instruments, is recommended. This insight is not recent, and the few applications on first generation dynamic SIMS relied on optical microscopy to confirm morphological identifications (Lorey, Morrison et al. 2001). With the high-resolution capabilities of the NanoSIMS, optical microscopy is not always sufficient, and the use of more resolutive techniques such as TEM has been reported (Grovenor, Smart et al. 2006). This trend is further confirmed by improvements like SIMS sample holders customized to accept TEM grids, that have been reported in this thesis and by other groups (Guerquin-Kern, Wu et al. 2005; McMahon, Glassner et al. 2006).

The novelty of NanoSIMS also requires the definition of “best practice” guidelines to standardize the acquisition of ion micrographs in order to improve the quality and the reproducibility of SIMS measurements. The investigation of complex and interlocking factors influencing the secondary ion emission is a recurrent topic in SIMS, and subjects range from the determination of the matrix effect on cryofixed specimens (Chandra, Ausserer et al. 1987), use of cluster primary ion beams (Fahey, Gillen et al. 2006; Hill, Blenkinsopp et al. 2006) to sample stage cooling (Miwa, Nomachi et al. 2006). A study presented in this thesis focused on the characterisation of the primary ion implantation and its effect on secondary ion yields, and proposed several experimental improvements such as increased primary ion current implantation or large scale preimplantation of Cs^+ on another dynamic SIMS. This last

improvement increased daily acquisitions by 50%. Additionally, a better understanding of the implantation of organic samples and a standardization of the Cs^+ dose, required to enter the dynamic regime in relation to the primary ion current and the analysed sample area, greatly improved the quality of individual ion micrographs at acquisition.

The scarceness of software utilities for handling NanoSIMS acquisition data required the development of additional image processing tools. The utilities presented in Chapter II feature the file conversion between various image formats, the extraction of metadata and the post-acquisition treatment of image data. The processing algorithm implemented in the utility permits the relative quantification of elements, based on the ratiometric analysis of isotopic images in the HSI colour space (Tsien and Harootunian 1990; Benson and Lechene 2005; Benson 2007). An algorithm, based on intensity histogram equalisation, to enhance heterogeneously implanted images, provided a better contrast at low intensities and allowed to discern otherwise invisible intracellular features. In addition to the NanoSIMS software utility, a tool to process confocal image data from a confocal laser scanning microscope (Zeiss LSM 510) was also presented.

Both software utilities have been successful since their public release, as measured by the number of users, further confirming the need of custom tools for the analysis of instrumental image data in the respective scientific communities.

In the preceding chapters, a multitude of applications have been explored. From these, several show potential and should be recognized as incentives for further investigations. Even considering the difficulties encountered during sample preparation of lichens, the NanoSIMS showed promising results in the detection of trace metals caused by atmospheric pollution. With growing environmental awareness, the NanoSIMS should prove to be an excellent tool in the detection of atmospheric pollutants in the future. Indeed, in the last few months, some papers have been released that seem to support this affirmation (Herrmann, Clode et al. 2007; Krein, Audinot et al. 2007).

The capability to discriminate biologically relevant isotopes at high resolution has only recently been acknowledged. In Chapter VI and Chapter VII, two applications have been presented that make use of these unique abilities. The first application follows metabolically labelled antigens during their uptake by antigen presenting cells. The metabolic labelling efficiency is studied by MALDI-TOF mass spectrometry and NanoSIMS, and the complementarity of both techniques in determining the incorporation of the isotope is shown. The uptake of the labelled antigen was corroborated by flow cytometry. The second application describes the production of a metabolically labelled antibody that binds

specifically to a viral structural protein of the measles virus. An immunolabelling experiment on cells infected with this pathogen was conducted and the label was observed by NanoSIMS. It is the first reported immunolabelling experiment using metabolically labelled antibodies. These results were backed up by the determination of the chronology of a measles infection, and the imaging of two viral proteins by confocal microscopy. Furthermore, an experiment based on an isotopically labelled amino acid pulse revealed the increased protein production rate of the infected cell machinery. Metabolic labelling is a powerful tool that allows either fine-grained labelling, illustrated in this study with a highly specific antibody, or coarse-grained labelling, as with the labelled antigens or the pulse labelling experiment. To further investigate the amino acid pulsing, a pulse-chase experiment could be devised. It starts with a *starvation* phase, where the cell medium is depleted for a given metabolic compound. During the subsequent *pulse* phase, the missing metabolic compound is added under labelled form. In the following *chase* phase, the medium is replaced by medium contained the unlabelled metabolic compound. Whereas in a regular pulse-chase experiment the metabolic compounds are usually radiolabelled, the results presented in Chapter VII suggest the utility of stable isotopes as an alternative. While radiolabelled molecules are generally cheaper than their stable equivalents, the use of stable isotopes does not require the safety measures that precede the use of radioisotopes. Furthermore, as stable isotopes do not decay, the samples are valid for longer periods of time.

Closing Words – Personal Opinion

When studying SIMS literature, life science made its first notable appearance in the eighties and nineties by a large number of prospective papers that assessed the first SIMS ion microscopes and their potentiality for biology. A period of almost ten years followed, during which the literary output slowed down to a trickle until the release of the NanoSIMS. The main reason preventing its large-scale dissemination in life science laboratories are the maintenance and reproducibility issues that still have to be addressed. However, it has become clear that the NanoSIMS features several unique capabilities that make it an attractive tool for the study of trace elements, the study of protein turnover and the imaging of isotopically labelled molecules.

Nevertheless, interested parties should not rely on NanoSIMS alone, and should complement their studies with alternative techniques. The wealth and the technological advancement at the disposal of today's scientist have been addressed in the article of Roger Y. Tsien about the future of imaging, where he predicts the advent of imaging techniques that would permit the

visualisation of biomolecules at high resolution (Tsien 2003). The NanoSIMS confirms this trend, earning its right to the hall of fame of emerging imaging techniques. The schematic representation of novel visualisation systems (Figure 74, adapted Figure 1, Chapter I) has been updated adequately to accurately position ion microscopy amidst its competitors. The small area held by NanoSIMS, mostly overlaps with EM, which has the same fixation dependant duality that impacts on time resolution (Figure 74A).

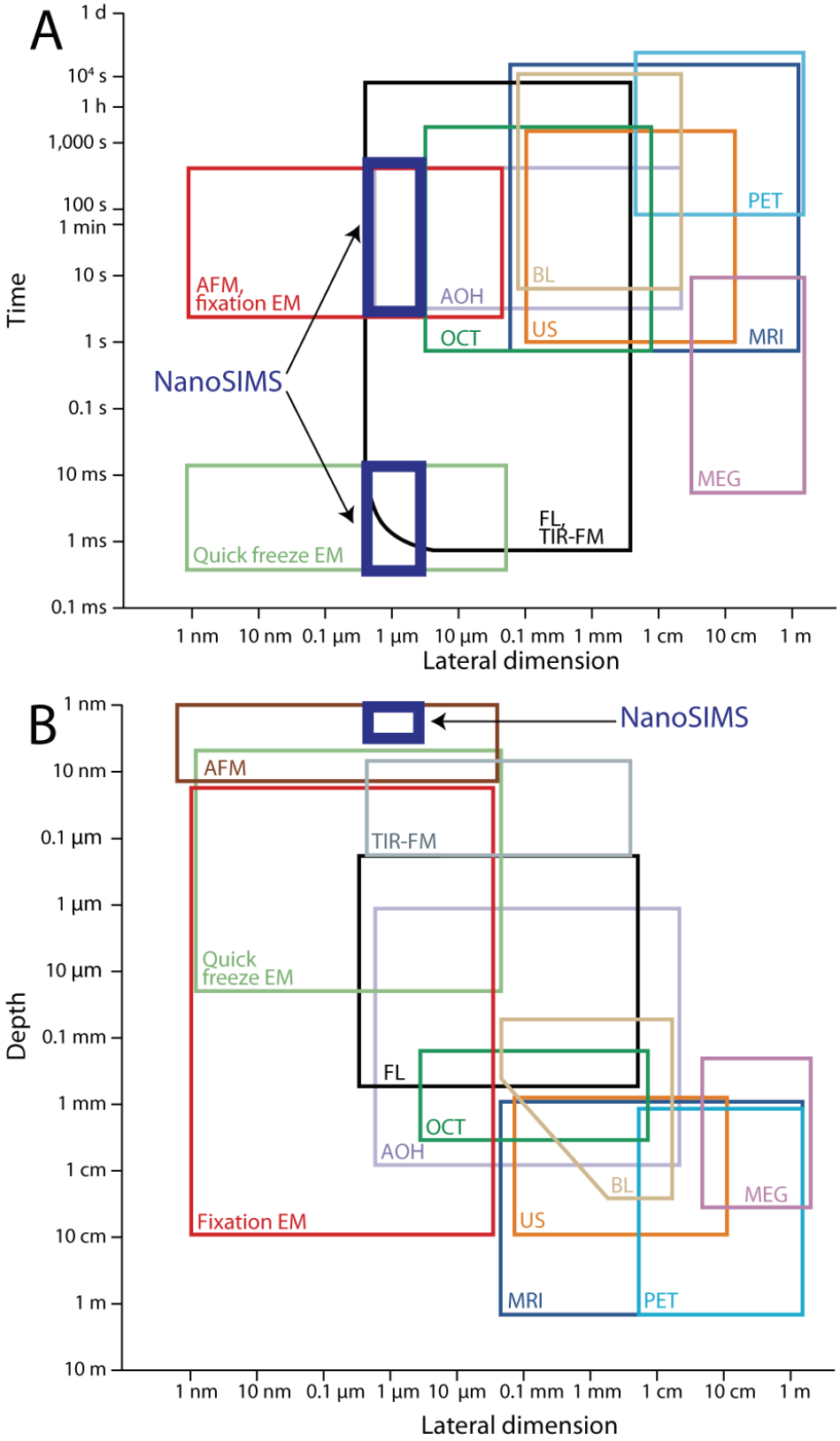

Figure 74 : The schematic representation of imaging methods shown in Chapter I: Introduction was adapted to show the NanoSIMS. *The legend of the imaging techniques can be found in the original figure (Figure 1) (A) NanoSIMS is represented by two dark blue rectangles. The upper rectangle corresponds to the observation of chemically fixed samples. The lower rectangle corresponds to cryofixed samples. (B) NanoSIMS is located by a dark*

blue rectangle. The original figure is reproduced with permission from Nature Reviews Molecular Cell Biology (Tsien 2003) copyright (2003) Macmillan Magazines Ltd.

Strikingly, even with its similar depth resolution, the actual surface representing NanoSIMS is less pronounced than atomic force microscopy. As this illustration does not account for specificities of the presented imaging methods (e.g. ion mapping in NanoSIMS) and only compares general imaging parameters such as lateral, depth and time resolution, it may seem an excessive simplification of the ion microprobe. Defined in *Chapter I: Introduction* for SIMS, TEM and confocal microscopy, the notion of resolution is totally arbitrary and depends solely on the technique. Consequently, it does not necessarily credit the technique most fitting for a specific application. However, by mainly considering resolutive aspects, the illustration sets all the imaging techniques to a common denominator and therein may lie the most simple explanation for the apparent slow acceptance of SIMS.

If dedicated solely to imaging, many alternatives to ion microprobe exist that offer imaging at better resolution, faster sample throughput and easier handling. For the identification of elements, other techniques easier to use, are available, such as GCMS, which also offers absolute quantification. It is only at the borderline between both approaches that NanoSIMS offers genuine advantages to researchers that agree to the trade-offs in resolution and quantification of elements. NanoSIMS is then relayed to the purpose of bridging other techniques, whose role becomes apparent in the validation of otherwise deadlocked hypothesis. Rather than hoping to cover ground held by the big names in microscopy, such as TEM, SEM and confocal microscopy, NanoSIMS should nest itself in those applications that rely most on the attributes of the techniques.

In his *Memoir on Inventing the Confocal Scanning Microscope*, Marvin Minsky stated that "*The price of single-point illumination is being able to measure only one point at a time.*" (Minsky 1988). Behind the obvious statement about the time consuming process of scanning microscopy (including the NanoSIMS), hides another problem. The smaller the point of illumination (e.g. the resolution), the least the signal that can be extracted. In confocal microsopy, the area targeted by a *single-point illumination* can only take up a limited amount of energy and emit a limited amount of photons as fluorescence. Similarly, in SIMS, the spot diameter of the primary beam defines the microvolume of extraction and thus high-resolution SIMS corresponds to a reduced extraction of ions. To partially counteract this phenomenon, brighter primary ion sources are currently under development, which present a higher density of ions to increase the extraction in primary ion beams of smaller diameter (oral presentation

at SIMS XVI, 29.10-2.11 2007, Kanazawa, JP by N. Smith, entitled "*A New High Brightness Source For NanoProbe Secondary Ion Mass Spectrometry"*).

However, the lateral and depth resolution of SIMS, as the ability to detail small features, may not always be favourable to ion imaging and its utility should be balanced against the expected elemental concentration.

As illustrated in Figure 74, the growing number of imaging techniques results in an increased overlap and competition amongst them is unavoidable. This further confirms my recommendation to position NanoSIMS in several chosen applications where it is best suited. An article from the early nineties identified and discussed the merits and disadvantages of the main competitors of microprobe techniques for compositional imaging and grouped them as: (i) analytical electron microscopy (e.g. TEM, SEM, EELS), (ii) X-Ray microprobe (EDS, XPS), (iii) nuclear microprobe (e.g. PIXE), (iv) laser microprobe mass spectrometry (e.g. LAMMS) and (v) SIMS (Linton and Goldsmith 1992). Other promising techniques, such as near-field Raman microscopy may tip the scale in favour of non-invasive optical compositional imaging. Combining near-field optics and Raman microscopy, it breaks the resolution barrier of 200 nm set by the diffraction of light in standard optics, and achieves an unsurpassed resolution of 15 nm (Anderson, Hartschuh et al. 2005).

It is interesting to note that in 1992 Richard Linton and Jack Goldsmith already discussed the future of SIMS and concluded that the main contribution of SIMS would be in the fields of physiological and trace elements, and that the main challenge of SIMS would be the quantitative imaging at high resolution. The preceding chapters on isotopic imaging have shown that the NanoSIMS, at the pinnacle of imaging dynamic SIMS, is well suited to address these points.

This century has seen the rise and progress of a wealth of new ways to observe our surroundings, all witnessing the ingenuity of humankind. However, it all started with a simple piece of glass in the hands of a curious mind, bridging the gap from *seeing* to *understanding*.

References

Aebersold, R. and M. Mann (2003). "Mass spectrometry-based proteomics." Nature **422**(6928): 198-207.

Aebi, M., J. Fah, et al. (1989). "cDNA structures and regulation of two interferon-induced human Mx proteins." Mol Cell Biol **9**(11): 5062-72.

Anderson, N., A. Hartschuh, et al. (2005). "Near-field Raman microscopy." Materials Today **8**(5): 50.

Armbruster, B. L., E. Carlemalm, et al. (1982). "Specimen preparation for electron microscopy using low temperature embedding resins." J Microsc **126**(Pt 1): 77-85.

Asta, J., W. Erhardt, et al. (2002). "Mapping lichen diversity as an indicator of environmental quality." 273-9.

Audinot, J. N., S. Schneider, et al. (2004). "Imaging of arsenic traces in human hair by nano-SIMS 50." Applied Surface Science **231-232**: 490.

Ayrault, S., R. Clochiatti, et al. (2007). "Factors to consider for trace element deposition biomonitoring surveys with lichen transplants." Science of The Total Environment **372**(2-3): 717.

Babul, J. and E. Stellwagen (1969). "Measurement of protein concentration with interferences optics." Anal Biochem **28**(1): 216-21.

Balaguer, L., F. Valladares, et al. (1996). "Potential effects of rising tropospheric concentrations of CO2 and O3 on green-algal lichens." New Phytologist **132**(4): 641-652.

Baron, S., A. Caplanusi, et al. (2005). "Role of mitochondrial Na+ concentration, measured by CoroNa red, in the protection of metabolically inhibited MDCK cells." J Am Soc Nephrol **16**(12): 3490-7.

Bennett, J. P. and C. M. Wetmore (1999). "Changes in element contents of selected lichens over 11 years in northern Minnesota, USA." Environmental and Experimental Botany **41**(1): 75.

Benninghoven, A. (1969). "Analysis of submonolayers on silver by negatice secondary ion emission." Phys. Status Solidi **34**(K169): 71.

Benninghoven, A., F. G. Rüdenauer, et al. (1987). Secondary Ion Mass Spectrometry: Basic Concepts, Instrumental Aspects, Applications, and Trends. New York, Wiley.

Benson, D. (2007). NRIMS analysis module, National Resource for Imaging Mass Spectrometry.

Benson, D. and C. Lechene (2005). "Quantitating MIMS Ratios Using Hue, Saturation, and Intensity Displays."

Berry, J. P. (1996). "The role of lysosomes in the selective concentration of mineral elements. A microanalytical study." Cell Mol Biol (Noisy-le-grand) **42**(3): 395-411.

Besmehn, A. and P. Hoppe (2003). "A NanoSIMS study of Si- and Ca-Ti-isotopic compositions of presolar silicon carbide grains from supernovae." Geochimica et Cosmochimica Acta **67**(24): 4693.

Biersack, J. P. and W. Eckstein (1984). "Sputtering studies with the Monte Carlo Program TRIM.SP." Applied Physics A: Materials Science & Processing **34**(2): 73.

Biersack, J. P. and L. G. Haggmark (1980). "A Monte Carlo computer program for the transport of energetic ions in amorphous targets." Nucl. Instr. and Meth. **174**: 257.

Bohn, W. (1978). "A fixation method for improved antibody penetration in electron microscopical immunoperoxidase studies." J Histochem Cytochem **26**(4): 293-7.

Briancon, C., J. Jeusset, et al. (1992). "Significance of SIMS microscopy for the radioiodine detection in animal and human thyroid tissue." Biol Cell **74**(1): 75-80.

Budka, D., W. J. Przybylowicz, et al. (2002). "Elemental distribution in lichens transplanted to polluted forest sites near Krakow (Poland)." Nuclear Instruments and Methods in Physics Research Section B: Beam Interactions with Materials and Atoms **189**: 499.

Caprioli, R. M., T. B. Farmer, et al. (1997). "Molecular imaging of biological samples: localization of peptides and proteins using MALDI-TOF MS." Anal Chem **69**(23): 4751-60.

Carlemalm, E., J. D. Acetarin, et al. (1982). "Heavy metal-containing surroundings provide much more "negative" contrast by Z-imaging in STEM than with conventional modes." J Ultrastruct Res **80**(3): 339-43.

Carlemalm, E., R. M. Garavito, et al. (1982). "Resin development for electron microscopy and an analysis of embedding at low temperature." J Microsc(126): 123-143.

Castaing, R. and G. Slodzian (1962). "Microanalyse par émission ionique secondaire." J Microscopy(1): 395-410.

Chabala, J. M., S. Edward, et al. (1988). "Elemental imaging of dental hard tissues by secondary ion mass spectrometry." Swed Dent J **12**(5): 201-12.

Chandra, S., W. A. Ausserer, et al. (1987). "Evaluation of matrix effects in ion microscopic analysis of freeze-fractured, freeze-dried cultured cells." J Microsc **148**(Pt 3): 223-9.

Chandra, S., W. A. Ausserer, et al. (1992). "Subcellular imaging of calcium exchange in cultured cells with ion microscopy." J Cell Sci **102 (Pt 3)**: 417-25.

Chandra, S., C. Fewtrell, et al. (1994). "Imaging of total intracellular calcium and calcium influx and efflux in individual resting and stimulated tumor mast cells using ion microscopy." J Biol Chem **269**(21): 15186-94.

Chandra, S., C. S. Fullmer, et al. (1990). "Ion microscopic imaging of calcium transport in the intestinal tissue of vitamin D-deficient and vitamin D-replete chickens: a 44Ca stable isotope study." Proc Natl Acad Sci U S A **87**(15): 5715-9.

Chandra, S. and G. H. Morrison (1988). "Ion microscopy in biology and medicine." Methods Enzymol **158**: 157-79.

Chandra, S. and G. H. Morrison (1992). "Sample preparation of animal tissues and cell cultures for secondary ion mass spectrometry (SIMS) microscopy." Biol Cell **74**(1): 31-42.

Chehade, F., C. de Labriolle-Vaylet, et al. (2005). "Secondary ion mass spectrometry as a tool for investigating radiopharmaceutical distribution at the cellular level: the example of I-BZA and (14)C-I-BZA." J Nucl Med **46**(10): 1701-6.

Chehade, F., J. Michelot, et al. (1996). "Localization of N-(2-diethylaminoethyl)4-iodobenzamide in the pigmented mouse eye: a microanalytical study." Cell Mol Biol (Noisy-le-grand) **42**(3): 343-50.

Clark, B. M., N. F. Mangelson, et al. (1999). "Analysis of lichen thin sections by PIXE and STIM using a proton microprobe." Nuclear Instruments and Methods in Physics Research Section B: Beam Interactions with Materials and Atoms **150**(1-4): 248.

Cohen, S. L. and B. T. Chait (1996). "Influence of matrix solution conditions on the MALDI-MS analysis of peptides and proteins." Anal Chem **68**(1): 31-7.

Conti, M. E., M. Tudino, et al. (2004). "Heavy Metal Accumulation in the Lichen Evernia prunastri Transplanted at Urban, Rural and Industrial Sites in Central Italy." Journal of Atmospheric Chemistry **49**(1): 83.

Crewe, A. V., J. Wall, et al. (1970). "Visibility of Single Atoms." Science **168**(3937): 1338-1340.

Cuny, D. (1999). Communal, physiological and cellular impacts of metal trace elements on lichenic symbiosis evidencing tolerance mechanisms in Diploschistes muscorum (Scop.) Université de Lille.

Dauphas, N. and O. Rouxel (2006). "Mass spectrometry and natural variations of iron isotopes." Mass Spectrom Rev **25**(4): 515-50.

Davidovits, P. and M. D. Egger (1973). "Photomicrography of corneal endothelial cells in vivo." Nature **244**(5415): 366-7.

Dickinson, M., P. J. Heard, et al. (2006). "Dynamic SIMS analysis of cryo-prepared biological and geological specimens." Applied Surface Science **252**(19): 6793.

Eylar, E. H., S. Brostoff, et al. (1971). "Basic A1 Protein of the Myelin Membrane. The complete amino acid sequence." J. Biol. Chem. **246**(18): 5770-5784.

Fahey, A. J., G. Gillen, et al. (2006). "Performance of a C60+ ion source on a dynamic SIMS instrument." Applied Surface Science **252**(19): 7312.

Fenton, M. J. and D. T. Golenbock (1998). "LPS-binding proteins and receptors." J Leukoc Biol **64**(1): 25-32.

Finck, H. (1960). "Epoxy Resins in Electron Microscopy." J. Cell Biol. **7**(1): 27-30.

Fink, L., W. Seeger, et al. (1998). "Real-time quantitative RT-PCR after laser-assisted cell picking." Nat Med **4**(11): 1329-33.

Floss, C., F. J. Stadermann, et al. (2006). "Identification of isotopically primitive interplanetary dust particles: A NanoSIMS isotopic imaging study." Geochimica et Cosmochimica Acta **70**(9): 2371.

Foundation, F. S. "GNU General Public License." from http://www.gnu.org/licenses/gpl.html.

Fournel, S., S. Wieckowski, et al. (2005). "C3-symmetric peptide scaffolds are functional mimetics of trimeric CD40L." Nat Chem Biol **1**(7): 377-82.

Fournier, P. (1997). Defintion of functional activities of antibodies against linear epitopes of measles virus proteins. Laboratoire National de Santé - Département d'Immunologie. Luxemburg, Eberhardt-Karls-Universität Tübingen. **PhD**.

Fournier, P., W. Ammerlaan, et al. (1996). "Differential activation of T cells by antibody-modulated processing of the flanking sequences of class II-restricted peptides." Int Immunol **8**(9): 1441-51.

Fraschini, A., C. Pellicciari, et al. (1981). "The effect of different fixatives on chromatin: cytochemical and ultrastructural approaches." Histochem J **13**(5): 763-9.

Frese, M., G. Kochs, et al. (1996). "Inhibition of bunyaviruses, phleboviruses, and hantaviruses by human MxA protein." J Virol **70**(2): 915-23.

Frese, M., G. Kochs, et al. (1995). "Human MxA protein inhibits tick-borne Thogoto virus but not Dhori virus." J Virol **69**(6): 3904-9.

Fuoco, E. R., G. Gillen, et al. (2001). "Surface Analysis Studies of Yield Enhancements in Secondary Ion Mass Spectrometry by Polyatomic Projectiles." J. Phys. Chem. B **105**(18): 3950-3956.

Gaio-Oliveira, G., L. Dahlman, et al. (2005). "Nitrogen uptake in relation to excess supply and its effects on the lichens Evernia prunastri (L.) Ach and Xanthoria parietina (L.) Th. Fr." Planta **220**(5): 794-803.

Gaio-Oliveira, G., L. Dahlman, et al. (2005). "Nitrogen uptake in relation to excess supply and its effects on the lichens Evernia prunastri (L.) Ach and Xanthoria parietina (L.) Th. Fr." Planta **220**(5): 794.

Galiano, M. R., A. Andrieux, et al. (2006). "Myelin basic protein functions as a microtubule stabilizing protein in differentiated oligodendrocytes." J Neurosci Res **84**(3): 534-41.

Galle, P. (1982). "Tissue Localization of Stable and Radioactive Nuclides by Secondary-Ion Microscopy." J Nucl Med **23**(1): 52-57.

Galle, P. (1991). "Cartographies moléculaires ultrastructurales par microscopie ionique." **7**(9): 944-952.

Galle, P., R. Levi-Setti, et al. (2004). "Subcellular localization of aluminum and indium in the rat kidney." Applied Surface Science **231-232**: 475.

Galli Marxer, C., M. L. Kraft, et al. (2005). "Supported Membrane Composition Analysis by Secondary Ion Mass Spectrometry with High Lateral Resolution." Biophysical Journal **88**(4): 2965.

Gao, Y. (1988). "A new secondary ion mass spectrometry technique for III-V semiconductor compounds using the molecular ions CsM[sup +]." Journal of Applied Physics **64**(7): 3760.

Garrison, B. J., A. Delcorte, et al. (2003). "Big molecule ejection--SIMS vs. MALDI." Applied Surface Science **203-204**: 69.

Gilbert, R. J., L. Beales, et al. (2005). "Hepatitis B small surface antigen particles are octahedral." Proc Natl Acad Sci U S A **102**(41): 14783-8.

Glauert, A. M. and R. H. Glauert (1958). "Araldite as an embedding medium for electron microscopy." J Biophys Biochem Cytol **4**(2): 191-4.

Glauert, A. M., R. H. Glauert, et al. (1956). "A new embedding medium for electron microscopy." Nature **178**(4537): 803.

Gloser, J. (2002). "Kranner, I., Beckett, R.P., Varma, A.K. (ed.): Protocols in Lichenology: Culturing, Biochemistry, Ecophysiology and Use in Biomonitoring." Photosynthetica **40**(3): 348.

Gnaser, H. (1995). "Correlations in secondary-ion yields from Cs-implanted semiconductors." Surface Science **342**(1-3): 319.

Goldenthal, K. L., K. Hedman, et al. (1985). "Postfixation detergent treatment for immunofluorescence suppresses localization of some integral membrane proteins." J Histochem Cytochem **33**(8): 813-20.

Gomori, G. (1952). Microscopic Histochemistry: Principles and Practice. Chicago, The University of Chicago Press.

Gonzalez, R. C., R. E. Woods, et al. (2004). Digital Image Processing using Matlab, Prentice Hall.

Grovenor, C. R. M., K. E. Smart, et al. (2006). "Specimen preparation for NanoSIMS analysis of biological materials." Applied Surface Science **252**(19): 6917.

Guerquin-Kern, J. L., M. Coppey, et al. (1997). "Complementary advantages of fluorescence and SIMS microscopies in the study of cellular localization of two new antitumor drugs." Microscopy Research And Technique **36**(4): 287.

Guerquin-Kern, J. L., F. Hillion, et al. (2004). "Ultra-structural cell distribution of the melanoma marker iodobenzamide: improved potentiality of SIMS imaging in life sciences." Biomed Eng Online **3**: 10.

Guerquin-Kern, J. L., T. D. Wu, et al. (2005). "Progress in analytical imaging of the cell by dynamic secondary ion mass spectrometry (SIMS microscopy)." Biochim Biophys Acta **1724**(3): 228-38.

Haguenau, F., P. W. Hawkes, et al. (2003). "Key events in the history of electron microscopy." Microsc Microanal **9**(2): 96-138.

Hallegot, P., J. N. Audinot, et al. (2006). "Direct NanoSIMS imaging of diffusible elements in surfaced block of cryo-processed biological samples." Applied Surface Science **252**(19): 6706.

Hallegot, P., C. Girod, et al. (1990). "Scanning ion microprobe assessment of biological sample preparation techniques." Scanning Microsc **4**(3): 605-12.

Hallegot, P., R. Peteranderl, et al. (2004). "In-situ imaging mass spectrometry analysis of melanin granules in the human hair shaft." J Invest Dermatol **122**(2): 381-6.

Hellebrand, E., J. Snow, et al. (2005). "Trace element distribution between orthopyroxene and clinopyroxene in peridotites from the Gakkel Ridge: a SIMS and NanoSIMS study." Contributions to Mineralogy and Petrology **150**(5): 486.

Herrmann, A. M., P. L. Clode, et al. (2007). "A novel method for the study of the biophysical interface in soils using nano-scale secondary ion mass spectrometry." Rapid Commun Mass Spectrom **21**(1): 29-34.

Hill, R., P. Blenkinsopp, et al. (2006). "The development of a range of C60 ion beam systems." Applied Surface Science **252**(19): 7304.

Hillenkamp, F., M. Karas, et al. (1991). "Matrix-assisted laser desorption/ionization mass spectrometry of biopolymers." Anal Chem **63**(24): 1193A-1203A.

Hillion, F., B. Daigne, et al. (1993). A new high performance instrument: the Cameca Nanosims 50,. Proceedings IXth Conference on SIMS, Yokohama, Elsevier.

Hindie, E., P. Hallegot, et al. (1988). "Ion microscopy: a new approach for subcellular localization of labelled molecules." Scanning Microsc **2**(4): 1821-9.

Holopainen, T. and L. Karenlampi (1984). "Injuries to lichen ultrastructure caused by sulphur dioxide fumigations." New Phytologist **98**(2): 285-294.

Hoppe, P. (2006). "NanoSIMS: A new tool in cosmochemistry." Applied Surface Science **252**(19): 7102.

Hopwood, D. (1967). "Some aspects of fixation with glutaraldehyde. A biochemical and histochemical comparison of the effects of formaldehyde and glutaraldehyde fixation on various enzymes and glycogen, with a note on penetration of glutaraldehyde into liver." J Anat **101**(Pt 1): 83-92.

Hunt, D. F., R. A. Henderson, et al. (1992). "Characterization of peptides bound to the class I MHC molecule HLA-A2.1 by mass spectrometry." Science **255**(5049): 1261-3.

Johannes, L. (2002). "The epithelial cell cytoskeleton and intracellular trafficking. I. Shiga toxin B-subunit system: retrograde transport, intracellular vectorization, and more." Am J Physiol Gastrointest Liver Physiol **283**(1): G1-7.

Johannes, L. and B. Goud (1998). "Surfing on a retrograde wave: how does Shiga toxin reach the endoplasmic reticulum?" Trends Cell Biol **8**(4): 158-62.

John, C. S., W. D. Bowen, et al. (1993). "A malignant melanoma imaging agent: synthesis, characterization, in vitro binding and biodistribution of iodine-125-(2-piperidinylaminoethyl)4-iodobenzamide." J Nucl Med **34**(12): 2169-75.

Johnson, R. S. and K. Biemann (1989). "Computer program (SEQPEP) to aid in the interpretation of high-energy collision tandem mass spectra of peptides." Biomed Environ Mass Spectrom **18**(11): 945-57.

Kanerva, M., K. Melen, et al. (1996). "Inhibition of puumala and tula hantaviruses in Vero cells by MxA protein." Virology **224**(1): 55-62.

Karas, M. and F. Hillenkamp (1988). "Laser desorption ionization of proteins with molecular masses exceeding 10,000 daltons." Anal Chem **60**(20): 2299-301.

Kellenberger, E., E. Carlemalm, et al. (1981). "In vitro studies of the fixation of DNA, nucleoprotamine, nucleohistone and proteins." Eur J Cell Biol **25**(1): 1-4.

Kellenberger, E., E. Carlemalm, et al. (1986). "Z-contrast in biology. A comparison with other imaging modes." Ann N Y Acad Sci **483**: 202-28.

Kerdiles, Y. M., C. I. Sellin, et al. (2006). "Immunosuppression caused by measles virus: role of viral proteins." Reviews in Medical Virology **16**(1): 49-63.

Kim, K. H., C. Buehler, et al. (1999). "High-Speed, Two-Photon Scanning Microscope." Applied Optics **38**(28): 6004-6009.

Kim, M. J., I. H. Liu, et al. (2007). "Agrin is required for posterior development and motor axon outgrowth and branching in embryonic zebrafish." Glycobiology **17**(2): 231-247.

Klumpp, C., L. Lacerda, et al. (2007). "Multifunctionalised cationic fullerene adducts for gene transfer: design, synthesis and DNA complexation." Chem Commun (Camb)(36): 3762-4.

Knoll, M. and E. Ruska (1932). "Das elektonenmikroskop." Zeitschrift fur Physik(78): 318-329.

Kochs, G. and O. Haller (1999). "Interferon-induced human MxA GTPase blocks nuclear import of Thogoto virus nucleocapsids." Proc Natl Acad Sci U S A **96**(5): 2082-6.

Kochs, G., C. Janzen, et al. (2002). "Antivirally active MxA protein sequesters La Crosse virus nucleocapsid protein into perinuclear complexes." Proc Natl Acad Sci U S A **99**(5): 3153-8.

Kochs, G., M. Trost, et al. (1998). "MxA GTPase: oligomerization and GTP-dependent interaction with viral RNP target structures." Methods **15**(3): 255-63.

Kohn, E. C., M. A. Sandeen, et al. (1992). "In Vivo Efficacy of a Novel Inhibitor of Selected Signal Transduction Pathways Including Calcium, Arachidonate, and Inositol Phosphates." Cancer Res **52**(11): 3208-3212.

Kraft, M. L., S. F. Fishel, et al. (2006). "Quantitative analysis of supported membrane composition using the NanoSIMS." Applied Surface Science **252**(19): 6950.

Krein, A., J. N. Audinot, et al. (2007). "Facing hazardous matter in atmospheric particles with NanoSIMS." Environ Sci Pollut Res Int **14**(1): 3-4.

Kussmann, M., U. Lassing, et al. (1997). "Matrix-assisted laser desorption/ionization mass spectrometric peptide mapping of the neural cell adhesion protein neurolin purified by sodium dodecyl sulfate polyacrylamide gel electrophoresis or acidic precipitation." J Mass Spectrom **32**(5): 483-93.

Land, C. M. and G. R. Kinsel (2001). "The mechanism of matrix to analyte proton transfer in clusters of 2,5-dihydroxybenzoic acid and the tripeptide VPL." J Am Soc Mass Spectrom **12**(6): 726-31.

Leapman, R. D., P. E. Gallant, et al. (1997). "Phosphorylation and subunit organization of axonal neurofilaments determined by scanning transmission electron microscopy." Proc Natl Acad Sci U S A **94**(15): 7820-4.

Lechene, C. and J. Bonventre (2003). "DNA replication and protein turn-over in post-ischemic kidney repair studied with multi-isotope imaging mass spectrometry (MIMS)." 14th International conference on Secondary Ion Mass Spectrometry (SIMS XIV).

Lechene, C., F. Hillion, et al. (2006). "High-resolution quantitative imaging of mammalian and bacterial cells using stable isotope mass spectrometry." J Biol **5**(6): 20.

Lees, M. B., B. H. Chao, et al. (1983). "Amino acid sequence of bovine white matter proteolipid." Arch Biochem Biophys **226**(2): 643-56.

Levi-Setti, R. (1988). "Structural and microanalytical imaging of biological materials by scanning microscopy with heavy-ion probes." Annu Rev Biophys Biophys Chem **17**: 325-47.

Levi-Setti, R., J. M. Chabala, et al. (1997). "Imaging of BrdU-labeled human metaphase chromosomes with a high resolution scanning ion microprobe." Microsc Res Tech **36**(4): 301-12.

Levi-Setti, R., J. M. Chabala, et al. (1994). "Nucleotide and protein distribution in BrdU-labelled polytene chromosomes revealed by ion probe mass spectrometry." J Microsc **175**(Pt 1): 44-53.

Lhuissier, F., F. Lefebvre, et al. (2000). "Secondary ion mass spectrometry imaging of the fixation of 15N-labelled NO in pollen grains." J Microsc **198 (Pt 2)**: 108-15.

Linton, R. W. and J. G. Goldsmith (1992). "The role of secondary ion mass spectrometry (SIMS) in biological microanalysis: technique comparisons and prospects." Biol Cell **74**(1): 147-60.

Lodding, A. (1983). "Quantitative ion probe microanalysis of biological mineralized tissues." Scan Electron Microsc(Pt 3): 1229-42.

Lorey, D. R., 2nd, G. H. Morrison, et al. (2001). "Dynamic secondary ion mass spectrometry analysis of boron from boron neutron capture therapy drugs in co-cultures: single-cell imaging of two different cell types within the same ion microscopy field of imaging." Anal Chem **73**(16): 3947-53.

Lucy, J. A. and A. M. Glauert (1964). "Structure And Assembly Of Macromolecular Lipid Complexes Composed Of Globular Micelles." J Mol Biol **8**: 727-48.

Luft, J. (1961). J. Biophys. Biochem. Cytol. **9**: 409.

Lundgren, T., L. G. Persson, et al. (1998). "A secondary ion mass spectroscopic study of the elemental composition pattern in rat incisor dental enamel during different stages of ameloblast differentiation." Arch Oral Biol **43**(11): 841-8.

Mallard, F., C. Antony, et al. (1998). "Direct pathway from early/recycling endosomes to the Golgi apparatus revealed through the study of shiga toxin B-fragment transport." J Cell Biol **143**(4): 973-90.

Mayer, L. (2000). "Mucosal immunity and gastrointestinal antigen processing." J Pediatr Gastroenterol Nutr **30 Suppl**: S4-12.

Mazarov, P., A. V. Samartsev, et al. (2006). "Determination of energy dependent ionization probabilities of sputtered particles." Applied Surface Science **252**(19): 6452.

McDonnell, L. A. and R. M. Heeren (2007). "Imaging mass spectrometry." Mass Spectrom Rev **26**(4): 606-43.

McMahon, G., B. J. Glassner, et al. (2006). "Quantitative imaging of cells with multi-isotope imaging mass spectrometry (MIMS)--Nanoautography with stable isotope tracers." Applied Surface Science **252**(19): 6895.

Medzhitov, R. and C. Janeway, Jr. (2000). "The Toll receptor family and microbial recognition." Trends Microbiol **8**(10): 452-6.

Millanes, A. M., B. Fontaniella, et al. (2004). "Cytochemical location of urease in the cell wall of two different lichen phycobionts." Tissue Cell **36**(6): 373-7.

Minsky, M. (1988). "Memoir on Inventing the Confocal Scanning Microscope." Scanning **10**: 128-138.

Miwa, S., I. Nomachi, et al. (2006). "SIMS analysis using a new novel sample stage." Applied Surface Science **252**(19): 7318.

Molina, M. C., E. Muniz, et al. (1993). "Enzymatic activities of algalbinding protein and its algal cell wall receptor in the lichen Xanthoria parietina. An approach to the parasitic basis of mutualism." Plant Physiol. Biochem. **31**: 131–142.

Moller, W. and W. Eckstein (1984). "Tridyn -- A TRIM simulation code including dynamic composition changes." Nuclear Instruments and Methods in Physics Research Section B: Beam Interactions with Materials and Atoms **2**(1-3): 814.

Moller, W., W. Eckstein, et al. (1988). "Tridyn-binary collision simulation of atomic collisions and dynamic composition changes in solids." Computer Physics Communications **51**(3): 355.

Mony, M. C. and E. Larras-Regard (1997). "Imaging of subcellular structures by scanning ion microscopy and mass spectrometry. Advantage of cryofixation and freeze substitution procedure over chemical preparation." Biology of the Cell **89**(3): 199.

Mostefaoui, S., G. W. Lugmair, et al. (2004). "Evidence for live 60Fe in meteorites." New Astronomy Reviews **48**(1-4): 155.

Nash, T. H. I. (1996). Photosynthesis, respiration, productivity and growth. Lichen Biology. T. H. N. III. Cambridge, Cambridge University Press**:** 88-120.

Nelson, A. C. (1988). Scanning electron microscope for visualization of wet samples. U. P. Office. United States of America, Electro-Scan Corporation.

Nimis, P. L., M. Castello, et al. (1990). "Lichens as Biomonitors of Sulphur Dioxide Pollution in La Spezia (Northern Italy)." The Lichenologist **22**(03): 333.

Palade, G. E. (1952). "A study of fixation for electron microscopy." J Exp Med **95**(3): 285-98.

Pavlovic, J., H. A. Arzet, et al. (1995). "Enhanced virus resistance of transgenic mice expressing the human MxA protein." J Virol **69**(7): 4506-10.

Pavlovic, J., O. Haller, et al. (1992). "Human and mouse Mx proteins inhibit different steps of the influenza virus multiplication cycle." J Virol **66**(4): 2564-9.

Pavlovic, J., T. Zurcher, et al. (1990). "Resistance to influenza virus and vesicular stomatitis virus conferred by expression of human MxA protein." J Virol **64**(7): 3370-5.

Peteranderl, R. and C. Lechene (2004). "Measure of carbon and nitrogen stable isotope ratios in cultured cells." J Am Soc Mass Spectrom **15**(4): 478-85.

Pino, A., A. Alimonti, et al. (2007). "Determination of twenty-five elements in lichens by sector field inductively coupled plasma mass spectrometry and microwave-assisted acid digestion." Rapid Communications in Mass Spectrometry **21**(12): 1900-1906.

Pirrotte, P., J. N. Audinot, et al. (2006). ImageJ plugin based on ImageIO to extract images and data from Cameca Secondary Ion Mass Spectrometer data files. First ImageJ User and Developer Conference. Luxembourg.

Pirrotte, P. and J. Mutterer (2004). "Image Gallery Database: multi-user image management software " Microscopy and Analysis **18**(5): 13-15.

Poenie, M., J. Alderton, et al. (1986). "Calcium rises abruptly and briefly throughout the cell at the onset of anaphase." Science **233**(4766): 886.

Quintana, C. (1994). "Cryofixation, cryosubstitution, cryoembedding for ultrastructural, immunocytochemical and microanalytical studies." Micron **25**(1): 63-99.

Quintana, C., S. Bellefqih, et al. (2006). "Study of the localization of iron, ferritin, and hemosiderin in Alzheimer's disease hippocampus by analytical microscopy at the subcellular level." J Struct Biol **153**(1): 42-54.

Quintana, C., T. D. Wu, et al. (2007). "Morphological and chemical studies of pathological human and mice brain at the subcellular level: correlation between light, electron, and nanosims microscopies." Microscopy Research And Technique **70**(4): 281.

Ramachandra, L., R. S. Chu, et al. (1999). "Phagocytic antigen processing and effects of microbial products on antigen processing and T-cell responses." Immunol Rev **168**: 217-39.

Roepstorff, P. and J. Fohlman (1984). "Proposal for a common nomenclature for sequence ions in mass spectra of peptides." Biomed Mass Spectrom **11**(11): 601.

Römer, W., T. D. Wu, et al. (2006). "Sub-cellular localisation of a 15N-labelled peptide vector using NanoSIMS imaging." Applied Surface Science **252**(19): 6925.

Roth, M. P., L. Malfroy, et al. (1995). "The human myelin oligodendrocyte glycoprotein (MOG) gene: complete nucleotide sequence and structural characterization." Genomics **28**(2): 241-50.

Rothman, J. H., C. K. Raymond, et al. (1990). "A putative GTP binding protein homologous to interferon-inducible Mx proteins performs an essential function in yeast protein sorting." Cell **61**(6): 1063-74.

Rouse, J. C., W. Yu, et al. (1995). "A comparison of the peptide fragmentation obtained from a reflector matrix-assisted laser desorption-ionization time-of-flight and a tandem four sector mass spectrometer." Journal of the American Society for Mass Spectrometry **6**(9): 822.

Sabatini, D. D., K. Bensch, et al. (1963). "Cytochemistry and electron microscopy. The preservation of cellular ultrastructure and enzymatic activity by aldehyde fixation." J Cell Biol **17**: 19-58.

Sanita Di Toppi, L., R. Musetti, et al. (2004). "Responses of Xanthoria parietina thalli to environmentally relevant concentrations of hexavalent chromium." Functional Plant Biology **31**(4): 329-338.

Sanita Di Toppi, L., R. Musetti, et al. (2005). "Cadmium distribution and effects on ultrastructureand chlorophyll status in photobionts and mycobionts of Xanthoria parietina." Microscopy Research and Technique **66**(5): 229-238.

Scheidegger, C. and B. Schroeter (1995). "Effects of ozone fumigation on epiphytic macrolichens: ultrastructure, CO2 gas exchange and chlorophyll fluorescence." Environ Pollut **88**(3): 345-54.

Schneider-Schaulies, S., J. Schneider-Schaulies, et al. (1994). "Cell type-specific MxA-mediated inhibition of measles virus transcription in human brain cells." J Virol **68**(11): 6910-7.

Schnorr, J. J., S. Schneider-Schaulies, et al. (1993). "MxA-dependent inhibition of measles virus glycoprotein synthesis in a stably transfected human monocytic cell line." J Virol **67**(8): 4760-8.

Schuhmacher, M., H. N. Migeon, et al. (1992). Comparative useful yield measurements under oxygen, cesium and gallium bombardment, Amsterdam, Elsevier.

Senhou, A., A. Chouak, et al. (2002). "Sensitivity of biomonitors and local variations of element concentrations in air pollution biomonitoring." Journal of Radioanalytical and Nuclear Chemistry **254**(2): 343.

Shichi, H., K. Umemura, et al. (1992). "Microarea element analysis using Cs LMIS incorporating SEM/SIMS." SIMS XII: 259.

Simon, A., J. Fah, et al. (1991). "Interferon-regulated Mx genes are not responsive to interleukin-1, tumor necrosis factor, and other cytokines." J Virol **65**(2): 968-71.

Slodzian, G., B. Daigne, et al. (1991). A thermal ionization source for a Cs^+ ion probe. Proceedings VIIIth Conference on SIMS, Amsterdam, Elsevier.

Slodzian, G., B. Daigne, et al. (1992). "Scanning secondary ion analytical microscopy with parallel detection." Biol Cell **74**(1): 43-50.

Slodzian, G., B. Daigne, et al. (1991). A high resolution scanning ion microscope with parallel detection of secondary ions. Proceedings VIIIth Conference on SIMS, Amsterdam, Elsevier.

Smets, I., A. Caplanusi, et al. (2004). "Ca2+ uptake in mitochondria occurs via the reverse action of the Na+/Ca2+ exchanger in metabolically inhibited MDCK cells." Am J Physiol Renal Physiol **286**(4): F784-94.

Smith, A. R. (1978). Color gamut transform pairs. Proceedings of the 5th annual conference on Computer graphics and interactive techniques, ACM Press.

Smith, D. R., S. Chandra, et al. (2001). "Quantitative imaging and microlocalization of boron-10 in brain tumors and infiltrating tumor cells by SIMS ion microscopy: relevance to neutron capture therapy." Cancer Res **61**(22): 8179-87.

Sod, E. W., A. R. Crooker, et al. (1990). "Biological cryosection preparation and practical ion yield evaluation for ion microscopic analysis." J Microsc **160**(Pt 1): 55-65.

Solomko, V., M. Verstraete, et al. (2006). "Modeling the dissociation and ionization of a sputtered organic molecule." Applied Surface Science **252**(19): 6459.

Stadermann, F. J., C. Floss, et al. (2006). "Circumstellar aluminum oxide and silicon carbide in interplanetary dust particles." Geochimica et Cosmochimica Acta **70**(24): 6168.

Staeheli, P., P. Dreiding, et al. (1985). "Polyclonal and monoclonal antibodies to the interferon-inducible protein Mx of influenza virus-resistant mice." J Biol Chem **260**(3): 1821-5.

Staeheli, P., F. Pitossi, et al. (1993). "Mx proteins: GTPases with antiviral activity." Trends Cell Biol **3**(8): 268-72.

Storm, H. A., J. D. Stein, et al. (1976). ARL probe news. Joint US/Japan seminar on SIMS technique, Honolulu.

Strick, R., P. L. Strissel, et al. (2001). "Cation-chromatin binding as shown by ion microscopy is essential for the structural integrity of chromosomes." J Cell Biol **155**(6): 899-910.

Strissel, P. L., R. Strick, et al. (2004). "Specific Mg2+ binding at human and Indian muntjac chromosomal Giemsa bands." Applied Surface Science **231-232**: 485-489.

Takaya, K., M. Okabe, et al. (2003). "Fine structures and ion images on fresh frozen dried ultrathin sections by transmission electron and scanning ion microscopy." Applied Surface Science **203-204**: 684.

Tarhanen, S., J. Poikolainen, et al. (2000). "Severe photobiont injuries of lichens are strongly associated with air pollution." New Phytologist **147**(3): 579-590.

Todd, P. J., T. G. Schaaff, et al. (2001). "Organic ion imaging of biological tissue with secondary ion mass spectrometry and matrix-assisted laser desorption/ionization." J Mass Spectrom **36**(4): 355-69.

Tokuyasu, K. T. (1973). "A technique for ultramicrotomy of cell suspensions and tissues." J. Cell Biol. **57**(2): 551-565.

Tsien, R. Y. (2003). "Imagining imaging's future." Nat Rev Mol Cell Biol **Suppl**: SS16-21.

Tsien, R. Y. and A. T. Harootunian (1990). "Practical design criteria for a dynamic ratio imaging system." Cell Calcium **11**(2-3): 93-109.

Tsuchiya, S., M. Yamabe, et al. (1980). "Establishment and characterization of a human acute monocytic leukemia cell line (THP-1)." Int J Cancer **26**(2): 171-6.

Tuleta, M. (2006). "Effect of primary oxygen ion implantation on SIMS depth profiling in glasses." Applied Surface Science **252**(18): 6107.

Urrutia, R., J. R. Henley, et al. (1997). "The dynamins: redundant or distinct functions for an expanding family of related GTPases?" Proc Natl Acad Sci U S A **94**(2): 377-84.

Walter, J., K. Tellerb, et al. (2006). Handling multi-dimensional images with Sync_Windows and Image5D. ImageJ User and Developer Conference 2006. Luxembourg.

Wickner, W. (1975). "Asymmetric orientation of a phage coat protein in cytoplasmic membrane of Escherichia coli." Proc Natl Acad Sci U S A **72**(12): 4749-53.

Willingham, M. C., S. S. Yamada, et al. (1978). "Ultrastructural antibody localization of alpha2-macroglobulin in membrane-limited vesicles in cultured cells." Proc Natl Acad Sci U S A **75**(9): 4359-63.

Wilson, R. G. (1995). "SIMS quantification in Si, GaAs, and diamond - an update." Int. J. Mass Spectrometry. Ion Proc.(143): 43.

Wittmaack, K. (2006). "Secondary ion emission from polymer layers by atomic and molecular ion bombardment: Data evaluation based on linear-cascade sputtering theory." Applied Surface Science **252**(19): 6413.

Yao, J., J. R. Scott, et al. (1998). "Importance of matrix:analyte ratio for buffer tolerance using 2,5-dihydroxybenzoic acid as a matrix in matrix-assisted laser desorption/ionization-Fourier transform mass spectrometry and matrix-assisted laser desorption/ionization-time of flight." J Am Soc Mass Spectrom **9**(8): 805-13.

Yu, M. L. (1986). "Chemical enhancement effects in SIMS analysis." Nuclear Instruments and Methods in Physics Research Section B: Beam Interactions with Materials and Atoms **15**(1-6): 151.

Zacher, A. N., 3rd, C. A. Stock, et al. (1980). "A new filamentous phage cloning vector: fd-tet." Gene **9**(1-2): 127-40.

Zhao, H., B. P. De, et al. (1996). "Inhibition of human parainfluenza virus-3 replication by interferon and human MxA." Virology **220**(2): 330-8.

Ziegler, J. (1977-1985). The Stopping and Range of Ions in Matter, Pergamon Press. **2-6**.

Annexe

Le résumé suivant a été soumis à l'université Louis Pasteur le 21 mai 2007. Certaines informations contenues dans ce résumé ne correspondent plus au document final de la thèse. Un résumé mis-à-jour se trouve en début du manuscrit.

Résumé de thèse de doctorat (court)

Discipline : Sciences du vivant, Aspects moléculaires et cellulaires de la biologie

Spécialité : Imagerie biologique

Présentée par : PIRROTTE Patrick

Titre: Applications biologiques du NanoSIMS

Unité de recherche:

[1] UMR N° 7168 Institut des Neurosciences Cellulaires et Intégratives - Strasbourg
[2] Laboratoire National de Santé – Département d'Immunologie - Luxembourg

Directeur de thèse: Professeur François Lasbennes[1]

Directeur de thèse: Professeur Claude P. Muller[2]

Thèse rédigée en anglais
Soutenance en français et anglais

I.1 Introduction

La spectrométrie de masse à ions secondaires (« Secondary Ion Mass Spectrometry », SIMS), évoquée pour la première fois dans les travaux de thèse de Georges Slodzian en 1963, est une technique d'analyse de surface répandue dans les laboratoires d'analyses des matériaux. Son principe, qui n'est pas sans rappeler celui d'un microscope électronique à balayage, réside dans l'utilisation le plus souvent d'une source de césium, de gallium ou d'oxygène, émettant un faisceau à ions primaires érodant un échantillon sous ultra-haut vide (10^{-10} Torr). L'impact des ions primaires provoque une cascade de collisions atomiques provoque un déplacement des éléments constitutifs de l'échantillon. Une fraction de ces ions, réelle empreinte caractéristique de la composition chimique du spécimen, est émise sous forme d'ions mono- ou polyatomiques, extraite sous forme de faisceau d'ions secondaires et séparée selon les critères d'énergie et de masse par un spectromètre.
Cette technique de microanalyse, ultrasensible (ppm au ppb) est très répandue dans les domaines des semi-conducteurs, de la métallurgie, de l'industrie du verre, de la céramique et des polymères où elle est un outil de choix aussi bien pour le contrôle-qualité que pour la caractérisation formelle.

En dehors de quelques applications relevant pour la plupart de cas d'école, les conditions d'analyses astreignantes pour des échantillons biologiques et la méconnaissance de la méthode en sciences de la vie, ont été un frein à l'essor de la microscopie ionique en dehors de l'analyse des matériaux. Les travaux présentés dans ma thèse de doctorat, intitulée «Applications biologiques du NanoSIMS » tentent de mieux définir l'utilité et la place de la microscopie ionique dynamique en sciences de la vie. Ils se basent sur le NanoSIMS 50, récemment développé par Georges Slodzian pour CAMECA et faisant partie d'une nouvelle génération de spectromètres de masse à ions secondaires, construit pour l'imagerie ionique à haute résolution latérale (inférieure à 50 nm) et dont la bonne résolution en masse permet la discrimination isotopique. Mes travaux peuvent se résumer en quatre axes principaux :

- Développements techniques et préparation d'échantillons
- Développement d'outils informatiques.
- Utilisation et comparaison au NanoSIMS de techniques d'imagerie diverses
- Recherche d'applications dans les domaines de la biologie favorables à des études NanoSIMS

II Résultat

II.1 Développement technologiques et préparation d'échantillons.

L'outil SIMS ayant un caractère expérimental et dont de nombreux processus ne sont pas encore bien connus, il a fallu optimiser de nombreux paramètres afin d'obtenir des résultats reproductibles. La préparation d'échantillons, apparentée à celle pour la microscopie électronique à transmission (MET) doit tenir compte de plusieurs facteurs tel que (i) la sensibilité de la technique où les pollutions élémentaires sont à éviter dans le cas d'une analyse de ces mêmes éléments, (ii) le type de support utilisé (plot acier, feuillet de cuivre, plaques de Si), (iii) le type de fixation à préférer selon le type d'analyse afin d'éviter la diffusion des ions mobiles de petite masse (cryogénique versus chimique).
Une étude de modélisation du phénomène d'implantation et des effets de la modulation de paramètres (intensité du faisceau d'ions primaires et surface) a été réalisée afin de mieux

comprendre les processus physiques responsables de l'émission d'ions secondaires élémentaires. Ces travaux, en phase de rédaction pour publication, ont permis de standardiser l'analyse par microscopie ionique d'échantillons inclus en résine et de trouver un bon compris entre l'intensité du faisceau primaire, la durée d'implantation et la qualité de la cartographie des zones implantées. Une implantation préalable dans un SIMS tel que l'IMS6f, qui permet l'implantation d'une surface jusqu'à 40 fois supérieure, suivi d'un transfert au NanoSIMS a permis de gagner un temps considérable lors des analyses.

II.2 Développement d'outils informatiques.

Lors de mes travaux j'ai été amené à utiliser des logiciels peu adapté au traitement post acquisition de cartographies ioniques SIMS. J'ai développé un nouveau logiciel incluant des méthodes the traitement d'images de type ratio isotopiques telle que la méthode dite « standard » ou la transformation « Hue, Saturation, Intensity »). Cette méthode permet de multiplier le ratio entre les pixels de deux images par des facteurs de poids variables d'attribuer une palette couleur hautement contrastée à l'image du ratio afin de rehausser des signaux faibles du bruit de fond. Cette méthode, courante en calcul de ratios calciques a été introduite pour la première fois en SIMS par Claude Lechene. En plus de ces méthodes de traitement analytique, le logiciel propose des fonctions de conversions et de traitements automatisés des fichiers images. En sus, il extrait tous les paramètres d'acquisition présents dans les fichiers et est à ma connaissance le seul le permettant. Par ailleurs, ayant l'occasion de travailler en microscopie confocale lors de ma thèse, j'ai également continué le développement, débuté lors de mon DESS, d'un outil de traitement d'images confocales.

II.3 Utilisation et comparaison au NanoSIMS de techniques d'imagerie diverses.

Lors de mes travaux, j'ai été amené à utiliser différentes techniques d'imagerie telle que la microscopie à épifluorescence, la microscopie confocale et la MET. Il s'est avéré que le NanoSIMS est un outil d'imagerie complexe dont les résultats biologiques doivent être confirmés par d'autres techniques (marquages isotopiques par MALDI-Tof, immunomarquages par immunofluorescence). La similitude des préparations d'échantillons en SIMS et MET font de la microscopie électronique une technique de comparaison de choix.

III.4 Recherche d'applications dans les domaines de la biologie favorable à des études NanoSIMS.

Développement de marquages spécifiques.

A ce jour, les quelques marquages utilisés en SIMS sont des molécules de faible masse, à spécificité variable, contenant les éléments halogènes. Les plus communs sont le 5'-bromo-2'-deoxyuridine, un analogue de la thymidine et l'iodobenzamide ciblant la mélanine. Afin d'augmenter la palette des marqueurs utiles en SIMS, j'ai développé une sonde hautement spécifique à base d'anticorps monoclonaux dirigée contre la nucléoprotéine du virus de la rougeole. Afin de profiter au mieux de la haute résolution en masse du NanoSIMS, ces anticorps ont été marqués par les isotopes stables ^{13}C et ^{15}N. L'intégration des isotopes a été confirmée par spectrométrie de masse MALDI-Tof. La reconnaissance des sites antigéniques par l'anticorps a été confirmée par immunofluorescence. L'identification du marquage par NanoSIMS est en cours.

Etudes de la distribution de métaux dans des organismes bioindicateurs

Les lichens sont composés d'algues en symbiose avec un champignon. Ces organismes sont considérés comme d'excellents bioindicateurs grâce à leur capacité d'accumulation de métaux proviennent de l'environnement. Des lichens provenant de plusieurs sites pollués au Portugal nous ont été fournis dans le cadre d'une collaboration avec les universités d'Aveiro au Portugal et de Léon en Espagne. Une étude GCMS a déterminé des concentrations jusqu'à 30 fois supérieures à la normale pour certains métaux. Néanmoins, la localisation exacte de ces accumulations est inconnue et nous espérons pouvoirs y répondre grâce au NanoSIMS.

Marquage métabolique

Le marquage métabolique par addition de nutriments composés d'isotopes stables a été démontré lors d'une étude de l'incorporation de bactéries marquées par des monocytes différenciées en macrophages. Il a été possible de suivre le devenir de la bactérie phagocytée et une étude en parallèle par MET devrait préciser les organelles directement impliquées. Cette expérience m'a également convaincu de la faisabilité de marquages de type « pulse-chase » en SIMS.

III. Discussion

La discussion tentera de répondre directement à la question de l'utilité et de la praticabilité du NanoSIMS en Sciences de la Vie. Elle portera sur la faisabilité des préparations d'échantillons, les applications potentielles des SIMS actuels et présentera d'hypothétiques modifications permettant d'améliorer l'outil et le rendre plus attractif aux biosciences.

IV. Communications

- Fred Fack, Jacques Kremer, Dominique Revets, Patrick Pirrotte, Wim Ammerlaan, Jenny Renaut, Claude P. Muller. Qualitative and Quantitative insights in virus host-cell interactions investigated with differential proteomics, multiplex western blot and quantitative PCR. Proteomlux 2006, Luxembourg, 11-14.10.2006. **Abstract et communication orale**
- Patrick Pirrotte, Fred Fack, Dominique Revets, Jean-Nicolas Audinot, Henri-Noël Migeon, Claude P. Muller. Stable isotope labelling of antigens for the study of phagocytic processes by nanoSIMS, Imvie3, Paris, France, 20.-21.06.2006. **Abstract et communication orale.**
- Patrick Pirrotte, Jean-Nicolas Audinot, Claude P. Muller. ImageJ plugin based on ImageIO to extract images and data from Cameca Secondary Ion Mass Spectrometer data files. Imagej user and developer conference, CRP-HT, Luxembourg, 18.-19.5.2006. **Abstract et communication orale.**
- Patrick Pirrotte and Claude P. Muller. Analyse de tissues biologique par Nano/SIMS. BIOSIMS in Luxembourg Meeting, 11.05.2005. **Communication orale.**
- Patrick Pirrotte, Jean-Nicolas Audinot, Henri-Noël Migeon, François Lasbennes, Claude P. Muller. Biological Imaging with NanoSIMS. Congrès d'Imagerie Imvie2, Strasbourg, France, 01.-03.03.2005. **Abstract et communication orale.**

(orateur en souligné)

V. Publications

Pirrotte P, Guerquin-Kern JL, Audinot JN, Migeon HN, Muller CP Secondary Ion Mass Spectrometry in Life Sciences. In: Emerging Imaging Techniques. Eds.: M Faupel, P Smigielski, R Grzymala. FontisMedia. In press. **Chapitre de livre.**

Pirrotte P, Audinot JN, Migeon HN, Muller CP «Implantation on NanoSIMS 50 : Relevance for the analysis of biological samples" **En phase de rédaction.**

The following article was published as

Pirrotte P, Guerquin-Kern JL, Audinot JN, Migeon HN, Muller CP Secondary Ion Mass Spectrometry in Life Sciences. In: Emerging Imaging Techniques. Eds.: M Faupel, P Smigielski, R Grzymala. FontisMedia. In press. **Book Chapter**

Secondary Ion Mass Spectrometry in life sciences

Patrick Pirrotte[1], Jean-Luc Guerquin-Kern[2], Jean-Nicolas Audinot[3], Henri-Noël Migeon[3], Claude P. Muller[1]

[1] Institute of Immunology, Laboratoire National de Santé, 20A Rue Auguste Lumière, L-1011 Luxembourg, Luxembourg

[2] Laboratoire de Microscopie Ionique, Institut Curie Recherche, Bât 112, Centre Universitaire, 91405 Orsay Cedex, France

[3]Laboratoire d'Analyse des Matériaux, Centre de Recherche Public - Gabriel Lippmann, 41, rue du Brill, L-4422 Belvaux, Luxembourg

1. Introduction

For many biologists, material science belongs to the arcane domain of physics. While several surface analysis techniques such as atomic force microscopy (AFM) or scanning electron microscopy (SEM) have been successfully used in life sciences, others are less known outside the material science community. Secondary ion mass spectroscopy (SIMS) is one of those techniques that is still largely unknown to biologists even after almost forty years of existence, partially because of its complexity and difficulties of communication between physics and biology. Nevertheless, the last decades have seen a number of applications in biology, suggesting that SIMS may also be useful beyond material sciences.

Secondary ion mass spectroscopy (SIMS) allows the analysis of the surface composition of inorganic and organic materials based on mass spectral analysis of secondary ions extracted from the surface (1-2 nm depth) of a solid sample under the impact of an energetic beam of primary ions. Essentially, SIMS produces spatial distribution maps of ions from a micro volume of a given sample.
Ion microscopy has been successfully applied to surface analysis in geology, metallurgy as well as by the glass, the ceramic and the semi-conductor industry and only recently to biological samples. The ability of modern ion microscopes to follow labelled tracers at high lateral resolution and sensitivity may warrant its success as an alternative e.g. to microautoradiography, avoiding the lengthy times of exposure of photographic emulsions. Another unique advantage of SIMS is its ability to differentiate between isobaric molecules, due to its high mass resolving power.
We will present a general overview over SIMS technology, before focusing on imaging examples of biological cells and tissues by a high resolution NanoSIMS50 (Cameca). Some of the challenges in sample preparation adapted from electron microscopy to the requirements of SIMS will be discussed. Examples in various fields of applications will be presented to show the potential of SIMS as a complementary imaging technology.

2. Methodology
2.1 Instrumentation
2.1.1 Basic principle of Secondary Ion Mass Spectrometry

In 1962, Castaing and Slodzian [1] proposed a novel instrument for the chemical microanalysis of surfaces based on the phenomenon of secondary ions emitted by the specimen under the impact of an energy primary ion beam. The principle of the Secondary Ion Mass Spectrometry (SIMS) is as follows: The impact of a primary ion onto the surface of a sample triggers a cascade of atomic collisions. Electrons, photons, atoms and clusters are ejected and are characteristic of the composition of the target area. In the ejection process, some of the atoms and clusters can be spontaneously ionized. In a SIMS instrument, these "secondary ions" are accelerated, separated in function of their mass/charge ratio (m/z) and detected.

2.1.2 The primary beam, impact, sputtering, and ionization

Primary beam
During SIMS analysis the impact of a primary particle, in the energy range of some keV, on a surface causes an energy and momentum transfer to a limited area surrounding the point of impact. This provokes the removal of atomic and molecular surface species and results in the erosion of the uppermost atomic layers of the bombarded surface (sputtering) and in the implantation of the primary ions into the condensed phase (fig. 1).

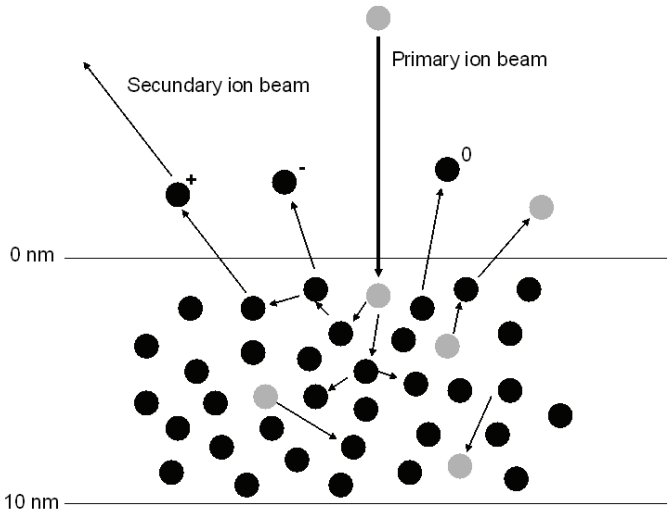

Figure 1: Light grey dots represent primary particles (atoms or clusters) Black dots represent sample atoms. SIMS process erodes the surface with perturbation of the lower layers [2].

Depending on the primary ion dose used during the SMS experiments two regimes are highlighted: (i) The so called static regime which uses a typical primary ion dose of less than 10^{13}at/cm^2 providing the sputtering of for less than the equivalent of one atomic layer out of the first atomic layers for the complete experiment. The operation of a SIMS instrument in the static regime provides elemental and molecular information from the very surface of the specimen. (ii) The dynamic regime for which the primary ion dose is greater by several orders of magnitude. This high dose used in dynamic SIMS restricts the SIMS signal to, primarily, elemental and isotopic information but provides much greater sensitivity and implies a "real" sputtering of the sample. This surface erosion continuously moves the actual surface down into the bulk material. It allows depth profiling of element concentration with high sensitivity, down to the ppb range. (semiconductor and integrated circuit analysis).
In this paper we will only discuss the dynamic SIMS regime (D-SIMS).

Primary ion beams

The primary ion probe density mainly depends on the brightness and energy spread of the source. The most common primary ions used on SIMS instruments are oxygen, gallium and caesium.
Oxygen beams are generally produced by a duoplasmatron source. This kind of source provides positive (O_2^+) or negative (O^-) oxygen ions.
Gallium beams are produced by liquid metal ion guns with a high brightness (10^5A/cm^2/sr), stability and a long lifetime. Because of the high energy dispersion of ions emitted from a field emission gun, the beam density of the probe focused onto the sample surface by the primary column is mainly limited by the chromatic aberrations.
In order to minimize them, the liquid metal ion gun operates at high accelerating voltage (> 25 kV), which deteriorates the depth resolution.
Caesium beams can be produced either by surface ionization sources or by liquid metal ion [3]. Surface ionization sources provide a stable caesium beam with a brightness (150 A/cm^2/sr at 10 keV energy) with a small energy dispersion (< 1eV). Cs from liquid metal ions are much brighter (in the range of 10^5 A/cm^2/sr) but have large energy dispersion, and due to the high reactivity of liquid caesium, such sources are not stable and have a short lifetime. Usually, thermal ionization sources are preferred.

Sputtering and Ionization efficiency

The ionization probability depends on the chemical state of the sample surface during the sputtering process. This chemical state results from the matrix composition itself, but also from the implantation of primary ions, the bombardment induced diffusion and the surface reaction with the vacuum gas phase. By bombarding the sample with reactive primary ions, it is therefore possible to change the surface chemistry in a way that increases ion yields. It is well known that the use of oxygen and caesium primary ions enhances the ion yield for the etched species with a low ionization potential and a high electron affinity, respectively. In a reverse way, sputtering under rare gases or gallium bombardment usually has a low ionization efficiency [4, 5].

2.1.3 The acceleration of secondary ions and their separation according the ratio mass/charge

The secondary ions are extracted from the surface of the sample by acceleration and after acceleration are injected into the mass spectrometer. In the design of conventional SIMS instruments, the objective lens of the primary column works with a rather long working distance (several centimetres), due to the presence of the secondary ion extraction system in front and near the sample surface (fig. 2).

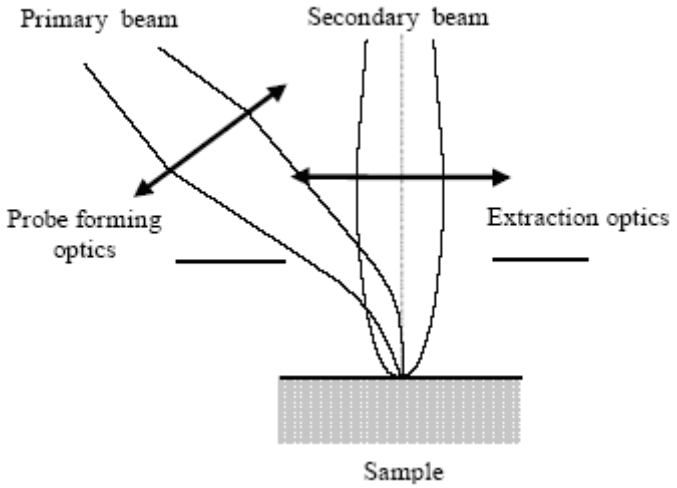

Figure 2: Schematic representation of the conventional probes forming systems [6].

After acceleration, the secondary ions are filtered according their ratio mass/charge (m/z).
There are three essential types of spectrometers: quadrupole, magnetic sector (single focusing) and spectrometer with association of an electrostatic sector with a magnetic sector (double focusing).

- The quadrupole is less expensive and has many uses. Yet, compared to a double focusing ion spectrometer, it is less sensitive and it can only accept ions within a small energy band-pass. Its transmission depends on mass number and it has low mass resolution.
- Magnetic sector have excellent mass dispersive properties. The first-order chromatic aberration, however, deteriorates mass resolution when an ion beam with an intrinsic energy spread is analyzed by a single focusing magnetic sector field alone.
- The combination of a magnetic and an electrostatic sector produces a double focusing instrument. These double-focusing spectrometers provide high and constant transmission along the entire mass range. They are capable of achieving high mass resolution but, usually, at the expense of a loss in transmission (fig. 3). The ions are then detected and counted.

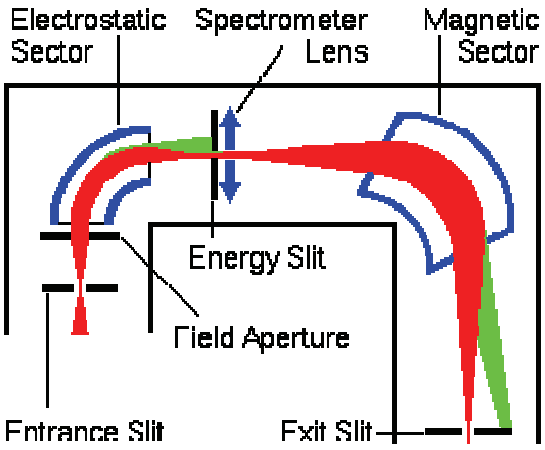

Figure 3: Combination of an electrostatic and a magnetic sector [7]

2.1.4 The detection

The detection of secondary ions is the ultimate step. In function of the mode of analysis selected, different mode of detection can be used.
With the direct imaging secondary ion mass spectrometer (Ion Microscope) the sample is illuminated by a large diameter primary ion beam and an image of the sample surface is projected through the mass analyzer to a fluorescent screen (channel plate). There, a magnified image of the sample surface may be observed in the "light" of the selected element. With the Scanning secondary ion mass spectrometer (Scanning Ion Microscope; Ion Microprobe) a highly focused primary ion beam is scanned across the sample surface and the secondary ion image is produced by synchronously detecting the mass-analyzed secondary ion signal. Essentially all the SIMS work as scanning ion microprobes. With this mode, it is possible to obtain depth profiles or surface images. The size of the focused primary beam (lateral resolution) is adapted to the selected mode. The intensity of the primary ion beam decreases (and consequently the secondary ion current) with the size of the primary ion beam. For imaging of biological samples, a lateral resolution lower than 100 nm, a good transmission and mass resolution is needed. For this purpose two prototype ion probes were developed. One prototype was developed by Levi-Setti at the Enrico Fermi Institute in Chicago. It uses a liquid metal primary ion beam (Gallium), which is extremely bright and can be tightly focused. It allowed chromosome mapping with a lateral resolution of 50 nm.
The mass resolution, however, was poor because masses were selected with a quadrupole mass filter [8]. The other prototype was developed under the direction of G. Slodzian, at ONERA (Office National d'Etudes et de Recherches Aerospatiales, the French agency for spatial research). This prototype, the NanoSIMS50, opens up new areas of applications, especially in medical biology and life science, where high lateral resolution must be consistent with good sensitivity and good mass resolution:

2.2 The NanoSIMS50

For this instrument a new design of the optical system has been developed by Slodzian et al [9]. It uses the same optical system to co-axially focus and collect both the primary ion probe and secondary ions. Compared to the conventional configuration (fig. 2), this optical arrangement (fig. 4) has the great advantage of considerably shortening the distance between the sample and the probe forming lens (few tenth millimeters). Thus, the focal length and aberrations of the objective lens are minimized, which leads to a smaller probe diameter at a given ion current. A second advantage of this experimental setup is to sputter the target with a normal

incidence of the primary beam with respect to the sample surface. This reduces the shadowing effects when sputtering non-flat surface with an oblique incidence.

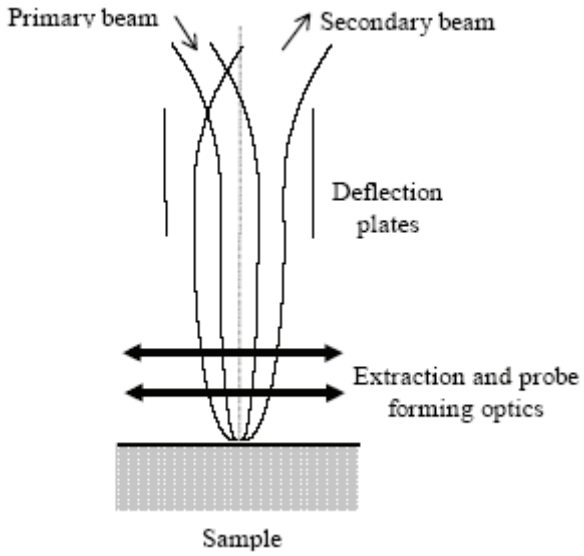

Figure 4: Schematic representation of the co-axial probes forming systems [6].

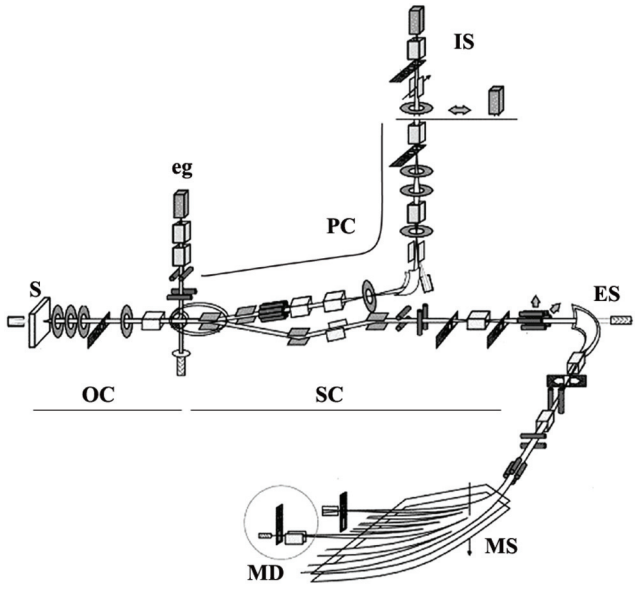

Figure 5: Schematics of the NanoSIMS ion optics. IS: Caesium and Duoplasmatron primary ion sources, S: Sample, eg: electron gun, PC: Primary column, OC: Objective column, SC: Secondary column, ES: Electrostatic sector, MS: Magnetic sector, MD: Multi-detection [10]

The main components of the NanoSIMS50 are (fig. 5):

- A primary column with a primary caesium ion or an oxygen ion source that enhances the useful yield of negative and positive secondary ions.
- An objective column where the same ion optic is used in a coaxial manner to focus the primary beam on the sample and to collect the secondary ions (fig. 4).
- An electron gun cancels positive charging on insulating samples.
- The mass spectrometer made of the combination of an electrostatic and a magnetic sector with a focusing along the focal plane of the magnet. The design of the mass spectrometer gives a transmission of 60% up to 4000 mass resolution.

- Five electron multipliers (EM) detectors (four moveable and one fixed) placed along the focal plane (acquisition of 5 mass simultaneous).

The 50 nm lateral resolution, combined with a high transmission at high mass separation opens up new areas of applications, especially in medical biology and life science, where high lateral resolution and high sensitivity are required. In comparison with X-Ray Fluorescence (about 1 micrometer of lateral resolution) and other techniques using radioactive isotopes, imaging by dynamic SIMS offers new possibilities for biological research. At this scale, it becomes possible to compare, in exactly the same subcellular compartments, the distribution of several molecules labelled with different stable isotopes (e.g. ^{15}N, ^{13}C, ^{2}H, ...) or radioactive tracers.

2.3 Sample preparation

Both the high resolution and the stringent ultra-high vacuum conditions required for SIMS analysis demand high-quality samples. In many ways, sample preparation, including fixation (chemical or cryofixation), dehydration and embedding in hydrophobic resin are similar to those applied in electron microscopy. In electron microscopy, sample preparation must preserve the morphological integrity of the sample. For elemental SIMS microanalysis it is crucial to preserve both the morphological and chemical integrity of the specimen. Loss or relocation of ions within cells or tissues can occur during chemical fixation. Two different sample fixation methods are commonly used in SIMS.

Chemical fixation is based on crosslinking of biomolecules. The most popular cross-linking agent used in optical as well as electron microscopy is glutaraldehyde, which reacts with amino-groups of proteins and lipids. The effect of chemical fixatives on cell membranes alters the activity of ion pumps and disturbs the osmotic equilibrium causing the relocation of diffusible ions and small soluble proteins. However, membrane proteins and large molecular complexes resist the disruption by these fixatives. Therefore chemical fixation is an attractive alternative to the very time-consuming cryofixation.

A straightforward protocol for sample preparation for SIMS analysis involves the fixation in 2.5% glutaraldehyde in 0.1 M cacodylate buffer at pH 7.2 followed by dehydration in ethanol before embedding in a hydrophobic resin. Thorough dehydration is required before the sample can be introduced into the instrument to avoid degassing and compromising of ultra-high vacuum.

Another fixative, osmium tetroxide, is used also a contrasting agent in transmission electron microscopy (TEM). Contrast in TEM increases with the atomic number (**Z**) of the elements in the sample and is associated with increased electron scattering. Since biological molecules are composed of light atoms (C, H, O, N, P and S), thin sections of biological material are made visible by selective staining with electron opaque heavy metal salts based on uranium, lead or osmium. In SIMS, where an ion current is measured, electron density only relates to conductivity and sample charge, the use of heavy metal salts as contrasting agents is not necessary. The use of osmium tetroxide as a fixative should be balanced against the chemical distortion caused by its elevated atomic mass. Elements in the proximity of osmium may ionize more easily, because of a matrix effect, causing counting artefacts.

Cryofixation is an alternative fixation method, where redistribution of soluble molecules is prevented by flash-freezing. Rapid freezing at ultra-low temperatures (< 123 K) favours the formation of vitreous ice instead of destructive crystalline ice that causes morphological damage. Cryofixation can be achieved by (i) slam-freezing of the sample on a precooled mirror-polished metal surface; (ii) by plunging the sample into nitrogen-cooled liquid propane or (iii) by high-pressure freezing. Also, sandwich freeze-fracturing used in electron microscopy [11] has been successfully applied to SIMS [12]. Cultured cells were frozen between two silicon wafers separated by spacer beads. By prying apart the wafers, the cells are cleaved

at fracture planes within the membrane lipid bilayer exposing the membrane core and transmembrane proteins.
The analysis of cryosectioned samples requires a SIMS with an UHV chamber equipped with a cryo-stage. The very low temperatures of the cryo-stage must be rigorously maintained to prevent uncontrolled sublimation and major surface modifications caused by the high energy bombardment. Cold-stages for SIMS are now common on TOF-SIMS where impact energy density can be modulated and is lower than in dynamic SIMS. The continuous bombardment by the 16 keV energy beam is a major obstacle to any attempts at fitting a cryostage on a NanoSIMS.
Alternatively, the sample could be dehydrated by cryosubstitution or freeze-drying. Freeze-drying has the advantage that the water content of the sample is sublimated homogenously without transiting through a solvent (alcohol or acetone) phase as in cryosubstitution. Kellenberger investigated multiple cryofixation techniques for electron microscopy providing a better understanding of the physical processes of cryofixation [13]. Samples are commonly embedded at low temperature (263 K) in Spurr or similar resins. Resin blocs are sectioned on an ultramicrotome at 200-400 nm thickness. Semi-thin sections are mounted on a conductive sample holder (Cu, Si or stainless steel) mirror-polished to avoid effects that are due to an unfocused primary beam (e.g. energy dispersion). The smooth sample surface is well suited for SIMS examination as the compact matrix allows uniform ion implantation. Furthermore, undesirable effects, as differential sputtering during bombardment on structures in relief, are minimised.

3. Applications in life sciences

3.1 Cell biology

All living organisms are constituted of essentially four elements, carbon, nitrogen, oxygen and phosphorus. Mono- or diatomic ions of these elements generate a contrasted SIMS image of the morphology of the cell. All biomolecules yield $^{12}C^-$, carbon-nitrogen rich regions (e.g. proteins) generate recombined $^{12}C^{14}N^-$. All examples shown below were obtained by NanoSIMS unless stated otherwise.
Based on these recombined ions, we were able to observe for instance a $^{12}C^{14}N$ image of inclusion bodies in M-cells of the gut associated lymphoid tissue (GALT) and of lymphocytes with a strong $^{31}P^-$ (fig. 6) signal in the nuclei. The M-cells mediate the polarised transport of antigens from the gastric endothelium to macrophages and lymphocytes in the underlying Peyer's patches. Inclusion bodies taken up by the M-cells, visualized as CN^- hypersignals, migrate via transport vesicles from the apex to the basal lamina to be processed by the antigen presenting cells. The CN^- rich inclusion bodies are devoid of P^-.

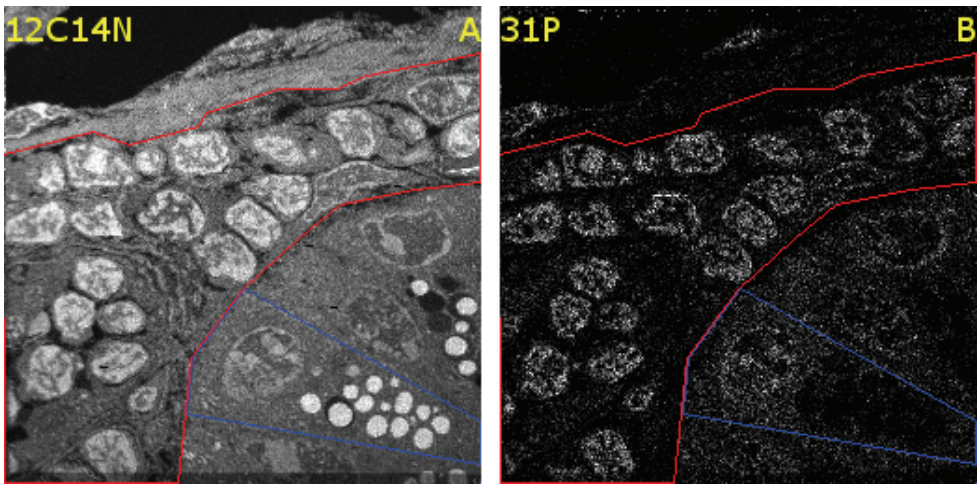

Figure 6: Mouse Peyer patches (Cs^+ beam: 16keV, 0.8pA, 256x256 pixels, 40µm x40µm, 50nm lateral resolution, Acquisition time 98min 18sec). Lymphocytes in red, M-cells in blue.

While in some cases such as in biomineralization studies, imaging of native ions can be of great interest, most other applications rely on isotopically labelled markers. To visualize a specific biomolecule it has to be brought out of a background abundant elemental C, N, O and P ions. Labels are usually based on rare atoms such as halogens or isotopes. Samples are either labelled with specific markers or isotopically labelled nutritional precursors. Recent SIMS studies investigated the turnover of proteins and fatty acids based on metabolically incorporated ^{13}C and ^{15}N labels. Isotopic ratios of the cyanide ions $^{12}C^{14}N$, $^{13}C^{14}N$, $^{12}C^{14}N$, $^{12}C^{15}N$ were compared with their natural abundance [14, 15]. The high mass resolution M/ΔM necessary to separate a $^{12}C^{15}N$ peak from an interfering $^{12}C^{14}N$ peak can be achieved at an excellent transmission by NanoSIMS. Galle demonstrated the utility of halogen-based nucleotide analogues such as bromodeoxyuridine (BrdU), iodouridine (IdU) incorporated preferentially to DNA, or fluorouracil (5-FU) favouring RNA [16]. The halogens were detected as elemental ions: Br^- (m = 79), F^- (m = 19) and I^- (m = 127).

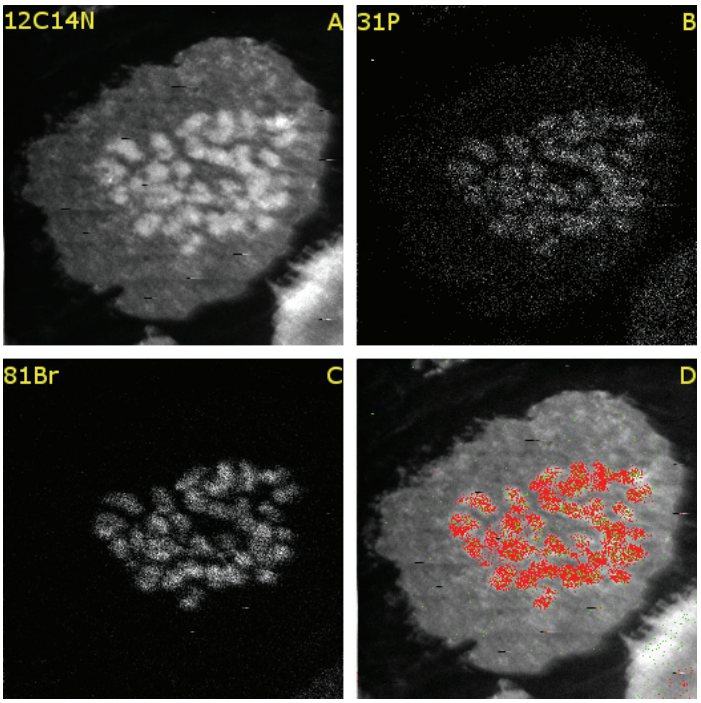

Figure 7: Ion distribution maps of human (THP-1) chromosomes labelled with BrdU. Cells were metabolically stained with 20 µM BrdU, arrested with colcemid 10 µg/mL for 45 minutes, fixed with 2.5% glutaraldehyde in cacodylate buffer 0.1 M pH 7.2 and embedded in Epon 812 and analysed under a Cs^+ primary ion beam **(a-c)** (Cs^+ beam: 16 keV, 0.8 pA, 256 x 256 pixels, 18x18µm, 100nm lateral resolution, Acquisition time 65 min 32 sec **(d)** thresholded false colour overlay $^{12}C^{14}N$: greyscale, ^{81}Br: red, ^{31}P: green panel. Panel D corresponds to an overlay of panels A, B, C.

Figure 7 shows the result of a similar experiment with THP-1 cells, a human monocyte precursor cell line. The cyanide (CN^-) image shows mostly carbon- and nitrogen-rich structural molecules, and images are similar to transmission electron micrograph. In the P^- image (fig. 7b) weak signals emerge mainly from nuclear DNA and RNA and to lesser degree from phospholipids. The Br^- image (fig. 7c) displays well defined hypersignals of brome incorporated into the de novo synthesized DNA of chromosomes in metaphase.
The above examples show that intracellular structures such as inclusion bodies, mitochondria or the nucleolus can be visualised by NanoSIMS at a resolution of 50 nm.
In recent studies, Levi-Setti et al. confirmed the existence of cation-chromosome interactions by SIMS [17, 18]. While Ca^{2+}, Na^{2+} and K^+ all seem to be generally essential for chromosome

condensation, the authors suggested a more specific role of Mg^{2+} in maintaining chromatin structure, a role that is difficult to be confirmed by other techniques. Previous studies have all tried to map the cellular distribution of physiological cations by indirect imaging techniques, but SIMS has allowed the direct mapping of intra-cellular cations.

3.2 Pharmacology

Boron neutron capture therapy (BNCT) is a new potential treatment for malignant brain tumour and melanomas. It is based on the neutron induced fission of ^{10}B resulting in unstable ^{11}B which decays to ^{7}Li and an α particle with a kinetic energy of 2.79 MeV. Several molecules are currently under investigation for the delivery of boron to tumour cells in the brain. Main candidates are the amino acid derivatives boronophenylalanine-fructose (BPA-f) and sodium borocaptate (BSH). Boron delivery was investigated in glioblastoma cells, co-cultured with LLC-PK_1 epithelial cells or skin fibroblasts [19]. In vitro glioblastoma cells showed an increased ^{10}B distribution mainly in the nucleus and the cytoplasm. However this pattern of BPA-f and BSH was also found in epithelial cells and fibroblasts. SIMS microanalysis on an IMS 3f was used to localize a rat gliosarcoma and measure ratios between boron isotopes at the interface between tumour and healthy tissue [20]. In these histological studies a gradient of ^{10}B suggested some degree of specificity of boron for the tumour. While the cell-type specific selectivity of boron remains controversial, SIMS proved to be an excellent technique to image the boron distribution directly and remains the method of choice for the study of the potential selectivity of boronated drugs.
SIMS could be used in pharmacology to study drug vectorization. Bacterial Shiga toxin and related toxins are composed of an A-subunit, which exhibits catalytic activities inducing cytotoxicity and a non-covalently bound B-subunit that acts as a transporter for the A-subunit. The B-subunit (STxB) has been demonstrated as a powerful vector for transporting attached peptides into cells [21, 22]. The STxB is known to transport to the endoplasmic reticulum via the Golgi apparatus through a retrograde route [23]. By using ^{15}N-enriched STxB, it has been proven that subcellular localization of an isotopic labelled vector could be visualized using NanoSIMS [24]. Figure 8 shows STxB binding to the plasma membrane followed by internalization into the cell and its accumulation in the Golgi region.

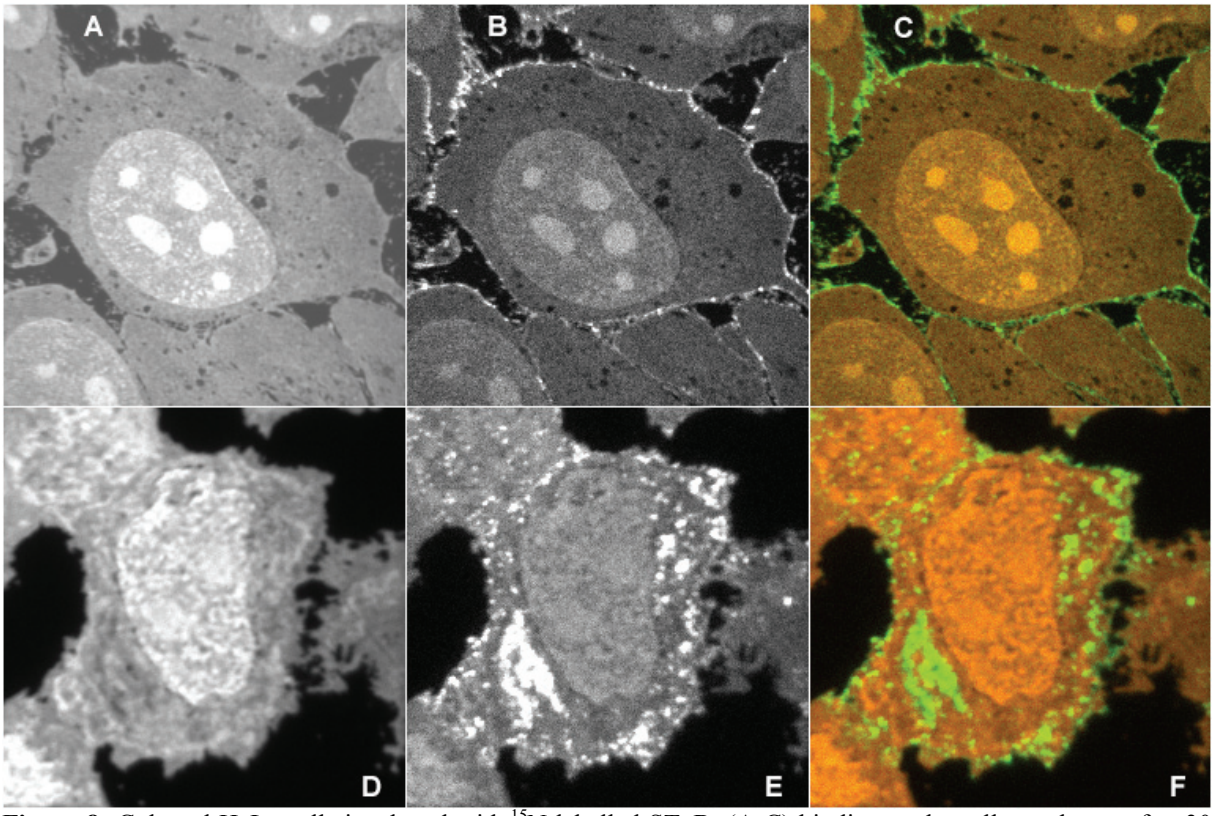

Figure 8: Cultured HeLa cells incubated with ^{15}N labelled STxB: (A-C) binding to the cell membrane after 30 min incubation on ice, raster 35x35 μm^2; (D-F) internalization after 40 min incubation at room temperature, raster 20x20 μm^2. Secondary negative ion images are recorded under Cs^+ primary bombardment. A and D, $^{12}C^{14}N^-$; B and E, $^{12}C^{15}N^-$; C and F superposition of pseudo-colours of $^{12}C^{14}N^-$ images (in red) and $^{12}C^{15}N^-$ images (in green). Counting time is 10ms/pixel. Institut Curie with L. Johannes and W. Roemer.

3.3 Toxicology

Metabolic pathways of toxic compounds have been investigated by scanning ion microprobe and by a related technique, electron probe x-ray microanalysis (EPMA) to complement chemical microanalysis. Toxic compounds can be elements, inorganic, or more or less complex organic molecules.

The accumulation of toxic group IIIA, lanthanide or actinide elements in the lysosomes of the kidney convoluted proximal tubular cells has been proposed as being the result of a selective concentration [25]. The accumulation was long thought to be the consequence of a dose-dependant pathological effect. Most analytical techniques such as EPMA, rely on the administration of high doses for the subcellular localization of toxic element. The high sensitivity of the NanoSIMS permitted the localization of trace quantities of aluminium and indium in the proximal tubules of rats previously treated with these compounds. Indium and aluminium were both visible in the cytoplasm probably because of accumulation in the lysosomes, while indium was also observed in the nuclei. Both metals were found as precipitates in the tubular lumen. This selective accumulation suggested a mechanism of concentration, precipitation and elimination [26] as previously observed by EPMA after a high dose administration and confirmed by NanoSIMS at more realistic doses.

In a recent article [27] arsenic distribution was examined by NanoSIMS in human hair sections to investigate signs of As poisoning. Natural concentrations in the hair typically range between 0.1 - 1ng/mg hair and As^- signals are homogenous throughout the hair cortex. Control hair exposed experimentally to arsenic salts showed a similar distribution pattern but with higher signal intensity. In contrast, hair from individuals who ingested arsenic over a longer time periods displayed a coarse speckled pattern of high doses of As in the medulla.

Accumulation of As during hair growth may explain this pattern but years of treatment with As containing products may have similar effects. SIMS could be used to further study As incorporation in hairs and could be crucial in the diagnostic of chronic arsenic poisoning e.g of historic figures.
Nitrogen oxides (NO_x) as a result of petrol combustion constitute one of the main air pollutants in industrialized countries and are thought to be an important cause for an increase in sensitivity to pollen allergens. Using SIMS, Lhuissier et al [28] observed an accumulation of ^{15}N in the sporoderm and cytoplasm of birch and cockfoot pollen exposed to ^{15}NO. This application is particularly interesting because it relies on SIMS' unique ability to follow stable isotopic markers. The low molecular mass nitrogen oxides could not have been traced by alternative techniques based on radioisotopes as oxygen only possesses short half-life isotopes and natural nitrogen radioisotopes do not exist.

3.4 Biomineralization

SIMS has proven to be an invaluable tool for the analysis of inorganic microagglomerates or of minerals. In biology, the high sensitivity and spatial resolution have been particularly useful to analyse biomineralization processes and the chemical composition of the resulting microagglomerates.
In odontology, amelogenesis, i.e. formation of dental enamel, has been investigated by SIMS microanalysis [29]. The fluorine distribution [30], normalized against P (F/P ratio) of Ca (F/ Ca ratio) has been studied to some extend. SIMS can detect minute traces of fluorine with high yield, because fluorine is the most electronegative element.
The development of enamel goes through several phases: (i) During the pre-secretory phase pre-ameloblasts differentiate to ameloblasts; (ii) in the secretory phase ameloblasts develop the Tome's process, a structure responsible for enamel secretion; (iii) in the maturation phase ameloblasts undergo morphological changes and evacuate organic components from the dental matrix. During the development of dental matrix the density of rod-like structures of hydroxyapatite increases. Chemical analysis of rat incisor enamel showed that inorganic ions (e.g. ^{31}P, ^{35}Cl) present a distinctive pattern and an increase in incorporation during enamel development [31]. During maturation phase ^{12}C, ^{19}F, ^{23}Na and ^{39}K were resorbed by ameloblasts, gradually reducing these elements in the enamel matrix.
Hydroxyapatite agglomerates were studied during mineralization in MDCK cells (fig. 9). Phosphorus, sulphur and calcium oxide are evenly distributed within the agglomerates. Carbon and cyanide ions accumulate specifically at the interface between tissue and agglomerate. This study also demonstrated that ion microprobe analysis and TEM imaging can be directly complementary when a SIMS sample holder compatible with TEM grids are used (fig. 9a).

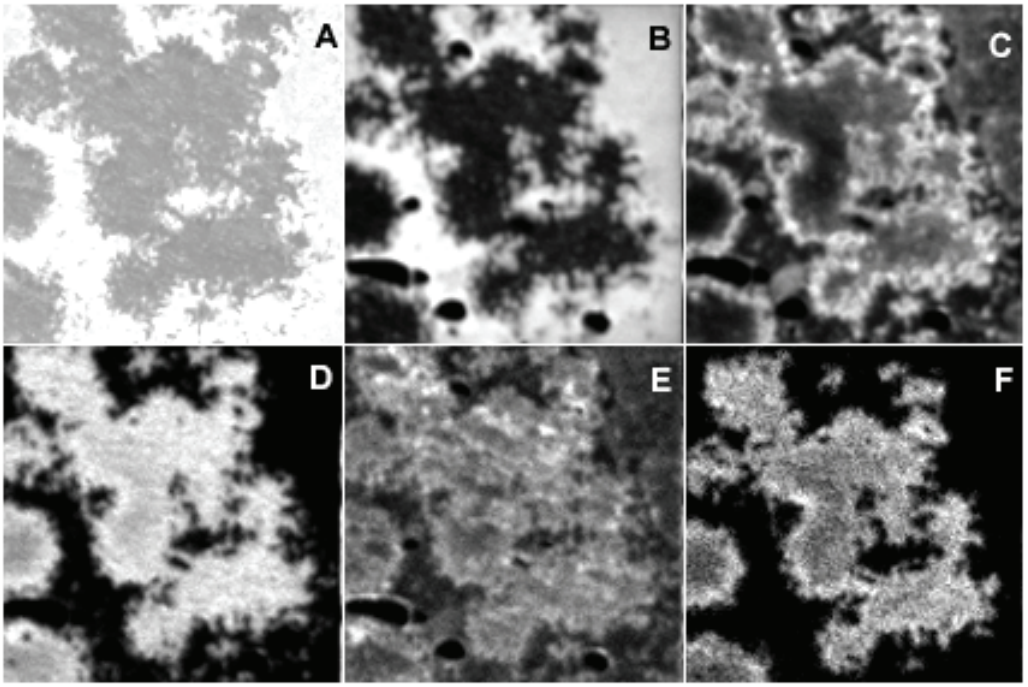

Figure 9: Correlative imaging between TEM **(A)** and NanoSIMS images **(B-F)** of a hydroxyapathite agglomerate in MDCK cells. Elemental distributions are obtained with the same thin section under Cs^+ primary bombardment **(B)** $^{12}C^-$ **(C)** $^{12}C^{14}N^-$ **(D)** $^{31}P^-$ **(E)** $^{34}S^-$ **(F)** CaO^- with a raster of 6x6 μm^2 (Institut Curie in collaboration with H. Vali, McGill University, Montreal).

3.5 Radiotoxicology and nuclear medicine

Iodine is an element of choice for SIMS studies because of its high electron affinity and effective ionisation yield τ_u. An ongoing study investigates the differential distribution of the iodine isotopes (^{127}I and ^{129}I) in the colloid of thyroid follicles. To study uptake patterns of exogenous iodine young rats were injected with the isotope ^{129}I and sacrificed after defined intervals. After fixation and embedding, thyroid sections were analysed by SIMS. Since the size of the detectors does not allow simultaneous detection of ^{127}I and ^{129}I isotopes, images represented in Fig 10, were recorded in two separate acquisitions. As expected, the natural isotope ^{127}I was homogenously distributed in the colloid region throughout the thyroid while exogenous ^{129}I given 6 hours earlier was only found at the periphery of the colloid. This differential distribution may be of interest to better understand the risk of accidental exposure to radioactivity.

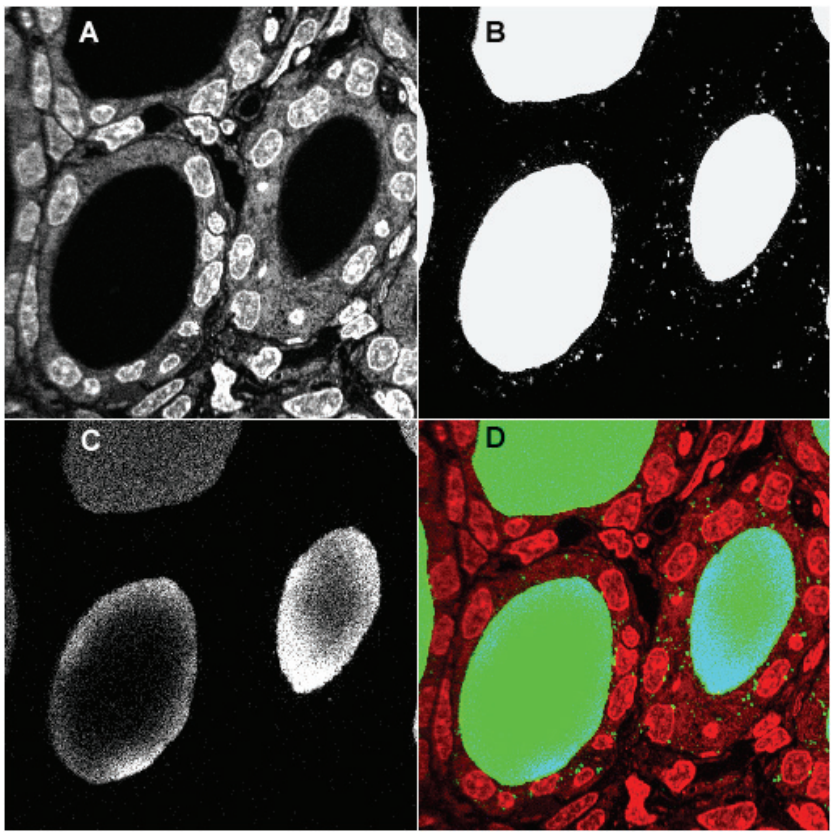

Figure 10: Negative ion analysis of a young rat thyroid section **(A)** $^{31}P^-$, **(B)** $^{127}I^-$, **(C),** $^{129}I^-$, **(D)** superimposition of P^- (red), $^{127}I^-$ (green) and $^{129}I^{-\ (blue)}$ images. The field of view was 30µm x30µm and images were recorded as 256x256 pixels, with a acquiring time of 10ms/pixel for $^{127}I^-$ nad 20 ms for P^- and $^{129}I^-$. (Institut Curie, collaboration with N.Colas-Linhard, Hôpital Bichat, Paris).

4. Concluding remarks

SIMS analysis has long been reserved for the analysis of surfaces of solids in material sciences. The technology is now also increasing applied to biological tissues and cells. Ubiquitous carbon and nitrogen atoms that recombine to CN^- ions provide pictures of the cell morphology similar to those obtained with transmission electron microscopy. More recently, a high resolution SIMS instrument ("NanoSIMS") has been developed that allows the high resolution imaging even of subcellular structures. Small biological molecular ions can be mapped directly but represent a major challenge for sample preparation. The detection of other structures requires the metabolic labelling of cells by rare isotopes or atomes, or the use of markers binding to specific structures. While the cell morphology can be preserved by chemical fixation similar to those used for TEM, the prevention of relocation of small molecular weight ions represents a major challenge for sample preparations.
SIMS technology is complex and expensive in comparison to competing imaging technologies, but more studies are warranted to demonstrate its potential in imaging of biological tissues and cells. In particular, the NanoSIMS with its lateral resolution in the order of several tens of nanometer may represent a major breakthrough.

5. Acknowledgements

Part of this work has been funded by the NANO programme of the "Fonds National de Recherche", Luxembourg. Patrick Pirrotte is a recipient of a "Bourse Formation Recherche" of the Ministry of Research. INSERM, the Curie Institute, the "Région Ile de France" , the "Ministère de la Recherche et de la Technologie", the EDF radioprotection agency and ARC (grant # 7401) are gratefully acknowledged for financial support of the "Laboratoire de Microscopie Ionique".

6. References

1. Castaing, R. and Slodzian, G. "Microanalyse par émission ionique secondaire" *J Microscopy* **1962** 395-410
2. Ziegler, J. "The Stopping and Range of Ions in Matter", *www.srim.org*
3. Shichi, H., Umemura, K. and Nomura, S. "Microarea element analysis using Cs LMIS incorporating SEM/SIMS" *SIMS XII* **1992** 259
4. Schuhmacher, M., Migeon, H. N. and Rasser, B. "Comparative useful yield measurements under oxygen, cesium and gallium bombardment" *SIMS VIII* **1992**
5. Storm, H. A., Stein, J. D. and Brown, F. K. "ARL probe news" *Joint US/Japan seminar on SIMS technique* **1976**
6. Schuhmacher, M. and Hillion, F. " Ultra fine feature analysis using secondary ion emission" *ISAM 95* **1995**
7. Charles Evans & Associates, *http://www.cea.com/cai/simsinst/m_anal.htm*
8. Levi-Setti, R., Crow, G. and Wang, Y. L. "Progress in high resolution scanning ion microscopy and secondary ion mass spectrometry imaging microanalysis" *Scan Electron Microsc* **1985** 535-52
9. Slodzian, G., Daigne, B., Girard, F., Boust, F. and Hillion, F. "Scanning secondary ion analytical microscopy with parallel detection" *Biol Cell* **1992** *74* 43-50
10. Stadermann, F. J., *http://presolar.wustl.edu/nanosims/schematic.html Washington University, St Louis, Missouri*
11. Aggeler, J. and Werb, Z. "Initial events during phagocytosis by macrophages viewed from outside and inside the cell: membrane-particle interactions and clathrin" *J Cell Biol* **1982** *94* 613-23
12. Chandra, S. and Morrison, G. H. "Sample preparation of animal tissues and cell cultures for secondary ion mass spectrometry (SIMS) microscopy" *Biol Cell* **1992** *74* 31-42
13. Kellenberger, E. "The potential of cryofixation and freeze substitution: observations and theoretical considerations" *J Microsc* **1991** *161 (Pt 2)* 183-203
14. Lechene, C. and Bonventre, J. "DNA replication and protein turn-over in post-ischemic kidney repair studied with multi-isotope imaging mass spectrometry (MIMS)" *14th International conference on Secondary Ion Mass Spectrometry (SIMS XIV)* **2003**
15. Peteranderl, R. and Lechene, C. "Measure of carbon and nitrogen stable isotope ratios in cultured cells" *J Am Soc Mass Spectrom* **2004** *15* 478-85
16. Galle, P. "Cartographies moléculaires ultrastructurales par microscopie ionique" **1991** *7* 944-952
17. Strick, R., Strissel, P. L., Gavrilov, K. and Levi-Setti, R. "Cation-chromatin binding as shown by ion microscopy is essential for the structural integrity of chromosomes" *J Cell Biol* **2001** *155* 899-910
18. Strissel, P. L., Strick, R., Gavrilov, K. L. and Levi-Setti, R. "Specific Mg2+ binding at human and Indian muntjac chromosomal Giemsa bands" *Applied Surface Science* **2004** *231-232* 485-489
19. Lorey, D. R., 2nd, Morrison, G. H. and Chandra, S. "Dynamic secondary ion mass spectrometry analysis of boron from boron neutron capture therapy drugs in co-cultures: single-cell imaging of two different cell types within the same ion microscopy field of imaging" *Anal Chem* **2001** *73* 3947-53
20. Smith, D. R., Chandra, S., Barth, R. F., Yang, W., Joel, D. D. and Coderre, J. A. "Quantitative imaging and microlocalization of boron-10 in brain tumors and infiltrating tumor cells by SIMS ion microscopy: relevance to neutron capture therapy" *Cancer Res* **2001** *61* 8179-87

21. Johannes, L. "The epithelial cell cytoskeleton and intracellular trafficking. I. Shiga toxin B-subunit system: retrograde transport, intracellular vectorization, and more" *Am J Physiol Gastrointest Liver Physiol* **2002** *283* G1-7
22. Johannes, L. and Goud, B. "Surfing on a retrograde wave: how does Shiga toxin reach the endoplasmic reticulum?" *Trends Cell Biol* **1998** *8* 158-62
23. Mallard, F., Antony, C., Tenza, D., Salamero, J., Goud, B. and Johannes, L. "Direct pathway from early/recycling endosomes to the Golgi apparatus revealed through the study of shiga toxin B-fragment transport" *J Cell Biol* **1998** *143* 973-90
24. Römer, W. e. a. "Sub-cellular localization of a 15N-labelled peptide vector using NanoSIMS imaging" *Appl. Surface Science* **2005 (in press)**
25. Berry, J. P. "The role of lysosomes in the selective concentration of mineral elements. A microanalytical study" *Cell Mol Biol (**Noisy-le-grand??**)* **1996** *42* 395-411
26. Galle, P., Levi-Setti, R., Lamperti, A., Bourahla, K. and Escaig, F. "Subcellular localization of aluminum and indium in the rat kidney" *Applied Surface Science* **2004** *231-232* 475
27. Audinot, J. N., Schneider, S., Yegles, M., Hallegot, P., Wennig, R. and Migeon, H. N. "Imaging of arsenic traces in human hair by nano-SIMS 50" *Applied Surface Science* **2004** *231-232* 490
28. Lhuissier, F., Lefebvre, F., Gibouin, D., Demarty, M., Thellier, M. and Ripoll, C. "Secondary ion mass spectrometry imaging of the fixation of 15N-labelled NO in pollen grains" *J Microsc* **2000** *198 (Pt 2)* 108-15
29. Chabala, J. M., Edward, S., Levi-Setti, R., Lodding, A., Lundgren, T., Noren, J. G. and Odelius, H. "Elemental imaging of dental hard tissues by secondary ion mass spectrometry" *Swed Dent J* **1988** *12* 201-12
30. Lodding, A. "Quantitative ion probe microanalysis of biological mineralized tissues" *Scan Electron Microsc* **1983** 1229-42
31. Lundgren, T., Persson, L. G., Engstrom, E. U., Chabala, J., Levi-Setti, R. and Noren, J. G. "A secondary ion mass spectroscopic study of the elemental composition pattern in rat incisor dental enamel during different stages of ameloblast differentiation" *Arch Oral Biol* **1998** *43* 841-8

Résumé

La spectrométrie de masse à ions secondaires (SIMS) est une technique de caractérisation chimique de la matière par balayage avec un faisceau d'ions primaires. L'impact des ions primaires provoque une cascade de collisions atomiques causant un déplacement des éléments constitutifs de l'échantillon, émis sous forme d'ions, et séparés selon les critères d'énergie et de masse par un spectromètre. Le NanoSIMS fait partie de la famille des microscopes SIMS dynamiques capable d'imager à haute résolution la distribution d'ions élémentaires dans un échantillon.

Les travaux présentés dans cette thèse sont axés sur le développement de techniques de préparations d'échantillons biologiques pour le NanoSIMS, et sur la recherche d'applications biologiques spécifique. Plusieurs outils informatiques ont été développés afin de permettre le traitement d'images provenant de cet instrument. Des suggestions sont proposées afin d'améliorer les conditions d'analyses et d'acquérir des images de meilleure qualité.

Grâce à sa résolution en masse, le NanoSIMS a permis de suivre directement des molécules marquées par des isotopes résultant d'un marquage métabolique, démontré lors d'expériences « pulse-chase » et d'immunomarquage par des anticorps marqués à l'^{15}N.

Il découle de nos travaux que la sensitivité et la résolution de l'instrument le rendent particulièrement intéressant pour des études de pollution atmosphérique. Cette affirmation est soutenue par une étude sur la distribution de métaux traces dans des lichens, comme bioindicateurs.

Lors de ces études, l'utilisation du NanoSIMS a été complémentée par des techniques d'imagerie alternatives telles que la microscopie confocale et électronique.

Mots-clés: SIMS, NanoSIMS, imagerie, isotopes stables, azote-15, immunomarquage, « pulse chase », marquage métabolique, détection de métaux-traces, implantation, analyse ratiométrique